DEVELOPMENT OF SOLAR SELECTIVE ABSORBER COATINGS FOR CONCENTRATED SOLAR THERMAL POWER APPLICATIONS

A THESIS

SUBMITTED TO THE

NATIONAL INSTITUTE OF TECHNOLOGY WARANGAL

FOR THE AWARD OF THE DEGREE OF

DOCTOR OF PHILOSOPHY

IN

PHYSICS

BY

M. SHIVA PRASAD

Roll No. 716055

Supervisor (s):

Dr. B. SOBHA, **ASSOCIATE PROFESSOR, DEPARTMENT OF PHYSICS,**

NIT, WARANGAL &

Dr. S. SAKTHIVEL, **SCIENTIST- "F" & HEAD OF THE DEPARTMENT,**

CSEM, ARCI, HYDERABAD

DEPARTMENT OF PHYSICS

NATIONAL INSTITUTE OF TECHNOLOGY

WARANGAL-506004, INDIA

MARCH – 2022

DEDICATED TO MY FAMILY

AND

FRIENDS

NATIONAL INSTITUTE OF TECHNOLOGY

DEPARTMENT OF PHYSICS

CERTIFICATE

This is to certify that the thesis entitled **"Development of Solar Selective Absorber Coatings for Concentrated Solar Thermal Power Applications"** being submitted by **Mr. M. Shiva prasad (Roll No.716055)** to the Department of Physics, National Institute of Technology, Warangal, India, is a record of bonafide research work carried out by him under our supervision and it has not been submitted elsewhere for the award of any degree.

Dr. S. Sakthivel
Scientist- "F" and Head of the Department
Centre for Solar Energy Materials
International Advanced Research Centre
for Powder Metallurgy and New Materials
Hyderabad
Thesis supervisor (External)

Dr. B. Sobha
Associate professor
Department of Physics
National Institutes of Technology
Warangal
Thesis supervisor (Internal)

DECLARATION

This is to certify that the work presented in the thesis entitled "**Development of Solar Selective Absorber Coatings for Concentrated Solar Thermal Power Applications**" is a bonafide work done by me under the supervision of **Dr. B. Sobha, Associate Professor, Department of Physics, NIT Warangal**, and **Dr. S. Sakthivel, Scientist-"F", ARCI, Hyderabad** was not submitted elsewhere for the award of any degree. I declare that this written submission represents my ideas in my own words, and where others' ideas or words have been included, I have adequately cited and referenced the original sources. I also declare that I have adhered to all principles of academic honesty and integrity and have not misrepresented or fabricated or falsified any idea/data/fact/source in my submission. I understand that any violation of the above will be a cause for disciplinary action by the Institute and can also evoke penal action from the sources which have thus not been properly cited or from whom proper permission has not been taken when needed.

M. Shiva Prasad

Roll No. 716055

Date: 03-03-2022

ACKNOWLEDGEMENTS

I take this opportunity to thank the people who have been involved in my efforts directly and indirectly to complete this dissertation. The words mentioned here may not be sufficient to express my gratitude towards them.

Foremost, I sincerely thank my supervisor(s), **Dr. S. Sakthivel**, scientist "F", Head of the CSEM, ARCI, Hyderabad, and **Dr. B. Sobha**, Associate Professor, Department of Physics at NIT, Warangal, for their valuable guidance, motivation, and encouragement throughout my Ph.D. work. It has been a great pleasure for me to work under their guidance. I am thankful to my supervisor(s) for believing in me and patiently bearing me. This thesis wouldn't have been possible without their immense support, academically and personally.

I would like to thank the Late **Dr. G. Padmanabham**, previous director, **Dr. T. N. Rao**, current director of ARCI, Hyderabad, and the **Prof. N. V. Ramana Rao**, Director of NIT-Warangal, for supporting my work.

I am thankful to my Doctoral Scrutiny Committee members, **Prof. D. Dinakar** (Chairman and Head of the Department), **Prof. R. L. N. Sai prasad** (Department of Physics), **Prof. S. Srinivas Rao (**Department of Mechanical engineering), and **Prof. K. Venugopal Reddy** (Department of Physics) for constantly reviewing my progress and providing valuable suggestions in a constructive way that helped me to carry forward my work successfully. I would like to extend my sincere thanks to all the faculty members, office staff, and scholars of the Physics department for their support whenever necessary.

I am deeply indebted to scientists **Dr. A. Srinivas Rao**, **Dr. Suresh**, **Dr. Sarada**, **Dr. Sreekanth**, **Dr. Ganapathy**, **Dr. Sanjay R. Dhage**, **Dr. Prashanth**, **Dr. Easwaramoorthy**, **Dr. Anandan**, and **Dr. Neha** at ARCI, Hyderabad for their help in characterization and analysis.

I sincerely thank my colleagues **K. Phani Kumar**, **C. Narendra**, **V. Saikrishna**, **N. Chander**, and **P. Samhita** for their valuable suggestions and advice on many occasions. I want to thank all my co-scholars of ARCI, Hyderabad, and NIT Warangal.

I thank projects **Solar Energy Research Initiative Programme** (DST/TM/SERI/DSS/328/G) and **Technology Research Centre** (AI/1/65/ARCI/2014) sponsored by the Department of Science and Technology (DST), Govt. of India, for supporting my work.

I am thankful to my friends **D. Karthik**, **K. Chandra Sekhar Reddy**, **G. Srihari**, **P. Kiran Seshu**, **T. Rajesh**, **G. Nagesh**, and **P. Shiva Shanker** for being with me in all tough times in my life. Finally, I would like to thank my family members **M. Pakeerappa**, **M. Devendramma, M. Narsimhulu**, and **M. Yogender** for everything. I gratefully acknowledge one and all once again.

Date: 03-03-2022 (M. Shiva Prasad)

Contents

Chapter 2: Experimentational section

Chapter 3: Development of Co-Cu-Mn-O_x based solar selective absorber coatings (SSACs)

List of notations

%	Percentage	h	Thickness of the coating
K	Kelvin temperature	η	Liquid viscosity
A°	Angstrom	i	Withdrawal speed
nm	Nanometre	γ	Surface tension of the liquid
cm	Centimetre	ρ	Liquid density
µm	Micrometre	g	Gravitational force
mm	Millimetre	n	Refractive index
km	Kilometre	k	Extinction coefficient
mg	Milligram	eV	Electron volt
W	Watt	ψ	Amplitude ratio
m^2	Square meter	Δ	Phase difference
°	Degree angle	T_{amb}	Ambient air temperature
z	Zenith angle	Q_{total}	Total heat loss
cos	Cosine	$Q_{Cond.}$	Conduction loss
°C	Degree Celsius	$Q_{rad.}$	Radiation loss
mbar	Milli bar	$Q_{conv.}$	Convection loss
α	Solar absorptance	A	Absorber surface area
ε	Spectral emittance	T_{abs}	Absorber surface temperature
I_s	Solar radiation intensity		
R	Reflectance		
λ	Wavelength		
η_T	Photothermal conversion efficiency		
ε_T	Thermal emissivity		
σ	Stefan-Boltzmann constant		
C	Concentration ratio		
I	Intensity of direct normal irradiance		
SiO_2	Silicon dioxide		
T	Temperature		

List of abbreviations

IEA	International Energy Agency
GW	Gigawatt
MW	Megawatt
AM	Air mass
ASTM	American society for testing and materials
DNI	Direct normal irradiance
DHI	Diffuse horizontal irradiance
GHI	Global horizontal irradiance
STS	Solar thermal system
HTF	Heat transfer fluid
CST	Concentrated solar thermal
CSP	Concentrated solar thermal power
SS	Stainless steel
SSAC	Solar selective absorber coating
PVD	Physical vapour deposition
DI	Deionized
UV	Ultraviolet wavelength range
Vis	Visible wavelength range
NIR	Near-infrared wavelength range
UMA	Universal Measurement Accessory
IR	Infrared radiation
FT-IR	Fourier-transform Infrared
XRD	X- ray diffraction
GI-XRD	Grazing incidence X-ray diffraction
TEM	Transmission electron microscope
FE-SEM	Filed emission scanning electron microscope
SAED	Selected area electron diffraction
XPS	X-ray photo electron spectroscopy
TG-DTA	Thermogravimetric and differential thermal analysis
UHV	Ultra-high vacuum
HPC	Hydroxy propyl cellulose
IPE	2-isopropoexy ethanol

ICDD	International centre for diffraction data
GPTS	3-Glycidyloxypropyl) trimethoxysilane
IPA	Isopropyl alcohol
NaOH	Sodium hydroxide

List of Figures

Chapter 1: Introduction

Chapter 2: Experimentational section

Chapter 3: Development of Co-Cu-Mn-O_x based solar selective absorber coatings (SSACs)

3.1. Development of SS/Co-Cu-Mn-O_x/SiO_2 SSACs

3.2 Development of High-Performance Tandem Layered Absorber with Wide-Angular Absorptance for Solar Thermal Systems

3.3. Development of Zirconia Nanoparticles Embedded Spinel Selective Absorber Coatings

Chapter 4: Development of Cu-Mn-Ni-O_x based solar selective absorber coatings (SSACs)

Chapter 5: Performance comparison of solar selective absorber coatings

Chapter 6: Upscaling of SS/Cu-Mn-Ni-O_x/SiO_2 SSACs

List of tables

Chapter 1: Introduction

Chapter 3: Development of Co-Cu-Mn-O_x based solar selective absorber coatings (SSACs)

3.1. Development of SS/Co-Cu-Mn-O_x/SiO_2 SSACs

3.2 Development of High-Performance Tandem Layered Absorber with Wide-Angular Absorptance for Solar Thermal Systems

3.3. Development of Zirconia Nanoparticles Embedded Spinel Selective Absorber Coatings

Chapter 4: Development of Cu-Mn-Ni-O_x based solar selective absorber coatings (SSACs)

Chapter 5: Performance comparison of solar selective absorber coatings

Chapter 6: Upscaling of SS/Cu-Mn-Ni-O_x/SiO_2 SSACs

Abstract

Solar selective absorber coatings (SSACs) play a vital role in solar thermal systems. SSACs selectively absorb and emit radiation at a cut-off wavelength depending upon the operating temperature. Several commercial SSACs coated receivers are developed by physical vapor deposition (PVD) methods. Most of the SSACs lack thermal stability in the case of vacuum breaches due to glass tube breakage. Notably, the development of SSACs by vapor deposition is costly due to vast and complex instruments requiring high capital investment. Hence, it could be a potential problem in delivering affordable, stable SSACs in non-vacuum conditions for solar thermal applications. In this regard, the present thesis focuses on the development of thermally stable SSACs (≤500 °C) by cost-effective wet chemical and dip-coating methods for concentrated solar thermal power applications. The spinel-structured materials have attracted significant attention in the field of SSACs. Spinel oxides comprise a complex crystal structure, with many degrees of freedom available to engineering optical properties, and they are well known for high thermal stability. Thus, transition metal precursors of Copper, Manganese, Cobalt, and Nickel were utilized to synthesize the absorber coating solutions to develop a spinel-structured thin film over on SS 304 substrate. Several SSACs were developed to obtain high absorption (≥0.95), low emittance (≤0.15), and thermal stability up to 500 °C. Among all, the SS/Co-Cu-Mn-O_x/SiO_2 and SS/ Cu-Mn-Ni-O_x/SiO_2 have exhibited an excellent solar absorptance of 0.93, 0.95, and emittance 0.19, 0.14 respectively, along with thermal stability at 500 °C for 250-hours in open-air atmospheric conditions. The SSACs (SS/Co-Cu-Mn-O_x/SiO_2 and SS/Cu-Mn-Ni-O_x/SiO_2) were compared in terms of thermal stability, corrosion rate, adhesion, wide-angular absorptance, and photothermal conversion efficiency. The SS/Cu-Mn-Ni-O_x/SiO_2 SSAC shows good optical properties, high corrosion resistance, higher wide-angular solar absorptance, and high photothermal conversion efficiency compared to SS/Co-Cu-Mn-O_x/SiO_2. Hence, SS/Cu-Mn-Ni-O_x/SiO_2 is utilised to develop prototype receivers having a 2-m length and 42 mm outer diameter (4 x 2-m). The non-evacuated commercial receivers (Hi-min, China) with the exact dimensions (4 Nos. of 2-m length with 42 mm outer diameter) were installed in the parallel row of a parabolic trough test rig for the performance comparison with the indigenous receivers. Heat gain and heat loss studies indicated that indigenous receivers exhibit better performance than commercial receivers. The cost-efficient indigenously developed receivers with open-air atmospheric stability have high performance compared to commercial receivers and are more promising candidates for concentrated solar thermal power applications

Chapter 1

1. Introduction

1 Energy and current statistics

Energy has been a crucial ingredient for all human activities, and it is playing a vital role in the development of the world. At present, the world's energy requirement majorly depends on fossil fuels such as Oil, Coal, and Natural gas, and it accounts for a total of 81.3%, as per International Energy Agency (IEA) in 2020 [1]. Developing countries like India and China are heavily reliant on fossil fuels to meet the increased energy demands. Fossil fuels are energy-rich and relatively cheap to process. However, the reliance on fossil fuels is leading to land, water, and air pollution. It is estimated that the 33513 Metric tons of carbon dioxide equivalent emissions are released every year because of burning fossil fuels worldwide [1]. Consequently, the emitted greenhouse gases are trapping the heat and leading to climate change, such as a rise in temperature, drought, and heat waves.

1.1 Renewable energy

The world is slowly shifting to a clean, affordable, and renewable source of energy due to ill effects of fossil fuels. Sources for renewable energies are sunlight, wind, tides, waves, and geothermal heat, and these tend to replenish on a human timescale naturally. Strong winds, sunny skies, abundant plant matter, heat from the Earth, and fast-moving water can provide a replenished supply of energy. In contrast to fossil fuels, most renewable energy sources produce little to no global warming emissions. In addition, emissions associated with the manufacturing, installation, operation, decommissioning of renewable energy technologies are minimal. In this connection, Renewable energies are playing an important role in generating electricity worldwide. India is set to achieve 450 GW of renewable energy installed capacity by 2030.

1.2 Solar energy

Solar energy can be a potential solution to growing energy needs due to its abundance & reliability. Sun emits radiation mainly in ultraviolet (UV), visible and infrared regions. The emitted solar radiation is attenuated by scattering and absorption by Earth's atmosphere constituents so that less power arrives at the surface (closer to 1,000 W/m^2) in clear conditions when the Sun is near the zenith. In this connection, the air mass coefficient is used to characterize the solar spectrum before and after the solar radiation has travelled through the atmosphere [2]. AM 1.5 is used to characterize terrestrial power-generating panels. The

American society for testing and Materials (ASTM) G173-03 reference spectra are shown in Figure 1.1 [3]. The solar radiation emitted from the Sun comprises ultraviolet, visible, and infrared radiation bands. Ultraviolet contains wavelengths between 100-400 nm. Visible light falls within the range of 400-700 nm, and infrared light includes wavelengths from 700 nm to over 1 mm.

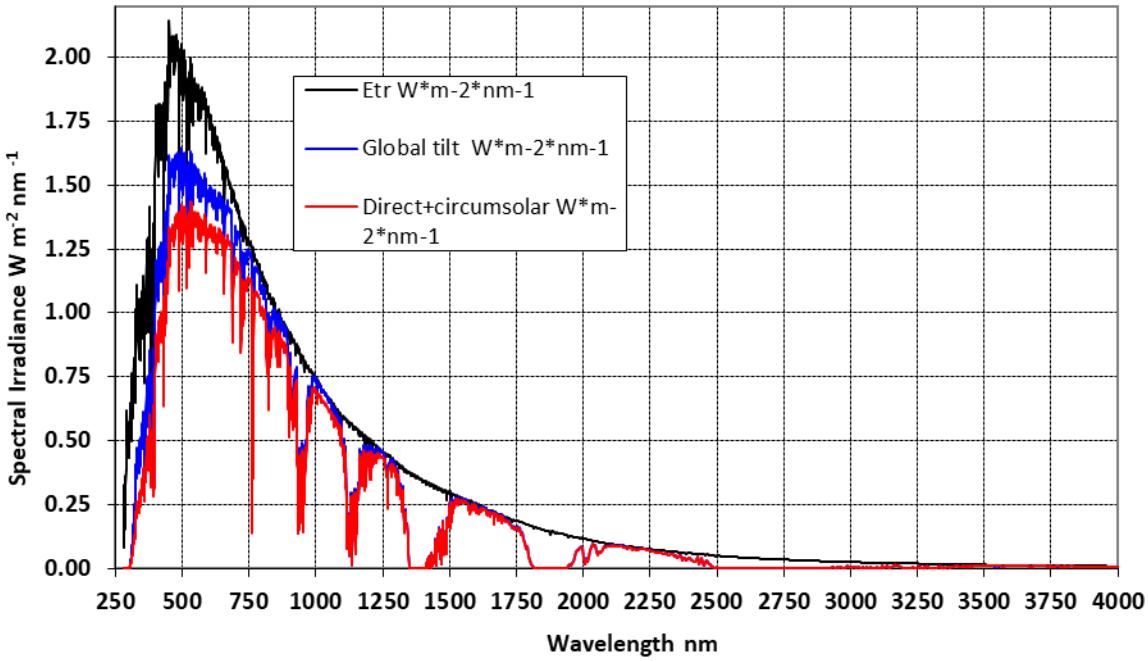

Figure 1.1. ASTM G173-03 Reference Spectra

The incident solar radiation on the Earth's surface can be categorized into three components as Global Horizontal Irradiance (GHI), Direct Normal Irradiance (DNI), and Diffuse Horizontal Irradiance (DHI). GHI is the total amount of solar radiation received from above by a surface horizontal to the ground. The GHI can be expressed as in the below equation

$$GHI = DHI + DNI * \cos(z) \quad \text{----------(1)}$$

where z is the solar zenith angle. DNI is solar radiation that comes in a straight line from the direction of the sun at its current position in the sky. The DNI map of India is shown in Figure 1.2 (Source: The map has been prepared by Solargis for The World Bank-2020). DHI is solar radiation that doesn't arrive directly from the sun but has been scattered by molecules and particles in the atmosphere and comes from all directions, rather than arriving on a direct path from the sun.

India is located in the equatorial sun belt of the earth, thereby receiving abundant radiant energy from the sun. In most parts of India, clear sunny weather is experienced 250 to 300 days a

year. The annual global radiation varies from 1600 to 2200 kWh/m^2, which is comparable with radiation received in the tropical and sub-tropical regions. The equivalent energy potential is about 6,000 million GWh of energy per year. The government of India recognized the potential of solar energy in the aspect of future needs and to reduce pollution. As per the Paris Accord on Climate Change, India pledged that by 2030, 40% of installed power generation capacity would be majorly from non-fossil fuel sources. Due to technological advancement, competition, and geographical advantages, solar energy investments are increasing compared to the other renewables in India [4].

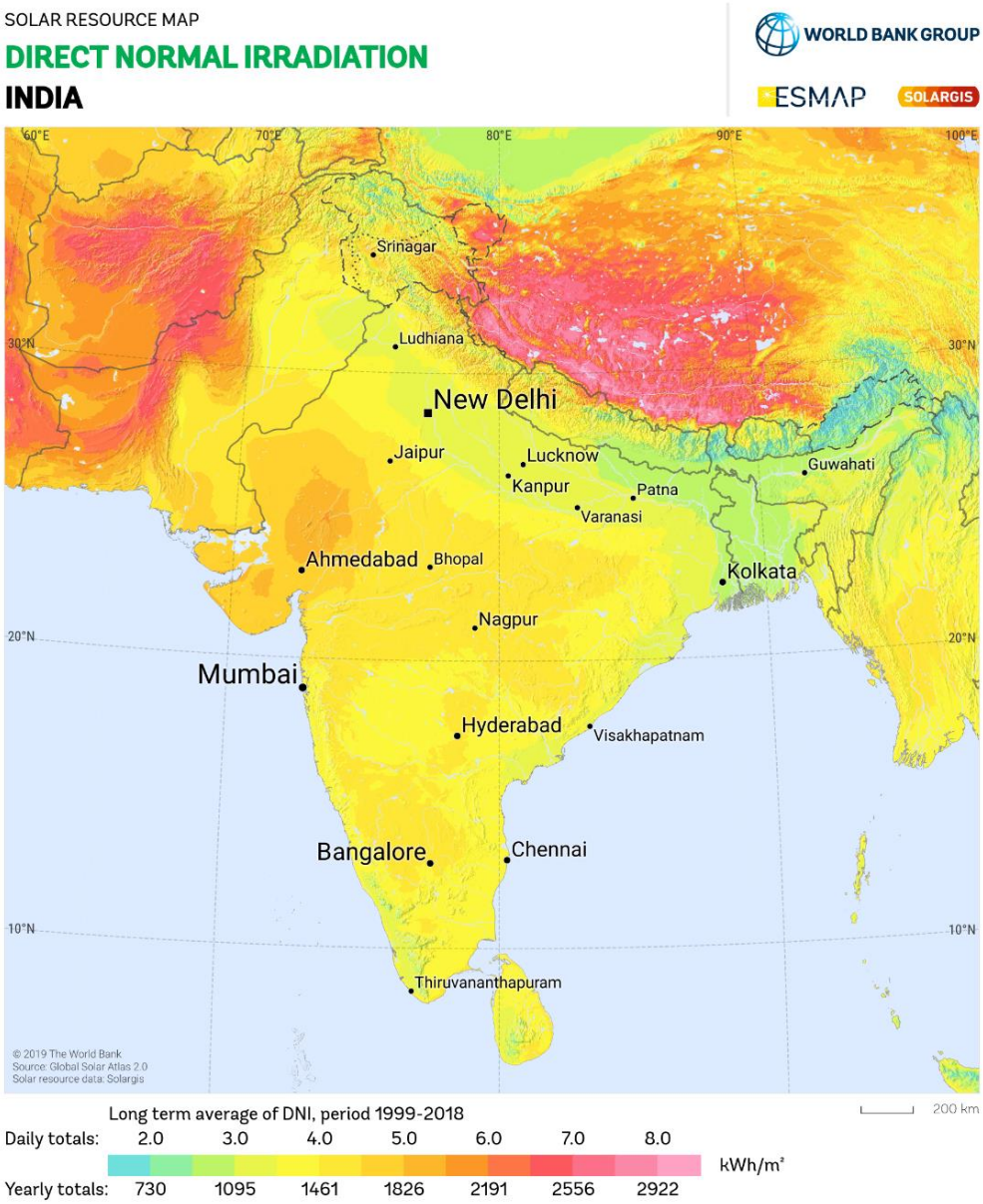

Figure 1.2. Map of Direct normal irradiance-India

1.3 Solar energy conversion technologies

Solar energy is harnessed majorly by three techniques i) Photovoltaics, ii) Photochemical processes, and iii) Solar thermal systems. These technologies have enormous potential to be part of the future energy sector [5]. The conversion of solar radiation into the required form of energy by different techniques is shown in the classification chart (Figure 1.3).

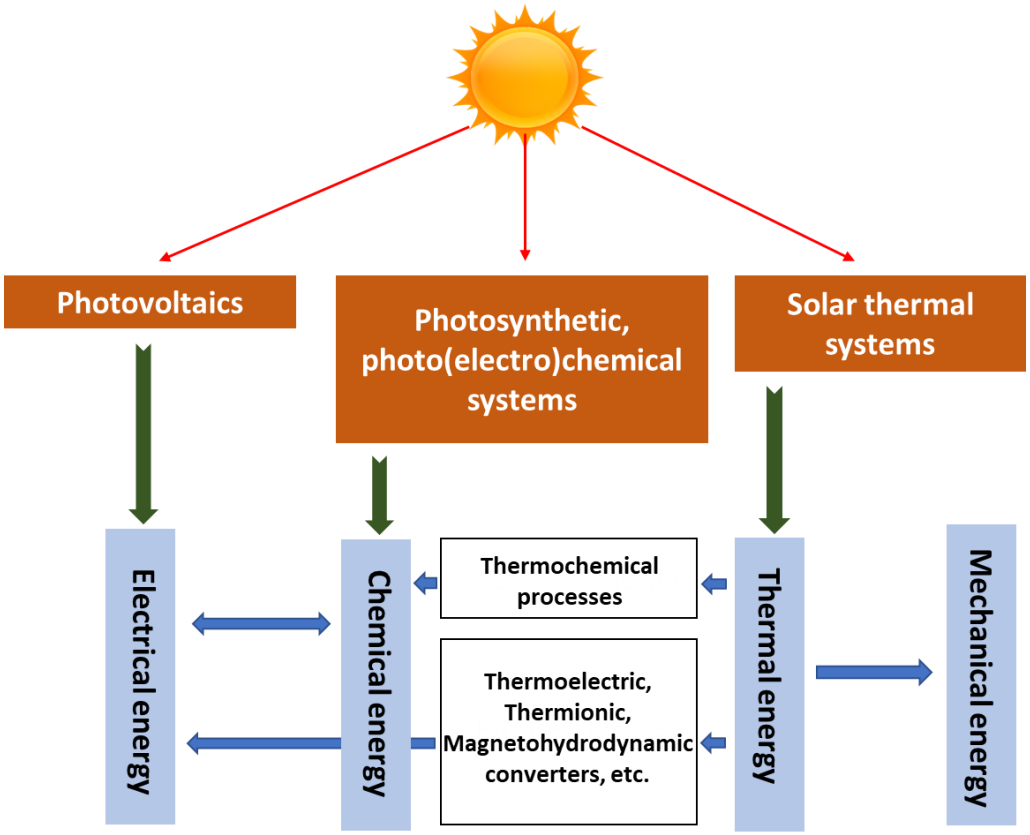

Figure 1.3. Solar energy conversion paths and technologies

1.3.1 Photovoltaics

Photovoltaics is based on the photovoltaic effect, where solar radiation is converted into electricity. The first working model of photovoltaic (PV) cell was developed in Bell Laboratories in 1954. The photocurrent was generated for the first time by irradiating the solar cell with sunlight. After that, several types of solar cells were developed to decrease the cost and improve photoconversion efficiency. Currently, silicon (Si) solar cells dominate the photovoltaics market (92%) followed by cadmium telluride (CdTe, 5%), copper indium gallium selenide ($CuInGaSe_2$ or CIGS, 2%) and amorphous silicon (a-Si:H, ~1%). However, the cost of Si wafer is a major concern [6]. Thus, scientists are vigorously working on new materials and methodologies to develop better photovoltaics cells. The highest achieved efficiency is 47.1%, according to the National renewable energy laboratory (NREL) cell

efficiency chart [7]. In PV energy conversion, solar panels are active only during daylight, and the storage of generated energy in a cost-effective way is a great challenge. In addition, the reduction in the efficiency of solar panels because of soiling could be a disconcerting phenomenon for these technologies.

1.3.2 Photochemical processes

Solar energy is also used to develop solar fuels directly by using artificial photosynthesis methods, and it has the potential to provide a scalable grid storage technology. The liquid fuels used in ships, aircraft, and heavy-duty trucks have total global demand, and they collectively become 40% of the current global transportation fuel demand. Thus, solar fuel technology attracted significant attention from researchers, and at present, it has reached different stages of research and development worldwide from proof of concept [8].

1.3.3 Solar thermal systems

Solar thermal systems (STS) convert direct and diffuse solar radiation into heat and can be used in various applications such as solar cooking, swimming pool heating, space heating, hot water, industrial heat processing, and power generation.

1.4 Solar collectors and their classification

Solar thermal systems comprise solar collectors to receive the solar radiation and to convert radiation into heat effectively using the components such as reflectors, receiver tubes and etc. Solar collectors transfer the energy obtained from the solar radiation to the heat transfer fluid (HTF). The delivery of the temperature is ideally dependent on the available solar flux at a particular time and geographical location. Solar collectors are classified into two types, depending upon the way they collect the radiation. They are concentrating and non-concentrating solar collectors. The classification of collectors is shown in Figure 1.4.

1.4.1 Non-concentrating solar collectors:

In non-concentrating systems, the collector area is the same as the absorber area, while in concentrating systems, collectors have a bigger interceptor (i.e., the area that intercepts the solar radiation) than the absorber. The non-concentrating systems use both direct and diffused solar radiation and don’t require a tracking system. In addition, they are simpler systems in comparison with concentrating collectors and thus require low maintenance. Examples of non-concentrating systems are Unglazed, Flat plate, and Evacuated tube collectors. The applications of non-concentrating systems are solar cooking, swimming pool heating, space heating, solar hot water heating, and solar air heaters.

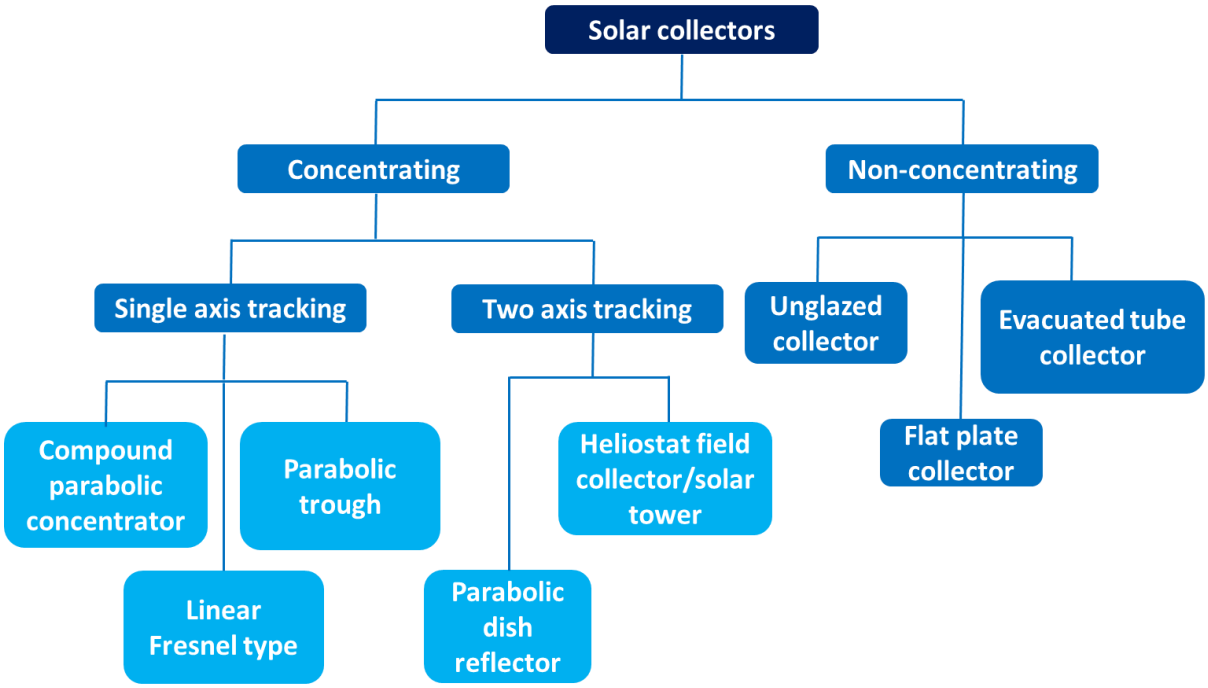

Figure 1.4. Chart representing the classification of solar collectors

1.4.2 Concentrating solar collectors:

Concentrating solar thermal systems (CST) technology can harness the immense solar resource and is emerging as a key technology to generate high temperatures with a low greenhouse gas emission level. In CST, high temperature can be obtained by concentrating the Sun's rays with reflectors to produce electricity. In CST power plants, thermal energy storage enables power generation even in the absence of solar radiation, which contributes to CST's distinctive ability to provide dispatchable power. The schematic of concentrating solar thermal systems with the parabolic collector is shown in Figure 1.5.

The objective for the development of concentrating solar collectors is to obtain high operating temperatures than non-concentrating solar collectors. It is achieved by employing the concentrators, i.e., reflectors or refractors and receivers. The shape of concentrators is cylindrical or surfaces of revolution and can be continuous or segmented. Receivers can be convex, flat, or concave and can be covered or uncovered. The collectors also comprise tracking systems single or dual-axis. The collectors are characterized by the concentration ratio (the ratios of collector aperture area to absorber area). The concentrators are treated in two groups: non-imaging collectors with a low concentration ratio and linear imaging collectors with intermediate concentration ratios.

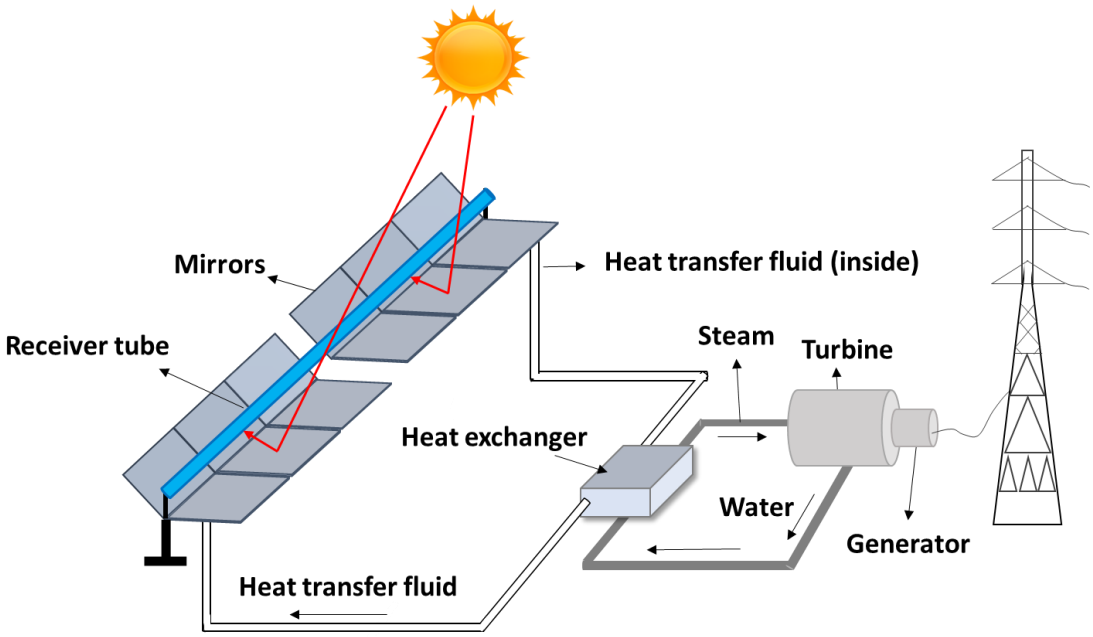

Figure 1.5. Schematic of a typical concentrating solar thermal system

The efficiency of the heat-to-electricity conversion process in CST systems is well known to be limited by Carnot efficiency. The total efficiency (η) is thus given by the product of the receiver efficiency and Carnot efficiency as per equation 2:

$$\eta = \left(\varepsilon\sigma\left(\frac{T_{abs}^4 - T_{amb}^4}{CI}\right)\right)\left(1 - \frac{T_{amb}}{T_{abs}}\right) \quad (2)$$

where α is receiver absorptance, ε is emissivity at the operating temperature, σ is the Stefan-Boltzmann constant, T_{abs} is the receiver temperature, T_{amb} is the ambient temperature, C is the concentrator ratio, and I is the solar insolation.

1.4.2.1 Status of concentrating solar thermal system technologies:

Various types of CST systems are installed globally, and their applications vary from solar heating, cooling, solar cooking to industrial applications. The developed CST systems may be different in terms of technology. However, the basic underlying principle is the same. Among all CST systems, Parabolic trough collector (PTC) technology is the most mature amongst the CST technologies contributing almost 4.4 GW of the worldwide installed capacity of 5.2 GW [9]. The total installed CST capacity in India is around 228.5 MW, with a significant contribution coming from Linear Fresnel Reflectors, which is approximately 125 MW. Other technologies like the Parabolic trough contributes close to 101 MW and Solar Tower is nearly 2.5 MW [9]. In this connection, India's industrial sector identified the significant potential in solar energy for process heat applications and slowly moving towards CST systems. United

Nations Industrial Development Organization (UNIDO) has identified a total market potential of 6.45GW for industrial applications in India during the preparation of CST Roadmap 2020. However, India lags behind other global leaders like China, Spain and the United States.

1.4.2.2 Challenges for CST in India

Industries are one of the biggest consumers of energy, and India alone accounts for the consumption of energy worth around USD 45 billion per annum. Recently, Indian industries have shown interest in exploiting renewable energies, especially solar power, due to their economic and environmental-friendly advantages. In this regard, Concentrating Solar Thermal (CST) technologies provide a viable solution for meeting the industrial process heat demands (≤ 250 °C). However, India lags behind other global leaders such as China, Spain and the United States. CST technologies have not yet been adopted widely throughout India. The critical challenges for the advancement of CST are 1) lack of reliable DNI for any location in the country, 2) low investor confidence, 3) low availability of skilled labour, and 4) the lack of indigenous CST components such as mirrors, receiver tubes, etc. The country does not have any indigenous manufacturing units/technologies of critical components such as mirrors, receiver tubes, etc. Most of the solar thermal companies import solar thermal components such as solar receiver tubes, concentrating mirrors, sun trackers, Anti-reflective coated glass envelops, and heat transfer fluids. Indigenous manufacturing of critical components like solar receiver tubes can bring down the capital cost as India can provide the required labour force at a low price. A study jointly conducted by the World Bank and Energy Sector Management Assessment Program (ESMAP) reported a cost reduction potential of 30% for receiver tubes, 28% for reflectors and 40% for support structures[10].

1.5 Solar receiver tube

The solar receiver tube is a vital component of solar thermal systems. The typical solar receiver tube is shown in Figure 1.6. It comprises a metal tube coated with solar selective absorber coating (SSAC) with high solar absorptance to convert solar radiation into heat effectively and low thermal emittance for generated infrared radiation. The tube is encapsulated with an Anti-reflective (AR) coated glass tube to increase the transmittance of solar radiation for better performance. Heat transfer fluid passes through the metal tube to transport the heat energy generated within the system.

Concentrating solar thermal systems are operated at high temperatures ≥100 °C, which could lead to high thermal losses, affecting the system's photothermal efficiency. To reduce the heat

losses, the vacuum is created in the order of 10^{-5} mbar in between the outer glass tube and metal tube. The outer glass tube of the receiver is connected to the inner steel tube by using stainless-steel bellows to compensate for different thermal expansion coefficients of glass and steel tubes at high operating temperatures. In addition, it helps to maintain the vacuum between the glass and metal tubes. One end of these expansion bellows is directly welded to the metal outer surface, while the other end is joined to the glass cover's end through a glass-to-metal welding process. In addition, chemical 'getters' are placed in the gap between the metal receiver pipe and the glass cover to absorb gas molecules passing from the fluid to the annulus through the steel pipe wall.

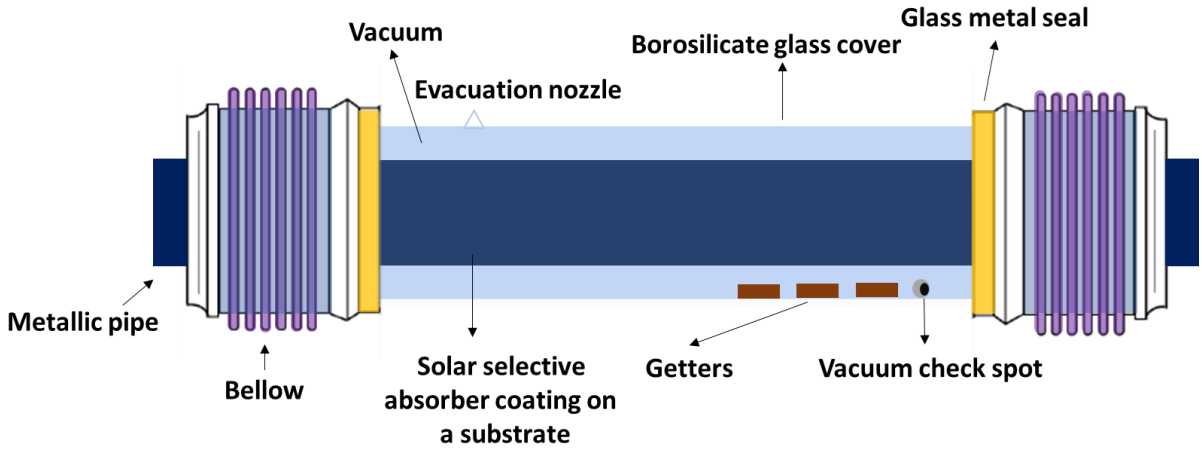

Figure 1.6. Schematic of an evacuated receiver tube

The development of evacuated receiver tubes is expensive and comprises of technical complexity, as mentioned above. Thus, only CST systems are preferred to obtain high efficiency. In this connection, non-evacuated receiver tubes play a crucial role in non-CST systems whose operating temperatures are less than 100 °C because thermal losses are not so critical at these temperatures. The length of receivers can be less than 5-m due to manufacturing constraints and depending upon the length of solar collectors. The receiver tubes can be welded parallelly and installed in collectors.

1.6 Solar selective absorber coating:

Solar selective absorber coating (SSAC) plays a significant role in a receiver tube's optical and thermal efficiency [11,12]. It absorbs concentrated or non-concentrated solar radiation that enters the metallic pipe and transfers the converted heat to the heat transfer fluid (HTF). The vacuum atmosphere inside metal and glass pipes reduces conduction and convection losses in receiver tubes, and the low thermal emittance of the selective absorber minimizes radiative

losses. The typical SSAC comprises a metal substrate, absorber, and AR layers. Metal substrate plays a vital role in obtaining high selectivity since metals are good reflectors in the infrared radiation (IR) wavelength region [8]. The absorber layer absorbs the incident solar radiation and converts it into heat, whereas the anti-reflective coating reduces the reflection to improve the overall absorption. The ideal SSAC spectrum exhibiting high absorptance and low emittance is presented in Figure 1.7.

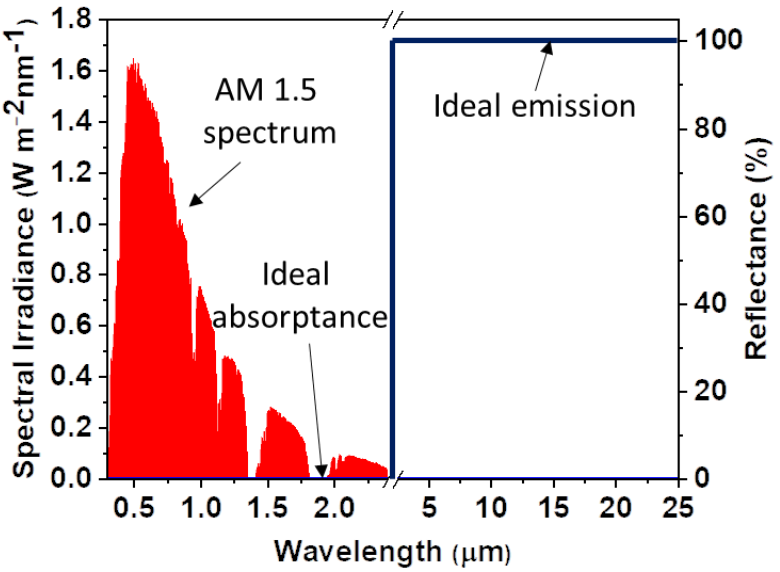

Figure 1.7. Ideal SSAC spectrum exhibiting high absorptance and low emittance.

SSACs are typically characterized by two key properties: solar absorptance and spectral emittance at an operating temperature. Practically, the mentioned properties are determined by measuring the reflectance of SSAC surface using spectrophotometers such as Ultraviolet/Visible/Near Infrared (UV-Vis-NIR) spectrophotometer Fourier Transform Infrared (FT-IR) spectrophotometer, respectively. The total normal solar absorptance (α) is calculated in the solar radiation region from 0.3 μm to 2.5 μm according to equation 3

$$\alpha = \frac{\int_{\lambda 1}^{\lambda 2} (1-R(\lambda)) I_s \, d\lambda}{\int_{\lambda 1}^{\lambda 2} I(\lambda) d\lambda} \quad \text{----------(3)}$$

where I_s is the intensity of solar radiation (AM 1.5, ASTM G173-03, ISO), R represents the total reflectance of the sample, λ_1 and λ_2 is the wavelengths.

According to Planck's blackbody radiation law, the sample heated by sunlight will thermally re-radiate the energy into the environment. The spectral emittance $\varepsilon\ (\lambda, T)$ is calculated by using

Kirchhoff's law in the infrared region from 2.5 μm to 25 μm for an opaque surface according to equation 4

$$\varepsilon\ (\lambda, T) = 1 - R\ (\lambda, T) \quad \text{----------(4)}$$

The measurements of absorptance and emittance were generally done at room temperature at near-normal incident angles. However, true absorptance and emittance depend on the SSACs at operating temperature and for varying angles. However, the mentioned method will still provide a reasonable estimate as long as the properties are not strongly dependent on temperature or incident angle, and using spectrophotometers is more common due to their convenience.

The solar thermal systems can attain high system efficiency by increasing the photothermal conversion efficiency (PTCE) with the aid of solar selective absorber coatings (SSACs). The PTCE of SSACs in a receiver is expressed (considering only radiative losses) by using equation (5)

$$\eta_{rec} = \alpha - \varepsilon\sigma\left(\frac{T_{abs}^4 - T_{amb}^4}{CI}\right) \quad \text{----------(5)}$$

where α is receiver absorptance, ε is thermal emissivity, σ is a Stefan-Boltzmann constant, T_{abs} is a receiver temperature, T_{amb} is a ambient temperature, C is a concentrator ratio, and I is solar insolation [13,14]. According to equation 4, SSAC should exhibit high solar absorptance and low emittance to obtain the high PTCE for the solar thermal systems. Typically, the transition from high to low emission should be between 1 to 2.5 μm, as shown in Figure 1.7. However, the ideal transition wavelength depends on the system's operating temperature [16].

1.6.1 Origin of SSAC and Selectivity Mechanisms:

SSAC's were initially proposed in the 1950s, and different physical mechanisms have been proposed to obtain high selectivity [11,12]. Based on the design principle, several mechanisms are reported [13,15,16]. Primary mechanisms are mentioned here, such as (a) Intrinsically selective, (b) Semiconductor coatings on metals, (c) Multi-layered stacks, (d) Metal-Dielectric composites, (e) Structured surface absorbers, (f) Photonic absorbers and (g) Dielectric-Metal-Dielectric (DMD) absorbers. At present, the combination of one or two mechanisms is used to achieve high absorption and low emittance. For example, multilayer cermet-based absorbers with intrinsically selective materials. Several mechanisms have already been explored for selective absorbers, and there is still room for further improvement by either enhancing the

light absorption or avoiding loss of heat after absorption. The schematics of SSACs are presented in the Figure 1.8.

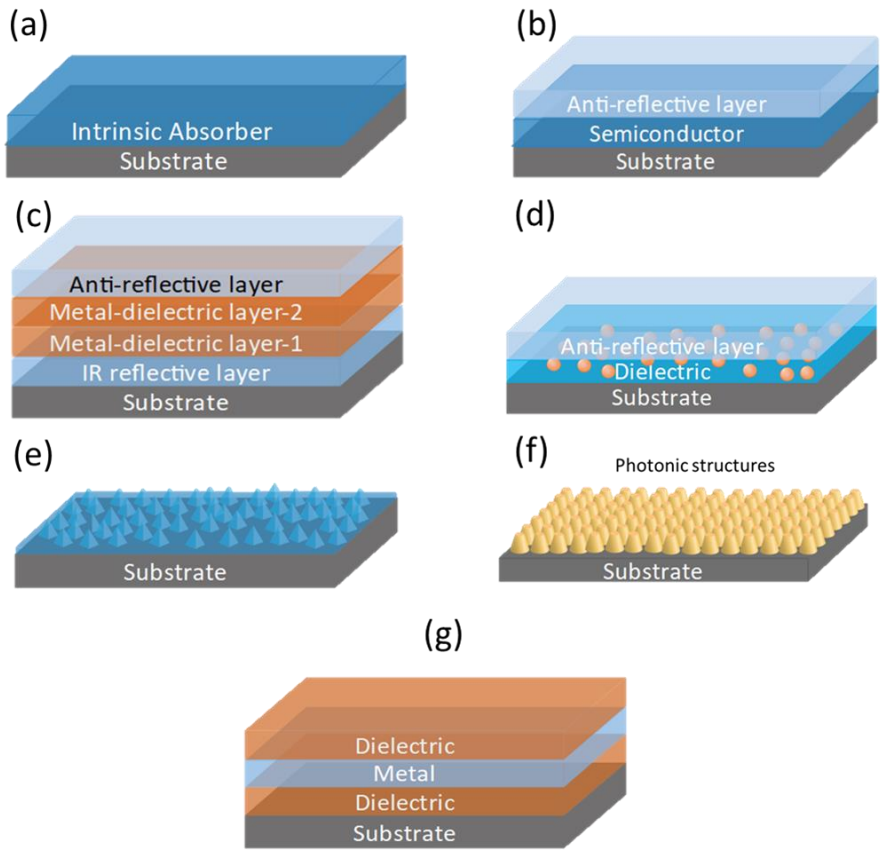

Figure 1.8. Schematic picture of solar selective absorber mechanisms.

The mechanisms as mentioned above were majorly reported in the literature. In practice, more than one mechanism is used to achieve better spectral selectivity. However, the typical SSAC comprises a metal substrate, absorber, and anti-reflective (AR) layers. It has been followed to develop SSACs in the present thesis and discussed in chapter 2.

1.7 Deposition methods for the development of solar selective absorber coatings

The deposition of coatings encompasses many different techniques and methods. Several deposition methods have been used to prepare the solar selective absorber coatings since Tabor proposed the first SSAC in 1955 [11,12]. There are several classifications for the deposition methods of thin films. However, the deposition methods for developing thin films like SSAC can be broadly classified into three categories depending on the nature of the deposition. They are 1) Physical vapor deposition (PVD), 2) Chemical vapor deposition (CVD), and 3) Solution-based deposition. The PVD and CVD come under vacuum-based depositions, whereas solution-based deposition comes under non-vacuum-based deposition methods. Vapor

deposition is a process in which materials in a vapor state are condensed through condensation, chemical reaction, or conversion to deposit thin films on different substrates. Vapor deposition techniques can be further classified into Physical vapor deposition (PVD) and Chemical vapor deposition (CVD). The classification of thin-film deposition methods is shown in Figure 1.9.

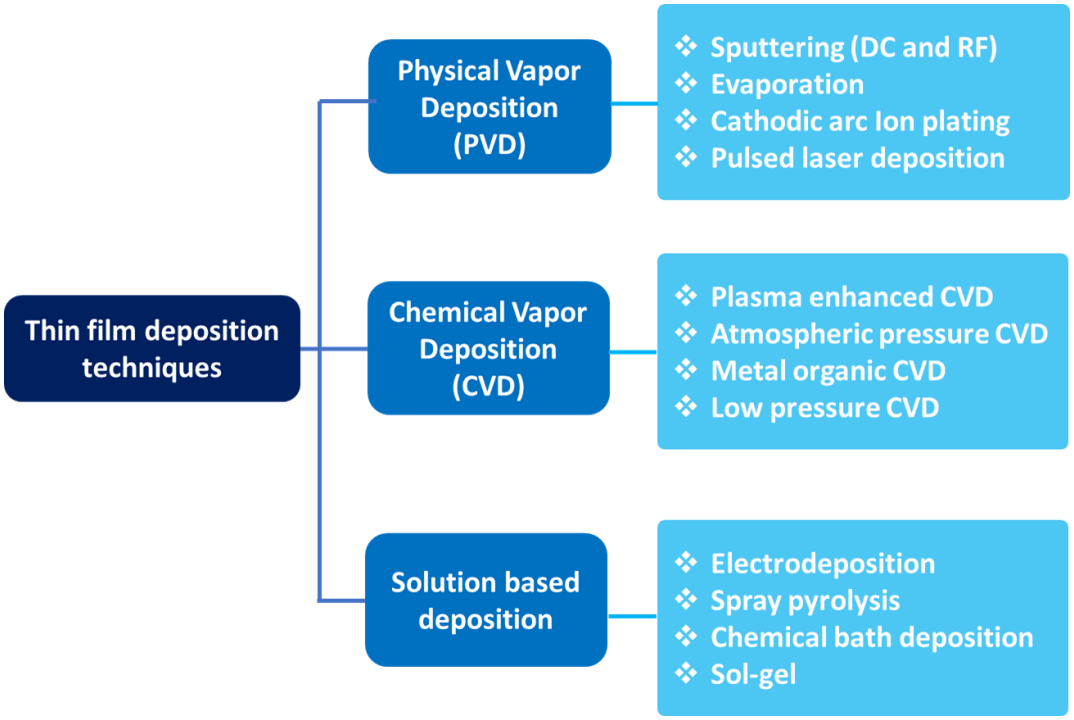

Figure 1.9. Classification of coating deposition techniques.

1.7.1 Physical vapor deposition (PVD):

A large number of SSACs for medium and high-temperature solar thermal applications were developed by PVD process since the 1970s [16]. PVD refers to various vacuum deposition methods that can be used to develop thin films and coatings. In the PVD method, the target material is vaporized and allowed to condense on a substrate placed in a chamber atom by atom. The most common PVD processes used for the development of SSAC are 1) Sputtering, 2) Evaporation, 3) Ion plating, 4) Pulsed laser deposition, etc.

The sputtering method is one of the efficient methods which has been widely used due to its numerous advantages like high deposition rates, reproducibility, precise control in thickness and deposition parameters, large-area deposition of various metallic and compound thin films, solar selective coatings used for mid-temperature applications [17,18]. Most commercially available SSACs are developed by a sputtering method. Some of the reported solar selective absorber coatings developed by PVD are tabulated in Table 1.1.

Table 1.1. Details of solar selective absorber coatings developed by physical vapor deposition techniques.

Material	**Substrate**	**Method**	**Optical properties**		**Stability**		**Ref.**
			α	**ε**	**Air (°C)**	**Vacuum (°C)**	
SS 304/TiB_2/Ti (B, N)/SiON/SiO_2	SS 304	Pulsed DC and RF magnetron sputtering	0.98	0.15 at 82 °C	2-hours in 450 °C	250 hours at 500 °C	[19]
AL/ZrB_2/Zr-B-N/PTEF	Al	Electron beam thermal evaporation	0.92	0.15	--	--	[20]
AlCrSiN/AlCrSiON/AlCrO	SS	Cathodic arc ion plating	0.95	0.14	600 °C for 600 hours	--	[21]
Al/Ti: Al_2O_3	Al	Pulsed laser deposition technique	0.95	0.05	--	--	[22]

1.7.2 Chemical vapor deposition (CVD):

CVD method is used to develop thin films by chemical reaction on the surface of substrates by using one or more gaseous compounds or elemental substances containing thin-film elements at elevated temperature, ranging from 500 to 1000 °C. The relatively high temperatures used in CVD guarantee the good adhesion of the coating to the substrate. The coating's thickness, uniformity, and density may be difficult to control with a high level of impurity in CVD processes. In the case of PECVD, undesired formation of microparticles and flakes can reduce the quality of the coatings and affect the vacuum systemSome of the reported solar selective absorber coatings developed by CVD are tabulated in Table 1.2.

Table 1.2. Details of solar selective absorber coatings developed by chemical vapor deposition techniques.

Material	Substrate	Method	Optical properties		Stability		Ref.
			α	ε	Air (°C)	Vacuum (°C)	
TiN/TiNO/ZrO2/SiO2	Si	PVD/PECVD	0.92	0.17 at 726 °C	--	726 °C for 150 hours	[23]
SiCH	Si	PECVD	0.92	0.08 at 500 °C	--	--	[24]
a-C:H/Ti	Al	PVD/PECVD	0.87	0.06	220 °C for 150 hours	--	[25]
a-Si:C: H/Ti	Al	PVD/PECVD	0.75	0.02	250 °C for 500 hours	--	[26]

1.7.3 Solution-based methods:

Solution-based methods have been used for the synthesis of nanomaterials and ceramics for many decades. Recently, researchers focused on developing solar selective solar absorbers by using a solution-based route. Synthesis of absorber and AR coating solutions by solution-based methods is simple, low-cost and has the potential to develop SSACs industrial level. The biggest challenge in solution-based methods is the synthesis of a uniform, stable precursor solution containing as-designed metal ions. Electrodeposition, spray pyrolysis, and Sol-gel are some of the solution-based methods, and these mentioned techniques developed a significant share of SSACs.

1.7.3.1 Electrodeposition or Electrochemical process:

Electrodeposition is considered a cost-effective alternative to vacuum-based deposition for the development of thin films. In the 1950s, Tabor developed black nickel, black chrome, and NiS-ZnS composites based SSACs using the electrodeposition method for flat plate collector

applications [11,12]. After that, several SSACs were extensively studied and reported by using the same process [27,28]. The significant advantages of the electrodeposition method are 1) easy to control coating composition, 2) relatively high purity, and 3) highly efficient utilization of the coating materials result in lower costs relative to other processes. In this way, the several coatings were upscaled and successfully commercialized in the worldwide market, and they are tabulated in Table 1.3. The SSACs developed by the Electrodeposition process are tabulated below.

Table 1.3. Details of solar selective absorber coatings developed by the Electrodeposition process.

Material	**Substrate**	**Method**	**Optical properties**		**Stability**		**Ref.**
			α	**ε**	**Air (°C)**	**Vacuum (°C)**	
Cu–$CuAl_2O_4$	Al	Electrodeposition	0.92	0.06	-	-	[29]
Co Nano cylinders -Al_2O_3	Al	Electrodeposition/ Femtosecond laser surface structuring	0.98	0.03	-	-	[30]
Black chrome	Cu	Electrodeposition	0.92	0.14	-	-	[31]
Black Ni	Cu	Electrodeposition	0.89	0.13	-	-	[32]

Despite having several advantages, the thermal and chemical stabilities of the electrodeposited coatings could not reach the requirements of the application, and the production processes were not environmentally friendly [17,33].

1.7.3.2 Spray Pyrolysis technique (SPT):

The spray pyrolysis technique (SPT) is used to develop powders, ceramic coatings, thin and thick films [34]. In SPT, the synthesised solution is sprayed on the heated surface to obtain the targeted chemical compound in the form of film. SPT method is simple, and it does not

consume much power compared to vacuum deposition methods. Some of the SSACs developed by SPT are presented in Table 1.4.

Table 1.4. Details of solar selective absorber coatings developed by the spray pyrolysis technique.

Material	**Substrate**	**Method**	**Optical properties**		**Stability**		**Ref.**
			α	**ε**	**Air (°C)**	**Vacuum (°C)**	
NiS-PbS and NiS-CdS	Al and galvanized Iron	Spray pyrolysis	--	--	250 °C	-	[35]
Cobalt Oxide	SS	Spray pyrolysis	0.93	0.14 at 100 °C	Up to 300 °C	-	[36]
$Al/Al_2O_3/NiO_x$	Al	Spray pyrolysis	0.92	0.03	-	-	[37]
CuO nanorods and CuO-PANI	Glass	Precipitation, In-situ polymerization and spray coating	0.94	0.01	-	-	[38]
$CuCo_2O_4$	Glass and SS	spray coating	0.79	0.10	-	-	[39]

Despite having several advantages, the reported coatings were not commercialized due to issues such as non-uniformity and stability at elevated temperatures. In addition, there were not many studies on thermal and corrosion studies of SSACs developed by SPT method.

1.8 Status of commercial SSACs:

Several solar selective absorber coatings have been reported by using vapor or non-vapor deposition methods for solar thermal applications in recent years. However, only some of them have been successfully commercialized [40]. Numerous companies such as Nitto Kohki, Tur-bosun, GRINM, Alanod Solar, Almeco-$TiNO_X$, Ikarus Coatings, S-Solar, Angelantoni-ENEA,

Siemens and SCHOTT, etc. are developed coatings for medium and high-temperature applications and have been successfully marketed worldwide. Table 1.5 provides information on the commercially available solar absorber coatings from some representative manufacturers, as well as product features [41].

Table 1.5. The commercialized solar absorber coatings/receivers

Company	Coatings/products	Absorptance & Emittance	Deposition method	Thermal stability
Schott Germany	PTR 7070 Premium	$\alpha \geq 0.95$, $\varepsilon \leq 0.095$ at 350 °C	PVD	500 °C in vacuum
Almeco-$TiNO_X$, Germany	$TiNO_X$ Energy $TiNO_X$ Nano $TiNO_X$ Artline	$\alpha=0.95$, $\varepsilon=0.04$ $\alpha=0.90$, $\varepsilon=0.05$ $\alpha=0.90$, $\varepsilon=0.05$	Activated reactive evaporation	400 °C in vacuum
Alanod solar Germany	Etaplus Mirotherm Mirosols TS	$\alpha=0.95$, $\varepsilon=0.04$ at 100 °C $\alpha=0.95$ $\alpha=0.95$	PVD PVD Coil coating	IEA Task X test
Nitto Kohki, Japan	SS–C	$\alpha=0.93$, $\varepsilon=0.04$ at 100 °C	--	300 °C in vacuum
S-Solar Sweden	SunStrip Lazerplate	$\alpha=0.96$, $\varepsilon=0.07$ $\alpha=0.95$, $\varepsilon=0.05$	Sputtering	IEA Task X test
TurboSun, China	W-AlN SS–AlN	α= 0.92–0.94, ε= 0.08–0.10 at 350 °C **α=** 0.94–0.95, ε= 0.12–0.14 at 350 °C	Magnetron sputtering	330–500 °C in vacuum
GRINM China	GRIST 70/90/42 and GRIST 70A	α =0.96, ε =0.09 at 400 °C α =0.95, ε =0.12 at 300 °C	--	400 °C in vacuum and 350 °C in air
Siemens Germany	Al_2O_3 cermet W–Al_2O_3	α =0.96, ε =0.10 at 400 °C α =0.96, ε =0.16 at 350 °C	---	350–500 °C in vacuum
Angelantoni-ENEA, Italy	Mo–SiO_2 W/W-Al_2O_3/Al_2O_3	α =0.94, ε =0.13 at 580 °C α =0.93, ε =0.14 at 550 °C	Magnetron sputtering technique	580 °C in vacuum
Maxorb	Black nickel NiS-ZnS	α =0.88-0.96, ε =0.03-0.10	Electrodeposition	<200 °C in air
Black Crystal	Ni-Sn	α=0.92-0.98, ε=0.08-0.25	Electrodeposition/Sol-gel	300 °C in air
TeknoTerm Energi Showa	Ni pigmented Al_2O_3	α=0.85-0.97, ε= 0.08-0.21	Anodization	300-400 °C

Although PVD processed coatings are chemically and thermally stable, the PVD process leads to high costs due to a large amount of material consumption complex and expensive equipment. The wet chemical methods such as electrodeposition and SPT can be used for the development

of cost-effective SSACs. Several SSACs were extensively studied and reported by using both methods. However, as mentioned earlier, the SSACs developed by the electrochemical process were not environmentally friendly. The coatings produced by the SPT method were not commercialized due to non-uniformity and stability at elevated temperatures.

In India, fewer indigenous solar selective absorber coating technologies are available that are matured and commercialized. For example. National Aerospace Laboratory (NAL) in Bangalore developed a solar selective absorber coating (Nalsun) technology in 1988 with solar absorptance >95% and emittance <20%. NALSUN coating is still commonly used in Flat plate collectors for water heating applications in the domestic, hospital, and hospitality industries. However, the developed technologies are suitable for low-temperature applications ranging from 45 to 80 °C and high-temperature CSP applications (vacuum stable coatings ranging from 350 °C to 550 °C). The improved NALSUN coating (NALSUN III and IV) is also used for water desalination for drinking water production and industrial water heating applications.

International Advanced Research Centre for Powder Metallurgy and New Materials (ARCI), Hyderabad, developed a cost-effective wet chemical process to prepare absorber coating on stainless steel tubes suitable for low and medium temperature applications. The receiver tubes achieved 95 ± 2 % absorptance and 14 ± 1 % emittance and, more importantly, exhibited high corrosion resistance and thermal stability up to 250 °C.

1.9 Sol-gel method:

Sol-gel is a facile, low-cost wet chemical method which can be done at room temperature. In the sol-gel process, inorganic or metal-organic precursors are dissolved in the aqueous or organic solvents. After that, the precursors are hydrolyzed and condensed to form inorganic polymers composed of M-O-M bonds [42,43]. A further process depends on the targeted products such as powder or xerogel, or aerogel. The schematic of the sol-gel method is shown in Figure 1.10. Typical precursors used in the sol-gel method are metal alkoxides and metal salts. The basic structure or morphology of the solid phase can range anywhere from discrete colloidal particles to continuous chain-like polymer networks. The applications for sol gel-derived products are numerous and widely used in different fields such as thin films, fibers, optomechanical, and medicine.

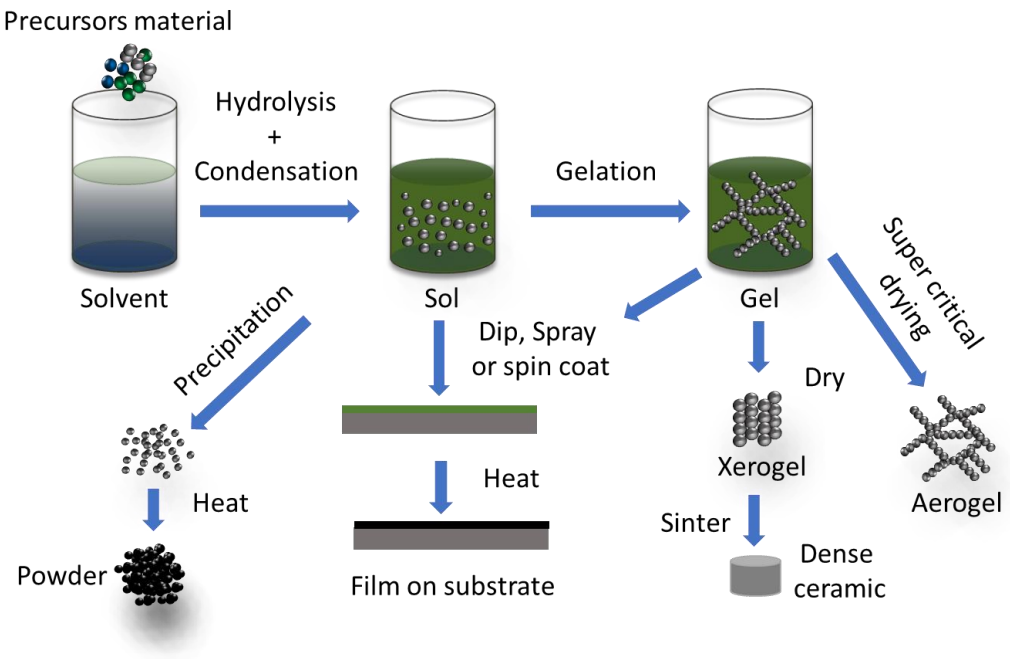

Figure 1.10. Schematic of sol-gel process for different applications

Development of SSACs by sol-gel method is widely reported [44]. The sol-gel method is considered a simple, viable alternative to vapor deposition techniques because it does not require expensive equipment, vacuum, and high temperatures. The sol-gel method offers control of coating parameters such as absorber particle size, homogeneity, and chemical composition. In addition, it shows good potential for scaling up to an industrial scale [45]. It had been proved that the sol-gel method was able to reduce production costs drastically for absorber thin film fabrication compared to the sputtering method because the cost for the coating itself could be neglected compared to the substrate cost and that at least half of the raw material costs could be reduced [46].

There are many different coating techniques capable of producing high-quality films at a low cost by utilizing the solution synthesised by the sol-gel method. The major coating techniques are Dip, spray, spin coating, doctor blading, etc. However, only flow, spray, dip, and roll-coatings are more industrially viable. Each processing technique has its own advantages and disadvantages and critical parameters that must be monitored carefully to achieve desired coatings.

1.9.1 Dip coating technique:

The dip-coating technique is simple, cost-effective, scalable, and feasible to coat complex-shaped substrates. The sol-gel process in combination with the dip-coating technique, assists in the development of films with precise thickness control, which is primarily determined by

the withdrawal speed and solution viscosity. The dip-coating process comprises several steps such as 1) Immersion, 2) Dwelling, 3) Withdrawal & drainage, and 4) Drying. In essence, the substrate is withdrawn vertically from the solution at a constant speed to form a wet film on the substrate. After the dip-coating process, the formed xerogel is dried in an ambient atmosphere or at 100 °C to evaporate the remaining solvent. Further, the dried xerogel needs hardening/chemical transformation by heat treatment. The dip-coating method is graphically presented in Figure 1.11.

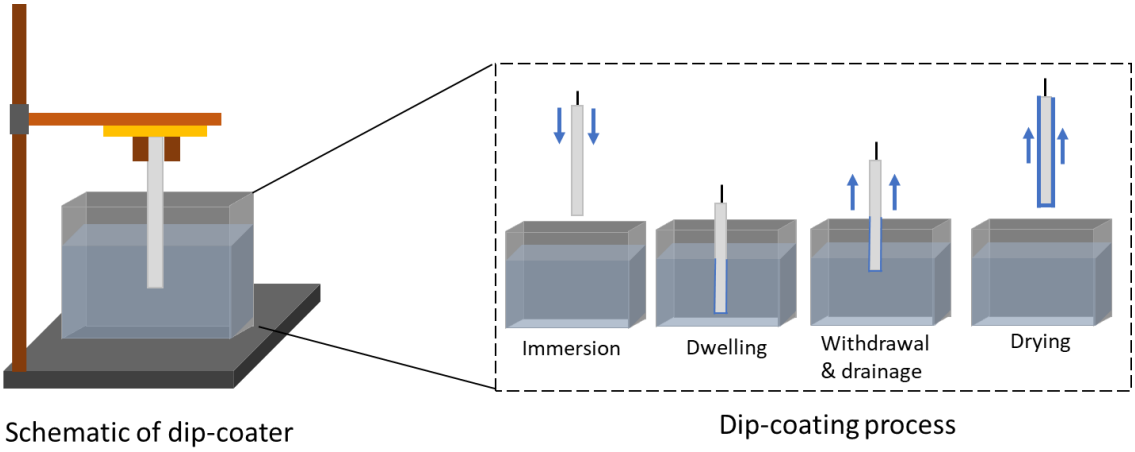

Figure 1.11. Schematic of dip-coating process

The thickness of film depends on several parameters and majorly on withdrawal speed as per by Landau and Levich equation[47]:

$$h_o = 0.94 \frac{(\eta U_o)^{2/3}}{r^{1/6}(\rho.g)^{1/2}} \text{----------(6)}$$

Where the constant is 0.94 is used for the Newtonian liquid, η is the liquid viscosity, U_o is the withdrawal speed, r is the liquid-vapor surface tension, ρ is the liquid density, and g is the acceleration due to gravity (Constant). The combination of sol-gel and dip coating method is feasible for the upscaling of SSACs, and it paves a route for commercialization of cost-effective SSACs compared to the vapor deposition methods.

1.10 Materials used for the development of solar selective absorber coatings:

The search for novel absorber materials is an extremely active area for the development of cost-efficient SSAC. Transition metals exhibit good intrinsic selective nature but individually may not show targeted optical properties. However, their performances can be improved by combining two or more transition metals with absorber-reflector, metal-dielectric or multilayered thin-film structures. The key literature on SSACs with individual transition metal

oxides, a combination of transition metal oxides and metal oxides composite blend is presented below in the table.

Table 1.6. Literature of Metal oxide based SSACs

Material	Substrate	Method	Optical properties		Stability		Ref.
			α	ε	Air (°C)	Vacuum (°C)	
CuO	Al	Spray pyrolysis	0.93	0.11 at 80 °C	-	-	[48]
$CuO–SiO_2$	SS	Sol-gel/Dip coating	0.92	0.20 at RT	-	-	[49]
Black Cobalt	Fe	Spray pyrolysis	0.91	0.12 at 100 °C	220 °C	-	[50]
Cobalt oxide	SS	Spray pyrolysis	0.93	0.14 at 100 °C	Not stable	-	[51]
CoFeO	SS	Spray pyrolysis	0.94	0.20 at 100 °C	400 °C	-	[52]
Cobalt oxide	SS	Spray pyrolysis	0.77	0.20 at 100 °C	Not stable	-	[53]
Cobalt oxide–nickel oxide	Mild steel	Electroplating and dip coating	0.90	0.10 at 80 °C, 0.25 at 300 °C	500 °C for 1000 hours	-	[54]
Black cobalt	SS	Sol-gel	0.88	0.12	-	-	[55]
Black cobalt–tin oxide	nickel & stainless steel	dip coating	0.72	0.04	-	-	[56]

Ruthenium oxide	Ti	Spraying or dipping method	0.74	0.12	-	-	[56]
Nickel oxide–alumina	Al	Spray pyrolysis	0.92	0.03	-	-	[37]
Nickel–alumina cermet	Al	Spin coating	0.97	0.05	-	-	[57]
Carbon–silica	Glass	Sol-gel	0.94	0.15	-	-	[58]
Carbon–NiO	Al	Sol-gel	0.84	0.04	-	-	[59]
Carbon–ZnO	Al	Sol-gel	0.71	0.06	-	-	[59]
Ni nanochain–alumina	SS	Solution-chemical processing	>0.9	<0.1	-	-	[60]
MWCNTs	NiO	Sol-gel	0.84	0.2 at 100 °C	-	-	[61]

Spinel structured materials have attracted substantial attention in applications of data storage, biotechnology, electronics, laser, sensor, conversion reaction, and energy storage/conversion. Spinels are a very large family, and they can contain one or more metal elements. Nearly all of the transition metals have been observed in spinels. Because of their manifold compositions, electron configurations, and valence states, spinels have demonstrated intrinsic magnetic, optical, electrical, and catalytic properties [62]. Structure of normal spinel with tetrahedral and octahedral voids is shown in the Figure 1.12.

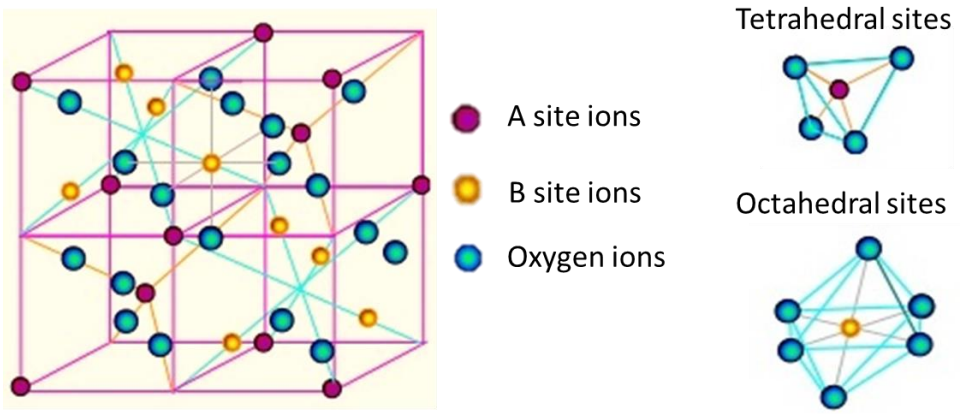

Figure 1.12. Structure of normal spinel with tetrahedral and octahedral voids

Typical spinels are briefly described as AB_2X_4, where metal A occupies the centres of tetrahedrally coordinated voids, metal B occupies the centres of octahedrally coordinated voids, and the anion (e.g., O^{2-}) sits at the polyhedral vertexes (for normal spinels) [63] [64,65]. In the recent decade, spinel materials have gotten a lot of attention in the field of SSACs. Spinels can be substituted with a variety of transition metals that can be chemically modified to obtain the required optical characteristics. Many research groups have already attempted the preparation of spinel structured SSACs using various materials for solar thermal energy conversion applications. Initially, pigment-based thickness-sensitive spectrally selective (TSSS) coatings were used as alternatives for the SSACs. The TSSS has used the pigments like Ferro 3060 pigment having the spinel structure of $CuFeMn_2O_4$, and they comprise transition metals such as Mn, Co, Fe, and Cr [66–70].

Kaluza et al. reported that a black-coloured $CuFeMnO_4$ spinel film deposited by sol-gel dip-coating technique exhibited a solar absorptance of α = 0.85 to 0.93, Still, the surfaces show unsatisfactory thermal emissivity (ε_T = 0.07–0.62)[66]. By replacing Fe with Co, thermal emissivity was altered to ε_T = 0.05. However, it is unclear if this layer keeps physical integrity at high temperatures [67]. Another research group reported the incorporation of Ti into spinel structured material of $CuCoMnO_x$, which in turn was deposited on Aluminum substrates. Despite good optical properties (α>0.85–0.91, and ε<0.036 at room temperature), there is no information on the stability of the spinel layer [68]. Rocio Bayon et al. reported several publications on CuMnOx spinels [71,72]. Unlike others, he reported the durability tests and up-scaling of selective absorbers based on copper–manganese oxides deposited by dip-coating [45]. He obtained 0.95 of solar absorptance using three layers, and the achieved absorptance is considered competitive in the solar absorber market. In addition, thermal stability and humidity

have been carried out according to the IEA-SHC Task X and upscaled coatings on 30 x 30 cm^2 samples. However, the thermal stability was limited up to 250 °C up to 200h only. For the first time, Martin Joly et al. reported the development of highly selective and scalable coatings up to 2m length by sol-gel method. Layers made of transition metals like copper, cobalt, manganese, and silicon mixed oxides form nanocrystalline films after annealing showed promising results. The solar absorptance and thermal emissivity of 0.95 & 0.12, respectively at 100 °C was observed but limited by thermal stability up to 360 °C [69]. Different from CuMn spinels, Amun Amri et al. studied the development of $M_xCo_yO_z$ (with M=Mn, Cu, Ni) spinel by dip-coating method [73,74]. He achieved the 83.4% of absorption for $CuCoO_x$ spinels and studied developed coatings thoroughly using X-ray photoelectron spectroscopy (XPS) techniques [75]. Tulchinsky et al. reported the thermal, chemical reaction between a Titania sol-gel precursor with the copper manganese spinel to form a new material, $Cu_{0.44}Ti_{0.44}Mn_{0.84}Fe_{0.28}O_3$, having a bixbyite structure. Although absorption of the film was reported around 97.4%, no measurement was done for thermal emittance and stability [70]. S. R. Atchuta et al. developed SSACs with metal oxides such as $Cu_xNi_yCo_{z-x-y}O_4$ spinel composite and spinel-structured cobaltite doped with nickel [76,77]. They obtained the high absorptance (95%), low emissivity (13%), and wide angular absorptance from 0 to 60° also [78]. In addition, he claimed the thermal stability up to 400 °C for 50-hours and corrosion resistance in salt spray test up to 12-hours with minimal change in the optical properties.

Among all of the SSACs developed by wet chemical methods, very few show high optical properties along with good thermal stability in an open-air atmosphere [78]. Some reports claimed the scalability but they were limited by thermal stabilities [45,69]. However, none of the reports thermal stability at a high operational temperature (≤500 °C) for a longer duration. From literature survey, it is evident that there is no commercially available SSAC globally stable in open-air atmospheric conditions at high temperatures. In this regard, the current thesis focuses on developing SSACs by using tri-transition metals to obtain high optical properties and good thermal stability in open-air atmospheric conditions. The developed SSACs are thoroughly studied by suitable state-of-the-art characterization techniques and compared to identify the best SSACs. Further, the best SSACs are upscaled and welded with glass tubes to develop the prototype receivers for the performance evaluation by the Parabolic test (PT) rig.

1.11 Objectives of thesis:

The objectives of the current thesis

- Synthesis of coating solutions and development of coatings by wet chemical method and dip coating technique for the development of cost-effective SSACs. Utilization of sol-gel method and dip coating technique will reduce the cost for the development of SSAC relatively in comparison with vapor deposition methods. This objective also includes the optimization sol concentration and reactants
- Development of solar selective absorber coatings (SSACs) with tri-transition metal salt precursors with targeted optical properties ($\alpha \geq 0.95$ & $\varepsilon \leq 0.20$). This objective indicates the attempt to achieve properties by transition metals-based absorber and low refractive index AR materials to obtain the optical properties equivalent to the vapor deposition methods. The objective also includes the optimization of several parameters and characterization to achieve the targeted optical properties
- Development of SSACs with high thermal stability & corrosion resistance in open-air atmospheric conditions. The reports on the study of thermal and corrosion resistance in the literature is less compared to the development of new SSACs. This objective deals with the study of thermal and corrosion resistance of developed SSACs with suitable characterization methods.
- Upscaling of SSACs with best optical properties up to 1-m length with good uniformity. Literature indicates that the reports on the development of SSACs with wet chemical methods along with good optical properties but upscaling of coating up to 1-m length is rare (Although, the sol-gel & dip coating technique has the potential to develop SSACs at 1-m length). This objective deals with the upscaling of coatings up to 1-m length for the development of indigenous receivers
- Development of 10 Nos. of absorber tubes having 1-m length with targeted optical properties and assembly of 5 Nos. of 2-m receiver tube with metal flanges and 2-m glass tubes (envelop). This objective aims to fulfil the need for Indigenous components like receiver tube for advancement of CST market in India.
- Performance evaluation (Heat gain and heat loss) of indigenous receiver tubes with commercially available receiver tubes by using the in-house PT rig. This study helps identify the performance of prototype receivers and indicates the suitability of indigenous receivers for the Indian market of CST components compared to other commercial receivers.

1.12 Outline of thesis:

Chapter 1:

Chapter 1 introduces the work carried out on the topic of "Development of solar selective absorber coatings for CST applications." Initially, it briefly describes the importance of energy and its global & national statistics. It also shares the importance of renewable energy, especially solar energy and their conversion technologies due to their distinct advantages over other renewable energies. It also deals with the solar thermal systems, types, and challenges in India for CST systems. Further, it gives information on solar selective absorber coatings (SSAC), their importance in solar thermal systems, mechanisms, development methods, and commercially available SSACs reported until now. Finally, it explains the significance of the sol-gel method, dip coating technique, and materials used to develop SSAC, commercially available SSACs, and related literature on the mentioned topics.

Chapter 2:

Chapter 2 is the experimental section of the thesis. It gives details of substrates used to develop SSACs, substrate cleaning process, synthesis process for the absorber coating solutions and anti-reflective (AR) coating solution. Further, it explains the preparation of absorber and AR coatings by dip-coating method and heating process to develop a final solar selective absorber coating. Finally, the chapter describes the characterization of developed materials and coatings using state-of-the-art instruments to understand the nature of coatings and their optical, morphological and structural studies.

Chapter 3:

Chapter 3 describes the development of absorber coatings using Manganese, Copper, and Cobalt precursors. The optimization of metal concentration in the absorber coating solution, withdrawal speed of the coatings, annealing temperature, and duration was explained. Further, the development of SiO_2 nanoparticle-based AR coating solution and coatings, optimization of process parameters similar to the development of absorber coatings were explained. Finally, the physiochemical properties of developed materials and coatings were detailly studied and explained to understand the nature of developed coatings.

Further, it describes a Molybdenum metal layer was introduced on a glass substrate to reduce the emittance of SSACs and studied the optical and structural properties of the developed tandem absorbers. In addition, the ZrO_2 nanoparticles were incorporated in the transitional metal precursor sol to study the temperature stability and optical properties of SSACs.

Chapter 4:

Chapter 4 describes the development of absorber coatings by using Nickel, Manganese, and Copper precursors. The optimization of metal concentration in the absorber coating solution, withdrawal speed of the coatings, annealing temperature, and duration was explained. Further, the development of SiO_2 nanoparticle-based AR coating solution and coatings, optimization of process parameters similar to the development of absorber coatings were explained. Finally, the physiochemical properties of developed materials and coatings were detailly studied and explained to understand the nature of developed coatings.

Chapter 5:

Chapter 5 deals with the performance comparison of developed SSACs in chapter 3 and chapter 4 regarding thermal stability, corrosion resistance, coating adhesion, uniformity, and wide-angle solar absorptance. Further, the PTCE of developed absorber systems (chapter 3 and chapter 4) were calculated and compared to determine the best SSAC for the upscaling, prototype development, and performance validation.

Chapter 6:

Chapter 6 describes the development of prototype non-evacuated receiver tubes and their performance validation by using PT rig. This chapter explains the detailed synthesis of absorber solution (6 litres) and preparation of multiple Nos. of absorber tubes (10 Nos.) having a length of 1-m (each tube) by a dip-coating method. Further, the developed absorber tubes were characterized to determine the properties such as solar absorptance, spectral emittance, and uniformity. Finally, the 10 Nos. absorber tubes having a 1-m length and 42 mm outer diameter were joined and welded to develop 2-m length prototype receiver tubes for the performance validation compared to the commercially available receiver tubes.

Chapter 7:

Chapter 7 summarizes the conclusion of the work completed and gives the future scope for the work carried out in the present thesis.

Chapter 2: Experimental section

Chapter 2 is the experimental section of the thesis. It gives details of substrate used to develop SSACs, substrate cleaning mechanism, synthesis process for the absorber coating and anti-reflective (AR) coating solution. Further, it explains the preparation of absorber and AR coatings by dip-coating method and heating process to develop a solar selective absorber coating (SSACs). Finally, the chapter describes the characterization of prepared materials and coatings using state-of-the-art instruments to understand the nature of coatings and their optical, morphological and structural studies.

As mentioned in the introduction section 1.6.1, Chapter 1, several configurations can be adopted to achieve high selectivity for SSACs. However, the typical SSAC has a metal substrate, absorber, and AR layers and offers high absorptance and low emittance. The typical SSAC design is presented in Figure 2.1.

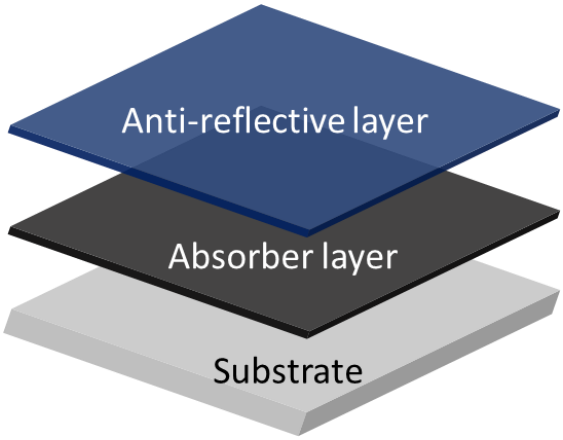

Figure 2.2. Schematic of typical SSAC.

The reflector-absorber mechanism has been followed for the development of SSACs in the present thesis. Initially, metal or alloy substrate is used to act as a base for the SSACs and exhibit low emittance since metals are good infrared reflectors. To develop the absorber layer over the substrate, the absorber coating solution is synthesised using the cost-effective sol-gel method by utilizing the transition metal-based precursors to exhibit the targeted properties. Finally, an AR layer was deposited over on absorber to reduce the reflections from the surface to obtain the high solar absorptance.

2.1 Substrate and its preparation

Metal substrate plays a vital role in obtaining high selectivity since metals are good reflectors in the IR region and absorb visible light. They exhibit good thermal stability due to high melting points at higher operating temperatures. In this connection, several metals or alloys such as Stainless steel, Aluminum, Inconel, Copper, Tungsten, and Molybdenum were investigated as IR reflectors for SSACs [13,33,40,79]. Stainless steel (SS) is used as a substrate because of its advantages in the present work. SS is readily available in the market with different variety of shapes such as plates and tubes. They are easily weldable according to our applications. Further, they are available with different grades to be tailored for good thermal and corrosion resistance depending upon the operating temperature. The available SS grades are 202, 304, 304L, 316, and 316L. The SS-304 is the most commonly used stainless steel among all grades. It offers good corrosion/oxidation resistance at a low cost compared to other grades. Thus, SS-304 is used as a substrate in the present work.

2.1.1 Preparation

Commercially available stainless steel (SS) 304-grade substrates having a roughness of >1 μm were used to develop SSACs. Substrates were polished using different grit abrasive wheels and further buffed using cotton wheels to obtain a mirror finish from the substrate. The digital image of polished and unpolished SS plates is shown in Figure 2.2.

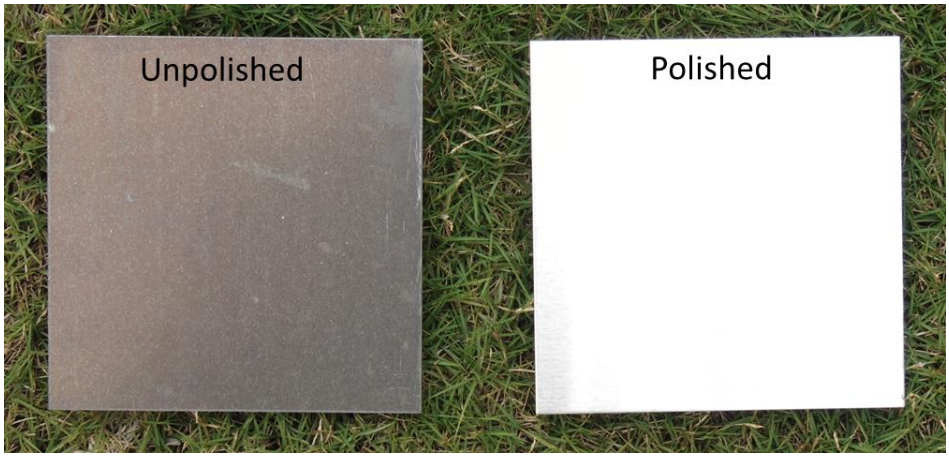

Figure 2.3. The digital image of unpolished and polished SS plates.

The polishing and mirror buffing help decrease the roughness of SS plates, and the obtained smooth surface has 100nm of roughness and low emittance.

For dip coating, heating process, and for different characterizations, the SS plates of dimensions of 50 mm (length) × 30 mm (width) × 1.5 mm (thickness) were used. The substrates are first cleaned with a surfactant solution then rinsed with deionized water to remove grease

marks. Further, they were subjected to ultrasonic cleaning in the water bath and rinsed with ethanol to eliminate the metal or dust particles associated with the polishing process.

2.2 Synthesis of absorber solution:

The ability to adjust the concentration of metal precursors ions to tailor the optical properties and deposition of material in the form of a layer at low temperatures with low cost is the most significant benefit of sol-gel over other existing coating techniques [44]. Thus, the Sol-gel process has been employed to synthesis the absorber coating solutions in the present work. The process involves the dissolution of transition metal precursors in the suitable solvent to form a stable coating sol comprised of an inorganic polymer (network) composed of oxo (M–O–M) or Hydroxo (M–μ(OH)–M) bonds [43]. Further, the sol is used for the preparation of wet xerogel on the substrate and heating to form a solid thin film. Several parameters need to be optimized in order to obtain the SSACs with the targeted optical properties. The parameters include an individual metal concentration in the sol, binder concentration, coating thickness, and calcination temperature. The synthesis process of all solutions was completed under an ambient environment. In the present work, two novel tri-transition metal-based spinels have been prepared and studied extensively for their properties.

2.2.1 Manganese-Copper-Cobalt precursors-based absorber solution

Commercially available precursors and chemical reactants were used without any further purification. Sequential steps were followed to synthesise the absorber coating solution. Manganese (II) acetate tetrahydrate, Copper (II) nitrate trihydrate, and Nickel (II) nitrate hexahydrate (>99%, Merck Millipore) were used as precursors for the synthesis of absorber solution. The precursors are dissolved in ethanol (>99%) under constant stirring. Further, Hydroxypropyl cellulose (HPC) (Alfa Aesar) was dissolved in a mixture of 2-isopropoxyethanol (IPE) and deionized water and added into a solution. After that, the solution was subjected to 1 h constant stirring for better dissolution. The digital image of the synthesised absorber solution is shown in Figure 2.3. The composition of metal precursors solvents and HPC were varied to optimize the composition of the absorber sol to obtain an absorber film with the best optical properties.

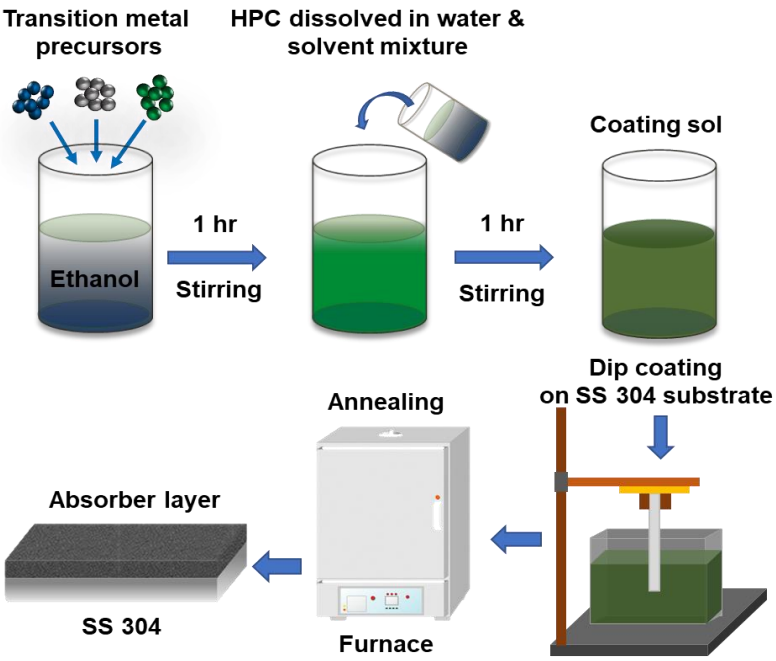

Figure 2.4. The schematic for the synthesis of absorber coating sol, dip coating, and annealing process.

The optimized composition of the absorber sol Copper (II) nitrate hexahydrate: Nickel (II) nitrate trihydrate: Manganese (II) acetate tetrahydrate: Ethanol: HPC: Deionized water (DI): Isopropoxyethanol (IPE) is 1.90:2.47:4.47:60.14:0.67:2.67:27.68 (wt %).

Figure 2.5. The digital image of synthesised absorber solution by using Manganese, Copper, and Cobalt precursors.

2.2.2 Nickel-Manganese-Copper precursors-based absorber solution

Sequential steps were followed to synthesise the absorber coating sol. Manganese (II) acetate tetrahydrate, Copper (II) nitrate trihydrate, and Nickel (II) nitrate hexahydrate (>99%, Merck Millipore) were used as precursors for the synthesis of absorber solution. The precursors are dissolved in ethanol (>99%) under constant stirring. Further, hydroxypropyl cellulose (HPC) (Alfa Aesar) was dissolved in a mixture of 2-isopropoxyethanol (IPE) and deionized water and added into a sol. After that, the sol was subjected to 1 h constant stirring for better dissolution. The digital image of the synthesised absorber solution is shown in Figure 2.5. The composition of metal precursors solvents and hydroxypropyl cellulose (HPC) were varied to optimize the composition of the absorber sol to obtain an absorber film with the best optical properties. The optimized composition of the absorber sol Copper (II) nitrate hexahydrate: Nickel (II) nitrate trihydrate: Manganese (II) acetate tetrahydrate: Ethanol: HPC: Deionized water (DI): Isopropoxyethanol (IPE) is 1.90:2.47:4.47:60.14:0.67:2.67:27.68 (wt %). The synthesis of coating sol is presented in the form of a schematic diagram in Figure 2.3.

Figure 2.6. The digital image of synthesised absorber solution by using Nickel, Manganese, and Copper precursors.

2.3 Preparation of absorber coating by dip-coating process

As mentioned in the introduction section, among all coating techniques, dip coating is considered a simple and scalable technique, and it is chosen for the development of SSACs in the present work. The coatings were developed by a dip-coating technique by using the synthesised stable absorber coating solutions mentioned in sections 2.2.1 and 2.2.2. A

customized dip coater from Holmarc Opto-Mechatronics Pvt. Ltd., Kochi, India, has been used for the development of coatings. The dip coater has a ball screw mechanism and a stroke length of 1 to 100 cm to develop coating up to 1-meter length substrate of SS tube in the view of scalability. The dip coater can vary the withdrawal speeds of the coatings from 0.5 mm/sec to 10 mm/sec with an interval of 0.1 mm/sec. The digital image of the dip coater is shown in Figure 2.6.

Figure 2.7. The digital image of Dip-coater.

In the dip-coating process, the cleaned SS 304 substrates were immersed in the synthesised stable absorber coating solutions at a constant speed and left for 2 minutes in the sol tank to avoid the disturbances originating from the dipping of substrate and ambient. Finally, the substrate is withdrawn from the sol tank with different withdrawal speeds to obtain the coatings with different thicknesses. The thickness of coatings majorly depends on the withdrawal speed according to Landau and Levich equation[47]. The optical properties of coatings rely on the coating thickness. It is essential to optimize the withdrawal speeds of the coating during the dip-coating process. After the withdrawal of coated substrate from the sol tank, the solvent was allowed to evaporate for 2 minutes from the wet coating. All the coatings were processed in a

controlled atmospheric condition, i.e., 25 °C temperature and humidity in the range of 35 to 45% in a clean environment to avoid contamination. The prepared coatings are further dried in an oven at 70 °C to remove the excess solvent and to harden the film for further annealing and characterization. The withdrawal speeds for different absorber solutions have been optimized to obtain excellent optical properties.

2.4 Heating process:

The dip-coated substrates were annealed with the aid of an open-air atmospheric Muffle furnace to obtain the thin films of SSACs. A Nabertherm muffle furnace (Model: L5/12/P330) was employed to anneal the coated substrates, and a digital image of the used furnace is shown in Figure 2.7. Annealing of coated substrates is essential to obtain homogenous and compact thin films. In addition, annealing of coating at higher temperatures aids in improving the thin film quality in terms of phases, crystalline morphology, and etc.

Figure 2.8. The digital image of Muffle furnace.

The annealing temperature of coating plays an essential role in obtaining the desired phase and optical properties. Thus, the coated substrates were annealed from 100 °C to 600 °C to determine the optimum temperature, and 500 °C is considered as the best to obtain the targeted optical properties. The 10 °C/minute rate of heating and 1 hour of dwelling time were used for the annealing of the coated substrate at an optimized temperature. In addition, the same furnace was also utilized to carry on the thermal stability tests and the process mentioned in the other sections.

2.5 Synthesis of AR coating solution and development of AR layers over on absorber coatings

The AR coatings with optimum refractive index and thickness are used to reduce the reflection from the surface [80]. Several designs have been discovered for the development of AR coatings. However, the simple way to achieve the anti-reflection is to develop a layer having a refractive index between the air and the material to be coated. To improve the light absorption for SSACs, many researchers worked on different materials to function as AR layers [18,80]. Nanostructures of metal oxides such as SiO_2, TiO_2 are garnering a lot of research attention because of their wide variety of possible applications, including solar energy conversion methods.

In this connection, commercially available SiO_2 nanoparticles sol (Obermeier CS30 716P) was purchased and utilized to synthesise AR coating solution. The shape and size of particles with suitable characterization are discussed in the next chapters. Silica nanoparticles sol was dispersed in a solvent mixture of isopropyl alcohol (IPA) (99.5%, Alfa Aesar) and Isopropoxyethanol (99%, Sigma Aldrich) and stirred for 1 hour. Further, Glycidoxypropyltrimethoxysilane (GPTS) (≥98%, Sigma-Aldrich) is added to the mixture. The suspension is subjected to 24 h stirring, resulting in a solution. The digital image of the synthesised AR coating solution is shown in Figure 2.9. The amounts of precursors and reactants were varied to obtain the best optical properties. The optimized composition of the dual-functional coating sol SiO_2 nanoparticles: Isopropyl alcohol (IPA): 2-isopropoxyethanol (IPE): 3-glycidoxypropyltrimethoxysilane (GPTS) is 14.8: 56.1: 27.8: 1.2 (wt %). The overall stack (SS 304/absorber/A.R. layer) is designated as a tandem absorber. The development of the tandem absorber is presented in the form of a schematic diagram in Figure 2.8.

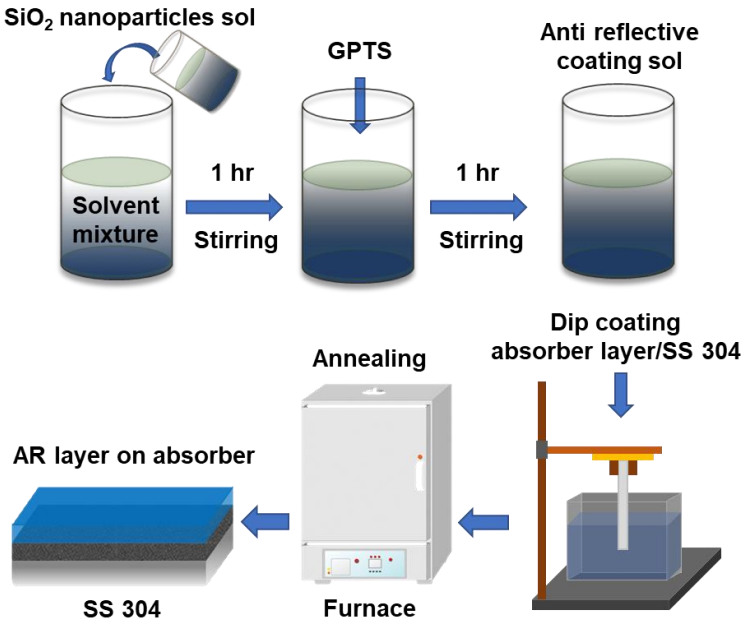

Figure 2.9. The schematic for the synthesis of AR coating sol, dip coating, and annealing process.

AR layers were prepared over absorber coatings similar to the absorber layer preparation mentioned in section 2.4 using the dip-coating technique. Further, AR-coated samples were annealed, similar to absorber-coated samples. The process parameters such as withdrawal speed and annealing temperatures were optimized to obtain the best optical properties.

Figure 2.10. The digital image of synthesised AR coating solution.

2.6 Characterization tools used for the study of SSACs:

The term "characterization" refers to the broad and generic process of probing and measuring material and thin films structure and properties. It helps the development of materials and thin films with targeted properties. Many characterization techniques have been practiced for centuries. However, new techniques/tools and methodologies are constantly emerging to probe effectively to understand the materials [81]. In this section, several characterization tools are described with relevant principles and used to investigate the properties of the developed materials and films. In addition, the sample preparation and method of measurement used in the characterization tool are explained.

2.6.1 Ultraviolet−Visible−Near-InfraRed (UV-Vis-NIR) spectrophotometer:

UV−Vis−NIR spectrophotometer is used to measure the properties such as reflectance, absorptance, and transmittance of the samples in various states such as powder, films, and liquids with suitable accessories [82]. UV−Vis−NIR spectrophotometer works on the principle of Beer-Lambert law. It correlates the absorbance to both the concentration and the thickness (path length) of the sample.

$$A = \varepsilon c l \text{ ----------(1)}$$

Where A is the measured absorbance, in Absorbance Units (AU), c is Molar concentration, and l is the optical path length.

In the present work, UV-Vis-NIR Spectrophotometer is used to measure the optical properties of coatings with the help of accessories such as diffusive reflectance accessory (DRA), transmission accessory, and universal measurement accessory (UMA). The digital image of the UV-Vis-NIR Spectrophotometer (Model: Varian Carry 5000) is shown in Figure 2.10.

Figure 2.11. The digital image of UV-Vis-NIR spectrophotometer.

a) Diffusive Reflectance Accessory (DRA)

The total reflectance of coatings was measured with the help of Diffusive reflectance accessory (DRA) from 0.3 μm to 2.5 μm wavelength range to determine the solar absorptance. The digital image of the DRA accessory and the reflection of light inside the integrating sphere is shown in Figure 2.11.

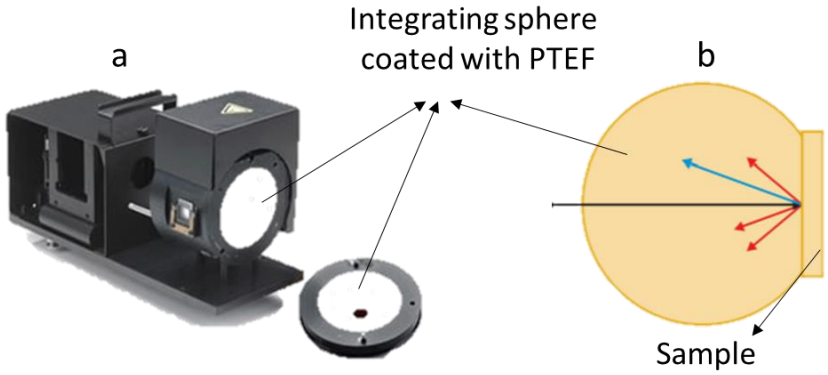

Figure 2.12. (a) The digital image of diffusive reflectance accessory (b) Schematic of light reflection from sample surface in the integrating sphere.

It comprises of integrating sphere with a diameter of 110 mm coated with Polytetrafluoroethylene (PTFE), and PTFE coated disk was used as a reference to measure the samples. The reflectivity of the PTFE is above 96% between 200–2500 nm, and greater than 99% between 350–1800 nm. The obtained reflectance from the DRA accessory is used to calculate solar absorptance, as shown in equation 3 (Chapter 1, section 1.6).

(b) Universal Measurement Accessory (UMA)

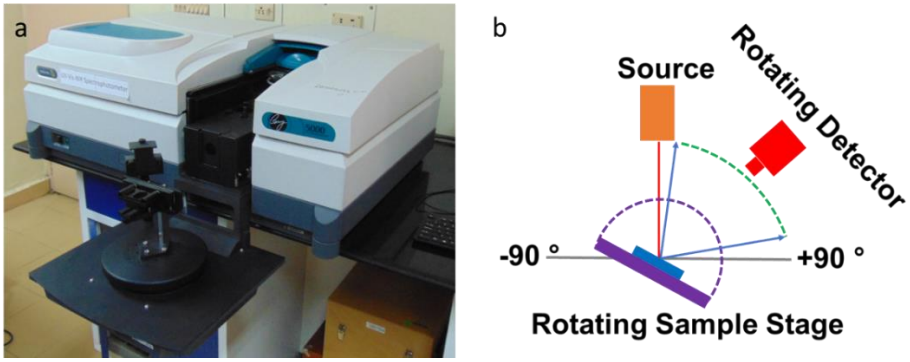

Figure 2.13. (a) The digital image of universal measurement accessory attached to the UV-Vis-NIR spectrophotometer (b) Schematic of measuring reflectance from sample surface in wide angles.

The Universal Measurement Accessory (UMA) is used to investigate the wide-angle nature of coatings by measuring the reflectance at different incident angles. The UV−Vis−NIR spectrophotometer attached with the universal measurement accessory (as shown in Figure 12(a)) provides the ability to measure the reflectance of developed coatings at different incident angles (as shown in Figure 2.12(b)) between 10 and 80° with a 10° interval and calculated the solar absorptance as mentioned in the equation 2 (Chapter 1, section 1.8).

(c) Transmission Accessory

The transmission accessory is used to measure the transmittance of soda-lime glass samples from 0.3 μm to 2.5 wavelength region. Transmission measurements involve shining light from the spectrophotometer on a sample and measuring the light transmitted through it. Initially, the light intensity was measured with air as a reference. Next, a sample was placed to measure the change in the light intensity to determine the sample transmittance with respect to air.

2.6.2 Fourier Transform Infrared (FT-IR) spectrophotometer

Fourier Transform Infrared (FT-IR) spectrophotometer is used to obtain the infrared spectrum of absorption, emission, and transmission of samples in the form of solid, liquid [82]. FT-IR collects high-resolution spectral data over a wide spectral range. Unlike UV-Vis-NIR spectrophotometer, FT-IR measures the intensity over a range of wavelengths at a time.

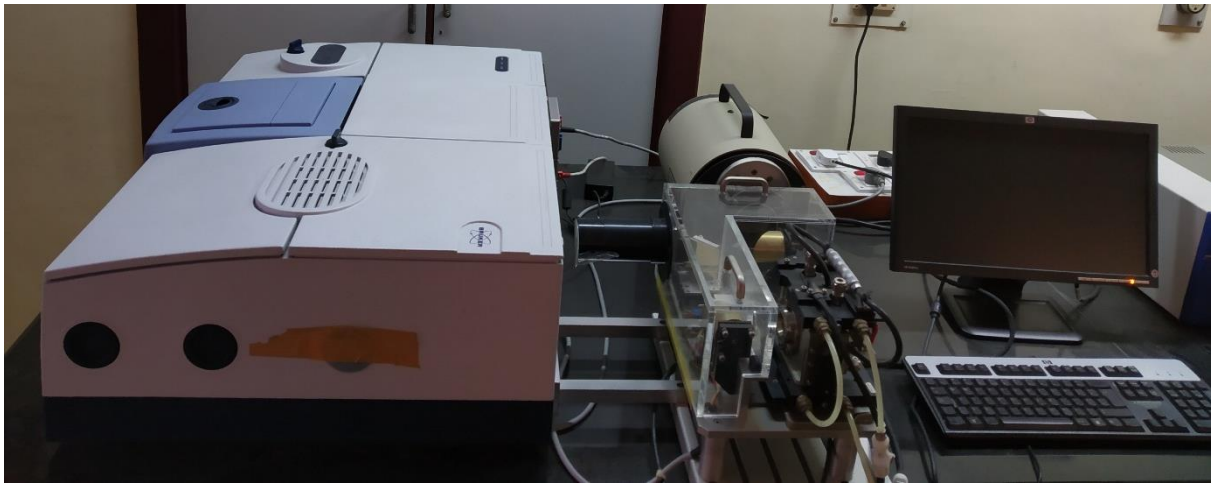

Figure 2.14. The digital image of FT-IR spectrophotometer.

In the present work, a Bruker FTIR (Vertex 70) has been used with the accessories such as integrating sphere accessory and high-temperature sample cell attached with Black-body. The digital image of the Fourier Transform Infrared spectrophotometer (Bruker, Model: Vertex 70) is shown in Figure 2.13.

a) Integrating Sphere Accessory

FTIR attached with integrating sphere accessory (A562-G) has been used to measure the emittance of developed coatings in the IR region. The integrating sphere accessory is gold coated 75 mm hollow sphere, and a gold-coated disc has been used as a reference. The emittance was measured from 2.5 μm to 25 μm wavelength region with the scanning speed of 2.5 kHz, and a gold-coated disc was used as reference. The digital image of FT-IR attached with the integrating sphere accessory is shown in Figure 2.14. Emittance was measured by using Kirchhoff's law. According to Kirchhoff's law, the emittance is equal to the absorptance at the same wavelength and temperature. The emittance was determined by measuring the reflectance from 2.5 μm to 25 μm wavelength region with FTIR attached with integrating sphere accessory (A562-G).

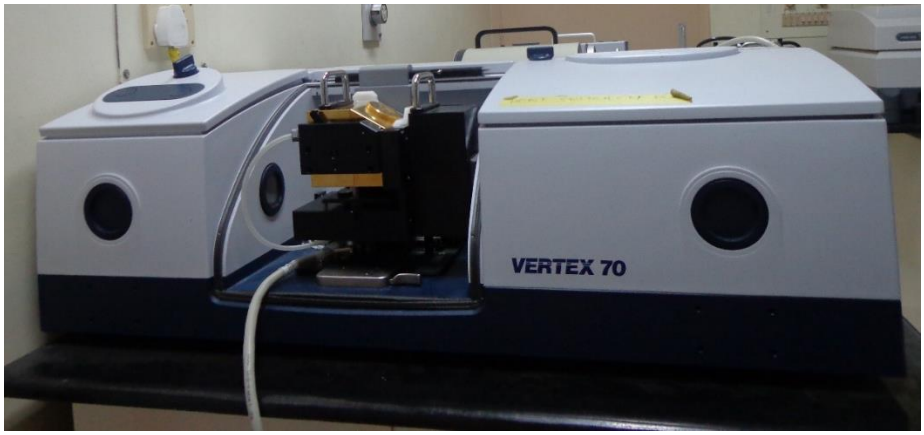

Figure 2.15. The digital image of FT-IR attached with integrating sphere.

b) High-Temperature Sample Cell with Blackbody

FTIR attached with a black body furnace and a high-pressure cell supplied by Bruker optic GmbH has been employed to measure the thermal emittance of samples up to 800 °C with the help of a temperature controller. The digital image of a high-temperature sample cell with a blackbody is shown in Figure 2.15. The high-pressure cell is made up of corrosion-resistant and vacuum-compatible material of SS EN58J and can be operated at pressures from 0.1 torrs to 1000 psi. A K-type NiCr/NiAl thermocouple is used to control the heaters, and the thermal emittance is used for the measurement from 100 °C to 500 °C with 100 °C intervals. In order to know the thermal emissivity of a sample, the black body was subjected to a temperature

from 100 °C to 500 °C with 100 °C intervals. Finally, thermal emissivity is calculated by using the below mentioned formula [83]

$$\varepsilon_T = \frac{\text{Thermal emittance of sample}}{\text{Thermal emittance of black body}} \text{ ----------(2)}$$

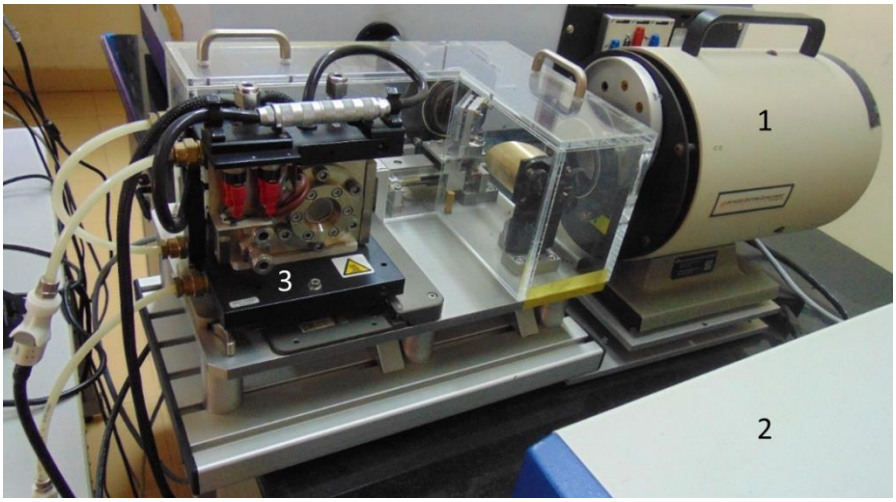

Figure 2.16. High-pressure cell accessory with the black body for the measurement of thermal emittance 1) Blackbody, 2) temperature controller, and 3) high-pressure cell.

Sample preparation:

The SSACs plates have been cut and ground into a circular shape with 13 mm diameter with the help of an abrasive cutter and grinder to fit into the sample chamber.

2.6.3 410-Visible / NIR portable reflectometer and ET-100 Thermal handheld emissometer

The coatings prepared with smaller dimensions can be characterized by using spectrophotometers to determine the optical properties. However, it is critical to measure the properties of coatings after upscaling up to 1-meter length with different shapes. In this regard, a portable reflectometer and emissometer from Surface optics corporation has been employed to measure the absorptance and emittance of developed SSACs.

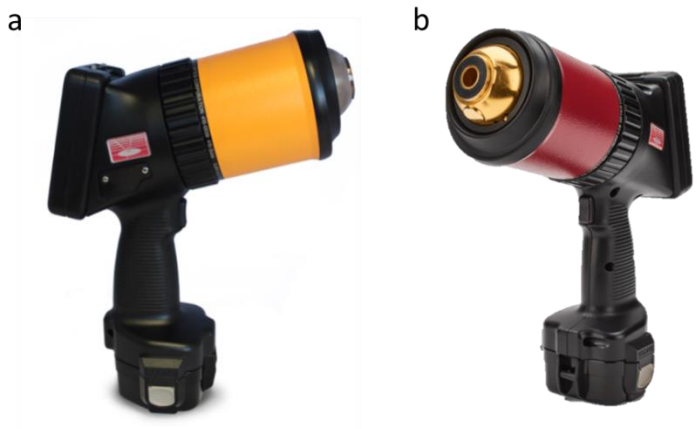

Figure 2.17. The digital image of (a) 410-Visible / NIR portable reflectometer and (b) ET-100 thermal handheld emissometer.

A 410-Visible/ NIR portable reflectometer and ET-100 Thermal Handheld Emissometer are portable contact measurement devices designed to take precise, accurate solar absorptance and emittance measurements for the developed coatings [84–86]. They are made with an ergonomic power-drill design, and measurements can be done in the field or around the lab— no cords or external batteries necessary. The digital image of the handheld reflectometer and emissometer are presented in Figure 2.16(a) and Figure 2.16(b), respectively. The 410 Visible/NIR measures total reflectance at combined 13 spectral bands. The reflectometer is used to determine the absorptance from 335nm to 2500nm, whereas the emissometer measures reflectance from 2.5 to 21 μm to determine the emittance.

2.6.4 X-ray Diffractometer

X-Ray Diffraction is the most widely used technique for the characterization of crystalline materials to identify the crystalline phases within the specimen and measure the structural properties of the identified phases [87]. The monochromatic X-rays will constructively interfere when reflected between the atomic planes resulting in a path difference equal to an integral multiple of wavelengths. This condition is defined as the Bragg law:

$$n\lambda = 2d\sin\theta \quad (3)$$

Where n is an integer, λ is the X-ray wavelength, d is the spacing between the atomic planes, and θ is the diffraction angle. In essence, Bragg's relation demonstrates that constructive interference will occur when X-rays interact with physical dimensions having sizes approximately equal to the wavelength of X-rays. The diffracted X-rays from the atomic layers of the specimen were detected, counted, and investigated. Each material has a unique d-

spacing, which can be determined by comparing it to standard patterns. Thus, the conversion of the diffraction peaks to d-spacing permits the identification of the material.

In the present work, an XRD from Rigaku (Smart lab II), Cu Kα) has been employed to analyse the powder samples to determine the crystalline phase, average crystallite size, lattice parameter, and thermal stability. The digital image of the X-Ray diffractometer (Rigaku smart lab II) is shown in Figure 2.17.

Figure 2.18. The digital image of X-Ray diffractometer.

a) Grazing incidence XRD:

Traditional θ/2θ scanning methods provide a modest signal from the film and a strong signal from the substrate in most conventional XRD measurements. To avoid the strong signal from the substrate and improve the signal from the top layer, a 2θ scan with a fixed grazing incident angle has been performed, and the fixed angle needs to be optimized to obtain the high signal from the layer of the researcher's interest. In the present work, the developed coatings on SS 304 substrates are measured by using the Grazing incidence angle mode of Rigaku (Smart lab II), Cu Kα). The grazing incidence angle has been varied from 0.2 to 1° to obtain a high signal corresponding to the interested layer in SSAC.

b) Micro X-ray Diffraction (μXRD):

μXRD technique enables us to characterize tiny areas of the sample for structural examination. It analyses remote features on the sample surface by focusing an excitation beam on a small

point on the sample surface using X-ray optics. In the present work, the film diffraction pattern recorded by Micro-XRD (RAPID-II-D/MAX, Rigaku Corporation, Japan) is performed with CuKα radiation to trace the low amounts of material.

Sample preparation:

The synthesised absorber coating sol is subjected at 70 °C to vaporize the solvent to obtain a powder. The obtained powder is used for the XRD measurements. In the case of films, the coatings developed on flat substrates are used for the measurements.

2.6.5 X-Ray Photoelectron Spectroscopy (XPS)

XPS is a photoelectric effect-based technique for assessing a material's surface chemistry [88]. XPS spectra are recorded by irradiating a solid sample surface with an X-ray beam while measuring the kinetic energy of electrons released from the top 1-10 nm of the material under investigation. All surface elements can be identified and quantified using the photoelectron peaks' energies and intensities. The digital image of the XPS is shown in Figure 2.18.

Figure 2.19. The digital image of X-Ray photoelectron spectrometer.

In the present work, the oxidation states of coatings were determined by using an XPS (Omicron-ESCA+) equipped with Al Ka anode.

Sample preparation:

Coatings were cut into small dimensions of 1 cm x 1 cm by using an abrasive cutter for the feasibility of measurement. Later, samples were placed in the XPS sample chamber for measurement.

2.6.6 Simultaneous Thermal Analyzer

A simultaneous thermal analyzer (STA) from 449 Jupiter - Netzsch GmbH, Germany, has been used for the Thermogravimetric (TG) analysis & Differential thermal analysis (DTA) analysis of the prepared materials in the present work [89]. TG analysis involves utilizing a precision balance with a sample pan within a furnace to continually measure the prepared powder mass as the temperature is altered over time. The measurement provides information about physical phenomena such as phase transitions, thermal decomposition and etc. The digital image of the simultaneous thermal analyzer is shown in Figure 2.19.

Figure 2.20. The digital image of Simultaneous thermal analyser.

In Differential thermal analysis, the material under investigation and an inert reference are subjected to identical thermal cycles, with any temperature differences between the sample and the reference being recorded. This temperature difference is then plotted against time or temperature. Glass transitions, crystallization, melting, and sublimation are all examples of transformations that can be found on a DTA curve. In the present work, TG & DTA analysis has been conducted for the prepared material to know the formation compounds and their thermal stability from 100 °C to 800 °C.

Sample preparation:

The synthesised absorber coating sol is subjected at 70 °C to vaporize the solvent to obtain a powder. The obtained powder is used for the TG-DTA measurements.

2.6.7 Field Emission Scanning Electron Microscope (FE-SEM)

A scanning electron microscope (SEM) produces images of a sample by scanning the surface with a focused beam of electrons [90]. In SEM, electrons interact with atoms of a sample, resulting in a variety of signals that provide information about the material. SEM instruments are employed with field emission guns (FEG) to produce the high primary electron brightness and small spot size even at low accelerating potentials. Thus, the instrument is called FE-SEM. A Carl Zeiss EVO 18 FE-SEM is used for the measurement of the morphology of coatings, particles, and thickness of coatings on Fluorine-doped tin oxide (FTO) glass substrates in the present work. The digital image of FE-SEM is shown in Figure 2.20.

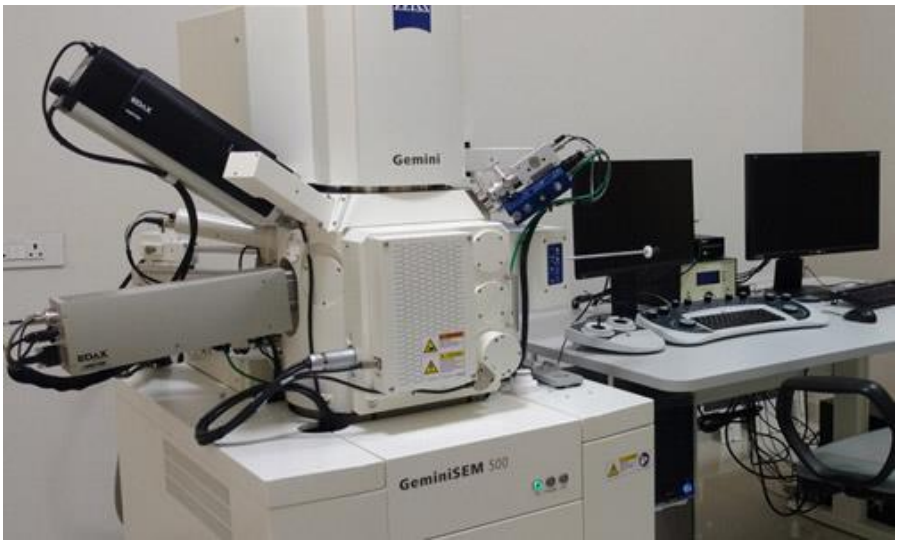

Figure 2.21. The digital image of Field emission scanning electron microscope.

In addition to morphology and thickness, Energy-dispersive X-ray spectroscopy (EDS) analysis is used to discover the surface elemental composition of materials or coatings at an interested region. EDS analysis is also called energy dispersive X-ray analysis, and it relies on the interaction of some source of X-ray excitation and a sample. EDS systems are typically integrated into FE-SEM and HR-TEM systems.

Sample preparation:

The sample preparation is essential to obtain the required information by FE-SEM. The samples need to be conductive to avoid the accumulation of electron cloud on the sample surface while seeing through FESEM. In the present work, the developed coatings are metal oxides. Thus, samples are gold-coated by sputtering to increase the conductivity. The exact process has been followed for the powder samples also.

2.6.8 Focused Ion Beam Microscope (FIB)

A Carl Zeiss dual beam system (Neon-40) using Ga as the ion source was employed for focused ion beam milling and imaging. Using 30 kV beam voltage, a trench was milled over the surface of the coatings (absorber and AR) to see the cross-section. To estimate the thickness of layers, cross-sectional pictures were acquired with the FIB and SEM at 36° angles to the film surface. The digital image of FIB is shown in Figure 2.21. The sample preparation is done according to the process mentioned for the FE-SEM.

Figure 2.22. The digital image of Focused Ion Beam Microscope.

2.6.9 High-Resolution Transmission Electron Microscope (HR-TEM)

In a transmission electron microscope, the micrographs of the sample are obtained by transmitting the beam of electrons through a specimen [91]. The interaction of the electrons with the sample as the beam passes through the specimen creates an image. Further, the formed image can be enlarged and focused into a fluorescent screen. In order to transmit the electron beam, the specimen needs to be very thin. The TEM is used to learn about the structure, crystallization, morphology, and stress of a sample.

Figure 2.23. The digital image of High-Resolution Transmission electron microscope.

In the present work, an FEI Tecnai G2 200 kV HR-TEM is used to record the high-resolution images, selected-area electron diffraction (SAED) patterns, and elemental maps of the particle clusters of interested materials. The digital image of HR-TEM used is shown in Figure 2.22.

Sample preparation:

SSACs thin films were scraped into powder and dispersed in ethanol. Further, the solvent is sonicated for the uniform distribution of particles in the sol. After that, one or two droplets of sonicated sol are dropped on the suitable TEM metal grids using a Micropipette. In the case of nanoparticles study, the optimum concentration of material is dispersed in the 5ml of solvent. Further, the same procedure has been followed as mentioned for the SSACs thin films.

2.6.10 Stylus surface profilometer

In the present work, a contact surface profilometer (Bruker DektakXT) is employed for the determination of surface roughness (S_a) by measuring the 3D sample topography [92]. A digital image of the contact stylus profilometer is shown in Figure 2.23. The 50nm tip of the diamond stylus is utilized to measure the 3D profile of SSACs with the help of Vision 64 software. The stylus is moved vertically across the sample to measure the surface variations as a function of position. The generated analogue signal is translated into a digital signal, stored, evaluated, and displayed based on its height position.

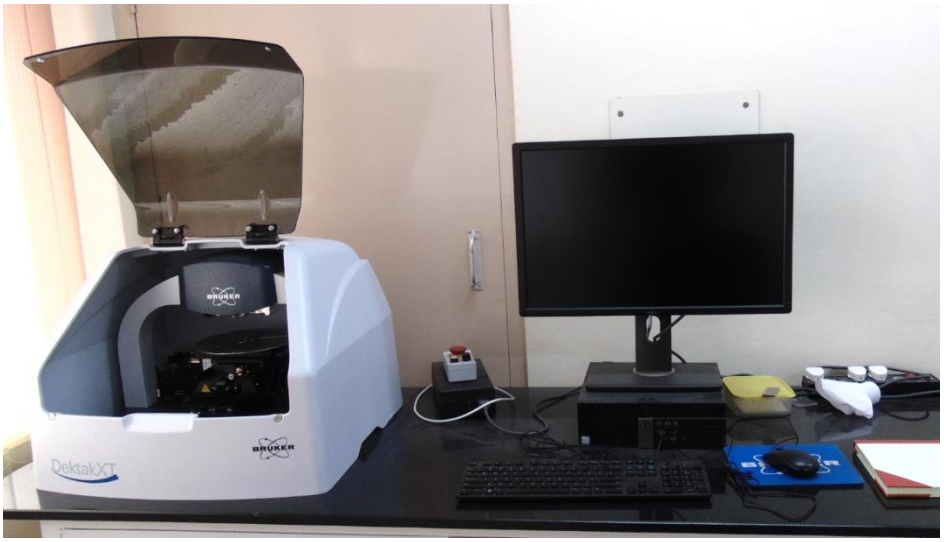

Figure 2.24. The digital image of Contact stylus profilometer.

2.6.11 Variable-Angle UV-Visible Spectroscopic Ellipsometer

The optical properties of thin films are mainly dependent on the optical constants, i.e., refractive index (n) and extinction coefficient (k). The refractive index of the individual layers has a significant effect in designing a high absorptance solar selective coating. A gradation in refractive index from top anti-reflection layer to bottom of the substrate in the multilayers stack significantly increases the absorption of the coating. A wide range of wavelengths in solar radiation can experience enhanced absorption due to multiple reflections at layer interfaces. Two factors are usually attributed to the absorption in thin films: One is because the phase difference between the top and bottom layers of the coating surface accounts for destructive interference of light and the other is band-to-band transitions. The refractive indices and extinction coefficients of the individual layers in the multi-layer stack determine the reflectance behavior, thereby, helping in better under-standing of the absorption mechanism and high solar selectivity (α/ε). In the present work, a Variable-Angle UV−Visible Spectroscopic Ellipsometer 32 (VASE-32) from J. A. Woollam Co. Inc is utilized to determine the thickness, n and k of the absorber and AR coatings in the present work [93–95]. The VASE can measure the change in the polarization of the light reflected from the films in the wavelength region of 400 nm to 1700 nm from an angle of incidence from 65 to 75°. A spectroscopic ellipsometer works on the ellipsometry technique where the change in incident light's polarization interacts with the material. The change in the polarization of light incident on the sample is measured by the amplitude ratio (Ψ) and the phase difference (Δ). They depend on the thickness of films, substrate, materials, and morphology of the films. The digital image of the spectroscopic ellipsometer is shown in Figure 2.24.

Figure 2.25. The digital image of Spectroscopic ellipsometer.

The polarized light reflected by the front coating surface in the visible area at three incident angles of 65 °, 70 °, and 75 ° was recorded to obtain the Ψ and Δ values. Further, the model is developed depending on the type of coatings such as absorber or AR, and the Ψ and Δ were simulated by a software WVASE 32. Finally, data fitting was done to find out the best fit between the generated and measured data. The optical constants are determined by considering a physical model that matches the sample and generates a generally suitable optical dispersion oscillator. In this regard, Cauchy's absorbent dispersion model was considered for main absorber layer, as this layer act as absorbing layer in the multilayer stack. The SiO_2 layers were curve fitted with the Tauc–Lorentz (TL) oscillator model. TL model is effective for nanocrystalline and amorphous thin films. The Mean Squared Error (MSE) is used to quantify the difference between generated and measured data.

Sample preparation:

In the case of AR coatings over glass samples, to measure the precise optical constants of the coating, the back surface of the coating was carefully ground and blackened with a black colour thick marker to eliminate its reflection. In the case of absorber coatings on top of SS 304 substrate, no sample preparation is required. However, coatings on very flat substrates were chosen to obtain the high signal while measuring the experimental data.

2.6.12 Electrochemical Analyzer

Potentiodynamic polarization measurement (PDP) is an electrochemical method used to measure corrosion in the present thesis [96]. A wide range of potential is applied to the working electrode in the PDP method. As a consequence, the current is generated as the sample experiences oxidation or reduction reaction. The developed coatings are studied by the Potentiodynamic polarization spectroscopy by using PARSTAT 4000 A, AMETEK [96]. The 3.5wt% NaCl standard electrolytic solution is used as an electrolyte to conduct corrosion studies. The digital image of the Electrochemical analyzer is shown in Figure 2.25.

Figure 2.26. The digital image of Electrochemical analyser.

The PDP measurements were carried out with 1 mVS^{-1} rate to obtain the voltage and current and both values were plotted to obtain the corrosion current (I_{corr}) and potential (E_{corr}) values. The polarisation resistance is calculated using the Stern-Geary equation, where b_c and b_a are the slops of cathodic and anodic Tafel lines, I_{corr} is corrosion current density (mA/cm^2), and R_P is the polarization resistance ($K\Omega\ cm^2$).

$$R_p = \frac{b_c \text{ x } b_a}{2.3 \text{ x } i_{Corr}\ (b_c + b_a)}\ (K\Omega\ cm^2) \text{ ----------(4)}$$

Polarization resistance (R_p) is defined as the resistance of the specimen to oxidation during the application of an external potential. High Rp of a developed coating implies high corrosion resistance and low R_p implies low corrosion resistance. Hence, I require high R_p for the developed coatings.

Sample preparation:

All SSACs were immersed for 30 minutes in an electrolyte solution to establish an open circuit potential (OCP) before carrying out PDP measurements.

2.6.13 Viscometer

A Viscolab 4100 (Cambridge Applied Systems, Inc.) is used to measure the viscosity of the synthesised sols. It can measure the viscosity from 0.2 to 10,000 centipoise. The viscosity of sols plays a significant role in the dip coating and affects the thickness of the coating according to the Landau-Levich equation. The digital image of the viscometer is shown in Figure 2.26.

Figure 2.27. The digital image of Viscometer.

Sample preparation:

The synthesised absorber and AR coating sols of 10 ml quantity are poured into the piston jacket and measured the viscosity as per the ASTM D7483 standard at 28 °C temperature. Each sample was measured three times for the consistency data.

Chapter 3: Development of Co-Cu-Mn-O_x based solar selective absorber coatings (SSACs)

Chapter 3 describes the development of absorber coatings using transition metal precursors of Manganese, Copper, and Cobalt. The optimization of metal concentration in the absorber coating solution, withdrawal speed of the coatings, annealing temperature, and duration was explained. Further, the synthesis and development of SiO_2 nanoparticle-based Anti-reflective (AR) coating solution and coatings, optimization of process parameters similar to the development of absorber coatings were explained. Finally, the physiochemical properties of developed materials and coatings were studied in detail and explained to understand the nature of developed coatings.

An attempt was made to understand the role of the substrate by developing coatings on Molybdenum (Mo) over on glass substrate by the sputtering method instead of SS 304 substrate. To reduce the emittance of SSACs, Mo layer is prepared on a soda-lime glass substrate and applied tri-transition metal absorber and SiO_2 AR layer by using sputtering and wet chemical methods, respectively. After optimizing the process parameters such as the thickness of the Mo layer, absorber, and AR layer, a tandem absorber (Glass/Mo/Nanocomposite base absorber/SiO_2) is developed to obtain the high solar absorptance and low spectral emittance. The physiochemical properties of developed tandem absorber coatings were studied in detail and explained to understand the nature of developed coatings.

Further, another attempt was made to improve the optical properties of absorber coatings by using ZrO_2 nanoparticles (NPs). The solvothermal method is used to synthesise the ZrO_2 NPs, and ZrO_2 NPs are incorporated in the absorber coating sol to develop the absorber coatings. Further, AR coatings were applied to improve the optical properties. Process parameters were optimized to enhance the optical properties. Finally, the physiochemical properties of developed tandem absorber coatings were studied in detail and explained to understand the emittance and temperature stability of the developed coatings.

3.1 Development of SS/Co-Cu-Mn-O_x/SiO_2 SSACs

3.1.1 Synthesis of the absorber coating solution

The synthesis procedure for absorber coating solution is described in chapter 2, section 2.2.1, with a schematic diagram. However, for better understanding, it is explained in detail here.

Commercially available precursors and chemical reactants were used without any further purification. Sequential steps were followed to synthesise the absorber coating solution. Manganese (II) acetate tetrahydrate, Copper (II) nitrate trihydrate, and Cobalt (II) nitrate hexahydrate (>99%, Merck Millipore) were used as precursors for the synthesis of the absorber coating solution. The precursors are dissolved in ethanol (>99%) under constant stirring. Further, Hydroxypropyl cellulose (HPC) (Alfa Aesar) was dissolved in a mixture of 2-isopropoxyethanol (IPE) and de-ionized water and added into a solution. After that, the solution was subjected to 1-hour constant stirring for better dissolution. The composition of metal precursors solvents and HPC were varied to optimize the composition of the absorber sol to obtain an absorber film with the best optical properties. The optimized ratio of composition of absorber sol is Cobalt (II) nitrate hexahydrate: Manganese (II) acetate tetrahydrate: Copper (II) nitrate hexahydrate: Ethanol: Hydroxypropyl cellulose: De-ionized water: 2-isopropoxyethanol (IPE) is 4.3: 3.9: 1.6: 56.8: 0.7: 29.9: 2.9 (wt%). The viscosity of the optimized solution was found to be 8.3 centipoise and processed for the coating.

3.1.2 Thermo Gravimetric (TG) and Differential thermal analysis (DTA) of coating material

TG & DTA analysis has been conducted for the prepared material to determine the temperature at which the formation of the compound occurred and its stability via thermal decomposition with respect to temperature. The synthesised absorber coating sol, as mentioned in the experimental section 2.2.1, was subjected to 70 °C to vaporise the solvent. Further, the coating material is studied by using the TG-DTA technique. The thermogravimetric graph in Figure 3.1.1 reveals the weight loss of coating material from room temperature to 800 °C in open-air atmospheric conditions, and it exhibits multiple-stage decomposition. The loss of weight is divided into three thermal events. The first event presents the loss of 12%, and it may be ascribed to evaporation of the solvent, water, and decomposition of the precursors. The mentioned process needs the absorption of heat, and it resulted in an endothermic peak in the DTA curve with maxima at 110 °C.

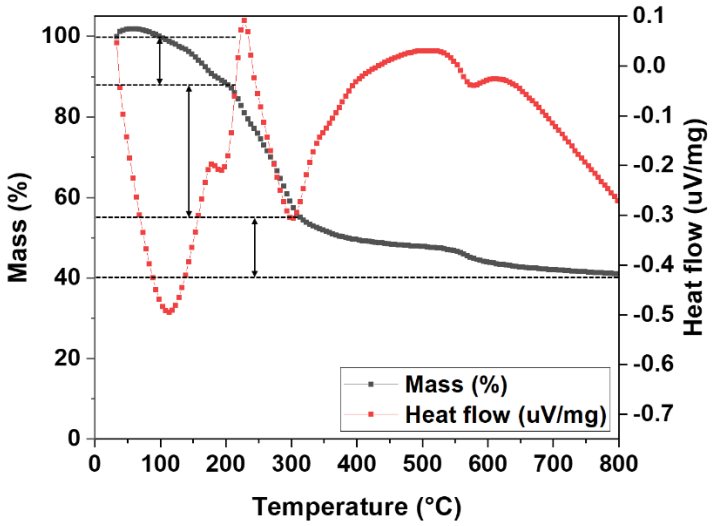

Figure 3.1.1 TG and DTA curves of the coating material over a range of ambient to 800 °C temperature.

The second thermal event results in a loss of 32%, and this is possibly due to the continuous decomposition of the precursors and the formation of spinels. The sharp exothermic and endothermic peaks with maxima at 235 °C and 305 °C can be linked to the heat released in the melting of precursors and formation of the compound, respectively. The endothermic peak at 305 °C may represent the formation of the spinel phase [66,97,98], and it is further studied by XRD for confirmation. The final thermal event exhibits a loss of 17% weight, and it could be because of the crystallization of the compound formed. The TG-DTA analysis confirms the formation of the compound at 300 °C and stability up to 800 °C.

3.1.3 Analysis of coating material by XRD

In the present work, an XRD has been employed to analyse the coating material to determine the crystalline phase and thermal stability majorly. The synthesised absorber coating sol was subjected to 70 °C to vaporise the solvent. Further, the coating material was subjected to temperatures from 100 °C to 800 °C and analyzed by XRD.

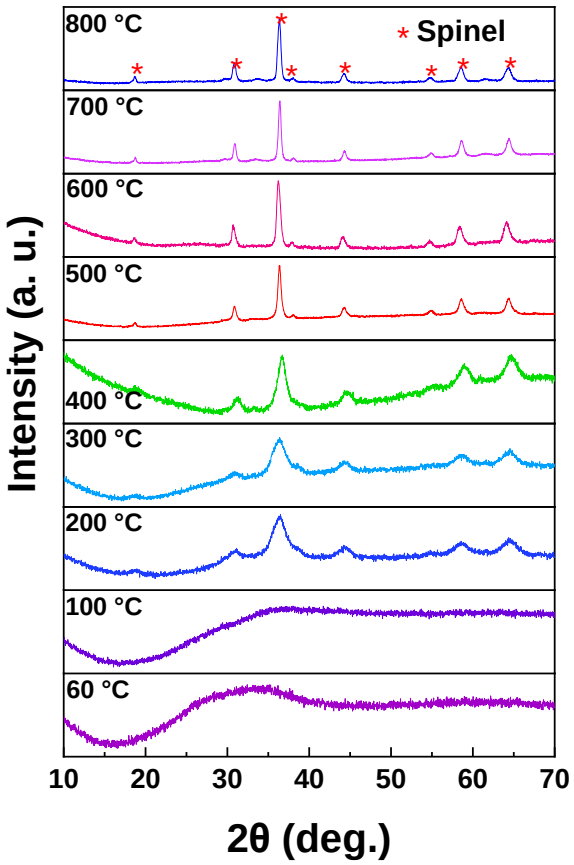

Figure 3.1.2. XRD pattern of the Co-Cu-Mn-O_x spinel.

Figure 3.1.2 represents the XRD pattern of coating material at different temperatures, and it indicates the formation of spinel phase at 300 °C with the peaks at 2θ=18.8°, 30.9°, 36.3°, 38.0°, 44.2°, 54.8°, 58.5°, and 64.2°. The diffraction peaks of synthesised coating material correspond to the crystal planes of Co-Cu-Mn-O_x with a cubic phase, and it is in good agreement with the Standard International Centre for Diffraction Data (ICDD) data (00-047-0324). Further, the non-existence of other phases on prolonged heat treatment from 300 °C to 800 °C confirms the formation of only pure spinel phase and stability at higher temperatures. Figure 3.1.2 also reveals the crystallization of the spinel phase over the temperatures from 300 °C to 800 °C with increment in the intensity of peaks at accurately assigned 2θ positions.

3.1.4 Absorber coating preparation

The absorber coating is prepared by the dip-coating method, as mentioned in chapter 2, Sections 2.3 and 2.4. The optimized absorber coating solution described in section 3.1.1 is utilized for the development of absorber coatings. The parameters such as withdrawal speed and heating temperature play an essential role in obtaining the crystalline compound with an

optimum thickness to get high optical properties. Thus, the mentioned parameters need to be optimized.

3.1.4.1 Optimization of temperature for the development of absorber layer

The formation of the spinel compound is confirmed at approximately 300 °C from XRD and TG-DTA. Thus, the sample's annealing temperature ranges from 300 °C to 600 °C to determine the optimum temperature for the prepared coating. The coatings were prepared with a constant withdrawal speed of 1 mm/sec, a constant heating rate of 10 °C per minute, and a 1-hour dwelling time (constant). The developed samples are characterized by using UV-Vis-NIR and FT-IR) spectrophotometer to determine the optical properties such as solar absorptance and spectral emittance. These values determine the optimum temperature for the annealing of coatings. Figure 3.1.3 shows the reflectance spectra of the samples annealed at different temperatures, and Table 3.1.1 gives the optical properties of the developed coatings from 300 °C to 600 °C.

Table 3.1.1. Solar absorptance and emittance data of absorber layers developed at different annealing temperatures with a constant withdrawal speed.

Annealing temperature (°C)	**Withdrawal speed (mm/sec)**	**Absorptance (AM 1.5) α**	**Emittance ε**
400	1	0.85	0.16
500	**1**	**0.90**	**0.17**
600	1	0.87	0.18

Table 3.1.1 and Figure 3.1.3 show that with increasing the annealing temperature, there is an increment in the solar absorptance and spectral emittance. The best solar absorptance of 0.90 and emittance of 0.17 can be observed at the 500 °C temperature. Thus, the annealing temperature of 500 °C can be considered an optimum to develop the absorber coatings to further optimize the withdrawal speed for absorber and tandem absorber coatings. The change in the optical properties with an increase in the annealing temperature can be attributed to the crystallinity of the spinel phase formed on the substrate, which is confirmed with XRD in Figure 3.1.2.

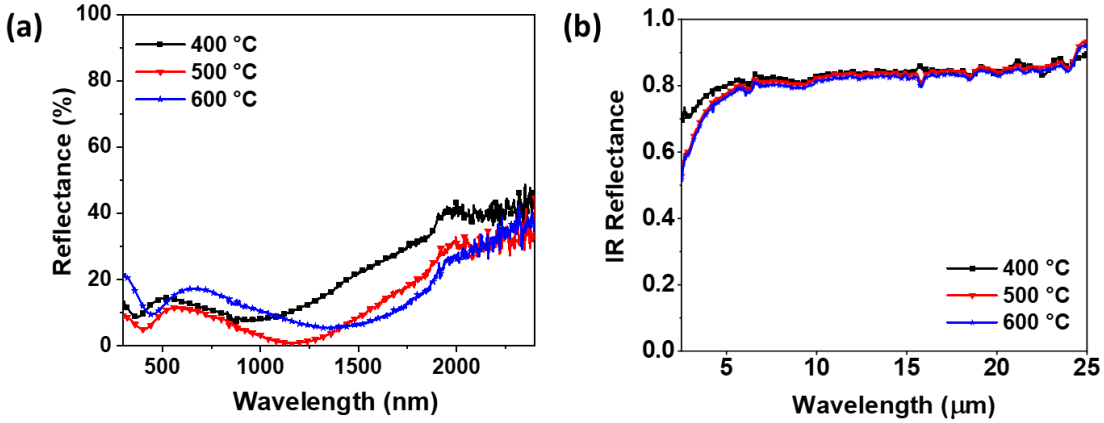

Figure 3.1.3. UV-Vis-NIR and (b) Infrared radiation (IR) reflectance spectra of absorber coatings annealed at temperatures from 400 °C to 600 °C.

To investigate the reason, the samples developed at different temperatures are further studied by GI-XRD. Figure 3.1.4 indicates the GI-XRD of samples at different temperatures. From Figure 3.1.4, it is observed that the presence of spinel phase peaks with high crystallinity after 500 °C, whereas at 400 °C, there is no presence of all spinel phase peaks except substrate. At 500 °C and 600 °C, the clear spinel phase peaks can be observed, which are responsible for good solar absorptance. The annealing temperature plays a vital role in the thickness of coatings, and SSACs exhibit high optical properties at an optimum thickness. It is observed that the annealing temperature influences the optical properties of developed coatings [99]. Thus, the decrement of solar absorptance is observed from 0.90 to 0.87 at 600 °C can be attributed to the change in the thickness of the developed coating. In addition, excess formation of Fe_2O_3 due to oxidation of substrate with air at 600 °C also leads to change in the optical properties which is clearly shown with the support of GI-XRD (Figure 3.1.4).

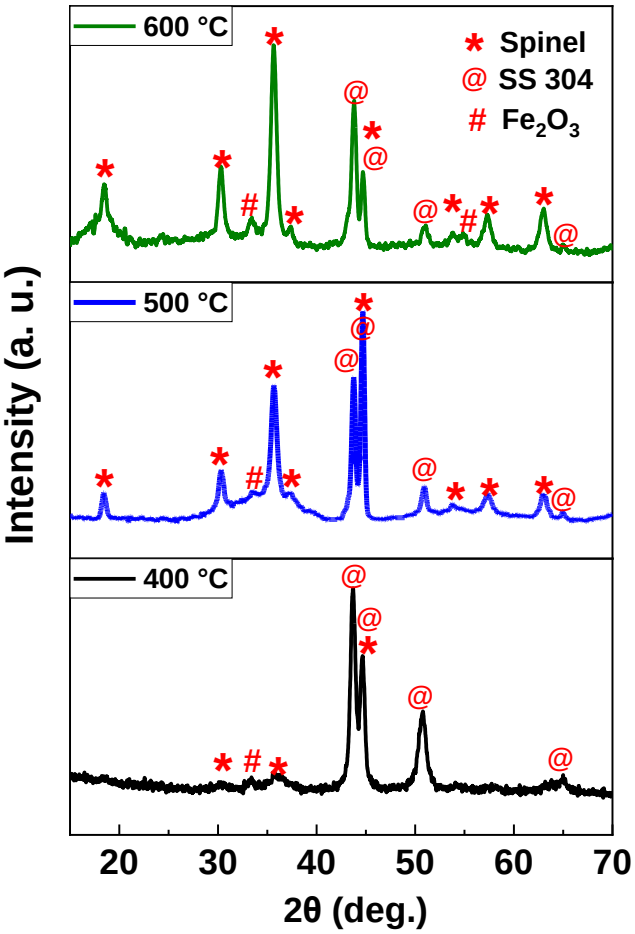

Figure 3.1.4. GI-XRD pattern of samples developed at 400 °C, 500 °C, and 600 °C temperatures.

In addition to substrate and spinel phases, there is a formation of Iron oxide from 400 °C to 600 °C, as shown in Figure 3.1.4, and it is due to oxidation of SS 304. The presence of Fe_2O_3 can be attributed to the increment in the spectral emittance from 0.16 to 0.18. A similar observation is reported by the author Sean Wu et al.[100]. The developed absorber is termed as spinel absorber in the current chapter for feasibility.

Role of the substrate:

The bare SS 304 substrate exhibits a solar absorptance (α)=0.32 and spectral emittance (ε)=0.12. To understand the role of the substrate in the optical properties of SSAC, the substrate was subjected to a temperature of 500 °C for one hour, and the optical properties were measured. The annealed SS 304 exhibited a solar absorptance (α)=0.53 and spectral emittance (ε)=0.12. The reflectance spectra for the bare and annealed substrate are shown in Figure 3.1.5

(a & b). The optical values of developed absorber coatings are shown in Table 3.1.2. The increment in the solar absorptance for the annealed substrate is due to the formation of Fe_2O_3, which is confirmed by the GI-XRD study in further sections [101].

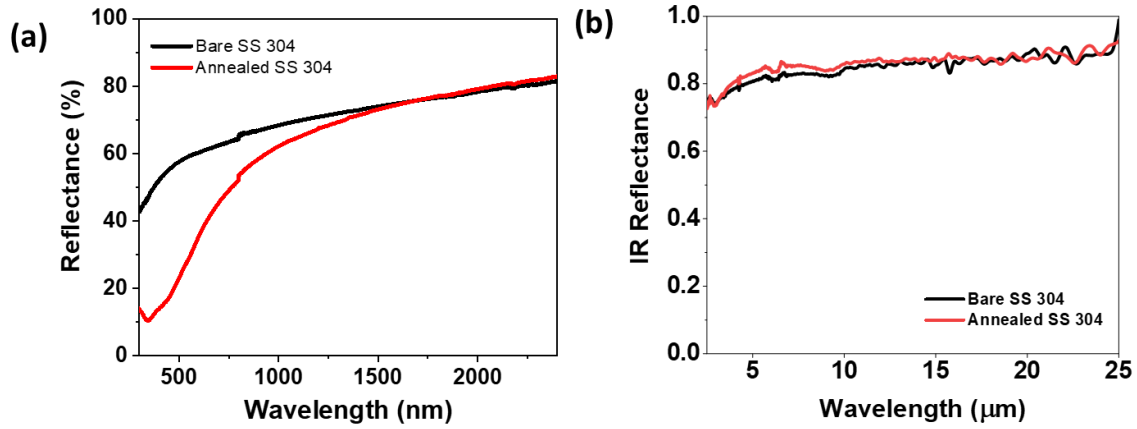

Figure 3.1.5. (a) UV-Vis-NIR and (b) IR reflectance spectra of SS 304 and annealed SS 304 at 500 °C.

Table 3.1.2. Solar absorptance and emittance values of the substrate, annealed substrate at 500 °C.

Withdrawal speed (mm/sec)	**Absorptance (AM 1.5) α**	**Emittance ε**
Bare SS 304	0.32	0.12
Annealed SS 304	0.53	0.12

3.1.4.2 Optimization of withdrawal speed of spinel absorber layer

The spinel absorber coatings were prepared with different withdrawal speeds over the bare substrate to obtain high absorptance and low emittance. The spinel absorber exhibited good solar absorptance (α)=0.90 and low spectral emittance (ε)=0.17 at an optimum withdrawal speed of 2 mm/sec. The absorption band edge at 612 nm with a reflectance of ~12% at 2 mm/sec withdrawal speed is shown in Figure 3.1.5(a). It may correspond to the energy transition from the oxygen anion to the M metal cation (where M is the metal: Co, Cu, and Mn) or between two metal cations induced by incident light on the absorber layer [102].

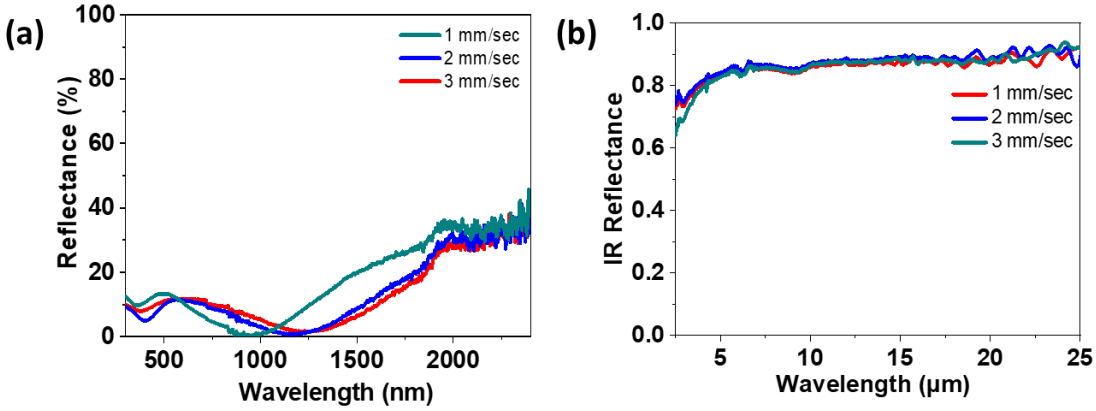

Figure 3.1.6 (a) UV-Vis-NIR and (b) IR reflectance spectra of spinel absorber coatings developed with different withdrawal speeds at 500 °C.

Table 3.1.3. Solar absorptance and emittance values of the absorber layers developed at different withdrawal speeds at 500 °C.

Withdrawal speed (mm/sec)	**Absorptance (AM 1.5) α**	**Emittance ε**
1	0.87	0.16
2	0.90	0.17
3	0.89	0.18

3.1.4.3 Optimization of withdrawal speed of AR layer over on absorber coating

The synthesis of SiO_2 nanoparticle-based AR coating solution is described in chapter 2 and section 2.5. The same sol has been utilized for the development of AR coatings over on absorber layer in the entire thesis. AR layer of the correct thickness and refractive index suppresses the reflections from the absorber and aid in improving the solar absorptance [13,80]. So, the thickness of the SiO_2 nanoparticle layer (tandem layer) on top of the spinel absorber is varied by changing the withdrawal speed of the coatings. The optical values of developed tandem absorber coatings are shown in Table 3.1.3. In the current chapter, the SSACs developed with absorber and AR layer used for the stack are termed tandem absorbers for feasibility.

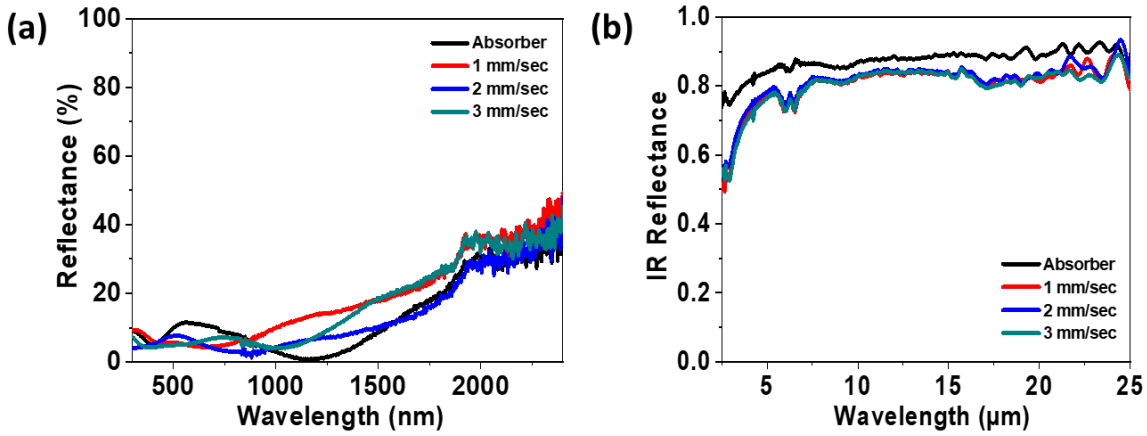

Figure 3.1.7. (a) UV–Vis-NIR and (b) IR reflectance spectra of AR layer developed with different withdrawal speed over a spinel absorber.

Table 3.1.4. Solar absorptance and emittance values of AR coatings over on absorber developed at different withdrawal speeds at 500 °C.

Withdrawal speed (mm/sec)	**Absorptance (AM 1.5) α**	**Emittance ε**
Absorber	0.90	0.17
1	0.91	0.18
2	0.93	0.19
3	0.92	0.20

The reflectance spectra for tandem absorbers with the variation of withdrawal speed are shown in Figure 3.1.7 (a & b). The tandem absorber exhibited the solar absorptance (α)=0.93 and spectral emittance (ε)=0.19 at an optimum withdrawal speed of 2 mm/sec. In Figure 3.1.7(a), the AR layer was applied over on spinel absorber with optimum withdrawal speed (2 mm/sec) creates a destructive interference, and it causes the shift in absorption band edge to a lower wavelength of 519 nm, having the reflectance of ~7%. The shift in the peak leads to decrement in the reflectance drastically ~ 4.8% in the region of 0.3-1.5μm, whereas spinel absorber exhibits the high reflectance ~ 8.7% for the wavelength range of 0.3-1.5μm. Spinel absorber in the IR region exhibits low spectral emittance (ε) of 0.17, and the tandem absorber exhibits 0.19 of thermal emittance(ε). The observed change in the emittance from spinel to tandem absorber

is attributed to the increment in the thickness of the overall stack, and it is further discussed in section 3.9.

3.1.5 Structural study of the Bare and annealed substrate, absorber, and tandem absorber by GI-XRD

The bare SS 304, annealed SS 304 at 500 °C, spinel, and tandem absorbers (spinel + AR) were analyzed by GI-XRD at grazing angles from 0.2 ° to 1 ° to determine the phase structure of coating with minimal contribution of the substrate. Figure 3.1.7 represents the GI-XRD pattern of bare SS 304, annealed SS 304, spinel, and tandem absorbers. In Figure 3.1.8(a), we could observe that the SS 304 has diffraction peaks at 2θ=43.7°, 51.1° and 75.0 °, that were assigned to Face Centered Cubic Iron (γ-FCC) phase of a substrate, and it is coinciding with the ICDD data (01-081-8766). The diffraction peaks at 2θ=44.2° and 64.8° were assigned to the Body-Centered Cubic Iron (α-BCC) phase of the substrate and is matched with the ICDD data (01-081-8766). The annealed SS 304 has Iron Oxide (Hematite) other than the γ-FCC, α-BCC, which is evident in Figure 3.1.8(b). The diffraction peak at 2θ=33.6° corresponds to the Iron Oxide (Hematite), coinciding with the Standard ICDD data (01-073-3825). This could be due to the oxidation of SS 304 in the air at 500 °C. According to the Fe-O phase diagram, the formation of Fe_3O_4 is favoured thermodynamically. However, during the oxidation process, many complex parameters are involved in the formation of phase fraction of final compounds, such as oxygen availability, local chemistry (presence of Cr, tendency to form Fe_2O_3 is dominant), surface characteristics, etc. Feng Cao et al. claimed that there is a formation of Fe_2O_3 layer after annealing the stainless-steel substrate at 500 °C in air and reported that diffusion of iron and carbon atoms into the top layers at high temperature might alter the optical properties over time [101]. As a solution, he introduced a diffusion barrier between the substrate and the absorber layer. Similarly, Jiushan Cheng et al. also confirmed that the substrates were covered with Fe_2O_3 by annealing the SS substrate at 500 °C for 30 min in air [103]. Similarly, the occurrence of Fe_2O_3 over on the SS 304 substrates leads to a change in the optical properties. At an optimum glazing incident angle (0.5°), we could observe the diffraction peaks related to the spinel phase, the substrate, and Hematite, as shown in Figure 3.1.8(c).

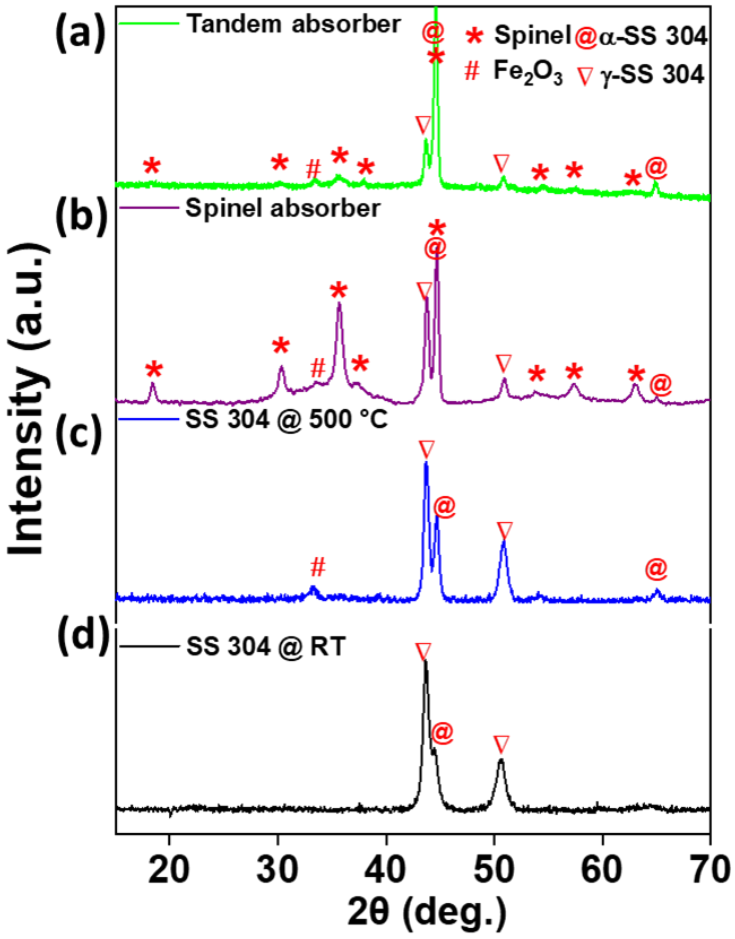

Figure 3.1.8. GI-XRD pattern of (a)SS 304, (b) annealed SS 304 at 500 °C, (c) spinel absorber (Co-Cu-Mn-O_x), and (d) tandem absorber (Co-Cu-Mn-Ox/SiO_2) on SS 304.

The diffraction peaks at 2θ=18.8°, 30.9°, 36.3°, 38.0°, 44.2°, 54.8°, 58.5°, and 64.2° are accurately assigned to the Co-Cu-Mn-O_x spinel phase with the cubic structure that matches with the ICDD data (00-047-0324). The results obtained by coating material XRD are well consistent with GI-XRD data for the spinel phase. The diffraction peak at 2θ=33.6° corresponds to the Iron Oxide (Hematite), precisely coinciding with the Standard ICDD data (01-073-3825). Like the spinel absorber, the tandem absorber also exhibits the diffraction peaks of the substrate, Hematite, and spinel phase, as shown in Figure 3.1.8(d). However, the tandem absorber does not reflect the SiO_2 diffraction peaks despite of covering the absorber layer completely since the SiO_2 nanoparticles are amorphous.

3.1.6 Structural study of tandem absorber coating by XPS

Figure 3.1.9 shows the Co 2p, Cu 2p, Mn 2p, Fe 2p, Si 2p, and O 1s photoelectron energy loss spectra of the optimized absorber layer measured by X-ray photoelectron spectroscope. All the photoelectron spectra were calibrated relative to the reference C 1s peak position (284.3 eV).

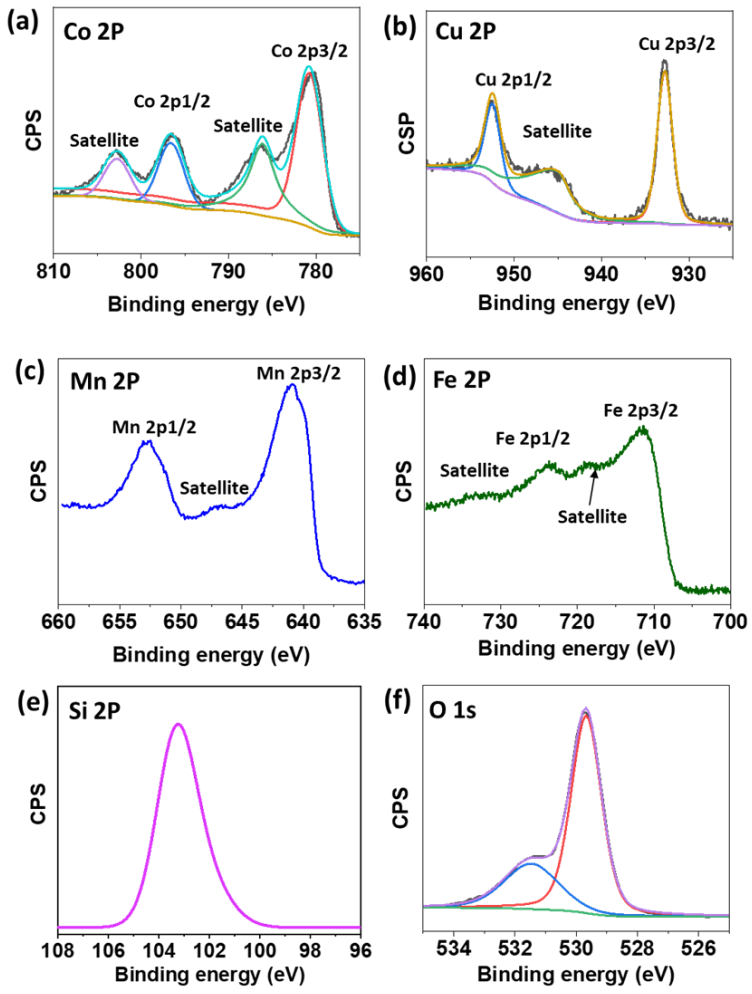

Figure 3.1.9. X-ray photoelectron spectra of tandem absorber coating.

The Co 2p spectrum [Figure 3.1.9(a)] had the strong spin-orbit doublet Co $2p^{3/2}$-Co $2p^{1/2}$ at 780 and 796 eV, respectively. The Co $2p^{3/2}$ peak at 780 and satellite feature at ~786 eV indicates that the Co may be in the oxidation state of 2+[75,104]. The presence of satellites in between the Co $2p^{3/2}$-Co $2p^{1/2}$ indicates that the Co may present in a partial spinel-type lattice arrangement and also indicates that the presence of Co^{3+} ions mixing with the Co^{2+} ions [105]. In addition, The presence of Co^{3+} and Co^{2+} ions is also confirmed by the asymmetry in the Co $2p^{1/2}$ peak. The photoelectron spectrum of Cu 2p [Figure 3.1.9(b)] reveals the doublet spin-orbit with the splitting of 19.7 eV at binding energies 932.8 and 952.5 eV corresponding to Cu

$2p^{3/2}$ and Cu $2p^{1/2,}$ respectively. The Cu 2p 3/2 at 932.8 eV and satellite feature indicates Cu may be in the oxidation state of 1+[75]. The Mn 2p spectrum [Figure 3.1.9(c)] had the strong spin-orbit doublet Mn $2p^{3/2}$-Mn $2p^{1/2}$ at 640.9 and 652.7 eV, respectively. The Mn $2p^{3/2}$ peak at 641 and satellite feature indicates that the Manganese may be in an oxidation state of 2+[106]. The Fe 2p core-level photoelectron spectrum [Figure 3.1.9(d)] shows the doublet spin-orbit peaks of Fe $2p^{3/2}$, Fe $2p^{1/2}$ with the splitting energy of 13 eV. The Fe $2p^{3/2}$ peak at 711 eV and satellite feature indicates that the Fe may be in an oxidation state of 3+ [88]. The Si 2p photoelectron spectrum presented in Figure 3.1.9(d) shows the peak at 103.3 eV represents the characteristic peak of SiO_2 [88]. The photoelectron spectrum of O 1s [Figure 3.1.9(d)] shows two peaks positioned at 529.6 and 531 eV, corresponding to the chemical state of M-O and -OH, respectively [75]. The oxidation states of the transition metals agree with the formed transition metal-based spinel oxide Co-Cu-Mn-O_x in a developed SSAC. In addition, XPS analysis confirms the presence of the transition elements Co, Cu, Mn, Fe, Si, and O in different oxidation states as mentioned above.

3.1.7 Structural and morphological study of absorber and tandem absorbers by HR-TEM

Figure 3.1.10 represents the TEM, HR-TEM, and SAED images of spinel nanoparticles. The micrographs comprise aggregated nanocrystals in the range of 25 nm to 120 nm with an irregular shape. The HR-TEM analysis reveals that the developed nanoparticles have a d-spacing of 2 A^o, and it coincides accurately with the d-spacing value of the X-Ray diffraction peak (hkl 311) of Co-Cu-Mn-O_x spinel. The SAED pattern obtained from spinel nanoparticles indicates that the developed particles are polycrystalline, and the obtained diffraction planes correspond to d_{111}, d_{220}, d_{311}, $d_{222,}$ indicating that particles are in the cubic phase. The interlayer spacing and d-spacings of diffraction planes in SAED patterns coincide with the allowed Bragg diffraction of the corresponding cubic spinel, which coincides with the XRD analysis. Figure 3.1.10(e) shows the TEM micrograph of SiO_2 nanoparticles used to synthesis of SiO_2 nanoparticle AR sol. The particle size is estimated and found to be in the range of 16-64 nm, and the average particle size is found to be 30nm.

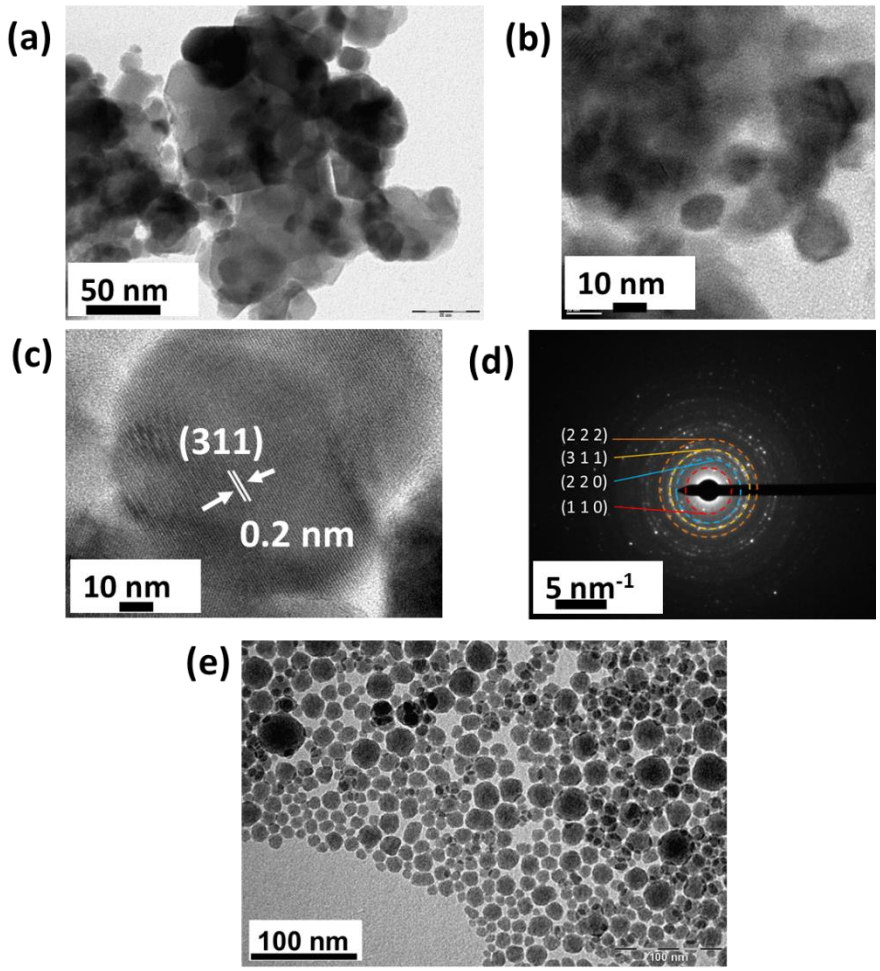

Figure 3.1.10. (a), (b)TEM (c) HR-TEM micrographs of spinel nanoparticles (d) SAED pattern of spinel nanoparticles, and (e)TEM micrograph of SiO_2 nanoparticles.

3.1.8 Roughness study of a bare substrate, absorber and tandem layer by a Stylus profilometer

The optimized absorber and tandem absorber samples were studied by the Stylus profilometer to determine the area roughness (S_a). A 50nm diamond tip is used for the scanning of a 1 mm x 1 mm area of absorber and AR coatings. The topography of bare substrate, absorber and tandem absorber samples is shown in Figure 3.1.11. The surface area roughness of the bare substrate (polished) is found to be 100nm, whereas the roughness of absorber and tandem absorber is 82 nm, and 75 nm respectively. The decrement in the roughness is also observed from substrate to absorber (S_a~82nm), and it is due to the formation of a uniform layer of spinel nanoparticles over on substrate. It is also evident from the topography of absorber shown in the Figure 3.1.11(b). Thus, the non-uniformity of substrate is visible in the topography of the absorber, as shown in Figure 3.1.11(a). Similarly, the roughness also decreased from the

absorber to the tandem layer due to SiO_2 nanoparticles covering the entire absorber layer. This accounts for the decrement in the observed surface area roughness from 82 nm to 75 nm.

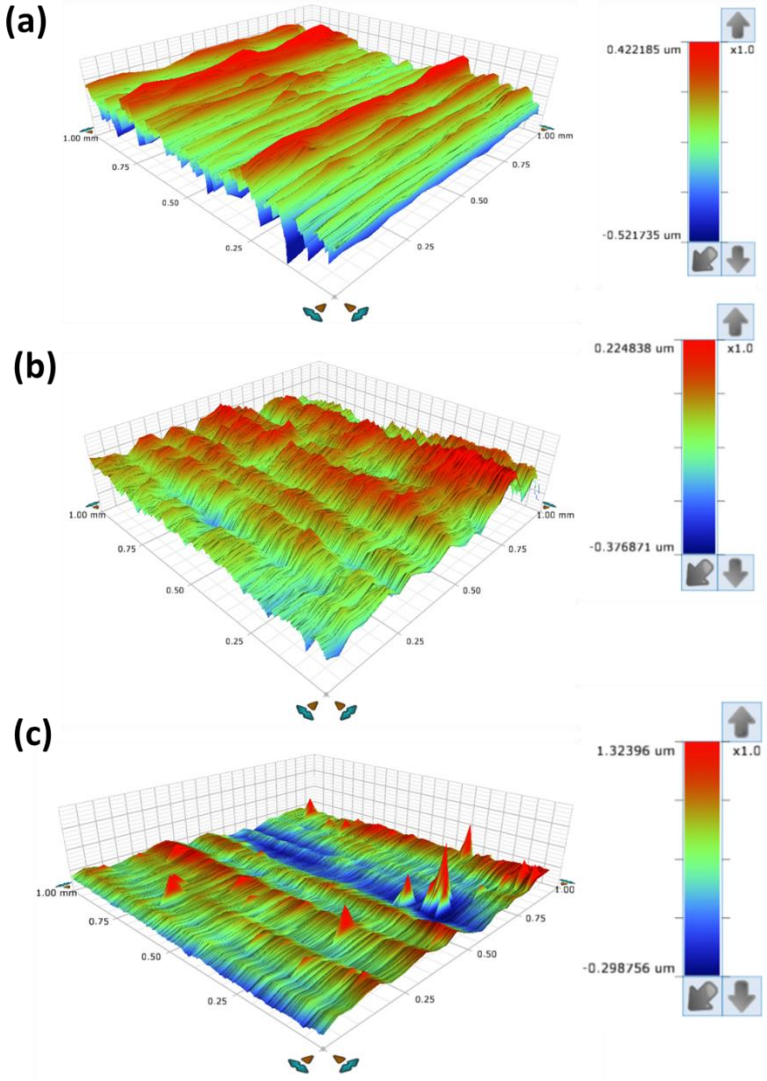

Figure 3.1.11. Topography of (a) bare substrate, (b)spinel absorber and (c) tandem absorber.

3.1.9 Morphological and thickness study of absorber and tandem layer by FE-SEM

The developed spinel and tandem absorbers were studied by FE-SEM to understand the morphology and to determine the thickness of optimized coatings. Figures 3.1.12(a) and (c) represent the morphology and thickness of the spinel absorber layer. The layer comprises spherical-shaped nanoparticles, nano cracks, and the thickness of the spinel absorber layer was found to be ~180 nm at an optimum withdrawal speed (2 mm/sec). To improve the absorption, an AR layer comprised of SiO_2 nanoparticles was deposited over on the spinel absorber. The commercial SiO_2 particles used for the AR layer were studied by TEM (Section 3.7) to identify the average particle size and found to be 30 nm. Figure 3.1.12(b) and (d) represent the morphology and thickness of the tandem absorber, respectively. At an optimized withdrawal

speed (2 mm/sec), the tandem absorber thickness was ~330nm, whereas the absorber and AR layer has a thickness of 180 nm and 150 nm, respectively.

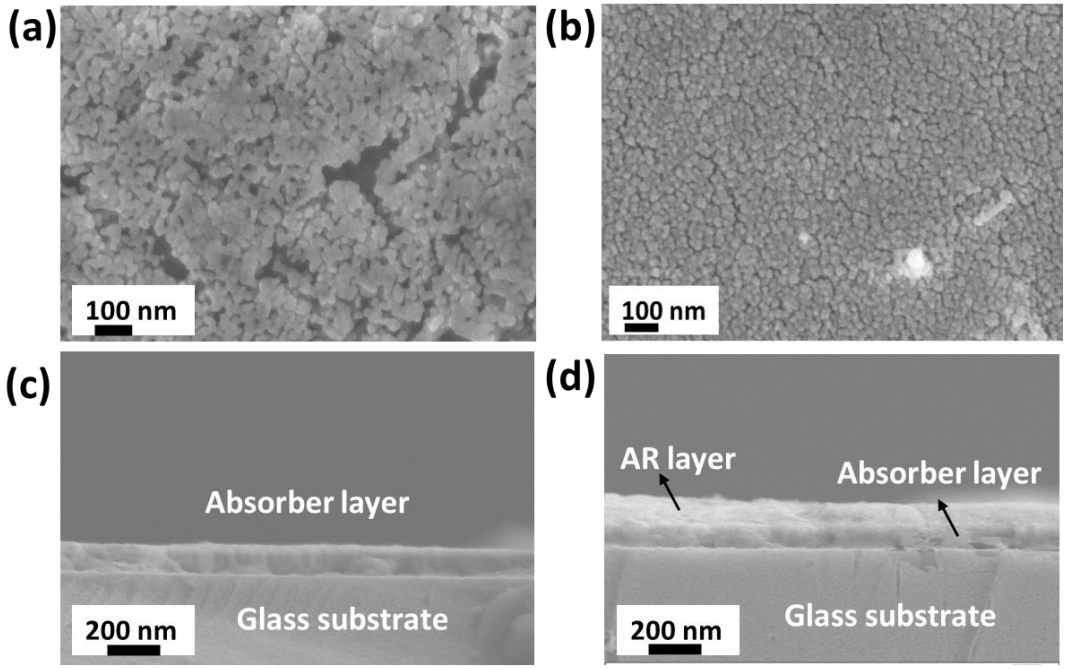

Figure 3.1.12. Morphology of (a) spinel absorber, (b) tandem absorber, a cross-section of (c) spinel absorber, and (d) tandem absorber coated over on a glass substrate.

3.1.9.1 Thickness and refractive index study of absorber and tandem absorber samples by Variable angle spectroscopic ellipsometry

In section 3.9, absorber and tandem samples were developed on a glass substrate and determined the thickness. The variable angle spectroscopic ellipsometry is utilized to measure the refractive index(η) and to confirm the thickness of the absorber and tandem coating on the SS 304 substrate. Figure 3.1.13 (a and b) shows the spectroscopic ellipsometer fit between the experimental and model data for absorber and tandem absorber samples on SS 304 substrate. Figure 3.1.13 (c and d) shows the spectral dispersions of n, k. Finally, the refractive index of the absorber and tandem samples is 1.82 ± 0.05 (at 550 nm) and 1.5 ± 0.05 (at 550 nm), respectively. The thickness of the absorber and tandem samples is 170 ± 5 nm and 145 ± 5 nm, respectively. The obtained thickness for both samples by spectroscopic ellipsometer is comparable with the thickness obtained by FE-SEM.

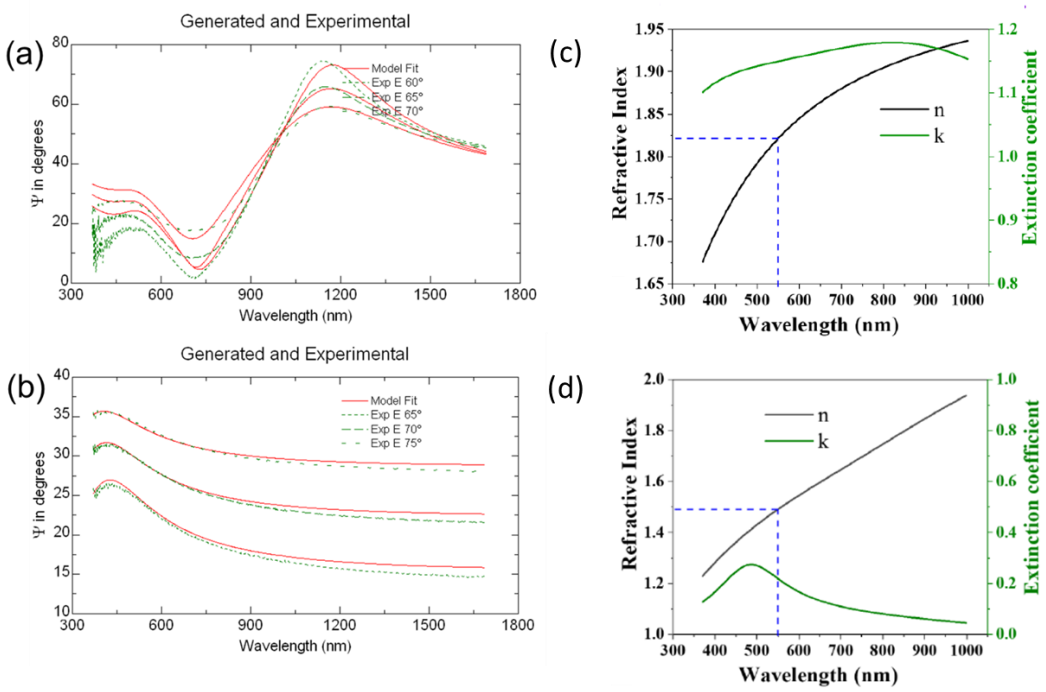

Figure 3.1.13. Ellipsometer spectra of experimental and model fit of (a) absorber and (b) tandem absorber, spectral dispersion of n and k for (c)absorber and (d)tandem coatings

The Mean Squared Error (MSE) quantifies the difference between generated and the measured data. A low MSE implies a good match between the model and experiment. The fitted result's mean squared error (MSE) value is for absorber and tandem samples is 10 and 7, respectively, which illustrates that the simulated optical constants are reliable due to the small value.

3.1.10 Thermal loss study

The spectral emittance (ε) characterizes the coating capability to reflect the IR radiation. However, it is a surface phenomenon, and it may not replicate the exact thermal loss behaviour of the absorber tube at operating temperature in a field. To replicate field performance, the developed spinel and tandem absorber samples were measured by the FT-IR spectrophotometer. To estimate the thermal emissivity, the prepared samples of spinel and tandem absorber coatings (13mm outer diameter) and blackbody were exposed at different temperatures from 100 °C to 500 °C with 100 °C intervals by using a temperature controller. Later, the emissivity was determined by fractionalizing the emittance of a sample and blackbody at a particular temperature. The thermal emissivity spectra of both spinel and tandem absorber samples are presented in Figure 3.1.14(a) & (b), and values at temperatures from 100 °C to 500 °C are mentioned in the table 3.1.4. It is observed that there is an increase in the emissivity from 100 °C to 500 °C in the case of both spinel and tandem absorbers.

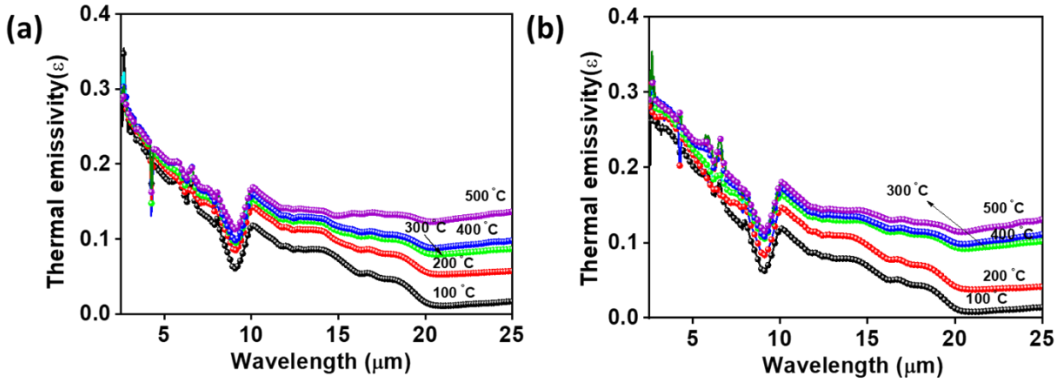

Figure 3.1.14. The thermal emissivity spectra of (a) spinel absorber (b) tandem absorber.

Table 3.1.5. The thermal emissivity of spinel absorber and tandem absorber at optimized withdrawal speeds.

Temperature (°C)	Spinel absorber	Tandem absorber
100	0.09	0.10
200	0.11	0.13
300	0.13	0.15
400	0.15	0.17
500	0.17	0.19

The spinel and tandem absorbers exhibited a low emissivity of 0.17 and 0.19, respectively, at 500 °C. The increase in the emissivity from spinel to tandem absorber may be due to an increment in the thickness of the stack in the case of the tandem absorber [107][108,109]. The light penetration depth (defined as the inverse of the absorption coefficient (α)) is closely related to the emissivity of coatings. The light penetration depth will be high for thicker coatings in comparison to low thickness coatings. Thus, the tandem absorber exhibits more emissivity in comparison with the spinel absorber.

3.1.11 Wide-angular selectivity of spinel and tandem absorber

To investigate the wide-angular selective characteristics, the specular reflectance spectra at different incident angles were measured for spinel and tandem absorbers using a Universal measurement accessory attached to the UV-Vis-NIR spectrophotometers (Carry 5000). Figure 3.1.15(a) and (b) show the contour plots of spinel and tandem absorber coatings at different

incident angles from 10° to 80°, and Figure 3.1.15(c) shows the angle of incidence (AOI) vs. Solar absorptance.

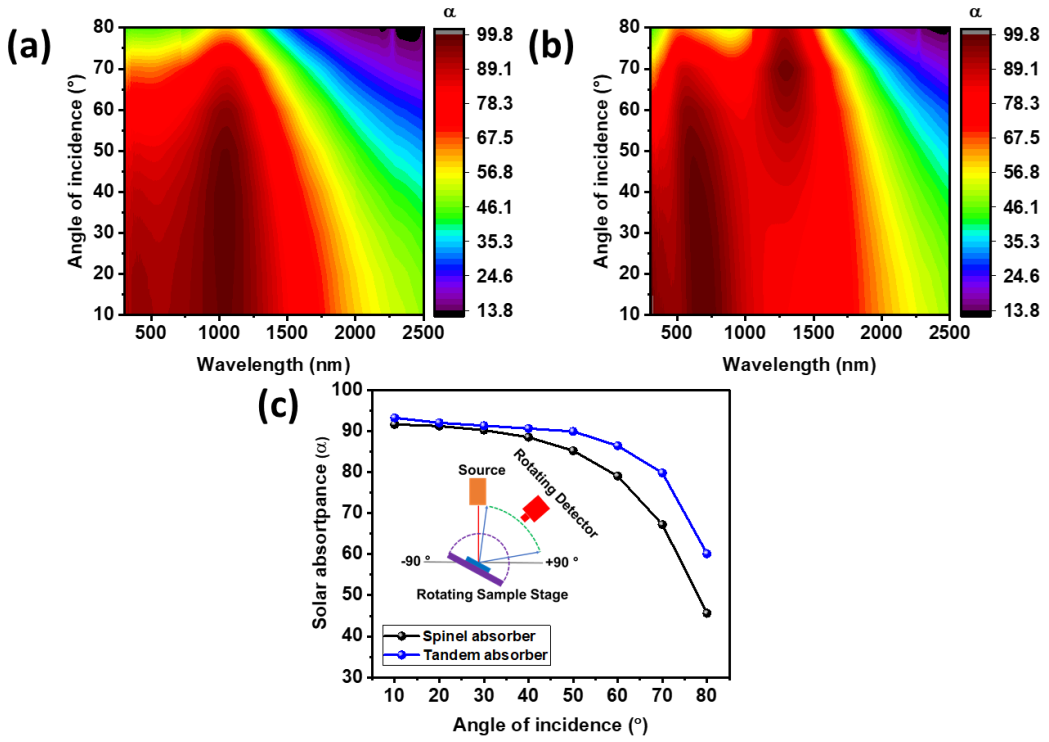

Figure 3.1.15. Contour plots of (a) spinel absorber, (b) tandem absorber, and (c) angular selectivity graph for spinel and tandem absorber.

The solar absorptance values of spinel absorbers and tandem absorbers are reported in Table 3.1.5. In the case of the spinel absorber, the solar absorptance decreases gradually as the incidence angle increases from 10° to 80°. According to Fresnel's equations, it can be attributed to the increment in the reflectance at large light angles [110]. However, the tandem absorber exhibits a high solar absorptance from 10° to 50° and a slight decrease from 50° to 80° compared to the spinel absorber layer. The tandem layer has exhibited outstanding wide-angular solar absorptance with a net enhancement of 1.7 to 31% over an angle of incidence ranging from 10° to 80°.

Table 3.1.6. Solar absorptance of spinel absorber and tandem absorber at different incident angles.

Incident angle (°)	**10**	**20**	**30**	**40**	**50**	**60**	**70**	**80**
Spinel absorber	0.91	0.90	0.88	0.85	0.80	0.72	0.59	0.37
Tandem absorber	0.93	0.92	0.91	0.90	0.89	0.86	0.79	0.60

The wide-angular selectivity of the tandem absorber may be explained by the mechanism of destructive interference, which occurs in the interface of two layers [111]. At a lower angle of incidence (10° to 50°), the reflected rays from the film surface interfere destructively and result in high solar absorptance. However, at higher incident angles, the reflected rays spread in all directions and may not interfere destructively, as it results in lower solar absorptance. Therefore, the developed tandem stack exhibit high solar absorptance at lower incident angles and low solar absorptance at higher incident angles, similar to the reported systems [112–117].

3.1.12 Conclusion

The development of Co-Cu-Mn-O_x/SiO_2 SSAC was described by using the wet chemical method and dip-coating technique. The developed SSACs exhibited a good solar absorptance of 0.93 and spectral emittance of 0.19. Further, physicochemical properties of developed materials and coatings were detailly studied with suitable characterization methods. Although developed SSACs have good solar absorptance, the spectral emittance and thermal emissivity (0.19 at 500 °C) are found to be high. The obtained thermal emissivity would lead to high thermal losses if receivers were developed with Co-Cu-Mn-O_x/SiO_2 SSAC and placed in a solar thermal system. It is because that thermal emissivity plays a vital role in the performance of a solar thermal system. Hence, an attempt was made to decrease the emittance of SSACs by replacing the Mo layer on glass instead of SS substrate, which is explained in the below section.

3.2 Development of High-Performance Tandem Layered Absorber with Wide-Angular Absorptance for Solar Thermal Systems

Metal substrate plays a vital role in obtaining low emittance since metals are good reflectors in the IR region [118]. Apart from that, they exhibit good thermal stability at high operating temperatures. In this connection, several metals or alloys such as Stainless steel, Aluminum, Inconel, Copper, Tungsten, and Molybdenum (Mo) were investigated as IR reflectors for SSACs [28–30]. Among all, Mo possesses a high melting point (2623 °C) and exhibits low emittance [120]. Various groups reported the development of SSAC by using Mo layer as an IR reflector and a few notable reports with good optical properties such as high solar absorptance ($\alpha \geq 0.95$) and low emittance($\varepsilon \leq 0.20$) are mentioned here [120–129]. For example, Liqing Zheng et al. developed Mo–SiO_2 double cermet SSAC by mid-frequency and radio frequency co-sputtering method using the Mo layer as an IR reflector. They obtained 0.95 of solar absorptance and 0.15 of spectral emittance at 400 °C [122]. Another report also claimed the angular absorptance of 0.94 from 0 to 60° for Mo-SiO_2 based SSAC developed by Magnetron co-sputtering [116].

In this connection, developing a high-performance tandem layered absorber with wide-angular absorptance is reported using cylindrical rotating direct current magnetron sputtering and wet chemical methods. Initially, a metallic Mo layer over the soda-lime glass substrate was deposited by a sputtering method to serve as a low emissive layer. Further, the tri-transition metal (Mn, Cu, and Co) based precursor absorber sol (reported in earlier section 3.1) was deposited on the Mo layer by the dip-coating method and annealed in a vacuum environment. The developed absorber is comprised of transition metal oxides, and they are responsible for the drastic improvement in solar absorptance. The SiO_2 nanoparticle AR layer was deposited by dip-coating method on absorber to enhance the solar absorptance. Here, the thickness and amount of metal concentration were also optimized inside the absorber and AR layers. Consequently, the developed tandem absorber exhibited high absorption and low emittance in the solar and IR regions, respectively. Additionally, the tandem absorber also showed excellent wide-angular absorption from 10 to 70°. The coatings were studied by using Glancing Incidence X-ray diffraction (GI-XRD), X-ray photoelectron spectroscopy (XPS), Field Emission Scanning Electron Microscope (FE-SEM), and High-resolution transmission electron microscopy (HR-TEM) techniques to understand structural and morphological properties.

3.2.1. Fabrication of low emissive metallic Mo layer for the development of tandem absorber

To develop a highly selective absorber coating with low emittance, a metallic layer made up of pure Mo metal was deposited on soda-lime glass (300 mm (L)× 300 mm (W)× 3 mm (T)) substrates by using direct current rotary tube magnetron sputtering [130]. For the present work, the Mo layer was sputtered at a deposition power of 2250 W and working gas (Argon) flow rate of 1000 Standard cubic centimetres per minute. Several samples were fabricated with different Mo thicknesses of 50, 100, and 200 nm, and optimum thickness was chosen to achieve high absorptance and low emittance. The process for the development of the Mo layer is shown in Figure 3.2.1(a).

3.2.2. synthesis of transition metal-based absorber coating solution and development of absorber coating on low emissive Mo layer

The synthesis of absorber coating sol is described in section 3.1, and the same sol was utilized to develop absorber coatings on the Mo layer by the dip-coating method. Several samples were developed by varying the withdrawal speed from 0.5 to 3 mm/sec. Finally, the samples were cured in a vacuum environment by using a tubular vacuum furnace. The quartz tube was evacuated using a rotary pump, and the pressure was stabilized inside the tube by purging the Nitrogen gas at regular intervals of time to avoid contaminations. The desired temperature and pressure ($1x10^{-3}$ m bar) were kept constant throughout the annealing process. After the annealing process, samples were cooled to room temperature by natural convection. The parameters such as withdrawal speed, annealing temperature, and duration were optimized to develop a highly selective absorber. The process for the development of the absorber layer is shown in Figure 3.2.1(b). The resultant stack is termed as a nanocomposite absorber, and it comprises several layers on Glass as Mo and base absorber.

3.2.3 Synthesis of AR coating solution and development of AR layer on nanocomposite base absorber coating

The synthesis of SiO_2 nanoparticle-based AR coating solution is described in chapter 2, section 2.5. Several samples were developed by utilizing the AR coating solution at withdrawal speeds from 0.5 to 2 mm/sec. The developed coatings were annealed in an open-air atmospheric oven at 200 °C for one hour. The resultant stack is termed as a tandem absorber, and it comprises of several layers on the Glass as Mo, nanocomposite base absorber, and AR layer. The process

parameters such as withdrawal speed, annealing temperature, and duration were optimized to achieve a highly selective absorber. The process for the development of the AR layer is shown in Figure 3.2.1(c).

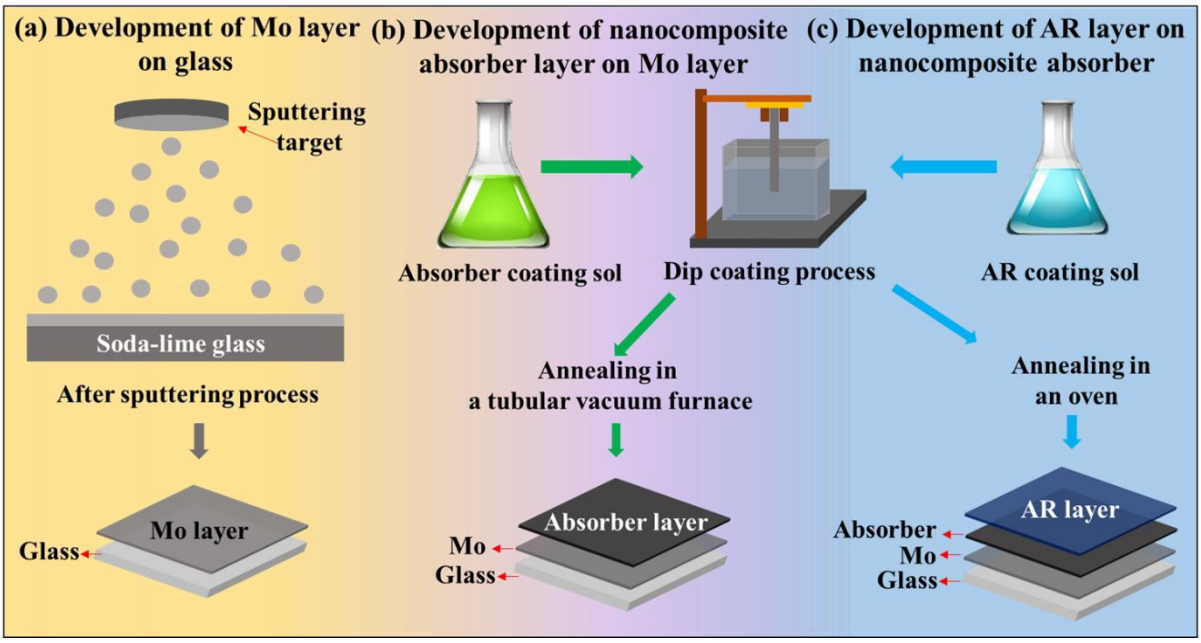

Figure 3.2.1. Schematic picture for the development of tandem absorber; development of (a) Mo layer, (b) nanocomposite absorber layer on Mo layer and (c) AR layer on nanocomposite absorber.

3.2.4. Optical properties of developed coatings

The soda-lime glass substrates were used for the development of Mo coatings. Figure 3.2.2 represents the (a) transmittance and (b) reflectance spectra of soda-lime glass from 0.3 to 25 µm, respectively. In Figure 3.2.2(a), the transmittance spectra show that the glass exhibits 81.4% of average transmittance from 300 to 2500 nm and 2.4% of average transmittance from 2.5 to 25 µm. In Figure 3.2.2(b), the glass exhibits 7.7% of average reflectance from 300 to 2500 nm and 25.8% of average reflectance from 2.5 to 25 µm.

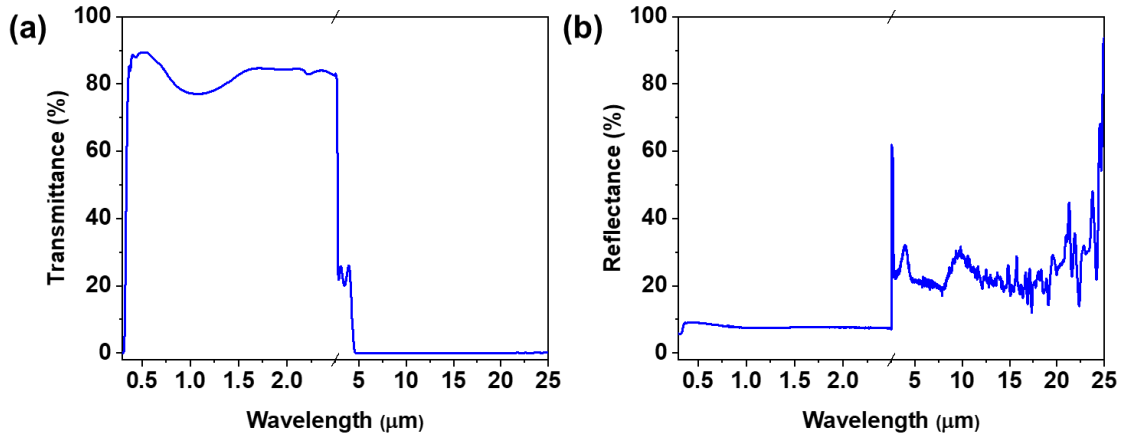

Figure 3.2.2.(a) Transmittance and (b) Reflectance spectra of soda-lime glass from 0.3 to 25 μm.

The Mo metallic layer coatings were developed with the thickness ranging from 50 to 200 nm over on soda-lime glass to fabricate a low emissive coating for the development of a tandem solar absorber. Here, the thickness of the Mo layer strongly affects the optical properties such as solar absorptance and spectral emittance. A similar observation was also reported by Yuping Ning et al. and reported elsewhere [120]. Thus, the absorptance and emittance properties of Mo samples having different thicknesses were measured and optimized the Mo layer thickness to obtain lower emittance. From Figure 3.2.3 and Table 3.2.1, it is clear that at an optimized thickness of 100 nm, the Mo layer has shown a very low emittance of 0.04 and an absorptance of 0.36. Here, the obtained optical properties are due to the Mo layer acting as an IR reflector. The intra-band transitions of the electrons in the conduction band of Mo metal are responsible for the low emittance and absorptance from IR to the visible light region. Hence, here onwards, the optimized Mo layer thickness of 100 nm is used as a low emissive layer for all the experiments to develop a tandem solar absorber.

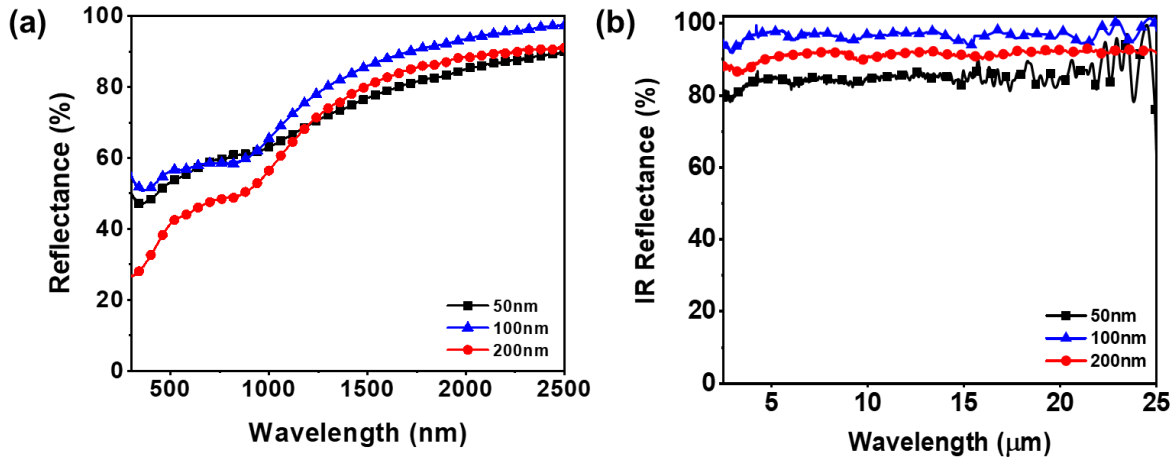

Figure 3.2.3. (a) UV-Vis-NIR and (b) IR reflectance spectra of Mo layer on soda-lime glass with different thicknesses.

Table 3.2.1. Optical properties of the Mo layer over on soda-lime glass.

The thickness of the Mo layer (nm)	**Mo layer over on soda-lime glass**	
	α (300-2500 nm)	**ε (2.5-25 μm)**
50	0.39	0.15
100	0.36	0.04
200	0.47	0.09

Further, a base absorber layer was applied over on Mo with different withdrawal speeds to improve the solar absorptance. The reflectance spectra of the nanocomposite base absorber layer at different withdrawal speeds are presented in Figure 3.2.4 (a & b), and corresponding values of optical properties are shown in Table 3.2.2. At an optimum withdrawal speed (0.5 mm/sec), the base absorber exhibited a high absorptance of 0.90 and a low emittance of 0.10.

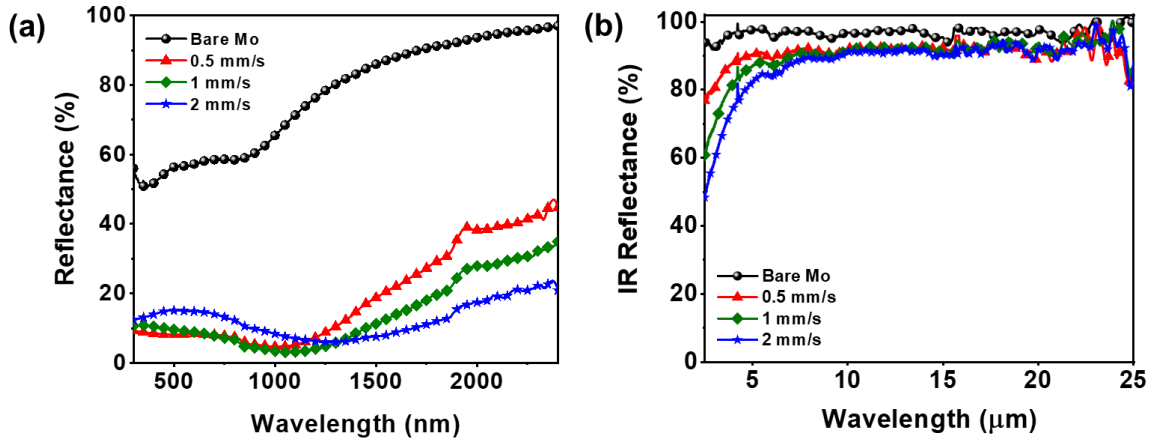

Figure 3.2.4. (a) UV-Vis-NIR and (b) IR reflectance spectra of nanocomposite base absorber layer on Mo/glass with different withdrawal speeds.

Table 3.2.2. Optical properties of nanocomposite base absorber layer on Mo/glass with different withdrawal speeds.

Withdrawal speed (mm/sec)	**Nanocomposite base absorber layer on Mo/glass**	
	α (300-2500 nm)	**ε (2.5-25 μm)**
Bare Mo (~100 nm)	0.36	0.04
0.5	0.90	0.10
1	0.91	0.11
2	0.88	0.15

The improvement in the solar absorptance for the base absorber from 0.36 to 0.90 is due to the intrinsic absorption of solar radiation caused by the transition metal or metal oxides present in the base absorber layer developed at an optimum withdrawal speed of 0.5 mm/sec [102]. The SiO_2 nanoparticles-based AR layer was applied over an on-base absorber to improve the optical properties. Consequently, the excellent solar absorptance of 0.96 and emittance of 0.12 were obtained at an optimum withdrawal speed (1 mm/sec), as shown in Figure 3.2.5 (a & b) and Table 3.2.3.

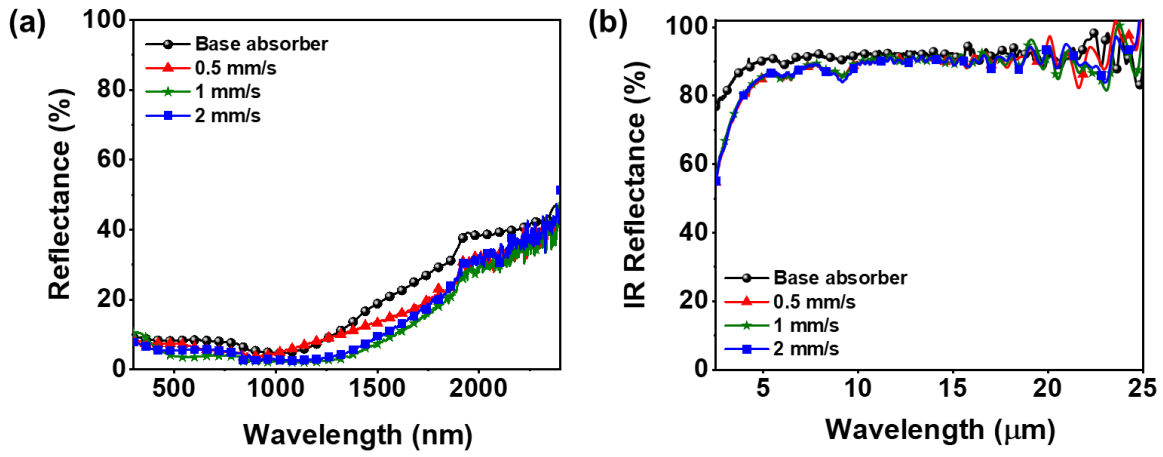

Figure 3.2.5. (a) UV-Vis-NIR and (b) IR reflectance spectra of SiO_2 nanoparticles-based AR layer with different withdrawal speeds on absorber/Mo/glass.

Table 3.2.3. Optical properties of AR layer on absorber/Mo/glass with different withdrawal speeds.

Withdrawal speed (mm/sec)	**SiO_2 nanoparticles AR layer on absorber/Mo/glass**	
	α (300-2500 nm)	**ε (2.5-25 μm)**
Base absorber	0.90	0.10
0.5	0.94	0.12
1	0.96	0.12
2	0.92	0.12

The improvement in the absorption is caused by the interband electronic transitions and the excitation of vibrational of SiO_2 present in the AR layer [12, 38]. In addition, destructive interference occurred at the base absorber interface and the AR layer at an optimum thickness may reduce the reflection. Thus, it enhances the absorption of solar light.

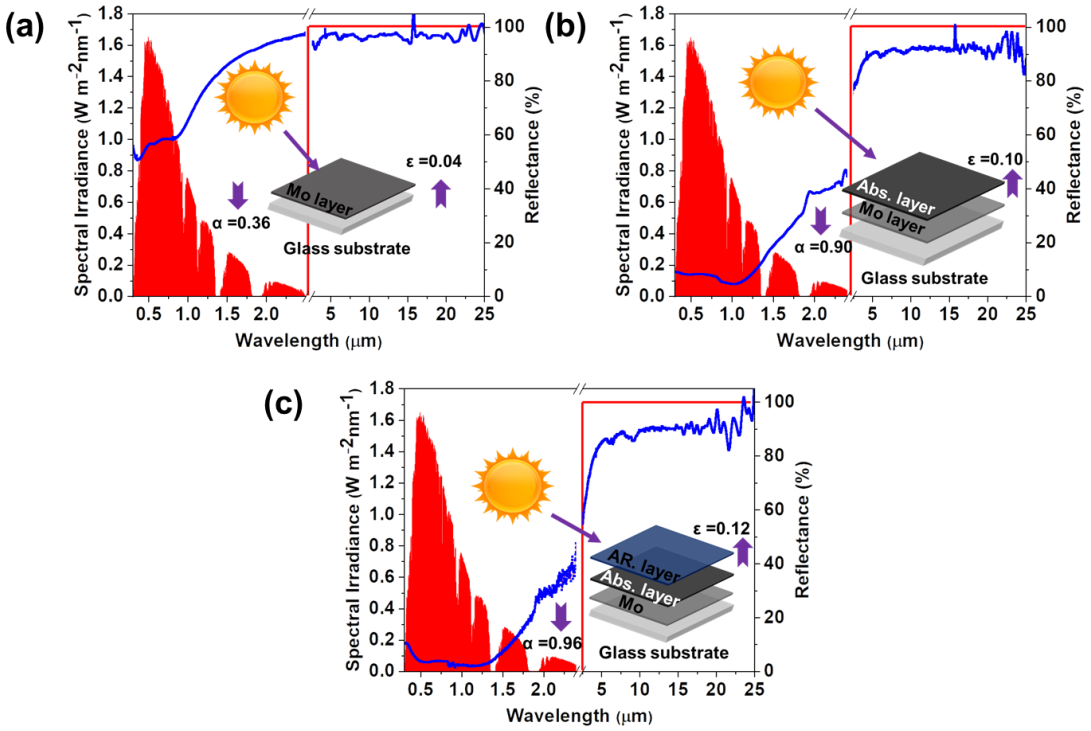

Figure 3.2.6. The combined reflectance spectra of (a) Mo layer (b) nanocomposite base absorber and (c) tandem absorber (SiO_2/absorber/Mo/glass) at an optimum withdrawal speed in the UV-Vis-NIR and IR region with reference to AM 1.5 solar spectrum and red lines represent high absorption and zero emittance of an ideal SSAC (Inset (a, b and c): Schematic diagrams of different layers on glass substrate).

The combined reflectance spectra of low emissive Mo layer, base absorber on Mo, and tandem absorber with AR layer at an optimized withdrawal speed are shown in Figure 3.2.6 (a, b & c) with reference to AM 1.5 solar spectrum. The schematics for the low emissive Mo layer, base absorber on Mo, and tandem absorber with AR layers are presented in the inset of Figure 3.2.6(a, b and c), respectively. From Figure 3.2.6c, it is clearly observed that the developed tandem SSAC exhibited the best optical properties, such as 0.96 of solar absorptance and 0.12 of emittance.

3.2.5 Structural characterizations of coatings

3.2.5.1 Structural study of the nanocomposite base absorber by XRD

The optimized base absorber coating on the Mo layer was characterized by XRD to understand the crystal structure of the coating material responsible for the high absorption. Figure 3.2.7(a) represents the XRD pattern of base absorber coating developed over Mo/glass. The observed

peaks at 40.5° and 58.7° are assigned to the Mo metal with the BCC phase, and it is in good agreement with the International Center for Diffraction Data (ICDD) data (00-004-0809) [130]. However, the diffraction peaks corresponding to the base absorber layer are unclear, and it could be due to weak signals obtained from the absorber film by conventional powder XRD. In this regard, the base absorber samples at a glancing incident angle of 0.5° were measured to obtain the signal from the absorber film and to minimize the contribution related to the Mo layer and substrate. Figure 3.2.7(b) represents the GI-XRD pattern of base absorber coating developed over on Mo/glass, and the observed diffraction peaks are assigned the Mo, MoO_2, MoO_3, $CuCo_2O_4$, and CuO, respectively.

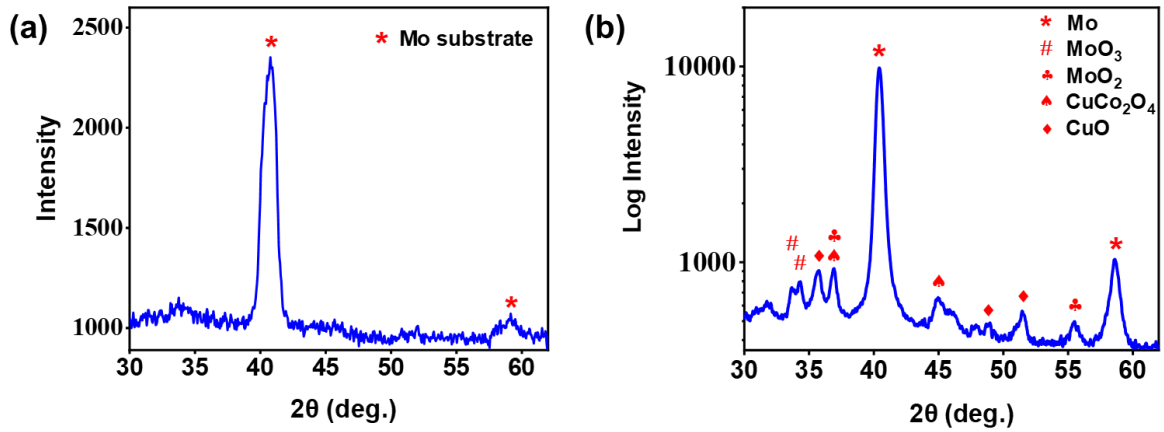

Figure 3.2.7. (a) XRD and (b) GI-XRD pattern of the base absorber/Mo layer/glass substrate.

The peaks at 40.5° and 58.7° in Figure 3.2.7(b) are assigned to the Mo metal with the BCC phase as shown in Figure 3.2.7(a), and it is in good agreement with the ICDD data (00-004-0809) [130]. The diffraction peaks observed at 33.6°, 34.0° and 36.9°, 55.5° are assigned to MoO_3 (00-004-6459) and MoO_2 (01-085-6326), respectively. The occurrence of MoO_3 and MoO_2 diffraction peaks is either due to the formation of passivation layer on low emissive (Mo) layer or reaction of diffused Mo metal ions with Oxygen evolved from the transition metal precursor layer while annealing [131]. Similarly, the transition metals such as Co and Cu available in the deposited coating are also found to have reacted with Oxygen and led to the formation of $CuCo_2O_4$ (00-066-0541) and CuO (00-048-1548). However, the formation of MnO (01-075-0626) is ambiguous since the diffraction peaks of MnO overlapped with the Mo peaks. So, the sample is characterized by XPS to analyze the presence of MnO. In conclusion, the occurrence of transition metal oxides present in the nanocomposite base absorber layer are

responsible for achieving the high solar absorptance of 0.90 at a 0.5 mm/sec withdrawal speed of coating.

3.2.5.2 XPS study of the nanocomposite base absorber

XPS measurement was carried out to determine the oxidation states of elements present in the nanocomposite absorber coating responsible for the good optical properties. The XPS spectra of Mo 3d, Cu 2p, Mn 2p, Co 2p, and O 1s are shown in Figure 3.2.8. The Mo 3d spectrum in Figure 3.2.8 (a) has strong two spin-orbit doublets (Mo $3d_{5/2}$ - Mo $3d_{3/2}$). The peaks at 229.2 eV and 232.2 eV characteristic of MoO_2, may be ascribed to Mo^{4+} $3d_{5/2}$ and Mo^{4+} $3d_{3/2}$, respectively [132]. The peaks at 232.5 eV and 235.5 eV characteristic of MoO_3, may be attributed to Mo^{6+} $3d_{5/2}$ and Mo^{6+} $3d_{3/2}$, respectively [132]. MoO_2 and MoO_3 phases are also observed in the XRD analysis, and it is also well reported in the literature [132]. The reason for the formation of MoO_2 and MoO_3 phases is attributed to the passivation layer on Mo substrate or diffusion of Mo metal ion and reaction with oxygen mentioned in section 3.2.1 [131,133]. Figure 3.2.8 (b) represents the Cu 2p XPS spectra, and the peaks at 932.1 eV and 952.1 eV characteristic of Cu_2O may be attributed to Cu $2p_{3/2}$ and Cu $2p_{1/2}$, respectively. The satellite peak at 946 eV indicates that the Cu might be in the 1+ state [134]. It could be due to the reaction of copper metal with the evolved oxygen in the furnace and led to the formation of Cu_2O. Although the occurrence of Cu_2O is contrary to the confirmation of CuO in XRD analysis, the presence of Cu^{1+} ions cannot be ruled out in the form of $CuCo_2O_4$ spinel. In addition, the XPS technique is a surface-sensitive, localized measurement and is different to bulk sensitive XRD technique. Figure 3.2.8 (c) represents the Mn 2p XPS spectra, and the peaks at 641.4 eV and 653.1 eV characteristic of MnO may be ascribed to Mn $2p_{3/2}$ and Mn $2p_{1/2}$, respectively. The satellite peak around 647 eV indicates that the Mn might be in the +2 state [135]. Thus, the presence of MnO is confirmed in the nanocomposite base absorber. Figure 3.2.8 (d) represents the Co 2p XPS spectra and the peaks at 778 eV and 792.8 eV characteristic of Co metal, respectively. Surprisingly, the Co metal diffraction peaks in the XRD pattern are missing. It could be due to either the material being amorphous or not enough volume to produce peaks of considerable intensity in XRD. The peaks at 779.8 eV, 795.2 eV, and 783.2 eV, 798.6 eV corresponds to the Co (III) and Co (II) respectively, and it might be characteristic of a mixed spinel ($CuCo_2O_4$) [76]. The satellite features due to the +2 and +3 states are observed at 787.6 eV and 803 eV, respectively [135]. Thus, the formation of $CuCo_2O_4$ spinel is confirmed by XPS and GI-XRD studies. The Si 2p photoelectron spectrum presented in Figure 3.2.8(e) shows the peak at 103.3 eV represents the characteristic peak of SiO_2 [88].

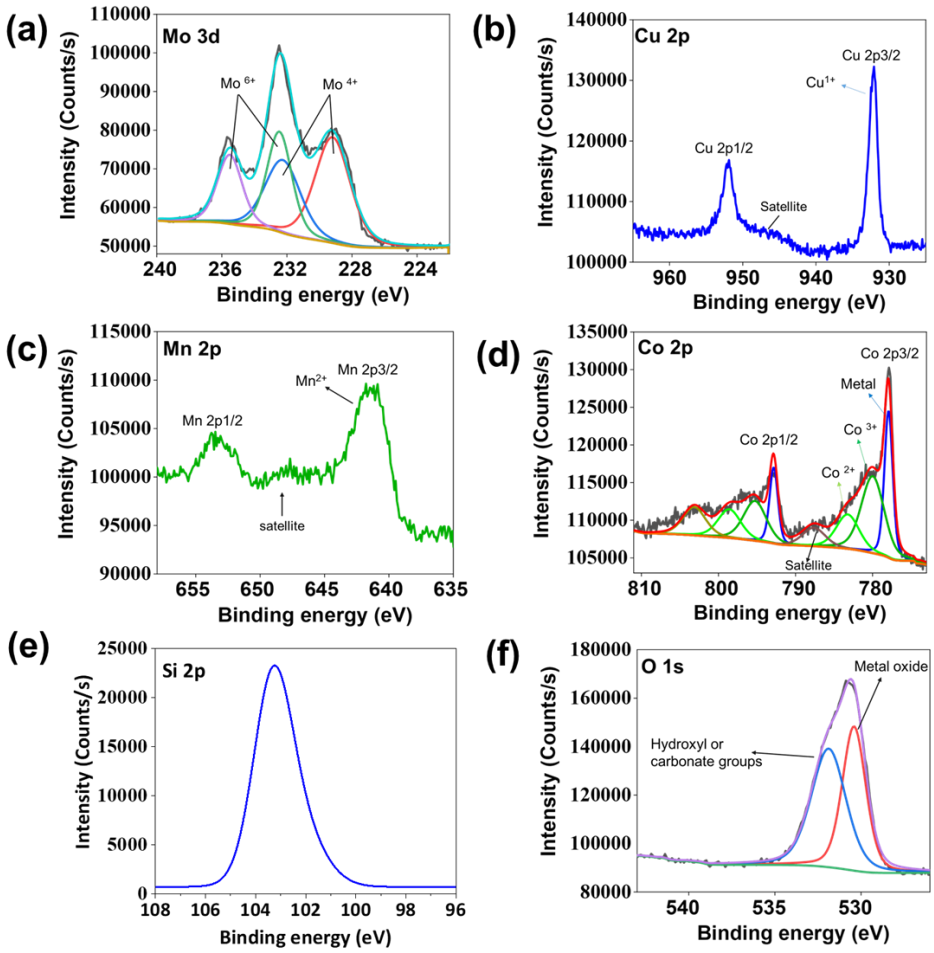

Figure 3.2.8. XPS spectra of the nanocomposite base absorber (a) Mo (b) Cu (c) Mn (d) Co (e) Si and (e) O.

Figure 3.2.8 (f) represents the O 1s XPS spectra and the peaks at 530.4 eV and 531.9 eV characteristic of metal oxides and as hydroxyl, carbonate groups, etc., respectively [75]. Hence, the obtained excellent optical properties are attributed to the developed transitional metal and metal oxides in the nanocomposite absorber layer, and the compositions were well correlated with XRD & XPS analysis.

3.2.6 Morphological study of the nanocomposite base absorber and tandem absorber

3.2.6.1 Morphological study nanocomposite base absorber by HR-TEM

The nanocomposite base absorber layer particles were studied by the TEM to understand the nature of particles. The TEM, HRTEM, and SAED micrographs were recorded and shown in Figure 3.2.9 (a, b, c and d), respectively. The micrographs shown in Figure 3.2.9 (a & b)

displays the aggregated nanocrystals of transition metal & metal oxides (as analyzed in XRD & XPS) with an irregular shape.

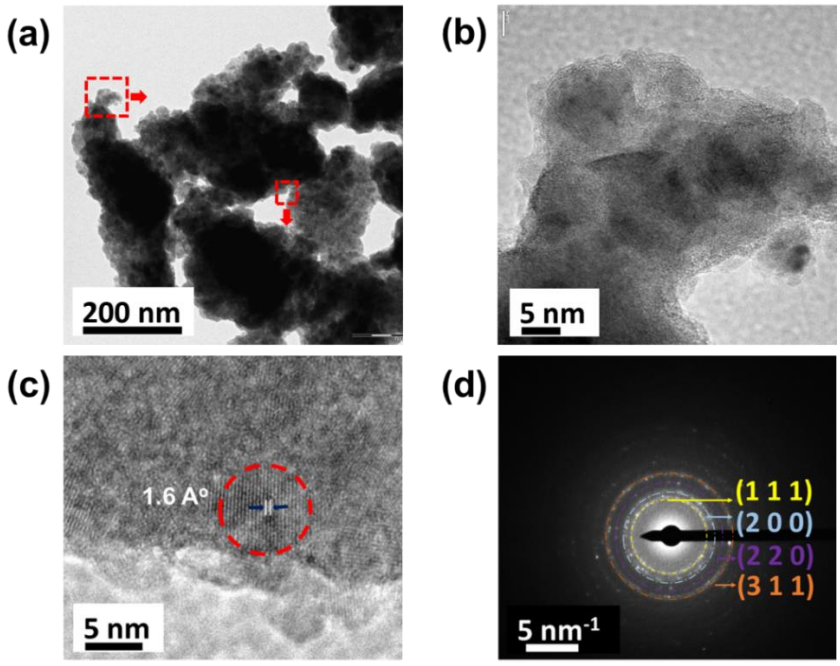

Figure 3.2.9. (a), (b) TEM, (c) HR-TEM micrographs, and (d) SAED pattern of nanocomposite base absorber layer particles.

The spacing of lattice fringes in the HR-TEM micrograph (Figure 3.2.9(c)) is 1.6 A^{o}, close to the d-spacing value of the MnO (2 2 0) plane. The close examination of localized SAED micrograph in Figure 3.2.9(d) disclosed that the developed absorber nanoparticles are in polycrystalline, and the SAED diffraction ascribed to d_{111}, d_{200}, d_{220}, d_{311} of MnO having cubic phase.

3.2.6.2 Morphological study of the Mo layer, nanocomposite base absorber, and tandem absorber by FE-SEM

The surface morphology of the Mo layer, nanocomposite base absorber, and tandem absorbers was investigated by FE-SEM, and the recorded micrographs are shown in Figure 3.2.10. The Mo layer is shown in Figure 3.2.10(a) has excellent uniformity without any cracks and pinholes.

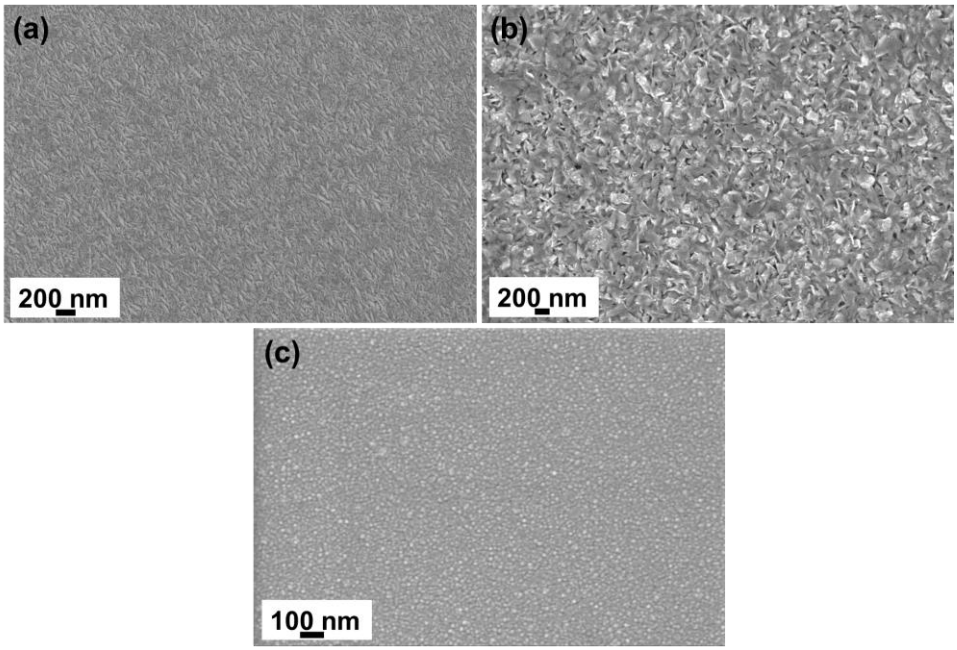

Figure 3.2.10. The micrographs of (a) Mo layer (b) nanocomposite base absorber and (c) tandem absorber layers by FE-SEM.

The nanocomposite base absorber layer, as shown in Figure 3.2.10(b), consists of uniform and denser nanoflakes throughout the coating. The tandem layer over on the base absorber shows that the coating of SiO_2 nanoparticles completely covered the absorber coating uniformly without any cracks, as shown in Figure 3.2.10(c).

3.2.7 Thickness studies of the Mo, nanocomposite base absorber, and tandem absorber layers by FE-SEM

The excellent absorptance and low emittance have been obtained for the tandem absorber stack of low emissive (Mo) layer (~100 nm), nanocomposite base absorber, and AR coating at optimized thickness. To measure the thickness, a cross-sectional micrograph of developed coatings has been recorded by using FESEM. The micrograph in Figure 3.2.11(a) displays the Mo layer deposited on the soda-lime glass with columnar grains having a thickness of 100 nm.

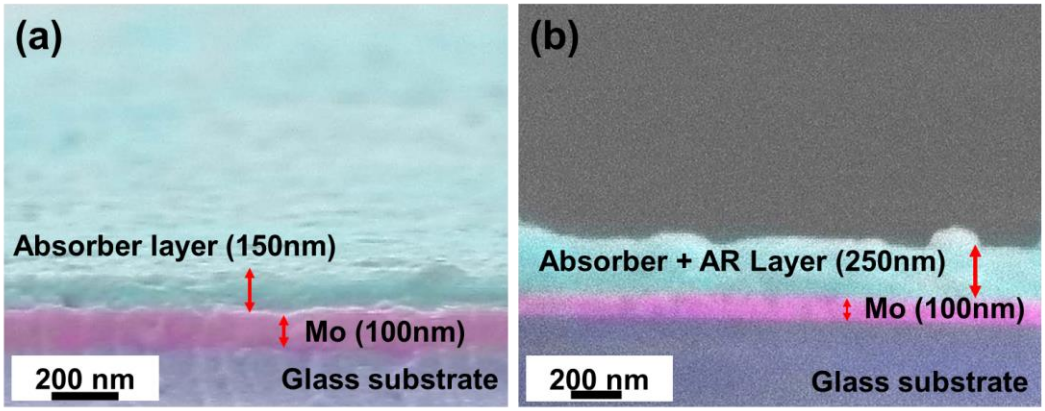

Figure 3.2.11. Cross-sectional micrographs of (a) Mo layer, nanocomposite base absorber, and (b) tandem absorber coating.

Figure 3.2.11(a) also displays the two layers (Mo and nanocomposite base absorber) with the interface over on glass substrate. The estimated thickness of the absorber layer is 150 ± 5 nm, respectively. Figure 3.2.11(b) displays the cross-sectional micrograph of a tandem absorber having a low emissive (Mo) layer, base absorber, and AR coatings over on glass substrate. The developed AR coating overlaps with the absorber and results in a combined stack (absorber + AR coating) with a thickness of 250 nm. It is estimated that the thickness of the AR layer is 100 nm.

3.2.8. Wide-angular absorptance of the nanocomposite base absorber and tandem absorber

In general, the measurement of reflectance for the SSAC is done at near-normal incident angles to obtain the solar absorptance values. However, the incident angle of the sun to the surface of SSAC will affect the solar absorptance, and the relative angle of the sun varies during the day and across seasons. Therefore, SSAC must possess wide-angular absorptance to obtain high photothermal conversion efficiency (PTCE). So, the reflectance of the developed nanocomposite base absorber and tandem absorber coatings has been measured from 10 to 70° to determine the wide-angular absorptance. Figure 3.2.12 (a & b) represents the contour plots of nanocomposite base absorber and tandem absorber coatings from 10 to 70°, respectively. The angle of incidence vs. solar absorptance graph is presented in Figure 3.2.12(c). The solar absorptance values of base and tandem absorbers at different incident angles are reported in Table 3.2.4.

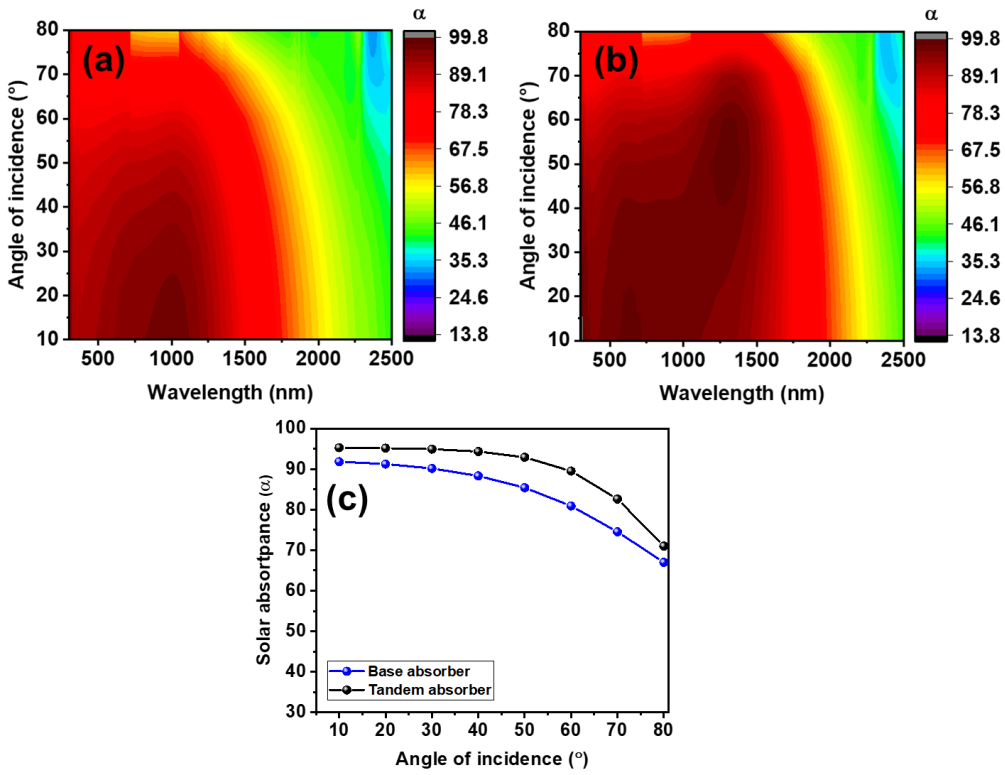

Figure 3.2.12. Contour plots of (a) base nanocomposite absorber and (b) tandem absorber; (c) solar absorptance of base and tandem absorber coatings at a different incident of angles.

Table 3.2.4. Solar absorptance of nanocomposite base absorber and tandem absorber at different incident angles.

Sample name	**Solar absorptance at different incident angles**							
	10°	**20°**	**30°**	**40°**	**50°**	**60°**	**70°**	**80°**
Nanocomposite base absorber	0.91	0.91	0.90	0.88	0.85	0.81	0.74	0.67
Tandem absorber	0.95	0.95	0.94	0.94	0.92	0.89	0.81	0.71

From Figure 3.2.12 and Table 3.2.4, it is observed that the solar absorptance of the nanocomposite base absorber is decreased from a low incident angle (10°) to a high incident angle (70°). It is due to an increment in the reflectance, which normally occurs when the incident angle increases from low to higher angles, as shown in Figure 3.2.12(c) [110]. However, the tandem layered SSAC exhibits the net enhancement in solar absorptance from

3.7% to 10.8% with increasing the incident angle from 10 to 70° respectively. The net enhancement in the solar absorptance may be attributed to the destructive interference that occurred at the interface of absorber and AR layers from 10 to 70°. Similar wide-angular absorption was observed in the several tandem absorber systems [78,116,136]. Hence, we can say that the developed high-performance tandem layered absorber coating has excellent absorption, low emission, and wide-angular absorption. The developed tandem system can be used as an efficient SSAC in a flat plate and parabolic collectors, where SSAC will convert solar radiation into heat with low thermal losses. The generated thermal energy can be utilized for various solar thermal applications.

3.2.9. Conclusion

The development of a high-performance tandem absorber (Glass/Mo/Nanocomposite base absorber/SiO_2) with wide-angular absorptance by using sputtering and wet chemical methods is described. After optimizing the process parameters such as Mo layer thickness, withdrawal speeds of coatings, and annealing conditions, the developed tandem absorber exhibited the solar absorptance of 0.96 and spectral emittance of 0.12. The tandem absorber also showed good wide-angular absorption with a net improvement of 3.7 to 10.8% from 10 to 70°. The nanocomposite base absorber is studied by the GI-XRD and XPS to understand the crystal structure of the materials responsible for the high absorption and found that the formed transition metal and metal oxides improve the absorption. The insight from this work will provide a new strategy for developing a low emissive and wide-angular SSAC by the combination of sputtering and wet chemical methods. It may significantly improve the photothermal efficiency of solar receiver tubes for solar thermal systems. However, the objective of the present work is to develop cost-effective SSACs by using wet chemical methods. So, the developed tandem absorber was not considered for further studies. In this connection, another attempt was made to develop the high thermal and spectrally selective coatings by incorporating ZrO_2 nanoparticles in the absorber coating sol, which is further discussed in the below section.

3.3. Development of Zirconia Nanoparticles Embedded Spinel Solar Selective Absorber Coatings

The development of high-temperature stable SSACs is one of the main objectives of the present thesis work. As mentioned earlier in chapter 1, section 1.15, spinel materials have attracted significant attention in spectrally selective absorber coatings in the last decade because of their inherent high temperature and oxidation stability. Several articles were reported based on spinel structured material based on transition materials as reported in section 1.15. Very few studies have also reported that high thermal stable and selective SSACs were developed by incorporating suitable nanoparticles into composite absorber sol. For example, Xavier Paquez et al. has reported a simple wet chemical route for a bilayer RuO_2/SiO_2 nanoparticles stack on a pre-oxidized stainless tube exhibiting thermal stability in the air up to 600 °C with a solar selectivity ($\alpha > 0.94$, and ε at 600 °C <0.28) [137].

The Zirconia (ZrO_2) is a well-known refractory material with excellent mechanical properties. It has a high melting point >2700 °C and good oxidation resistance [138]. The ZrO_2 has been used in several applications, such as thermal barrier coatings, metal components for gas turbines [139]. In this connection, we synthesised ZrO_2 nanoparticles using the solvothermal method and incorporated the transition metal-based precursor sol, synthesised by the we-chemical method. The nanocomposite SSACs were developed by the dip-coating method. Absorption was enhanced further by using different AR coatings such as MgF_2, SiO_2 nanoparticles, and ZrO_2-SiO_2 composite AR coatings. Additionally, the optical, structural, and temperature stability of developed SSACs were studied.

3.3.1. Synthesis of Zirconia Nanoparticles

A clear solution of Zirconium precursor mixture was prepared with n-propanol, Hydrochloric acid (HCl), and De-ionized water by sequential mixing in the molar ratio of 25: 2: 1: 1 (n-propanol: Zr precursor: HCl: De-ionized water). The mixture was stirred at room temperature until a clear suspension was obtained. After that, the mixture was transferred to a Teflon-coated autoclave and heated at 180 °C for 3-hours. After completing the autoclave process, the nanoparticles present in the solution were agglomerated by adding non-polar solvents, preferably acetone and butanone, for easy separation from unused precursors and solvent mixture. Finally, the agglomerated nanoparticles were separated by centrifugation and dried under vacuum at 60 °C for 4-hours. The prepared dry nanopowder was dispersed in water and utilized for the preparation of composite absorber coating sol. Figure 3.3.1 shows the synthesis

process for the ZrO_2 nanoparticles and digital image of stable ZrO_2 nanoparticle dispersion in the water.

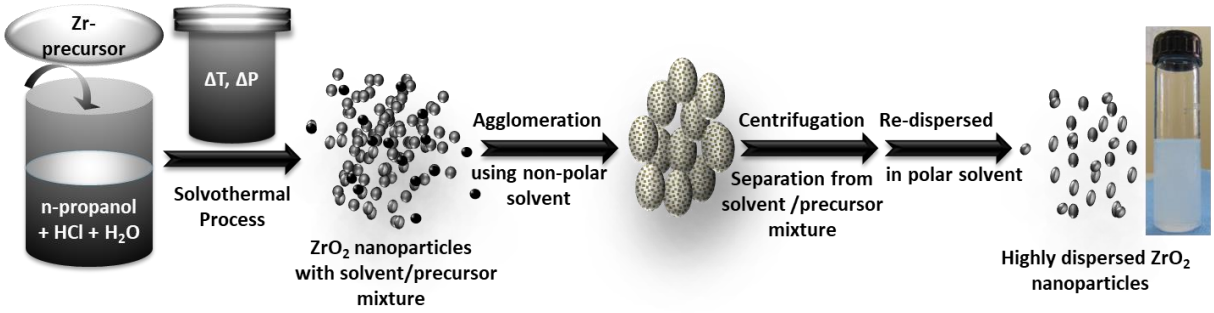

Figure 3.3.1. Schematic for the synthesis of highly dispersible ZrO_2 nanoparticles.

3.3.2. Structural and morphological study of ZrO_2 nanoparticles

The synthesised ZrO_2 nanoparticles were studied by FE-SEM, TEM, and XRD characterization techniques. The micrographs obtained from the methods are presented in Figure 3.3.2. Figure 3.3.2(a, b, and c) shows the micron-sized ZrO_2 particle clusters after the solvothermal synthesis. Figure 3.3.2(d, e) shows the individual ZrO_2 nanoparticles after being dispersed in the water. The morphological study (Figure 3.3.2(a, b, c, d, and e)) of the ZrO_2 nanoparticles by FE-SEM, TEM and HR-TEM revealed that most particles were spherical in shape. The average particle diameter is between 3 to 5 nm. The diffraction patterns from XRD analysis (Figure 3.3.2(f)) indicate that particles are crystalline and in the monoclinic phase, matching the ICDD no. 96-500-0039.

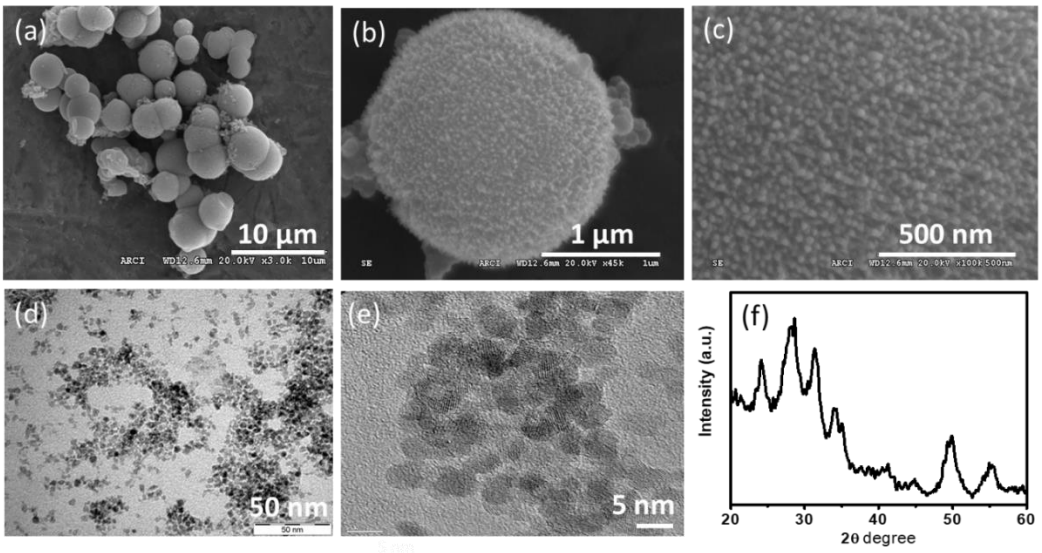

Figure 3.3.2. (a, b and c) FE-SEM, (d) TEM, (e) HR-TEM micrographs and (f) XRD patterns of ZrO_2 nanoparticles.

3.3.3. Synthesis of Co-Cu-Mn-O_x + ZrO_2 composite sol for preparation of Co-Cu-Mn-O_x + ZrO_2 nanocomposite coatings

Co-Cu-Mn-O_x+ZrO_2 composite absorber sol was synthesised by a combination of impregnation and sol-gel methods at room temperature. The hydrated salts such as manganese acetate, copper chloride, cobalt chloride were used to synthesise Co-Cu-Mn absorber sol. The schematic for the synthesis of Co-Cu-Mn-O_x+ZrO_2 composite absorber sol and generation of Co-Cu-Mn-O_x+ZrO_2 composite nanoparticle absorber and tandem layers is shown in Figure 3.3.3.

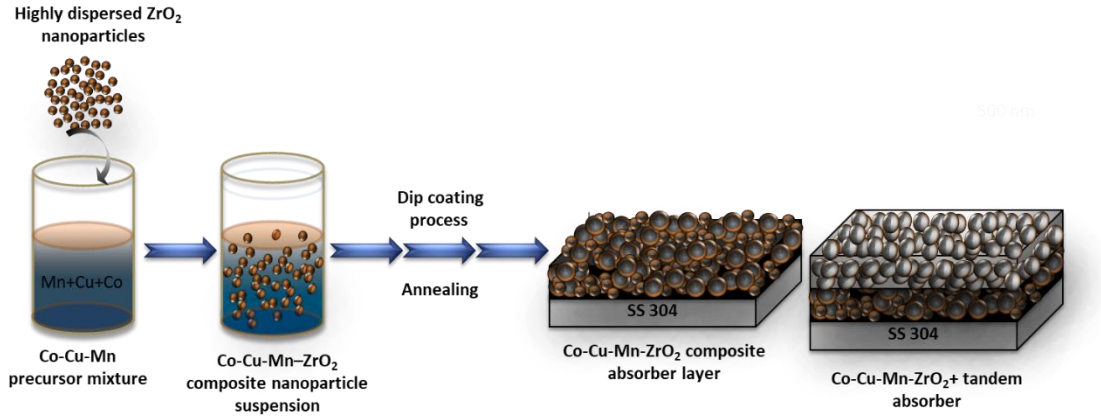

Figure 3.3.3. Schematic of Co-Cu-Mn-O_x+ZrO_2 composite absorber sol synthesis and generation of Co-Cu-Mn-O_x+ZrO_2 composite nanoparticle absorber and tandem layers.

All chemicals were purchased from E. Merck and used without further purification. A stable solution of Co-Cu-Mn-based absorber solution was obtained after dissolving these optimized amounts of precursors successively in alcohol, preferably ethanol. The weight ratio between Manganese, Copper, and Cobalt was optimized as 4.6:3.2:1.5, respectively, to obtain the best optical and thermal stability. After that, the nano zirconia suspension was added dropwise into Co-Cu-Mn composite sol. Finally, the mixture was stirred and aged for 24 h at room temperature.

3.3.4. Substrate preparation and deposition of absorber & tandem layers

The polished tube of austenitic stainless steel (304) was used as a substrate, and its typical size was 50 mm in length, 1 mm outer diameter, and 1.5 mm thickness. The samples were cleaned by ultrasonication for 15min, washed with water and a soap solution, rinsed with tap water, then de-ionized water, and finally wiped with soft cotton with solvent to make substrate free from oil and grease get uniform coating and better adherence. Subsequently, substrates were

dried in a hot air oven at 100°C for 10 min. Following the cleaning procedure, the film deposition was carried out on a substrate in a closed chamber under controlled atmospheric conditions (<25 °C and 40-50% RH) with the help of a dip coater and then dried at 100 °C for 15 minutes in a hot air oven.

After completion of the drying process, a stepwise procedure was followed in the annealing process. In the first step, we annealed samples at temperature 300 °C for 30 minutes with a ramp of 10 °C/min by a using forced hot air oven with controlled air circulation, subsequently annealed at 500 °C for 30 minutes by using a muffle furnace with a ramp of 10 °C/min and cooling was accomplished by normal convection. The following process conditions of withdrawal speed, annealing temperature, and duration were varied to obtain the best homogeneous film with high optical properties.

3.3.5. Optimization of ZrO_2 concentration Co-Cu-Mn-O_x sol and withdrawal speed for the Co-Cu-Mn-O_x+ZrO_2 composite absorber

Initially, the ZrO_2 nanoparticles dispersed sol with different concentrations such as 0 mg, 25 mg, 50mg, and 75 mg were added in the Co-Cu-Mn-O_x sol, and coatings were developed with a constant withdrawal speed (9 mm/sec) by the dip-coater. According to ISO 9845-1 procedure, the solar absorptance was calculated by weighted integration of the spectral reflectance with the hemispherical solar spectrum of AM 1.5. From Figure 3.3.4(A and B) & Table 3.3.1), it is evident that there is a drastic increment in solar absorptance (α =0.92) of composite nanoparticle absorber layer with optimum nano ZrO_2 (25 mg) compared to without ZrO_2 (α=0.85). The interband transition of electrons could be the reason for the high absorption in Co-Cu-Mn-O_x-ZrO_2.

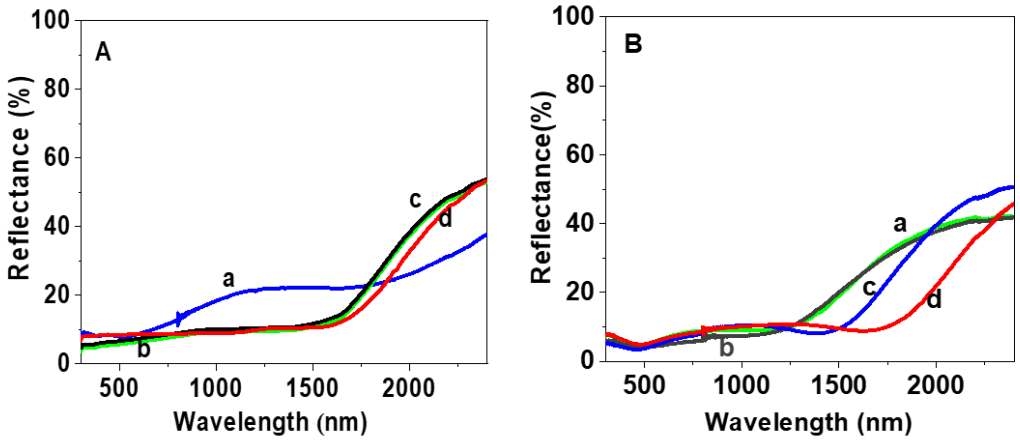

Figure 3.3.4. (A) UV-Vis-NIR reflectance spectra of single absorber layer (Co-Cu-Mn-O_x+ZrO_2) generated by varying ZrO_2 nanoparticle amount, (a) 0 mg, (b) 25 mg, (c) 50 mg, and (d) 75 mg, (B) Co-Cu-Mn-O_x+ZrO_2 absorber layer generated by varying thickness (varying withdrawal), (a) 5 mm/sec, (b) 7 mm/sec, (c) 9 mm/sec; and (d) 11 mm/sec.

Table 3.3.1. Solar absorptance of Co-Cu-Mn-O_x+ZrO_2 layer generated by varying of amount ZrO_2 nanoparticles and Co-Cu-Mn-O_x+ZrO_2 layer generated by varying thickness of absorber layer.

Co-Cu-Mn-O_x+ZrO_2 layer generated by varying of amount ZrO_2 nanoparticle			**Co-Cu-Mn-O_x+ZrO_2 layer generated by varying the withdrawal speed**		
ZrO_2 nanoparticles (mg)	**α_s***	**ε**	**Withdrawal speed (mm/sec)**	**α_s****	**ε**
0	0.85	0.20	5	0.90	0.17
25	0.92	0.18	7	0.91	0.17
50	0.91	0.19	9	0.92	0.19
75	0.89	0.18	11	0.91	0.20

*By using constant withdrawal speed (9 mm/sec), **by using a constant amount of ZrO_2 (25 mg), ε= measured by using emissometer

The reflectance spectra presented in Figure 3.3.4(A) illustrate a sharp transition from low to high reflectance that occurs in the range of 1500 nm to 2500 nm, induced by increasing ZrO_2 concentration. The reflectance of the composite nanoparticle film deposited by varying withdrawal speed (5 mm/sec to 11 mm/sec) is represented in Figure 3.3.4(B). It is clearly evident that the absorption of the film increases in visible and NIR wavelength, and the transition of peak shifts to a longer wavelength, possibly due to the increase in withdrawal speed (thickness) from 5 mm/sec to 9 mm/sec. However, the absorption percentage decreases

at 11mm/sec in the active solar range, 500-1500 nm. However, a thicker absorbing layer results in higher thermal emittance, and the overall spectral selectivity will be even lower.

3.3.6. Structural and morphological study of Co-Cu-Mn-Ox+ZrO_2 layer

To understand the reason behind the high optical properties of the Co-Cu-Mn-O_x+ZrO_2 layer, the coating layer is studied by TEM, HR-TEM, elemental mapping using EF-TEM, EDS, XPS, XRD & micro-XRD. The TEM (Figure 3.3.5a) and HR-TEM (Figure 3.3.5b, c, and d) images of Co-Cu-Mn-O_x+ZrO_2 layer composite nanoparticles of the absorber layer were observed after the removal of coating flake from the coated tube by scratching and subsequently ultra-sonication indicate that the two-stage annealing of a composite nanoparticle layer resulted in the nearly intact and irregular-shaped nanoparticles with agglomeration. It can be attributed to the contraction of nanoparticles due to two stages annealing and further condensation or crystallization of molecular precursors during annealing.

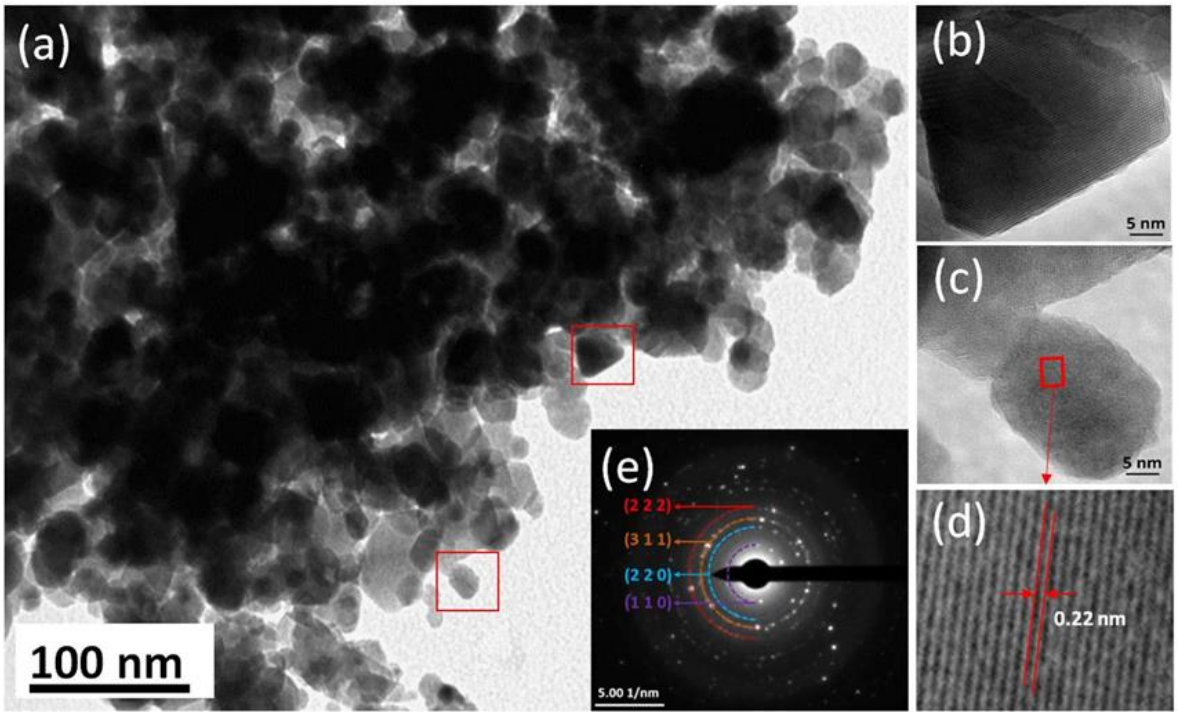

Figure 3.3.5. (a) TEM, (b, c & d) HR-TEM images and (e) Selected area electron diffraction (SAED) pattern of Co-Cu-Mn-Ox-ZrO_2 composite nanoparticles.

From the High-Resolution TEM analysis, the absorber layer comprises nanoparticles of sizes from 5 to 32 nm. The average diameter of composite nanoparticles in the obtained coating flake was estimated to be 21 nm. A typical SAED pattern of Co-Cu-Mn-O_x+ZrO_2 composite nanoparticles (Figure 3.3.5e) depicting ring patterns confirms that their crystalline nature. According to SAED analysis, those rings correspond to planes d110, d220, d311, d222 of,

indicating that cubic phase. The d-space value, d = 0.22 nm estimated from the HR-TEM image (Figure 3.3.5d), precisely matches the d-space value of the primary XRD peak (hkl311) $CuCoMnO_x$ spinel, respectively. This is also consistent with the results obtained from X-ray diffraction analysis which will be discussed in the further section (Figure 3.3.6). It is surprising to notice that no peak corresponding to ZrO_2 nanoparticles by TEM-EDS, EELS, and XRD measurements could be seen and may be attributed to less concentration in the absorber layer (<1%). However, from SEM-EDS, ZrO_2 presence was clearly noticed due to large area coverage for analysis (micron range). According to SEM-EDS, the elemental weight fraction of the coating flake was to be found 45.57, 34.19, 13.32, 6.44, and 0.48 (Wt %) for Mn, Cu, Co, O, and Zr, respectively.

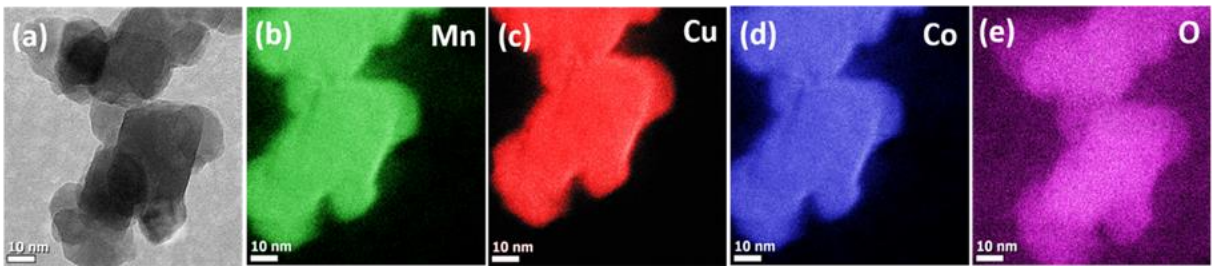

Figure 3.3.6. TEM elemental mapping analysis of Co-Cu-Mn-Ox-ZrO_2; (a) HR-TEM image of a cluster of Co-Cu-Mn-Ox-ZrO_2 spinel nanoparticles, distribution of (b) Manganese, (c) Copper, (d) Cobalt, and (e) Oxygen.

Elemental mapping images (Figure 3.3.6) illustrate that Mn, Cu, Co, O elements are uniformly distributed in each composite nanoparticle. An elemental map corresponding to Zr could not be carried out as the electron energy loss spectrum has not presented a corresponding core-loss peak may be because of less content of ZrO_2 nanoparticle in the whole sample. In combination these characterization results with the preparation procedure of the absorber layer, it can be concluded that the as-prepared layer was composed of spinel (Co-Cu-Mn-Ox-ZrO_2) and ZrO_2 nanoparticles. Moreover, ZrO_2 nanoparticles may distribute uniformly onto the internal/external surface of the Co-Cu-Mn-Ox-ZrO_2 spinel nanoparticles. This might be the reason that the absorber layer shows excellent thermal stability in an open atmospheric condition.

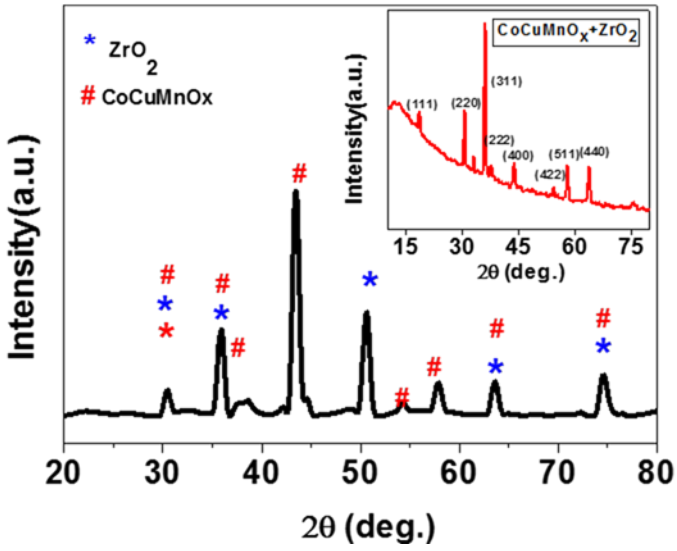

Figure 3.3.7. Micro XRD of Co-Cu-Mn-Ox-ZrO_2 composite nanoparticle layer on SS 304 (Inset – Normal incident angle XRD of Co-Cu-Mn-Ox-ZrO_2 composite nanoparticle layer).

Figure 3.3.7 illustrates the XRD and micro XRD diffraction patterns of the composite nanoparticle layer. From the normal incident angle XRD (inset), it is evident that all the diffraction peaks of the composite nanoparticle layer correspond to the crystal planes of the Co-Cu-Mn-O_x spinel structure material. All are in good agreement with the standard ICDD data (Diffraction file no. 00-047-0324). Similar to TEM-EDS, no peak corresponding to ZrO2 nanoparticles was observed in normal incident angle XRD due to a low amount used for the absorber layer deposition. However, we could trace the peaks of tetragonal phase Zirconia (t-ZrO_2) and Co-Cu-Mn-O_x from micro-XRD analysis, which are in good agreement with the standard ICDD diffraction file no. 00-047-0324 and 00-050-1089, respectively.

Surprisingly, we noticed the phase change of monoclinic phase Zirconia (m-ZrO_2) nanoparticles into a tetragonal after annealing of an absorber layer (@500 °C) which were initially in the monoclinic phase before incorporation into absorber sol. In general, the change in phase from m-ZrO_2 to t-ZrO_2 can be found after 1,170 °C only. A few percent of oxides like Y_2O_3, Ce_2O_3 blended with ZrO_2 may cause the phase change, which can be resulted in a stable phase ZrO_2 [38]. But without any phase change material (For example, Y_2O_3, Ce_2O_3) blending, nanocrystalline m-ZrO_2 changed to t-ZrO_2 at low temperature. A similar observation was already made by Shukla et al. where a tetragonal phase can be stabilized in the case of nanocrystalline ZrO_2 without doping any impurities, which differentiates the stabilization mechanism in micrometre sized ZrO_2 [39][40]. After annealing, the t-ZrO_2 in the absorber layer

with Co-Cu-Mn-O_x spinel resulted in a material that is responsible for superior thermal and optical properties.

3.3.7. Structural study of Co-Cu-Mn-Ox+ZrO_2 layer by XPS

Figure 3.3.8 shows spectra of the Mn 2p, Cu 2p, Co 2p, and Zr 3d, and O 1s photoelectron energy loss peak for the composite nanoparticle absorber (Mn-Cu-Co-O_x-ZrO_2 layer measured by X-ray photoelectron spectroscopy (XPS). All the photoelectron spectra were calibrated relative to the reference C 1s peak position (284.3 eV). The Mn 2p spectrum [Figure 3.3.8(a)] had the strong spin-orbit doublet Mn $2p^{3/2}$-Mn $2p^{1/2}$ with a splitting of 11.6 eV. Mn 2p photoelectron asymmetric peak at 641.5 eV is deconvoluted to two peaks, one at 641.3 eV and 643.5 eV associated with Mn^{3+} and Mn^{4+} respectively [42]. The position of manganese ions occupies preferably octahedral sites, which agree with the majority of the references [43]. The Cu 2p spectrum [Figure 3.3.8(b)] had the strong spin-orbit doublet Cu $2p^{3/2}$-Cu $2p^{1/2}$ with a splitting of 20 eV. Cu 2p photoelectron peak at 930.8 eV can be deconvoluted to two peaks, one at 931 eV associated with Cu^{1+} and at 933, 935 eV attributed to Cu^{2+}, respectively is in good agreement with Lenglet et al. [44]. The observed Cu^{+} and Cu^{2+} ion contributions might be ascribed to tetrahedral and octahedral sites. The Co 2p spectrum [Figure 3.3.8(c)] had the strong spin-orbit doublet Co $2p^{3/2}$-Co $2p^{1/2}$ with a splitting of 15.3 eV. The Co 2p photoelectron peak at 780.55 eV without deconvolution attributed to trivalent Cobalt. The observed Co $^{3+}$ contribution might be ascribed to octahedral sites only [45].

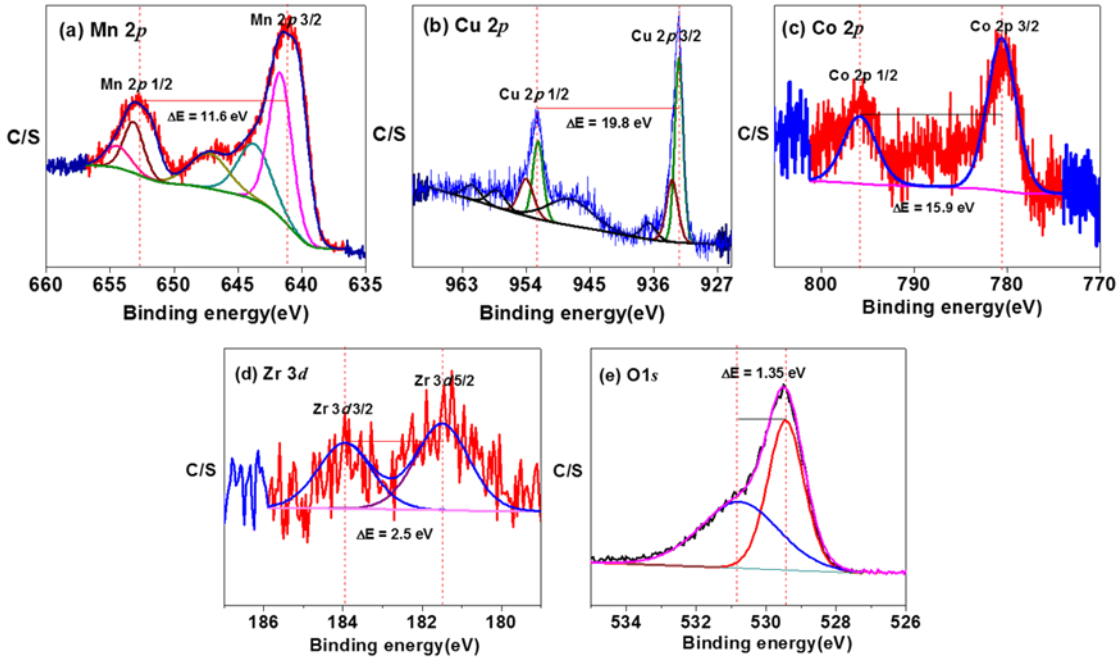

Figure 3.3.8. X-ray photoelectron spectra of Co-Cu-Mn-O_x-ZrO_2 composite nanoparticle layer on SS 304.

The Zr 3d doublet spectrum [Figure 3.3.8(d)] is deconvoluted into two distinct components. The binding energies were 181.4 and 183.9 eV, respectively, and the spectrum had a strong spin-orbit doublet Zr $3d^{5/2}$ and Zr $3d^{3/2}$ with a splitting of 2.5 eV. The binding energies & splitting for the Zr $3d^{5/2}$ and Zr $3d^{3/2}$ components are in good agreement with literature data for ZrO_2 [46]. The O 1s photoelectron peak [Figure 3.3.8(e)] presented a shoulder on the high binding energy side. Indeed, the spectrum was deconvoluted into two distinct components. The most intense, centred at 529.4 eV, was attributed to zirconium dioxide, in accordance with the literature [47]. The second one, located at 530.7 eV, was ascribed to the surface –OH groups or oxides of metals [47]. The detection of the second component in the O 1s signal can be traced back to two effects: (i) the sample was exposed to air before introduction to the XPS spectrometer; (ii) the sample is nanocrystalline, and its high surface-to-volume ratio favours surface hydration. Finally, we deduced the ion configuration of the Co-Cu-Mn-O_x spinel that we have prepared as $Cu^{+}_{0.65}Mn^{3+}_{0.35}[Cu^{2+}_{0.35}Co^{3+}Mn^{4+}_{0.65}]O_4$ which is in good agreement with the reported literature [48].

3.3.8. Synthesis of AR coating sols and preparation of AR coatings over on absorber layers

3.3.8.1 Synthesis of MgF_2 nanoparticle-based AR coating sol for the development of tandem absorber 1

To prepare the tandem absorber layer 1, high crystalline mesoporous MgF_2 nanoparticles were synthesised from micron size particles by Solvothermal synthesis. The synthesis procedure of MgF_2 nanoparticles was exactly followed, as mentioned in our group's previous work [94]. It comprises many steps; initially, 10 g of magnesium fluoride hydrate (MgF_2. XH_2O powder with an average particle size of around 35 µm, Alfa Aesar) was mixed with 60 mL of n-propanol, and 5 mL concentrated HCl (37%, Merck). A transparent solution was obtained by stirring the mixture at a constant rate at room temperature. Further, 2 mL de-ionized water was added to the mixture, followed by mechanical stirring for an hour. After that, the mixture was transferred into a Teflon-coated autoclave and heated at 200 °C for one hour to obtain high crystalline MgF_2 nanoparticles with uniform particle size, good weather, and thermal stability. The prepared dry powder could be easily dispersed uniformly in polar solvents for forming the coating solution.

3.3.8.2 Synthesis of SiO_2 nanoparticle-based AR coating sol for the development of tandem absorber 2

The synthesis of SiO_2 nanoparticle-based AR coating solution is described in chapter 2 and section 2.5. The synthesised AR coating solutions were deposited on the developed Co-Cu-Mn-based absorber coatings. Several coatings were developed by varying the withdrawal speeds to obtain high solar absorptance and low spectral emittance. The coatings were developed as mentioned in chapter 2 and section 2.5.

3.3.8.3 Synthesis of ZrO_2-SiO_2 AR coating sol for the development of tandem absorber 3

To prepare tandem absorber layer 3, ZrO_2-SiO_2 composite AR coating sol is synthesised by the sol-gel method. The synthesis procedure of ZrO_2-SiO_2 composite AR coating sol was exactly followed as mentioned in our group's previous work [140]. For ZrO_2–SiO_2 nanocomposite sol preparation, the specific amounts of zirconium n-propoxide and 3-glycidoxypropyltrimethoxysilane were dispersed in a solvent mixture of isopropyl alcohol and isopropoxy ethanol (70:30) for 24 h. The solution was allowed to stand at room temperature for an hour and finally used for the coatings. The final composition of the coating sol for this layer was in the ratio of Zr (n-Pro): IPA: IPE: GPTS = 6.94:78.52:12.94:1.60 (wt%). No binder/additive was used for the coating. The synthesised ZrO_2-SiO_2 AR coating solution was deposited on the developed Co-Cu-Mn-based absorber coatings. Several coatings were

developed by varying the withdrawal speeds o obtain the high solar absorptance and low spectral emittance. The coatings were developed as mentioned in section 4.

3.3.8.4 Optimization of withdrawal speed for the different AR layers

For further enhancement of solar absorptance, an AR layers were deposited on Co-Cu-Mn-O_x+ZrO_2 absorbers. As mentioned in the above section, several AR sols based on MgF_2, SiO_2 nanoparticles, and ZrO_2-SiO_2 composite were synthesised and deposited with different withdrawal speed to obtain high absorption and low emittance. Figure 3.3.9 represents the reflectance spectra of tandem absorbers developed with different AR layers on the absorber, and optical properties are presented in Table 3.3.2. Initially, a tandem absorber system was designed with an AR coating comprising MgF_2 nanoparticles with mesoporosity and a low refractive index (1.16) to create a perfect gradient in the tandem system. The AR layer with an optimum withdrawal speed of 4 mm/sec (349 nm thickness) exhibits a high solar absorptance of 0.97 from 300 nm to 1500 nm with maximum absorption of 99% at 616 nm, where peak reflectance was largely suppressed due to destructive interference. However, MgF_2 layers deposited by other than the optimum withdrawal speed exhibit lower absorption due to the destructive interference effect of AR coating misplaced.

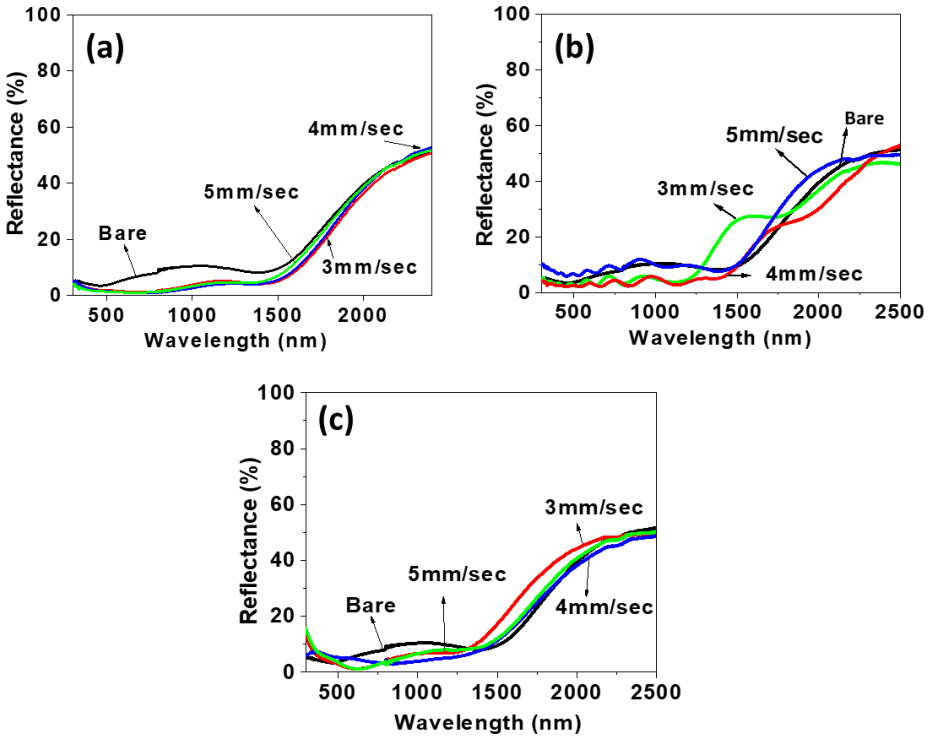

Figure 3.3.9. UV-Vis-NIR reflectance spectra of different AR layers on Co-Cu-Mn-O_x-ZrO_2 composite layer (a) MgF_2, (b) SiO_2, and (c) ZrO_2-SiO_2 layer.

Table 3.3.2. Optical properties of tandem absorber developed with different AR layers at different withdrawal speeds.

Co-Cu-Mn-Ox+ZrO_2/MgF_2 Tandem absorber			**Co-Cu-Mn-Ox+ZrO_2/SiO_2 Tandem absorber**		**Co-Cu-Mn-Ox+ZrO_2/ZrO_2-SiO_2 Tandem absorber**	
Withdrawal speed (mm/sec)	**α**	**ε**	**α**	**ε**	**α**	**ε**
Bare absorber	0.92	0.16	0.92	0.16	0.92	0.16
3	0.96	0.19	0.93	0.21	0.94	0.21
4	0.97	0.19	0.96	0.22	0.95	0.24
5	0.97	0.20	0.91	0.23	0.93	0.26

From Figure 3.3.9(b), it is evident that at the 4 mm/sec withdrawal speed of the SiO_2 layer, we obtained 0.96 of solar absorptance and 0.22 of emittance. In the case of the Co-Cu-Mn-O_x+ZrO_2/ZrO_2-SiO_2 tandem absorber, we obtained 0.95 of solar absorptance and 0.24 of emittance. Co-Cu-Mn-O_x+ZrO_2/MgF_2 exhibited the best solar absorptance of 0.97 and a low emittance of 0.19 compared to other tandem absorbers. The low refractive index of the MgF_2 nanoparticles layer having mesoporous nature could be the reason for obtaining the high absorption. However, the increment in the emittance is due to the increment in the withdrawal speed, which gives high thickness. Hence, the Co-Cu-Mn-O_x+ZrO_2/MgF_2 tandem absorber can be considered for further studies.

3.3.8.5 Morphology of absorber and tandem coatings by FE-SEM and FIB microscope

Figure 3.3.10 shows the morphology of Co-Cu-Mn-O_x+ ZrO_2 absorber, MgF_2 nanoparticle AR layer, ZrO_2-SiO_2 layer, and SiO_2 AR layers over on absorber. Figure 3.3.10(a) reveals that the base absorber layer consists of spherical particles with an average size of 20-25 nm and has a porous surface structure with nanovoids. It could be the reason for solvent evaporation and decomposition of precursor material during the annealing process. However, the base absorber layer's high porosity (nanovoids) was minimized after the deposition of an AR layer. Apart from tandem design, another advantage of the MgF_2 nanoparticle layer used here is the

potential to create uniform coatings comprising fine crystalline mesoporous nanoparticles, which show excellent uniformity with a minimum number of defects or pinholes.

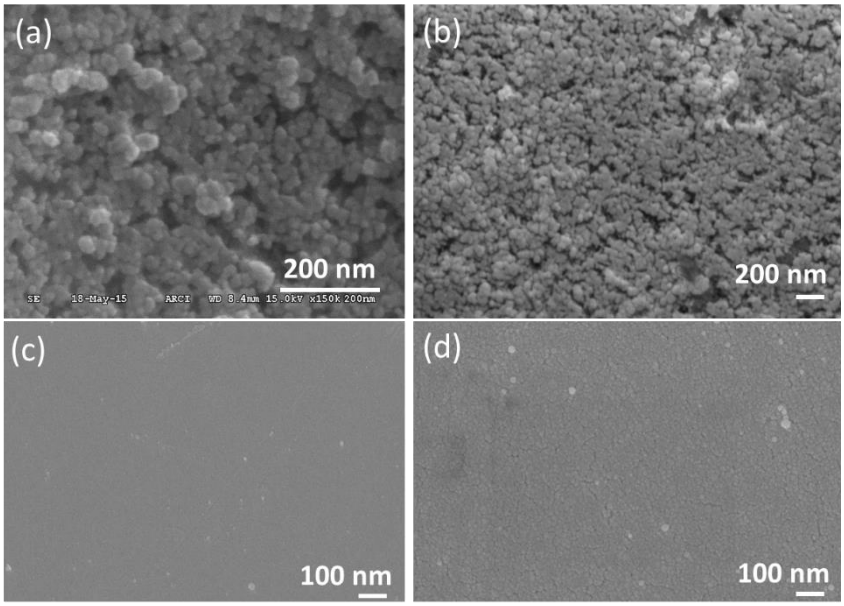

Figure 3.3.10. FE-SEM surface morphology of (a)Co-Cu-Mn-O_x-ZrO_2 absorber, (b)MgF_2 nanoparticle AR layer, (c)ZrO_2-SiO_2 layer, and (d)SiO_2 AR layers over on absorber.

From the FE-SEM images, it is revealed that the ZrO_2-SiO_2 layer was uniform without cracks and pinholes. However, we couldn't observe any particles. In the case of the nano SiO_2 tandem layer, we could observe the SiO_2 NPs with an average diameter of 20nm. The complete layer was uniform without any cracks and pinholes.

3.3.8.5.1. Thickness study of absorber and tandem coatings by FIB microscope and Ellipsometry

To understand the influence of the AR layer (MgF_2 layer) on a single absorber layer, we measured the effective refractive indices of the MgF_2 layer (top layer) and Co-Cu-Mn-O_x-ZrO_2 composite nanoparticle layer (bottom layer) by a spectrophotometric ellipsometer. The refractive index of the MgF_2 layer comprising mesoporous nanoparticles was found to be a lower value of 1.15, which is lower than the refractive index of the bulk material of 1.38. It is due to the presence of nanoporous and voids in the layer. However, the refractive index of the absorber layer comprising Co-Cu-Mn-O_x-ZrO_2 composite nanoparticles was observed to be 1.96, which is higher than the MgF_2 layer.

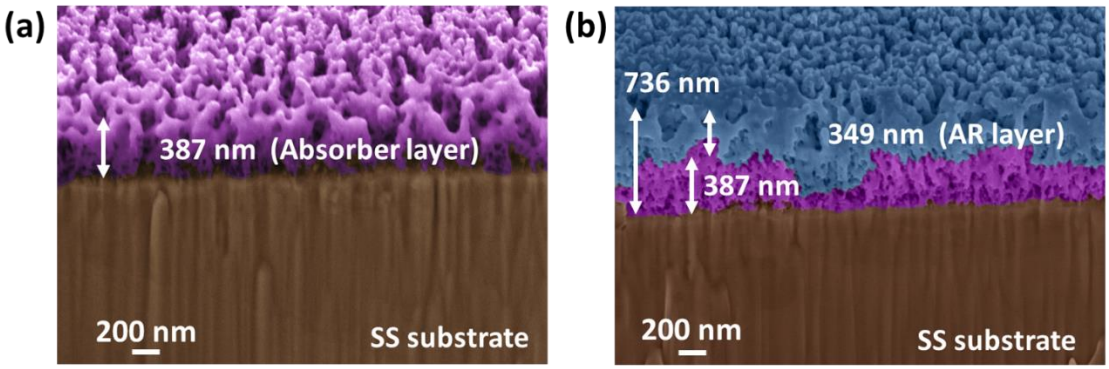

Figure 3.3.11. Cross-sectional micrograph of (a) single and (b) tandem absorber layer by FIB microscope.

The difference in the refractive index of the absorber and AR layer makes the perfect gradient system which finally caused high solar absorptance of the tandem system. The thickness of the MgF_2 layer (top layer) and Mn-Cu-Co-O_x-ZrO_2 composite nanoparticle layer (bottom layer) was measured by FIB microscope. The thickness of the deposited AR films comprising mesoporous MgF_2 nanoparticles (top layer) was 349 nm, whereas the absorber layer (bottom layer) containing Mn-Cu-Co-O_x-ZrO_2 composite nanoparticles was 387 nm.

3.3.9. Thermal loss study of absorber and tandem coatings by FT-IR spectrometer

To understand the thermal emissivity of single and tandem absorber systems, we recorded the thermal emittance of single and tandem absorbers individually and blackbody emittance and measured at different operating temperatures from 100 °C to 500 °C with an interval of 100 °C and are represented in Figure 3.3.12 and Table 3.3.3.

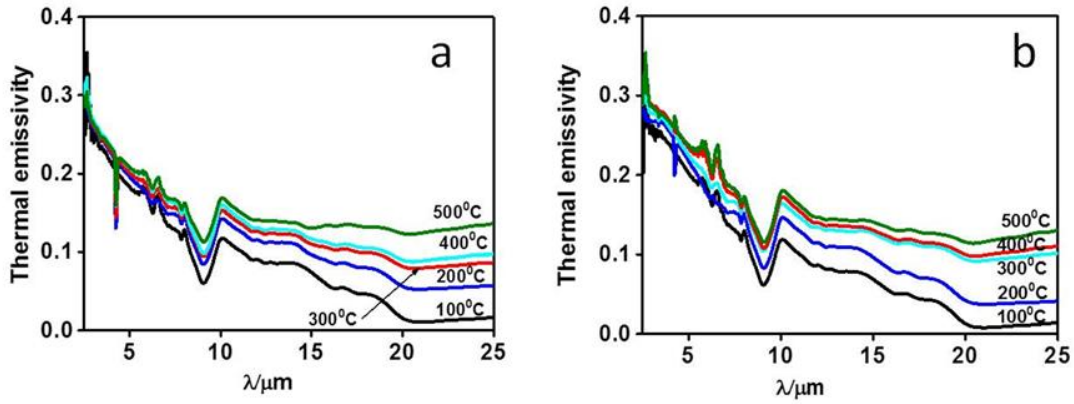

Figure 3.3.12. Thermal emissivity spectra of (a) single and (b) tandem absorber layer measured at different temperatures.

It is evident from emissivity spectra (Figure 3.3.12) that the thermal loss of the composite nanoparticles absorber (single (Figure 3.3.12a) and tandem absorber (Figure 3.3.12b)) increases drastically from 10 µm to 25 µm. The average thermal loss value of tandem nanoparticle layer was slightly higher (0.09-0.17 from 100 °C to 500 °C) compared to single composite nanoparticle absorber (0.08-0.15 from 100 °C to 500 °C). The reason could be the IR radiation transmittance characteristic of an MgF_2 layer or the high thickness of the tandem absorber layer. A similar observation is noted by Joly et al. for their graded structure of the absorber layer [28].

Table 3.3.3. Thermal emissivity data of single and tandem absorbers measured at different temperatures.

Temperature (°C)	**Thermal loss (ε) of single composite nanoparticle absorber**	**Thermal loss (ε) of tandem absorber**
100	0.08	0.09
200	0.11	0.13
300	0.12	0.14
400	0.13	0.16
500	0.15	0.17

The developed Co-Cu-Mn-O_x+ZrO_2/MgF_2 exhibit good solar absorptance of 0.97 & high-temperature stability (≤500 °C). However, the thermal emissivity is found to be very high (0.17)[108,109]. The light penetration depth (defined as the inverse of the absorption coefficient (α)) is closely related to the emissivity of coatings. The light penetration depth will be high for thicker coatings in comparison to low thickness coatings. Thus, the tandem absorber exhibits more emissivity in comparison with the spinel absorber.

3.3.10. Conclusion

The SS/Co-Cu-Mn-O_x+ZrO_2/MgF_2 SSACs were developed with a solar absorptance of 0.97 and a spectral emittance of 0.19. Initially, highly dispersible ZrO_2 nanoparticles were developed by the solvothermal method and dispersed in a Co-Cu-Mn-O_x absorber coating sol to synthesise the nanocomposite absorber sol. Further, process parameters such as ZrO_2 concentration and withdrawal speeds were optimized, and nanocomposite absorber coatings were developed by the dip-coating method. Furthermore, different AR coatings sols such as

SiO_2, ZrO_2-SiO_2, and MgF_2 were synthesised and applied an AR layer over nanocomposite absorber coatings to develop a tandem absorber. Developed coatings were studied by different characterization methods to understand the physicochemical properties. The among the three tandem absorbers, Co-Cu-Mn-O_x+ZrO_2/MgF_2, exhibited a high solar absorptance of 0.97 and spectral emittance of 0.19. The same coatings were tested for the thermal loss study and found that the developed tandem absorber has 17% thermal loss at 500 °C. It could be due to the thickness of the tandem absorber ~736 nm, which is confirmed from the cross-sectional study of samples by FIB microscope. In this regard, another system of SSAC developed with the transition metal precursors of Nickel, Manganese, and Copper is probed for better optical properties, which is explained in chapter 4.

Chapter 4: Development of Cu-Mn-Ni-O_x based solar selective absorber coatings (SSACs)

In previous chapter 3, the SSACs were developed using tri-transition metal precursors of Manganese, Cobalt, and Copper and optical properties such as solar absorptance of 0.93 and spectral emittance of 0.19 were obtained. Although developed SSACs have good solar absorptance, the spectral emittance is found to be high. In chapter 4, an attempt is made to develop transition metal based SSACs by using precursors based on Nickel, Manganese, and Copper. The Cobalt precursor is replaced with the Nickel and experimented to create a novel compound to obtain the targeted optical properties. The cost of Cobalt is relatively high compared to other precursors used, which is one of the main reasons for replacing cobalt as a precursor. In addition, it has disadvantages such as skin irritation upon the contact and causes respiratory tract irritation.

Chapter 4 describes the development of absorber coatings using transition metals such as Nickel, Manganese, and Copper. The optimization of metal concentration in the absorber coating solution, withdrawal speed of the coatings, and annealing temperature was explained. Further, the development of SiO_2 nanoparticle-based anti-reflective (AR) coating solution and coatings, optimization of process parameters similar to the development of absorber coatings were explained. Finally, the physiochemical properties of developed materials and coatings were detailly studied and explained to understand the nature of developed coatings.

4.1 Synthesis of the absorber coating solution

The synthesis procedure for absorber coating solution is described in chapter 2, section 2.2.2, with a schematic diagram. However, for better understanding, explained again here. Commercially available precursors and chemical reactants were used without any further purification. Sequential steps were followed to synthesise the absorber coating sol. Manganese (II) acetate tetrahydrate, Copper (II) nitrate trihydrate, and Nickel (II) nitrate hexahydrate (>99%, Merck) were used as precursors for the synthesis of absorber solution. The precursors are dissolved in ethanol (>99%) under constant stirring. Further, hydroxypropyl cellulose (HPC) (Alfa Aesar) was dissolved in a mixture of 2-isopropoxyethanol (IPE) and deionized water and added into a sol. After that, the sol was subjected to 1-hour constant stirring for better dissolution. The concentration of metal precursors, and hydroxypropyl cellulose (HPC) were varied to optimize the composition of the absorber sol to obtain an absorber film with the best

optical properties. The optimized composition of the absorber sol Copper (II) nitrate hexahydrate: Nickel (II) nitrate trihydrate: Manganese (II) acetate tetrahydrate: Ethanol: HPC: Deionized water (DI): Isopropoxyethanol (IPE) is 1.90:2.47:4.47:60.14:0.67:2.67:27.68 (wt %). The viscosity of the optimized solution was found to be 8 centipoise and processed for the coating.

4.2 Thermo Gravimetric (TG) and Differential thermal analysis (DTA) of coating material

The synthesised absorber coating sol, as mentioned in the experimental section 4.1, was subjected to 70 °C to vaporize the solvent. Further, the coating material is studied by using the TG-DTA technique. The thermogravimetric graph in Figure 4.1 reveals the weight loss of coating material from room temperature to 800 °C in open-air atmospheric conditions, and it exhibits multiple-stage decomposition. The loss of weight is divided into three thermal events. The first event presents the loss of 12%, and it may be ascribed to evaporation of the solvent, water, and decomposition of the precursors. The mentioned process needs the absorption of heat, and it resulted in an endothermic peak in the DTA curve with maxima at 110 °C.

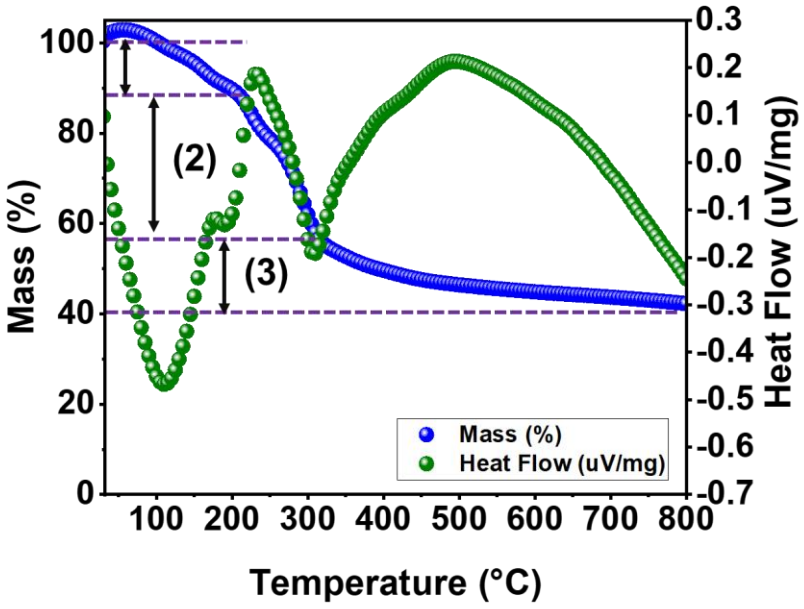

Figure 4.1. TG and DTA curves of the coating material over a range from ambient to 800 °C temperature.

The second thermal event results in a loss of 32%, possibly due to the continuous decomposition of the precursors and formation of spinels. The sharp exothermic and endothermic peaks with maxima at 235 °C and 305 °C can be linked to the heat released in the

melting of precursors and formation of the compound, respectively. The endothermic peak at 305 °C may represent the formation of the spinel phase, and it is further studied by XRD for confirmation [66,97,98]. The final thermal event exhibits a loss of 17% weight, which could be because of the crystallization of the compound formed.

4.3 Analysis of coating material by XRD

The synthesised absorber coating sol, as mentioned in the experimental section 4.1, was subjected to 70 °C to vaporize the solvent. Further, the coating material was subjected to temperatures from 100 °C to 800 °C and analyzed by XRD to determine the formation of the spinel phase and its stability. Figure 4.2 represents the XRD pattern of coating material at different temperatures, and it indicates the formation of spinel phase at 300 °C with the peaks at 2θ=18.5°, 30.5°, 35.9°, 38.5°, 43.7°, 54.2°, 57.8°, and 63.8°.

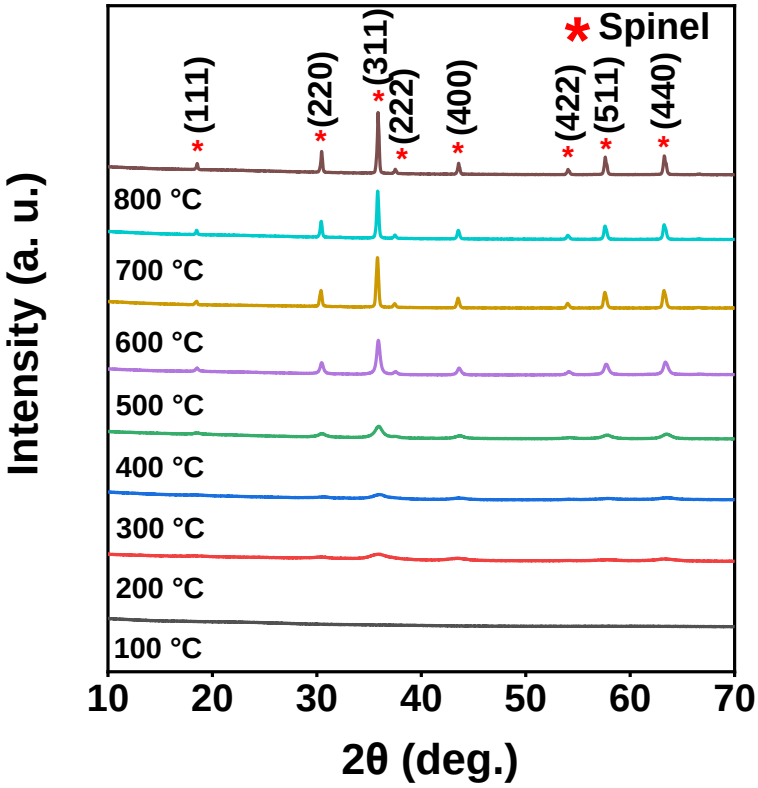

Figure 4.2. XRD pattern of the Cu $(Mn_{0.748}Ni_{0.252})_2O_4$ spinel.

The diffraction peaks of synthesised coating material correspond to the crystal planes of Cu $(Mn_{0.748}Ni_{0.252})_2O_4$ with a cubic phase, and it is in good agreement with the Standard International Centre for Diffraction Data (ICDD) data (01-070-8649). Further, the non-existence of other phases on prolonged heat treatment from 300 °C to 800 °C confirms the formation of only pure spinel phase and stability at higher temperatures. Figure 4.2 also reveals

the crystallization of the spinel phase over the temperatures from 300 °C to 800 °C with increment in the intensity of peaks at accurately assigned 2θ positions.

4.4 Absorber coating preparation

The absorber coating is prepared by the dip-coating method, as mentioned in chapter 2, sections 2.3 and 2.4. The optimized absorber coating solution described in section 4.1 is utilized for the development of absorber coatings. The parameters such as withdrawal speed and heating temperature play an important role in obtaining the crystalline compound with an optimum thickness to get high optical properties. Thus, these parameters need to optimize.

4.4.1 Optimization of temperature for the development of absorber layer

The formation of the spinel compound is confirmed at approximately 300 °C from XRD and TG-DTA. Thus, the sample's annealing temperature ranges from 300 °C to 600 °C to determine the optimum temperature for the prepared coating. The coatings were prepared with a constant withdrawal speed of 1 mm/sec, a constant rate of heating of 10 °C per minute, and a 1-hour dwelling time (constant). The developed samples are characterized by using UV-Vis-NIR and FT-IR) spectrophotometer to determine the optical properties such as solar absorptance and spectral emittance. These values determine the optimum temperature for the annealing of coatings. Figure 4.3 shows the reflectance spectra of the samples annealed at different temperatures, and Table 4.1 gives the optical properties of the developed coatings from 300 °C to 600 °C.

Table 4.1. Solar absorptance and emittance data of absorber layers developed at different annealing temperatures with a constant withdrawal speed.

Annealing temperature (°C)	**Withdrawal speed (mm/sec)**	**Absorptance (AM 1.5) α**	**Emittance ε**
300	1	0.69	0.12
400	1	0.85	0.13
500	**1**	**0.87**	**0.14**
600	1	0.84	0.15

Table 4.1 and Figure 4.3 show that with increasing the annealing temperature, there is an increment in the solar absorptance and spectral emittance. The best solar absorptance of 87.3%

and emittance of 0.14 can be observed at the 500 °C temperature. Thus, the annealing temperature 500 °C can be considered an optimum to develop the absorber coatings to further optimize the withdrawal speed for absorber and tandem absorber coatings. The change in the optical properties with an increase in the annealing temperature can be attributed to the crystallinity of the spinel phase formed on the substrate, confirmed with XRD in Figure 4.2.

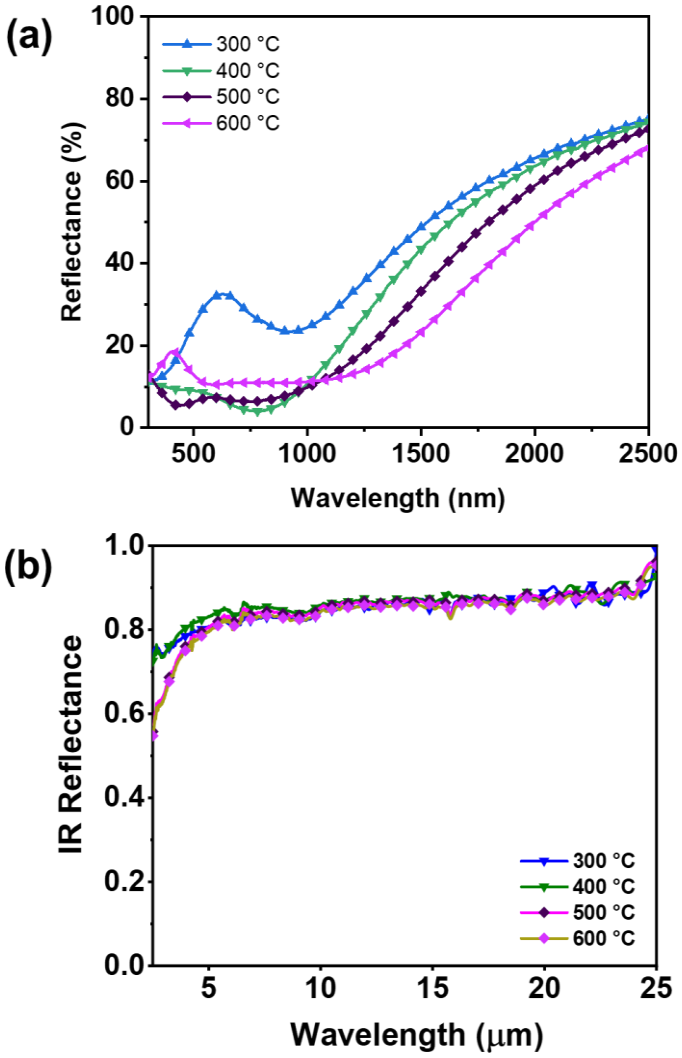

Figure 4.3. (a) UV-Vis-NIR and (b) infrared radiation (IR) reflectance spectra of absorber coatings annealed at temperatures at 300 °C to 600 °C.

To investigate the reason, the samples developed at different temperatures are further studied by GI-XRD. Figure 4.4 indicates the GI-XRD pattern of samples annealed at different temperatures. From Figure 4.4, it is observed that the presence of spinel phase peaks with high crystallinity after 500 °C, whereas at 300 °C, there is no presence of spinel phase peaks except substrate. At 500 °C and 600 °C, the clear spinel phase peaks can be observed, responsible for

good solar absorptance. The annealing temperature plays a vital role in the thickness of coatings, and SSACs exhibit high optical properties at an optimum thickness. It is observed that the annealing temperature influence the optical properties of developed coatings [99]. The decrease of thickness with annealing temperature can be attributed to shrinkage and densification of the thin films as the result of the particles aggregation and grains coalescence. In addition, excess formation of Fe_2O_3 due to oxidation of substrate with air at 600 °C also leads to change in the optical properties which is clearly shown with the support of GI-XRD (Figure 4.4). Thus, the decrement of solar absorptance at 600 °C from 87.3% to 84.9% is attributed to the change in the thickness of the developed coating

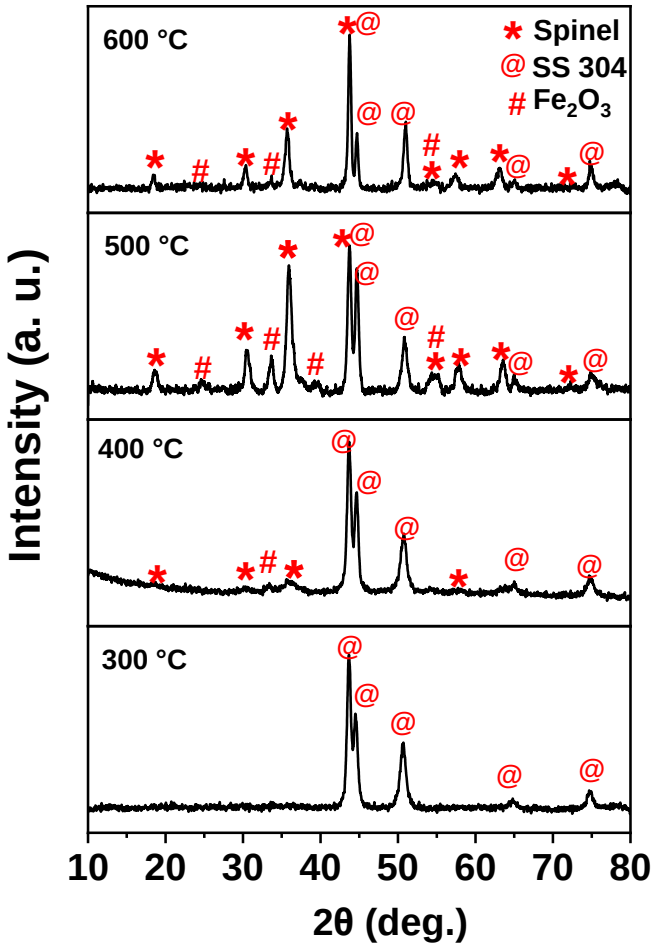

Figure 4.4. GI-XRD pattern of samples developed at 300 °C, 400 °C, 500 °C, and 600 °C temperatures.

In addition to substrate and spinel phases, iron oxide is formed from 400 °C to 600 °C as shown in Figure 4.5, and it is due to oxidation of SS 304. The presence of Fe_2O_3 can be attributed to

the increment in the spectral emittance from 0.12 to 0.15. A similar observation is reported by the author Sean Wu et al.[100]. The developed absorber is termed as spinel absorber in the current chapter for feasibility.

4.4.2 Optimization of withdrawal speed of spinel absorber layer

The bare substrate exhibits a solar absorptance (α) of 32% and spectral emittance (ε) of 0.12. To understand the role of the substrate in the optical properties of SSAC, the substrate was subjected to a temperature of 500 °C for 1-hour, and the optical properties were measured. The annealed SS 304 exhibited a solar absorptance (α) of 53% and spectral emittance (ε) of 0.12. The reflectance and emittance spectra for the bare and annealed substrate are shown in Figure 4.5 (a & b). The optical values of developed absorber coatings are shown in Table 4.2. The increment in the solar absorptance for the annealed substrate is due to the formation of Fe_2O_3 [101].

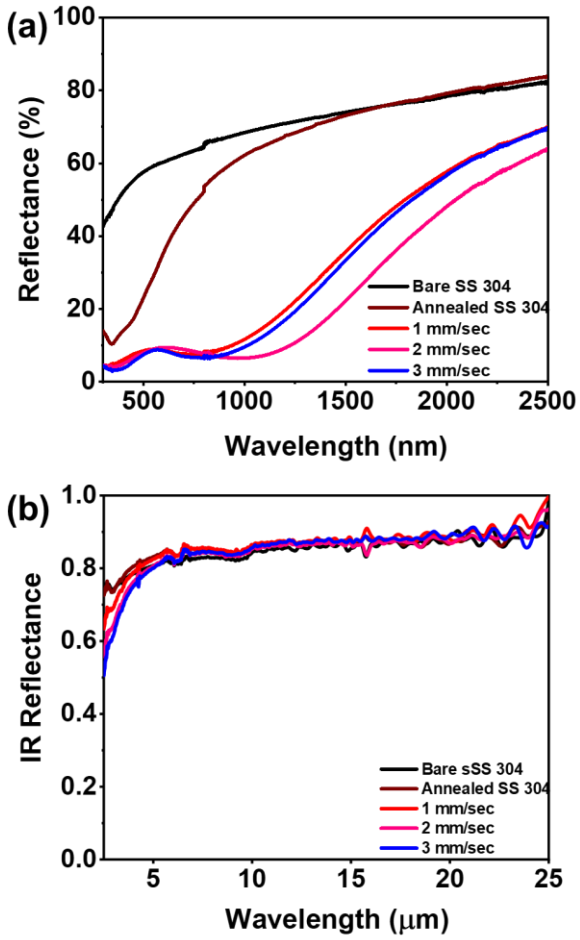

Figure 4.5. (a) UV-Vis-NIR and (b) IR reflectance spectra of SS 304, annealed SS 304 at 500 °C, and spinel absorber coatings developed with different withdrawal speeds at 500 °C.

The spinel absorber coatings were prepared with different withdrawal speeds on bare substrate to obtain high selectivity. The absorber layer exhibited the good solar absorptance (α)=0.88 and low spectral emittance (ε)=0.14 at an optimum withdrawal speed of 2 mm/sec. The absorption band edge at 612 nm with a reflectance of ~12% at 2 mm/sec withdrawal speed is shown in Figure 4.5(a). It may correspond to the energy transition from the oxygen anion to the M metal cation (where M is the metal: Cu, Mn, and Ni) or between two metal cations induced by incident light on the absorber layer [102].

Table 4.2. Solar absorptance and emittance values of the substrate, annealed substrate, absorber layers developed at different withdrawal speeds at 500 °C.

Withdrawal speed (mm/sec)	**Absorptance (AM 1.5) α**	**Emittance ε**
Bare SS 304	0.32	0.12
Annealed SS 304	0.53	0.12
1	0.87	0.14
2	0.88	0.14
3	0.86	0.15

4.4.3 Optimization of withdrawal speed of AR layer over on absorber coating

An AR layer of the correct thickness and refractive index suppresses the reflections from the absorber and aid in improving the solar absorptance [13,80]. So, the thickness of the SiO_2 nanoparticle layer (tandem layer) on top of the spinel absorber is varied by changing the withdrawal speed of the coatings. The optical values of developed tandem absorber coatings are shown in Table 4.3. In the current chapter, the SSACs developed with absorber and AR layer used for the stack are termed tandem absorbers for feasibility.

Table 4.3. Solar absorptance and emittance values AR coatings over on absorber developed at different withdrawal speeds at 500 °C.

Withdrawal speed (mm/sec)	**Absorptance (AM 1.5) α**	**Emittance ε**
Absorber	0.88	0.14
0.5	0.92	0.14
1	0.95	0.15
2	0.86	0.16

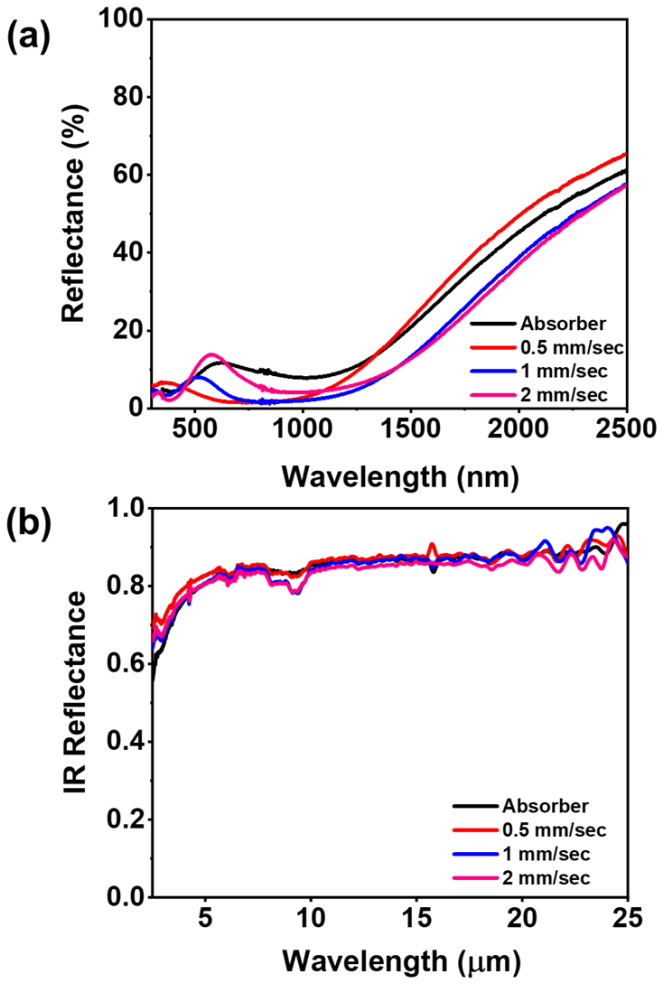

Figure 4.6. (a) UV-Vis-NIR and (b) IR reflectance spectra of AR layer developed with different withdrawal speeds over a spinel absorber.

The reflectance spectra for tandem absorbers with the variation of withdrawal speed are shown in Figure 4.6 (a & b). The tandem absorber exhibited the solar absorptance (α)=0.95 and spectral emittance (ε)=0.14 at an optimum withdrawal speed of 1 mm/sec. In Figure 4.6(a), the tandem absorber applied over on spinel absorber with optimum withdrawal speed (1 mm/sec) creates a destructive interference. It causes the shift in absorption band edge to a lower wavelength of 514 nm, having a reflectance of ~8%. The shift in the peak leads to decrement in the reflectance drastically ~ 4.6% in the region of 0.3-1.5μm, whereas spinel absorber exhibits the high reflectance ~ 10% for the wavelength range of 0.3-1.5μm. Spinel absorber in the IR region exhibits low spectral emittance (ε) of 0.14, and the tandem layer exhibits 0.15 of thermal emittance(ε). The observed minor change in the emittance from spinel to tandem absorber is attributed to a decrease in the roughness of the tandem layer (Ra ≤ 75nm) in comparison with the absorber layer (Ra ≤ 82nm), and it is further discussed in the section 4.11[141].

4.5 Structural study of coating by GI-XRD

The bare SS 304, annealed SS 304 at 500 °C, spinel, and tandem absorbers (spinel + AR) were analyzed by GI-XRD at grazing angles from 0.2 ° to 1 ° to determine the phase structure of coating with minimal contribution of the substrate. Figure 4.7 represents the GI-XRD pattern of bare SS 304, annealed SS 304, spinel, and tandem absorbers. In Figure 4.7(a), we could observe that the SS 304 has diffraction peaks at 2θ=43.7°, 51.1° and 75.0 °, that were assigned to Face Centered Cubic Iron (γ-FCC) phase of a substrate and it is coinciding with the ICDD data (01-081-8766). The diffraction peaks at 2θ=44.2° and 64.8° were assigned to the Body-Centered Cubic Iron (α-BCC) phase of the substrate and matched with the ICDD data (01-081-8766). The annealed SS 304 has Iron Oxide (Hematite) other than the γ-FCC, α-BCC, which is evident in Figure 4.7(b). The diffraction peak at 2θ=24.6° corresponds to the Iron Oxide (Hematite), coinciding with the Standard ICDD data (01-073-3825). This could be due to the oxidation of SS 304 in the air at 500 °C. According to the Fe-O phase diagram, the formation of Fe_3O_4 thermodynamically is favourable. However, during the oxidation process, many complex parameters are involved in forming phase fraction of final compounds, such as concentration oxygen availability, local chemistry (presence of Cr, tendency to form Fe_2O_3 is dominant), surface characteristics, etc. Feng Cao et al. claimed that there is a formation of Fe_2O_3 layer after annealing the stainless-steel substrate at 500 °C in air and reported that diffusion of iron and carbon atoms into the top layers at high temperature might alter the optical properties over time [101]. As a solution, he introduced a diffusion barrier between the substrate and the absorber layer. Similarly, Jiushan Cheng et al. also confirmed that the

substrates were covered with Fe_2O_3 by annealing the SS substrate at 500 °C for 30 minutes in air [103]. Similarly, the occurrence of Fe_2O_3 over on the SS 304 substrates leads to a change in the optical properties. At an optimum glazing incident angle (0.5°), we could observe the diffraction peaks related to the spinel phase, the substrate, and Hematite, as shown in Figure 4.5(c).

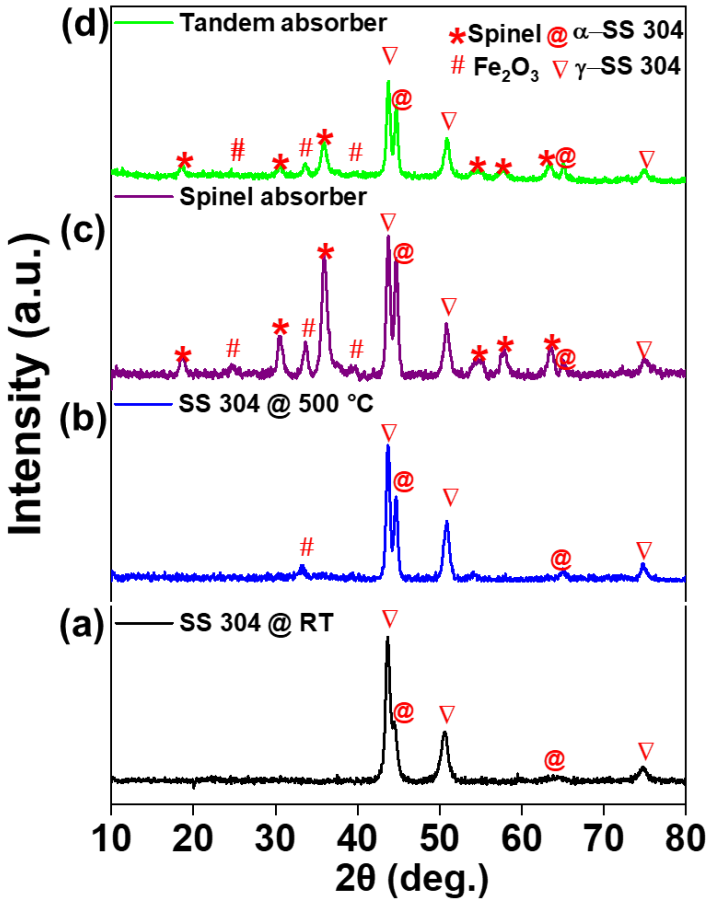

Figure 4.7. GI-XRD pattern of (a) SS 304, (b) annealed SS 304 at 500 °C, (c) spinel absorber (SS/Cu $(Mn_{0.748}Ni_{0.252})_2O_4$) and (d) tandem absorber (SS/Cu$(Mn_{0.748}Ni_{0.252})_2O_4/SiO_2$) on SS 304.

The diffraction peaks at 2θ=18.5°, 30.5°, 35.9°, 38.5°, 43.7°, 54.2°, 57.8°, and 63.8° is accurately assigned to the Cu $(Mn_{0.748}Ni_{0.252})_2O_4$ spinel phase with the cubic structure that matches with the ICDD data (01-070-8649). The results obtained by powder XRD are well consistent with GI-XRD data for the spinel phase. The diffraction peak at 2θ=24.6° and 33.6° corresponds to the Iron Oxide (Hematite), precisely coinciding with the Standard ICDD data

(01-073-3825). Like the spinel absorber, the tandem absorber also exhibits the diffraction peaks of the substrate, Hematite, and spinel phase, as shown in Figure 4.7(d). However, the tandem absorber does not reflect the SiO_2 diffraction peaks despite covering the absorber layer completely since the SiO_2 nanoparticles are amorphous.

4.6 Structural study of tandem absorber coating by XPS

Figure 4.8 shows the Mn 2p, Cu 2p, Ni 2p, Si 2p and O 1s photoelectron energy loss spectra of the optimized absorber layer measured by X-ray photoelectron spectroscope. All the photoelectron spectra were calibrated relative to the reference C 1s peak position (284.33 eV). The Mn 2p spectrum [Figure 4.8(a)] had the strong spin-orbit doublet Mn $2p^{3/2}$-Mn $2p^{1/2}$ at 641 and 652.7 eV, respectively. The Mn $2p^{3/2}$ peak at 641 and satellite feature indicates that the Manganese has an oxidation state of 3+[106]. The photoemission spectrum of Cu2p [Figure 4.8(b)] reveals the doublet spin-orbit with the splitting of 20 eV at binding energies 932.6 and 952.5 eV corresponding to $Cu2p^{3/2}$ and $Cu2p^{1/2}$ respectively, which represents Cu^{3+}[142]. The Ni 2p core-level photoemission spectrum [Figure 4.8(c)] shows the doublet spin-orbit peaks of $Ni2p^{3/2}$, $Ni2p^{1/2}$ with the splitting energy of 17.4 eV. The broad Ni 2p photoemission peaks were resolved into multiple peaks at 853.4, 870.9, and 855.2, 872.5 eV associated with Ni^{2+} and Ni^{3+}, respectively [143]. The Si 2p photoemission spectrum presented in Figure 4.8(d) shows the peak at 103.3 eV represents the characteristic peak of SiO_2 [88]. The photoemission spectrum of O 1s [Figure 4.8(d)] shows two peaks positioned at 529.6 and 531 eV corresponding to the chemical state of M-O and -OH, respectively [75]. The oxidation states of the transition metals agree with the formed transition metal-based spinel oxide $CuMnNiO_x$ in a developed SSAC. In addition, XPS analysis confirms the presence of the transition elements Mn, Cu, Ni, Si and O in different oxidation states as mentioned above.

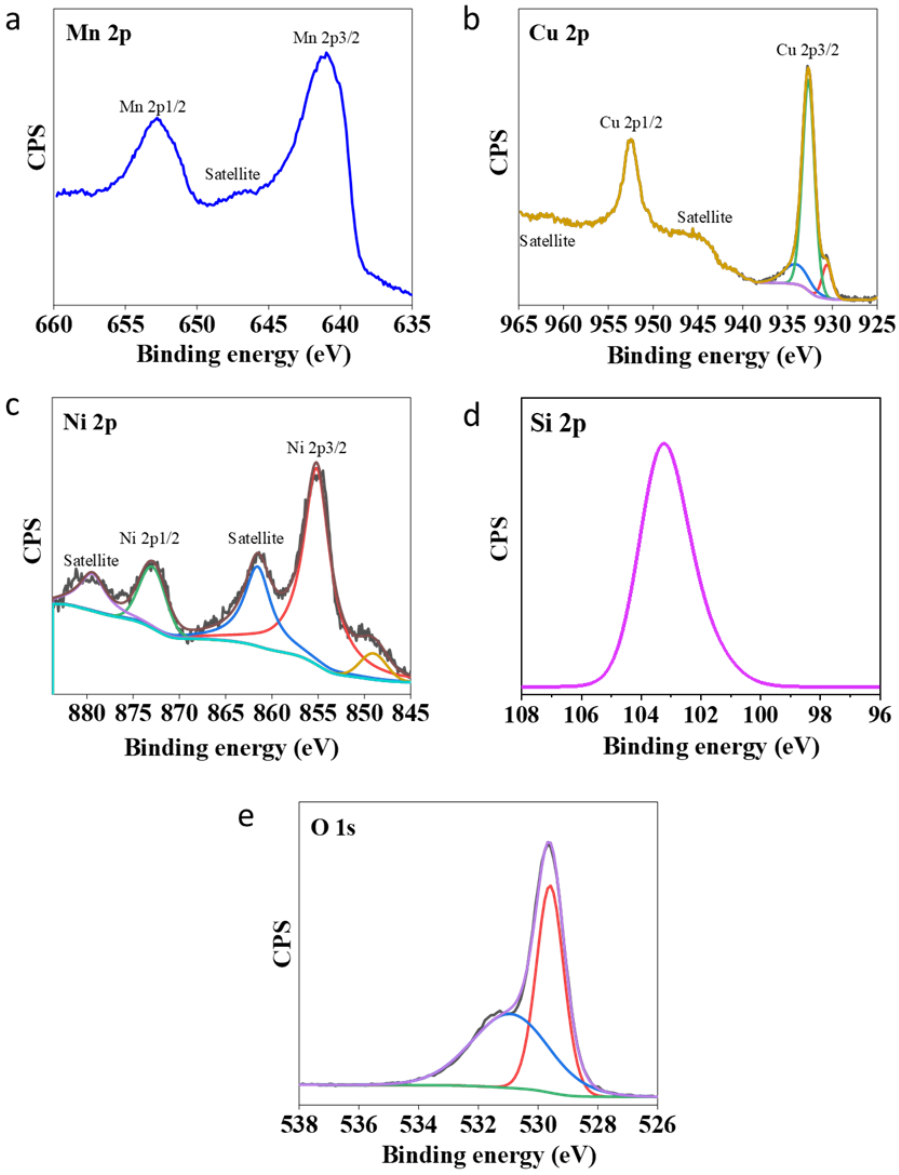

Figure 4.8. X-ray photoelectron spectra of tandem absorber coating.

4.7 Structural and morphological study by HR-TEM

Figure 4.9 represents the TEM, HR-TEM, and SAED images of spinel nanoparticles. The micrographs comprise aggregated nanocrystals in the range of 25 nm to 120 nm with an irregular shape. The HR-TEM analysis reveals that the developed nanoparticles have a d-spacing of 4.6 A^{o}. It coincides accurately with the d-spacing value of the X-Ray diffraction peak (hkl 111) of Cu $(Mn_{0.748}Ni_{0.252})_2O_4$ spinel. The SAED pattern obtained from spinel nanoparticles indicates that the developed particles are polycrystalline, and the obtained diffraction planes correspond to d_{111}, d_{220}, d_{311}, $d_{222,}$ indicating that particles are in the cubic phase. The interlayer spacing and d-spacings of diffraction planes in SAED patterns coincide

with the allowed Bragg diffraction of the corresponding cubic spinel, which coincides with the XRD analysis.

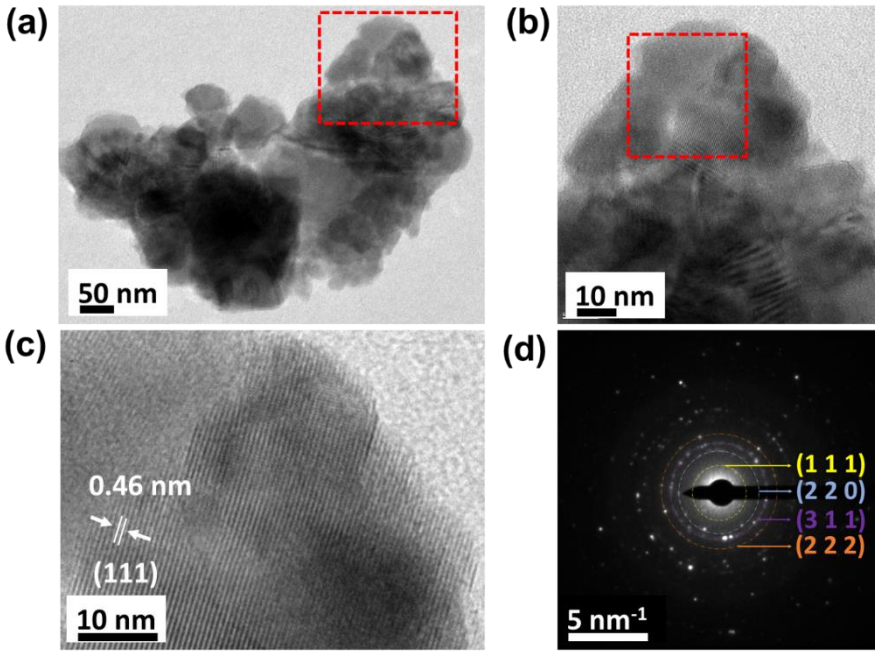

Figure 4.9. (a), (b), and (c) TEM and HR-TEM micrographs of spinel nanoparticles (d) SAED pattern of spinel nanoparticles.

An elemental mapping has been done on a cluster of spinel nanoparticles to understand the spatial distribution of elements across the absorber film. Figure 4.10 illustrates the elemental mappings of the spinel nanoparticle cluster by TEM. The elemental maps confirm the presence of four elements (Cu, Mn, Ni, and O). They appear to be evenly distributed throughout the cluster of nanoparticles, revealing a uniform chemical phase in an entire absorber film.

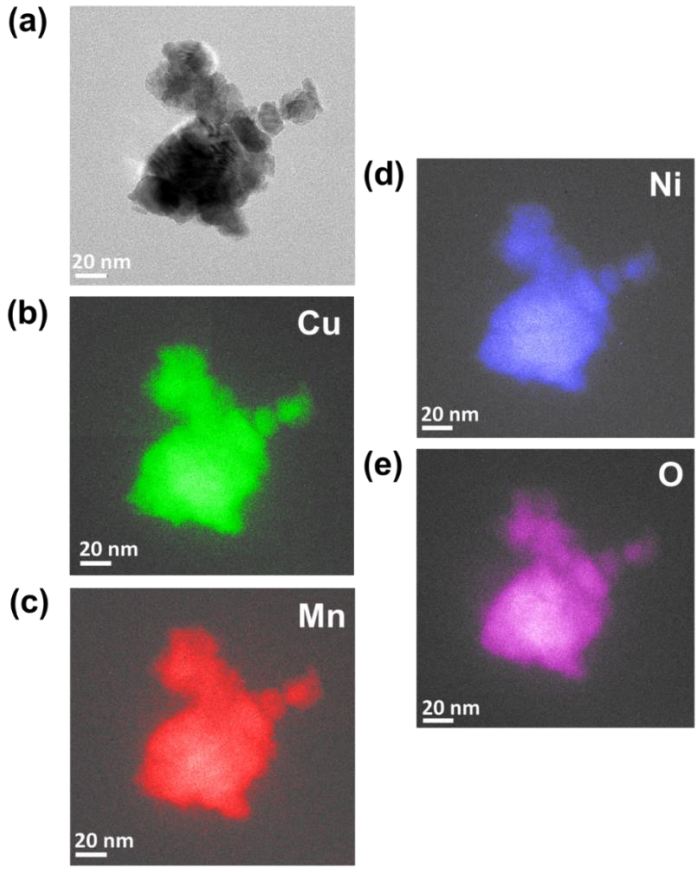

Figure 4.10. Chemical analysis of spinel structured nanoparticles cluster (a) TEM micrograph spinel nanoparticles (b) Copper (c) Manganese (d) Nickel and (e) Oxygen elemental mappings.

4.8 Roughness study of absorber and tandem layer by a Stylus profilometer

The optimized absorber and tandem absorber samples were studied by the Stylus profilometer to determine the area roughness (S_a). As mentioned in chapter 3, polished SS 304 substrates (S_a~100 nm) were utilized to develop and optimize the coatings to obtain the best optical properties. A 50 nm diamond tip is used for the scanning of a 1 mm x1 mm area of absorber and AR coatings. The topography of absorber and tandem absorber samples is shown in Figure 4.11. From Figure 4.11(a and b), It is evident that the surface area roughness of the absorber is 78 nm, whereas for the tandem absorber is 64 nm. The decrement in the roughness is observed from substrate to absorber (S_a~82 nm), and it is due to the formation of a uniform layer of spinel nanoparticles over on substrate. However, the layer thickness is in the order of nanometres as measured by FE-SEM (Discussed in next section). Thus, the non-uniformity of substrate is visible in the topography of the absorber, as shown in Figure 4.11(a). Similarly, the roughness is also decreased from the absorber to the tandem layer due to SiO_2 nanoparticles

covering the entire absorber layer. This accounts for the decrement in the observed surface area roughness from 78 nm to 64 nm.

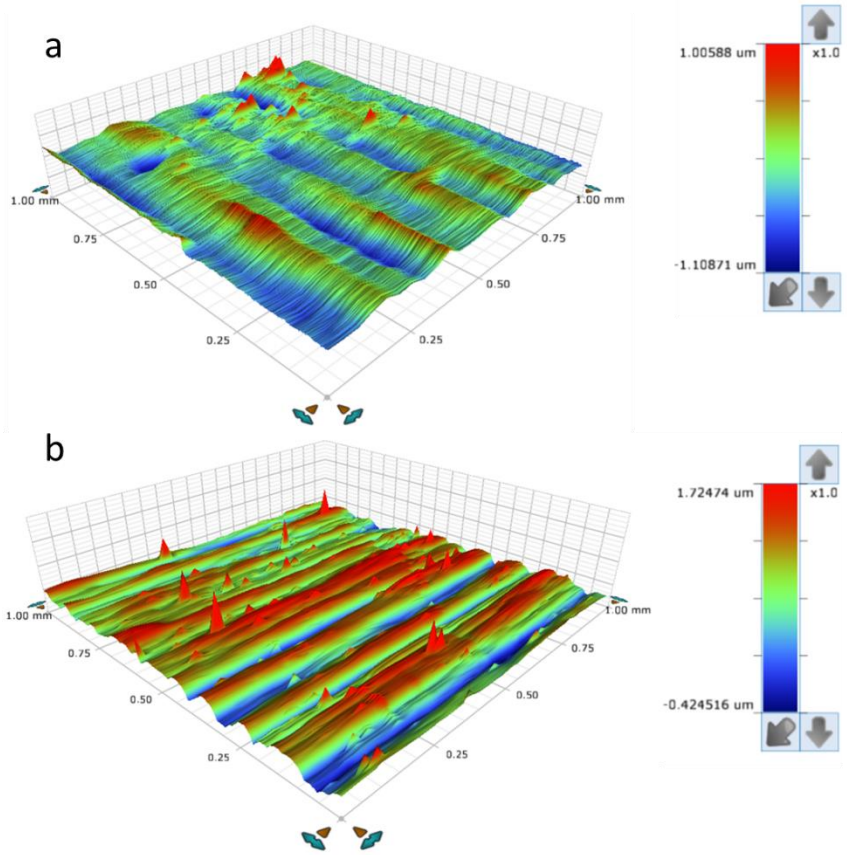

Figure 4.11. Topography of (a) spinel absorber and (b) tandem absorbers.

4.9 Morphological study of absorber and tandem layer by FE-SEM

The developed spinel and tandem absorbers were studied by FE-SEM to understand the morphology and to determine the thickness of optimized coatings. Figure 4.12(a) and (c) represent the morphology and thickness of the spinel absorber layer. The layer comprises nanoparticles in the range of 25-115 nm & irregularly shaped pores, and the thickness of the spinel absorber layer was found to be ~120 nm at an optimum withdrawal speed (2 mm/sec). To improve the thermal resistance and optical properties, we applied an AR layer over on spinel absorber comprised of spherical SiO_2 nanoparticles with a size of 16-64 nm.

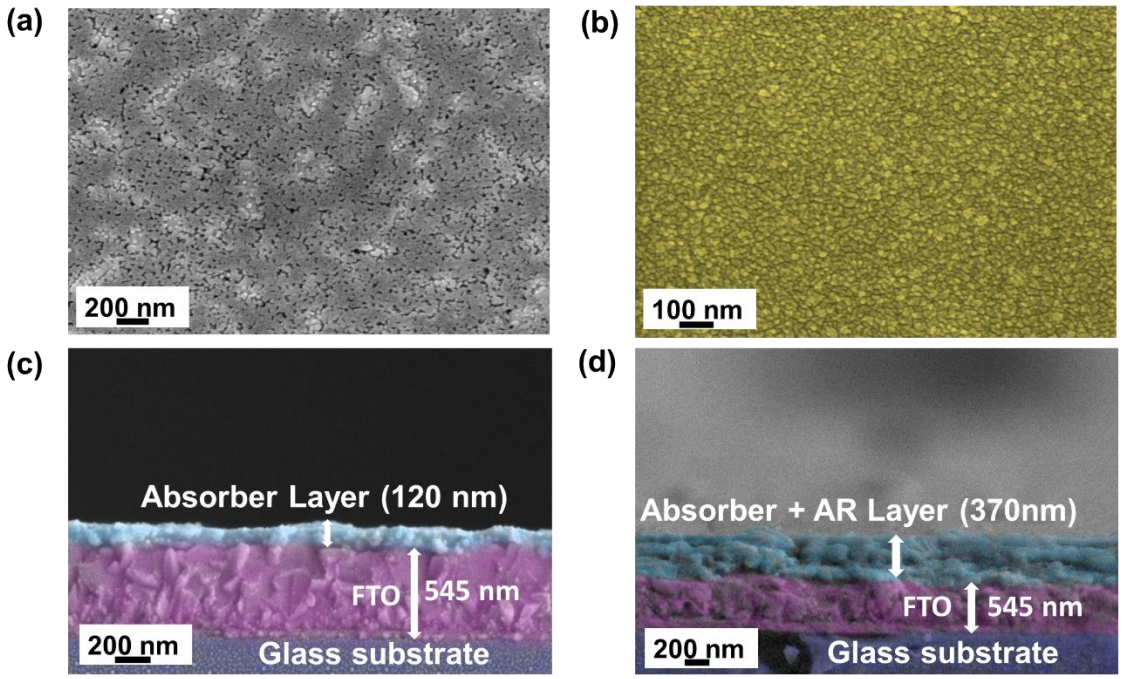

Figure 4.12. Morphology (a) absorber and (b) tandem absorber, cross-sectional images of (c) spinel absorber (d)tandem absorber coated over on an FTO glass substrate.

The commercial SiO_2 particles used for the AR layer were studied by TEM to identify the average particle size and found to be 30 nm. Figure 4.12(b) and (d) represent the morphology and thickness of the tandem absorber, respectively. At an optimized withdrawal speed (1 mm/sec), the tandem absorber thickness was found to be ~250 nm.

4.9.1 Thickness and refractive index study of absorber and tandem absorber samples by variable angle spectroscopic ellipsometry

In section 4.9, absorber and tandem samples were developed on FTO substrate and determined the thickness. The variable angle spectroscopic ellipsometry is utilized to measure the refractive index(η) and to confirm the thickness of absorber and tandem coating on the SS 304 substrate. The spectroscopic ellipsometry measurements and fitting was done for the spinel and tandem absorber samples as mentioned in the chapter 2 and section 2.6.11. Figure 4.13 (a and b) shows the spectroscopic ellipsometer fit between the experimental and model data for absorber and tandem absorber samples on SS 304 substrate. Figure 4.13 (c and d) shows the spectral dispersions of n, k. Finally, the refractive index of the absorber and tandem samples is found to be 1.69 ± 0.05 (at 550 nm) and 1.41 ± 0.05 (at 550 nm), respectively. The thickness of the absorber and tandem samples (Absorber + AR) is found to be 125 ± 5 nm and 245 ± 5

nm, respectively. The obtained thickness for both samples by spectroscopic ellipsometer is comparable with the thickness obtained by FE-SEM.

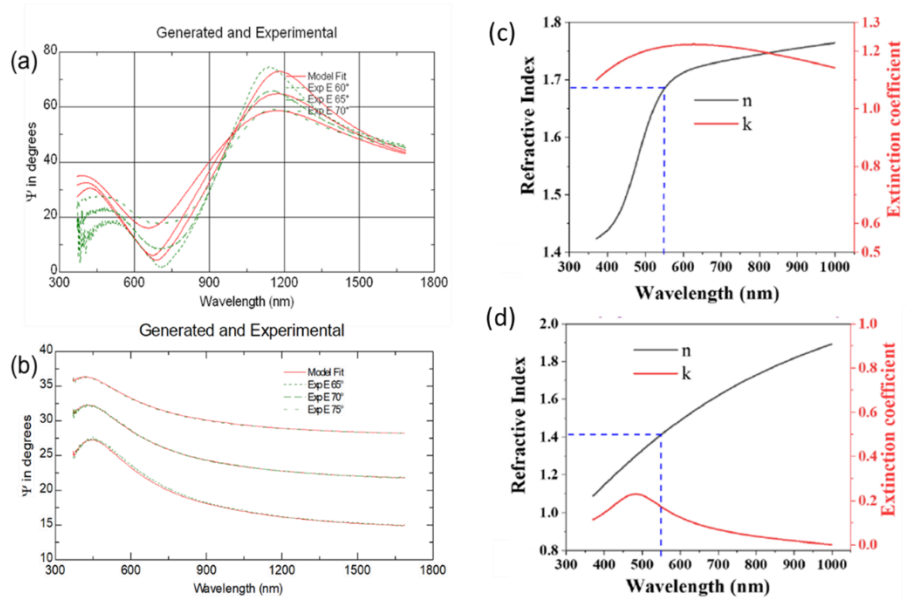

Figure 4.13. Ellipsometer spectra of experimental and model fit of (a) absorber, (b) tandem absorber, spectral dispersion of n and k for (c)absorber and (d)tandem coatings

The fitted result's mean squared error (MSE) value is for absorber and tandem samples is 12 and 2, respectively, which illustrates that the simulated optical constants are reliable due to the small value.

4.10 Thermal loss study

The spectral emittance (ε) characterizes the coating capability to reflect the IR. However, it is a surface phenomenon, and it may not replicate the exact thermal loss behaviour of the absorber tube at operating temperature in a field. To replicate field performance, the developed spinel and tandem absorber samples were measured by the FT-IR spectrophotometer. To estimate the thermal emissivity, the prepared samples of spinel and tandem absorber coatings (13mm outer diameter) and blackbody were exposed at different temperatures from 100 °C to 500 °C with 100 °C intervals by using a temperature controller. Later, the emissivity was determined by fractionalizing the emittance of a sample and blackbody at a particular temperature. The thermal emissivity spectra of both spinel and tandem absorber samples are presented in Figure 4.14(a) & (b), and values at temperatures from 100 °C to 500 °C are mentioned in table 4.4. It is observed that there is an increase in the emissivity from 100 °C to 500 °C in the case of both spinel and tandem absorbers.

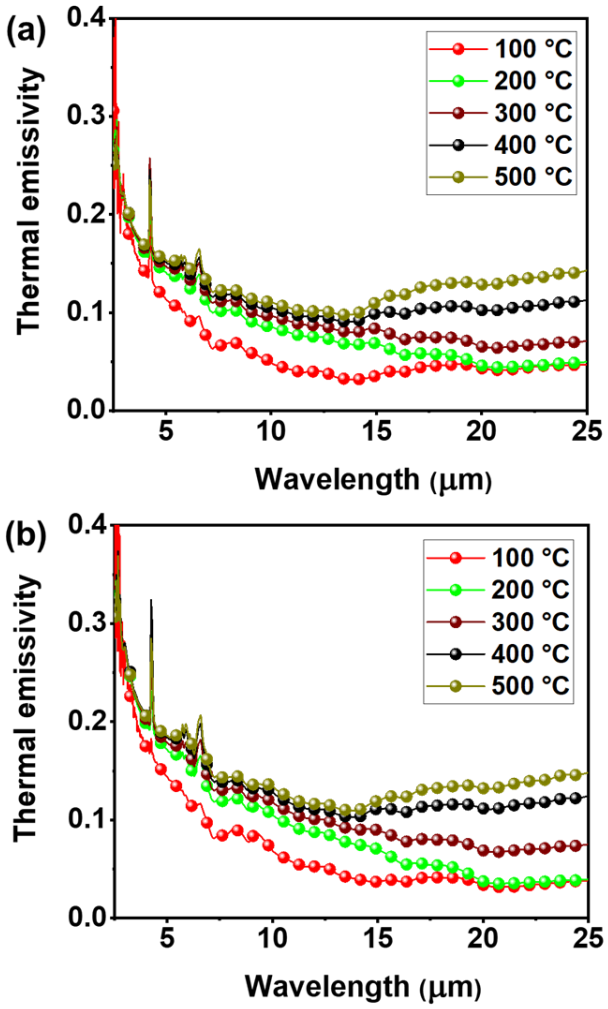

Figure 4.14. The thermal emissivity spectra of (a) spinel absorber (b) tandem absorber.

Table 4.4. The thermal emissivity of spinel absorber and tandem absorber at optimized withdrawal speeds.

Temperature (°C)	Spinel absorber	Tandem absorber
100	0.06	0.07
200	0.07	0.09
300	0.10	0.11
400	0.12	0.13
500	0.13	0.15

The spinel and tandem absorbers exhibited a low emissivity of 0.13 and 0.15, respectively, at 500 °C. The increase in the emissivity from spinel to tandem absorber may be due to an increment in the thickness of the stack in the case of the tandem absorber [107–109]. The light penetration depth (defined as the inverse of the absorption coefficient (α)) is closely related to the emissivity of coatings. The light penetration depth will be high for thicker coatings in comparison to low thickness coatings. Thus, the tandem absorber exhibits more emissivity in comparison with the spinel absorber.

4.11 Angular selectivity of spinel and tandem absorber

To investigate the wide-angle selective characteristics, the specular reflectance spectra at different incident angles were measured for spinel and tandem absorbers using universal measurement accessory attached to the UV-Vis-NIR spectrophotometers (Carry 5000). Figure 4.15(a) and (b) shows the contour plots of spinel and tandem absorber coatings at different incident angles from 10° to 80° and Figure 4.15(c) shows the angle of incidence (AOI) vs Solar absorptance. The solar absorptance values of spinel and tandem absorbers are reported in Table 4.5. In the case of the spinel absorber, the solar absorptance decreases gradually as the incidence angle increases from 10 to 80°. According to Fresnel's equations, it can be attributed to the increment in the reflectance at large light angles [110]. However, the tandem absorber exhibits a high solar absorptance from 10° to 50° and a slight decrease from 50° to 80° compared to the spinel absorber layer. The tandem layer has exhibited outstanding wide-angle solar absorptance with a net enhancement of 5 to 74% over an angle of incidence ranging from 10 to 80°.

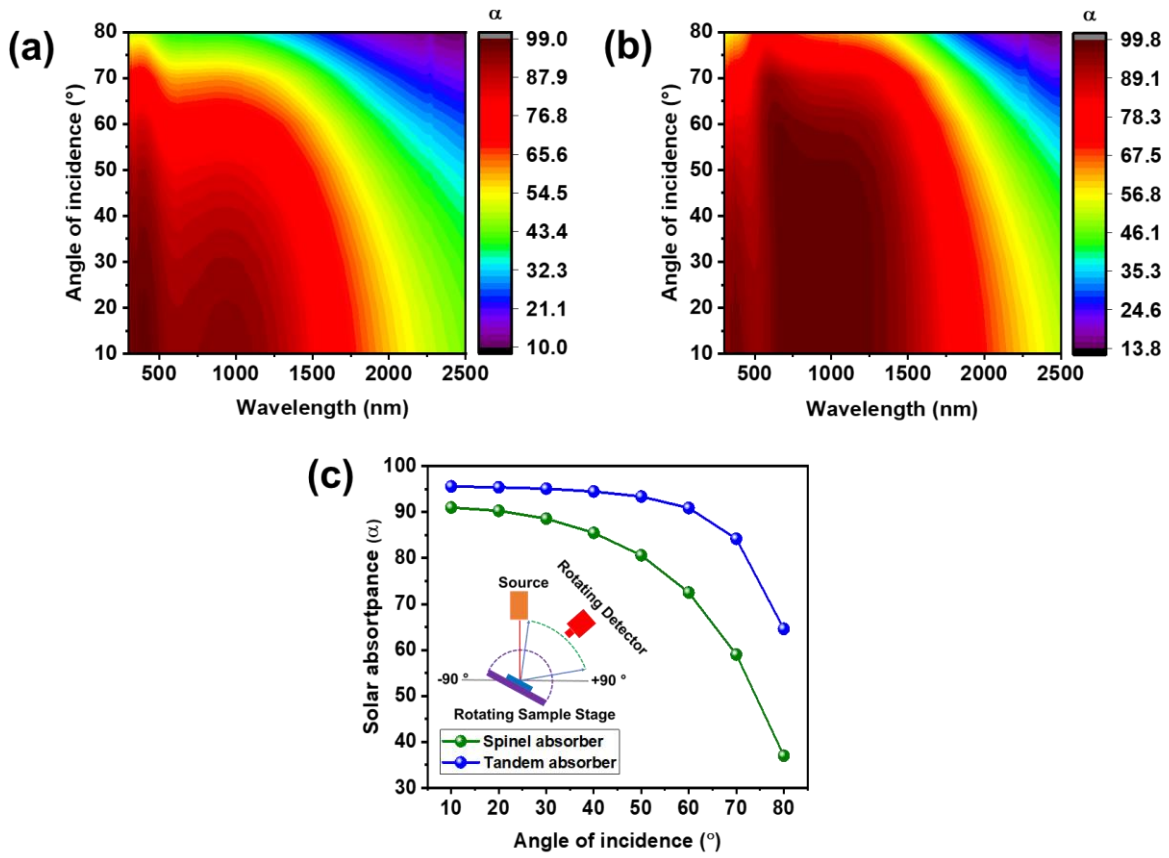

Figure 4.15. Contour plots of (a) spinel absorber (b) tandem absorber (c) angler selectivity graph for spinel and tandem absorber.

Table 4.5. Solar absorptance of spinel absorber and tandem absorber at different incident angles.

Incident angle (°)	**10**	**20**	**30**	**40**	**50**	**60**	**70**	**80**
Spinel absorber	0.91	0.90	0.88	0.85	0.80	0.72	0.59	0.37
Tandem absorber	0.95	0.95	0.95	0.94	0.93	0.91	0.84	0.64

The wide-angle selectivity of the tandem absorber may be explained by the mechanism of destructive interference, which occurs in the interface of two layers[111]. At a lower angle of incidence (10° to 50°), the reflected rays from the film surface interfere destructively and result in high solar absorptance. However, at higher incident angles, the reflected rays spread in all directions and may not interfere destructively, as it results in lower solar absorptance.

Therefore, the developed tandem stack exhibit high solar absorptance at lower incident angles and low solar absorptance at higher incident angles similar to the reported systems [112–117].

4.12 Conclusion

In this chapter, the development of a novel spinel (Cu ($Mn_{0.748}Ni_{0.252}$)$_2O_4$) SSAC by a facile wet chemical method is described by using tri-transition metal precursors. A SiO_2 nanoparticle layer is applied over on spinel absorber to serve as an AR layer to improve the optical properties. The tandem absorber (Spinel+AR layer) exhibited an excellent solar absorptance of 0.95 and a low spectral emittance of 0.15. Moreover, the developed tandem absorber exhibited outstanding wide-angle solar absorptance with a net enhancement of 5 to 74% over an angle of incidence ranging from 10° to 80°. Additionally, the thermal loss study indicates that the tandem absorber exhibited a very low thermal emissivity (15%) even at 500 °C. The high thermal stable wide-angle SSAC presents an excellent steadiness of solar absorptance and spectral emittance in the air at higher temperatures makes them ideal candidates for medium and high temperature solar thermal applications.

Chapter 5: Performance comparison of solar selective absorber coatings

Chapter 5 deals with the performance comparison of developed SSACs in chapter 3 and chapter 4 in terms of thermal stability, corrosion resistance, coating adhesion, and wide-angular solar absorptance. Further, the photothermal conversion efficiency of developed absorber systems (chapter 3 and chapter 4) were calculated and compared to determine the best SSAC for the upscaling, prototype development, and performance validation by parabolic test rig facility.

The optical, morphological, and structural study of SSACs is significant to analyze the performance and optimize the coatings to obtain the targeted properties. However, other parameters such as thermal stability in the air, corrosion resistance, coating adhesion, and wide-angular solar absorptance also govern the performance of SSACs. In addition, these properties also indicate the long-term durability of SSAC. In this regard, the above-mentioned parameters were studied and compared to the developed SSACs described in chapters 3 and 4 in the present chapter.

5.1 Thermal stability study

Thermal stability, also known as thermal shock resistance, refers to the capacity of a material to withstand structural and performance changes as a function of temperature or duration at a constant temperature. It is an essential parameter of SSACs for low to high-temperature applications [40]. In general, the SSACs coated receivers with the evacuated environment may not oxidize at higher temperatures if the vacuum stays. In contrast, once the vacuum gets breached, the absorber coating in the receiver suddenly reacts with air and leads to degradation of performance. However, the main objective of the thesis is to develop high temperature stable SSACs in open-air atmospheric conditions for evacuated or non-evacuated receivers. Thus, SSACs described in chapters 3 and 4 were studied at 500 °C in the air using a customized thermal stability testing method. The customized testing experiment is flexible and very simple. It is only needed to select a proper annealing time and temperature in an air or vacuum atmosphere. Thereafter, the optical properties of the samples were measured. This method is usually adopted during the research and development stage.

The developed SSACs (Co-Cu-Mn-O_x/SiO_2 and Cu-Mn-Ni-O_x/SiO_2) were tested for their thermal stability at 500 °C temperature for 250 h with an interval of 50-hours in a muffle

furnace. The thermal cycle profile is shown in Figure 5.1, and the samples were heated to the coatings to 500 °C with a heating rate of 10 °C per minute, a dwell time of 50-hours, and then suddenly cooled down from 500 °C to room temperature. The total thermal test cycle duration is 56-hours, and five cycles were conducted to estimate the thermal stability of developed SSACs.

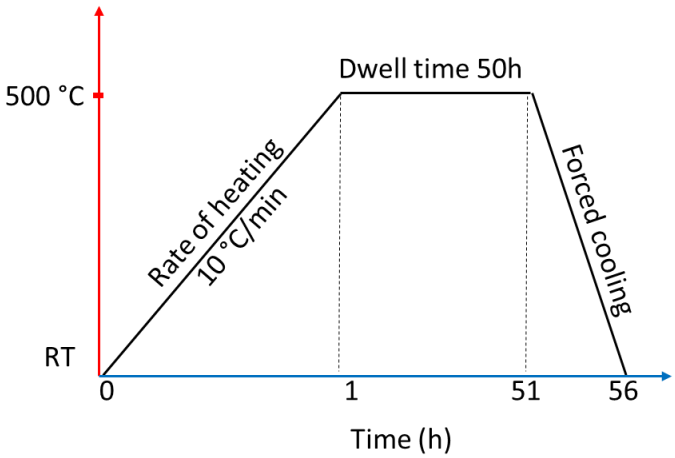

Figure 5.1. The schematic of the thermal stability test.

The optical properties of the thermal stability tested SSACs samples were measured at every 50-hours of a cycle, and the corresponding spectra are shown in Figure 5.2. The changes in optical properties for every 50-hours of the tests up to 250-hours are tabulated in Table 1.

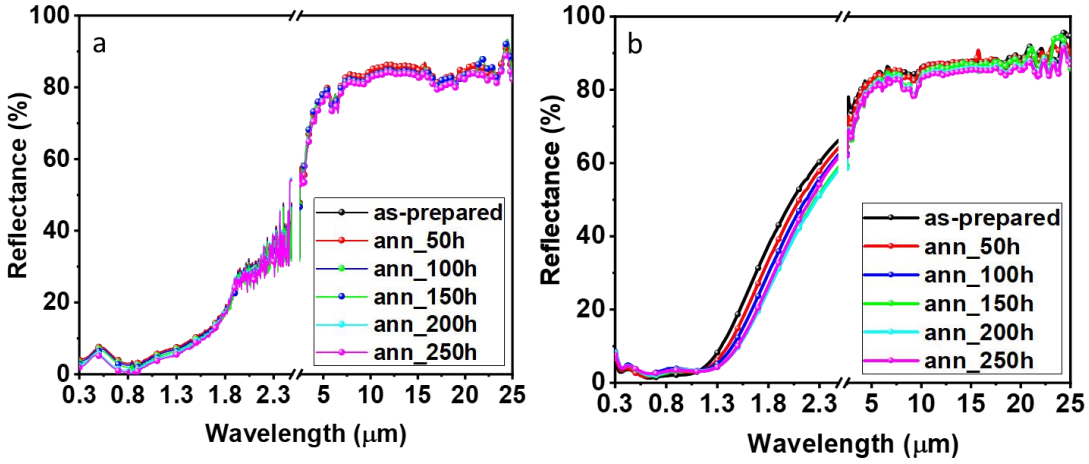

Figure 5.2. UV-Vis-NIR and IR reflectance spectra of thermal stability tested samples: (a) Co-Cu-Mn-O_x and (b) Cu-Mn-Ni-O_x layers at 500 °C for 250 hours.

Table 5.1. Optical properties of thermal stability tested SSAC samples at 500 °C with 50-hours interval.

Duration (Hours)	Co-Cu-Mn-O_x/SiO_2 SSACs		Cu-Mn-Ni-O_x/SiO_2 SSACs	
	Solar absorptance (AM1.5) α (%)	Emittance ε (%)	Solar absorptance (AM1.5) α (%)	Emittance ε (%)
As prepared	93.3	17.0	95.0	14.0
50	93.5	17.2	95.2	14.1
100	93.6	17.2	95.5	14.3
150	93.5	17.4	95.5	14.6
200	93.6	17.6	95.7	14.8
250	93.8	17.8	95.6	14.9

From Figure 5.2 and Table 5.1, it is observed that the developed SSACs are well stable, and no drastic changes in the optical properties are observed at 500 °C for 250-hours. It is also observed that there is a slight increment in solar absorptance and emittance in both SSACs samples. The reason for this change in the roughness of coatings is due to the sample being subjected to thermal stability tests of longer durations. The difference in the roughness on top of SSACs may result in the scattering of light, leading to a change in the optical properties. We can conclude that the developed SSACs are thermally stable at 500 °C up to 250-hours in open-air atmosphere conditions. Although both SSACs are thermally stable, the Cu-Mn-Ni-O_x SSAC samples exhibit high absorption and low emittance compared to Co-Cu-Mn-O_x SSAC samples. Thus, Cu-Mn-Ni-O_x SSACs can be used for the upscaling and development of 1-m receivers, which can be used in evacuated and non-evacuated receivers.

5.2 Corrosion resistance study by Potentiodynamic polarization (PDP) method:

The understanding of corrosion behaviour is essential for spectrally selective absorber coatings because it affects the durability of SSACs in the long run and could be deciding factor in the performance of the solar thermal system. To estimate the corrosion resistance and corrosion rate of developed SSACs, the samples such as SS 304, Co-Cu-Mn-O_x absorber, Co-Cu-Mn-O_x/SiO_2 tandem absorber, Cu-Mn-Ni-O_x absorber, and Cu-Mn-Ni-O_x/SiO_2 tandem absorber

are studied systematically. The electrochemical analyser is used with 3.5wt% of NaCl standard electrolytic solution for the Potentiodynamic polarization (PDP) measurements as mentioned in the experimental section 2, section 2.6.12. The linear sweep measurements are collected for the samples mentioned above at 1 mVS^{-1}. These measurements are used for Tafel analysis to estimate the polarization potential (R_p), corrosion rate (mm/y) by extrapolating the straight-line of the anodic and catholic Tafel lines. The measured voltage versus logarithmic of current results are summarised as Tafel plots in Figure 5.3 for the samples mentioned above and the estimated polarisation potential; the corrosion rate is summarised in Table 2. The corrosion current (I_{corr}) and potential (E_{corr}) are taken at the intersection points of extrapolated anodic and cathodic Tafel curves of Figure 5.3 by using C View 2 software. The polarisation potential is calculated using the Stern-Geary equation mentioned below [144]

$$R_p = \frac{b_c \text{ x } b_a}{2.3 \text{ x } i_{Corr}\,(b_c + b_a)} \text{ (K}\Omega \text{ cm}^2\text{)} \quad \text{----------1}$$

where b_c and b_a are the slopes of cathodic and anodic Tafel lines, I_{corr} is corrosion current density (mA/cm^2), and R_P is the polarization potential (KΩ cm^2). The values of b_a, b_c, I_{corr}, E_{corr}, R_p and C_R are obtained using C View 2 software after extrapolating anodic and cathodic Tafel curves.

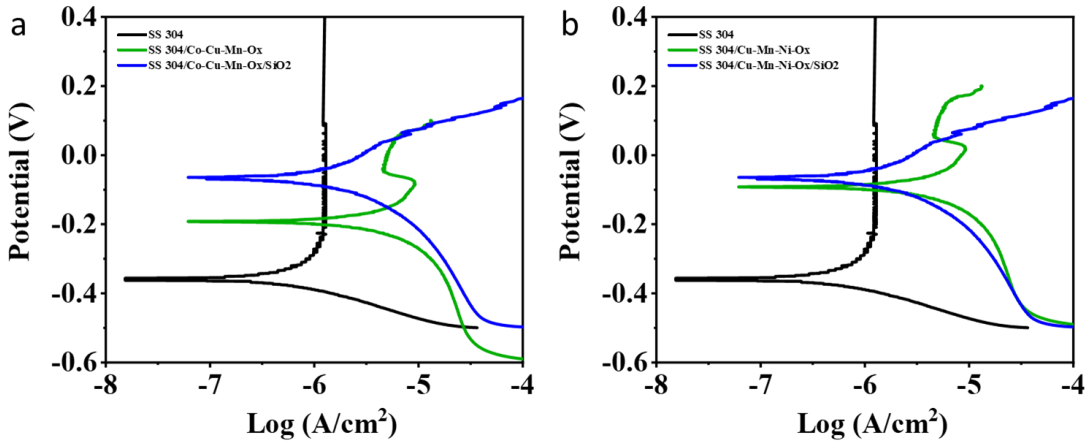

Figure 5.3. Potentiodynamic polarization (Tafel) curves for (a) bare SS 304, Co-Cu-Mn-O_x absorber, Co-Cu-Mn-O_x/SiO_2 tandem absorber, (b) bare SS 304, Cu-Mn-Ni-O_x absorber, and Cu-Mn-Ni-O_x/SiO_2 tandem absorber.

Table 5.2. The polarisation potential (R_p), corrosion rate (C_R) of SS 304, Co-Cu-Mn-O_x absorber, Co-Cu-Mn-O_x/SiO_2 tandem absorber, Cu-Mn-Ni-O_x absorber, and Cu-Mn-Ni-O_x/SiO_2 tandem absorber.

Sample	**Polarisation potential (R_p) KΩ.cm^2**	**Corrosion rate (C_R) mmpy**
SS 304	383.5	0.00087
Co-Cu-Mn-O_x absorber	742.0	0.00052
Co-Cu-Mn-O_x/SiO_2 tandem absorber	870.4	0.00040
Cu-Mn-Ni-O_x absorber	765.6	0.00046
Cu-Mn-Ni-O_x/SiO_2 tandem absorber	890.0	0.00033

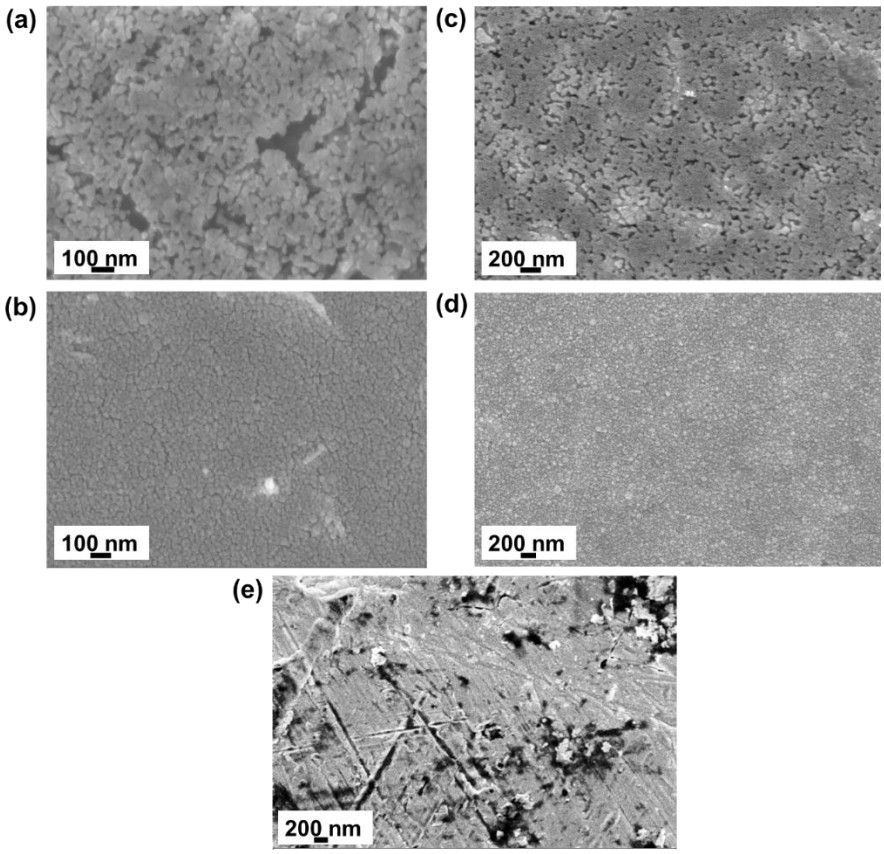

Figure 5.4. The morphology of (a) Co-Cu-Mn-O_x absorber (b) Co-Cu-Mn-O_x/SiO_2 tandem absorber, (c) Cu-Mn-Ni-O_x absorber, (d)Cu-Mn-Ni-O_x/SiO_2 tandem absorber, and (e) SS 304, respectively.

From Figure 5.4 and Table 5.2, it can be observed that the samples such as SS 304, Co-Cu-Mn-O_x absorber, Co-Cu-Mn-O_x/SiO_2 tandem absorber, Cu-Mn-Ni-O_x absorber, and Cu-Mn-Ni-O_x/SiO_2 tandem absorber exhibited the polarisation potential (KΩ.cm^2) of 383.5, 742.0, 870.4, 765.6 and 890.0 respectively. The obtained polarization potential of 383.5 for SS 304 is comparable with the reported literature by B.Usmani et al. [96]. The increment in the polarisation potential is observed for the Co-Cu-Mn-O_x absorber and Cu-Mn-Ni-O_x absorber compared to SS 304 substrate. It is due to the covering of surface defects such as microcracks, pores, and pinholes on SS 304 substrates by absorber layer by dip-coating process [96,145,146]. Further, polarisation potential is increased after applying the SiO_2 nanoparticles AR layer over on Co-Cu-Mn-O_x and Cu-Mn-Ni-O_x absorbers [147,148]. The morphology of substrate, absorber, and tandem absorbers is shown in Figure 5.4. It can be observed from Figure 5.4 that both the absorber layer of Co-Cu-Mn-O_x and Cu-Mn-Ni-O_x covering the scratches, cracks present in the SS 304 substrate. However, the annealing of absorber layers also leads to cracks or holes in some areas, as presented in Figure 5.4 (a and c). It is also essential to notice that the Co-Cu-Mn-O_x layer exhibit less polarisation potential than the Cu-Mn-Ni-O_x absorbers. It is due to increased nano cracks than the Cu-Mn-Ni-O_x absorbers, as shown in Figure 5.4(a). As mentioned earlier, covering the pinholes and cracks may decrease the chance of penetrating the electrolyte ions such as OH^-, Cl^- and Na^+ present in the electrolyte solution into substrate or absorber surface while measuring the PDP measurements [147]. A similar observation was made by B.Usmani et al. after developing the ZrO_x/ZrC-ZrN/Zr layer over on SS substrate by a physical vapor deposition method [96]. Finally, we obtained the 870 and 890 KΩ.cm^2 of polarisation potential for Co-Cu-Mn-O_x/SiO_2 and Cu-Mn-Ni-O_x/SiO_2 tandem absorbers, respectively compared to the substrate and absorber layers. Researchers often use oxide films and coatings made up of SiO_2, ZrO_2, Al_2O_3, and TiO_2 over substrates to improve the corrosion resistance [147,148]. In the present work, the SiO_2 nanoparticles layer is used as an AR layer to reduce the reflection, and it also aids in improving the corrosion resistance. The high corrosion resistance for tandem absorbers is due to cover the defects, cracks. In addition, it is also reported that the SiO_2 layer also plays a significant role in suppressing the inward diffusion of chlorine [147].

In this regard, the coatings developed with wetchemical methods often exhibit very low (realtively) polarisation potential in literature. For example, Ni-Co SSAC was developed on Al substrate with Electrochemical deposition method by Rajesh Kumar et al., and reported a polarisation potential of 135.03 k$\Omega\cdot$cm^2[149]. SSACs developed by vapor deposition methods

exhibit high polarisation potential (relatively) compare to the wet chemical methods. Usamni et al., developed a ZrO_x/ZrC-ZrN/Zr coatings on SS and Cu substrates by DC/RF magnetron sputtering and as deposited samples exhibited a polarisation potential of 1379 $k\Omega \cdot cm^2$ and 7.2 $k\Omega \cdot cm^2$[96] on SS and Cu substrates respectively. Zhang et al., reported a highly corrosion resistant and sandwich-like Si_3N_4/Cr-CrN_x/Si_3N_4 coatings by DC/RF magnetron sputtering. As depoisted SSACs exhibited a 3633 $k\Omega \cdot cm^2$ of polarisation potential. However, it is decreased to 13.759 $k\Omega \cdot cm^2$ after subjecting sample to 5.0% of the neutral salt spray test[150]. In this connection, the above results (Figure 5.3 and Table 5.2) emphasize that Cu-Mn-Ni-O_x/SiO_2 tandem absorbers exhibit good polarisation potential (relatively) and less corrosion rate than the substrate and absorber layers developed in the thesis. In comparision with the SSACs developed with vapor deposition methods, the Cu-Mn-Ni-O_x/SiO_2 tandem absorbers exhibit moderate polarisation potential. Thus, it can be considered for the further upscaling and development of prototype receiver tubes.

5.3 Adhesion study of SSACs by Cross-cut test

Adhesion plays an essential role in any coatings for functional applications, and the adhesion of the coatings ensures good performance in long-term duration. To estimate the adhesion of developed coatings, the Cross-cut test is used according to ASTM standard D3359–09. An X-cut of length (40mm) has been made with a sharp knife through the Co-Cu-Mn-O_x/SiO_2 and Cu-Mn-Ni-O_x /SiO_2 films at an angle of 30-45°. Further, 75mm long pressure-sensitive tape was applied over an incision area and rubbed firmly with the eraser on the end of a pencil. After 90 seconds, the tape was removed by holding the free end. Furthermore, the samples are examined carefully before and after the tape test under an optical microscope to estimate the adhesion rate. The optical microscope images of Co-Cu-Mn-O_x/SiO_2 & (b) Cu-Mn-Ni-O_x/SiO_2 SSACs are presented in Figure 5.5.

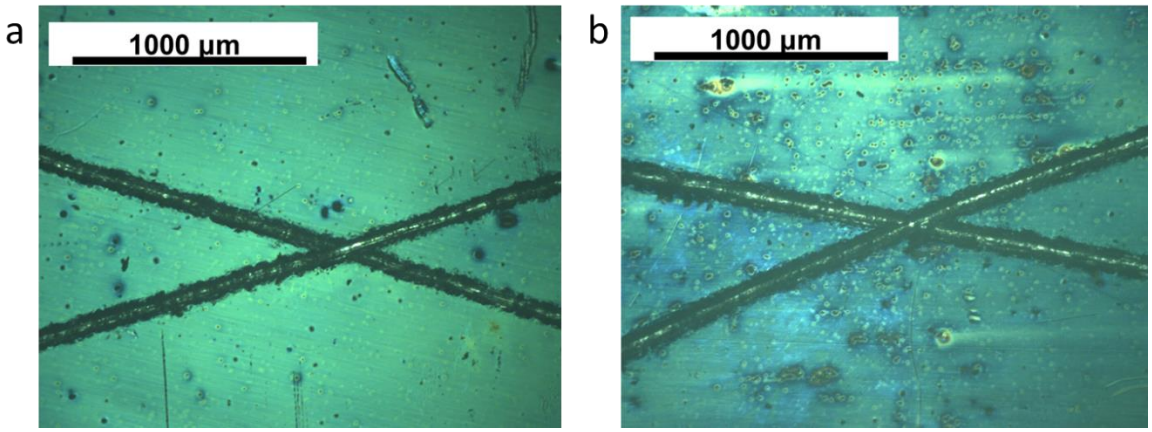

Figure 5.5. Optical microscope images of (a) Co-Cu-Mn-O_x/SiO_2 & (b) Cu-Mn-Ni-O_x/SiO_2 SSACs after conducting the Cross-cut test.

The samples were carefully inspected at X-cut area for coating removal from the samples and to estimate the rate of adhesion in accordance with the below scale as per ASTM standard D3359–09.

Table 5.3. Adhesion rating scale

Rating	Evaluation criteria
5	No peeling or removal of the coating
4	Trace peeling or removal along incisions or at their intersection
3	Jagged removal along incisions up to 1/16 inch (1.6mm) on either side
2	Jagged removal along most of the incisions up to 1/8 inch (3.2mm) on either side
1	Removal from most of the area of the X under the tape
0	Removal beyond the area of the X

From Figure 5.5 and Table 5.3, it can be observed that there is trace peeling of both coatings along the incisions. Hence, the rate of adhesion for both SSACs is 4. In addition, both developed SSACs exhibited the same adhesion rating.

5.4 Wide-angular selectivity of SSACs

SSAC having wide-angular selectivity [13] in a solar thermal system is of great advantage to improve the performance of a receiver since the solar absorptance is a function of the angle of the incident light. Our atmosphere comprises of substantial fraction (≈10%) of diffused sunlight from incident solar power. Thus, to achieve high photothermal conversion efficiency, SSAC is required to have a wide-angular selectivity to capture the diffused radiation [151]. Until now, several SSACs have been studied and reported with wide-angular absorption [112–

114,116,117,151]. To investigate the wide-angle selective characteristics of the coatings, the specular reflectance spectra at different incident angles were measured for developed SSACs using a universal measurement accessory attached to the UV-Vis-NIR spectrophotometers (As mentioned in Chapter 2, section 2.6.1(b)). The obtained reflectance spectra for the developed SSACs are converted into absorption spectra and plotted as contour plots (Solar absorptance vs. wavelength vs. angle of incidence). Figure 5.6 (a) and (b) show the contour plots of Co-Cu-Mn-O_x/SiO_2 and Cu-Mn-Ni-O_x/SiO_2 SSACs at different incident angles from 10 ° to 80 °, and Figure 5.6(c) shows the angle of incidence (AOI) vs. Solar absorptance. The solar absorptance values of Co-Cu-Mn-O_x/SiO_2 and Cu-Mn-Ni-O_x/SiO_2 SSACs are reported in Table 5.4.

Table 5.4. The solar absorptance values of Co-Cu-Mn-O_x/SiO_2 and Cu-Mn-Ni-O_x/SiO_2 SSACs at different incident angles.

Incident angle (°)	**10**	**20**	**30**	**40**	**50**	**60**	**70**	**80**
Co-Cu-Mn-O_x/SiO_2	93.2	92	91.3	90.6	89.9	86.4	79.8	60.1
Cu-Mn-Ni-O_x/SiO_2	95.6	95.4	95.1	94.5	93.4	90.9	84.2	64.6

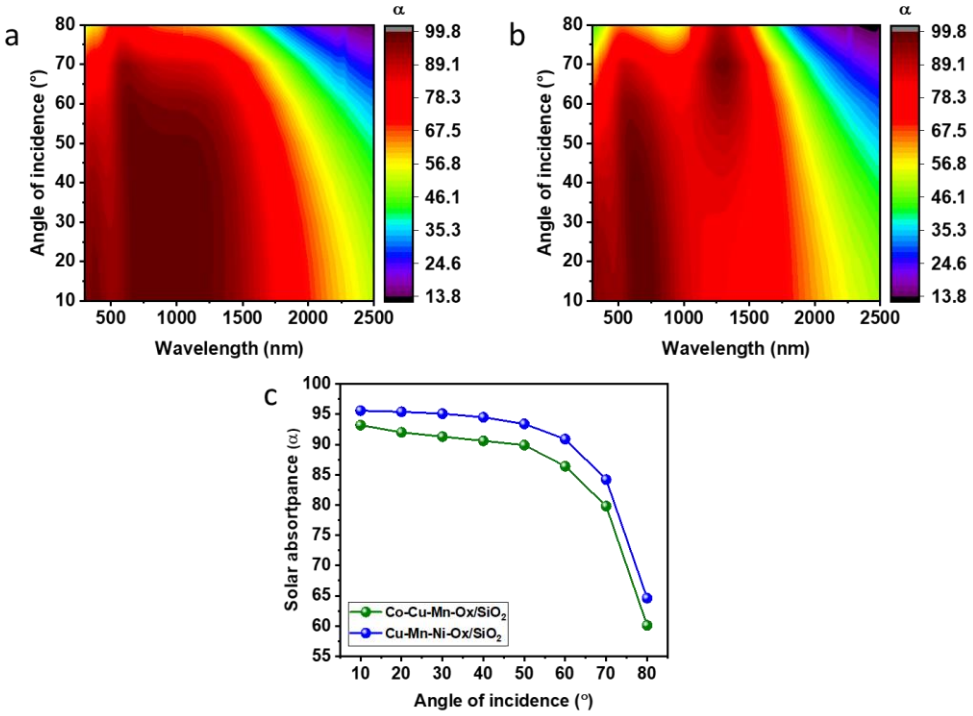

Figure 5.6. Contour plots of (a) Co-Cu-Mn-O_x/SiO_2, (b) Cu-Mn-Ni-O_x/SiO_2 SSACs, and (c) comparison graph of both SSACs from 10° to 80° incident angles.

From Figure 5.6 (a and b), it is observed that the decrement of solar absorptance from 10° to 80° in the wavelength region from 300 to 2500 nm for both developed SSACs. It can be attributed to the increment in the reflectance at large light angles according to Fresnel's equations [110]. Figure 5.6(c) shows the comparison of wide-angular solar absorptance of both SSACs and Cu-Mn-Ni-O_x/SiO_2 SSACs shows the good wide-angular absorption due to its high solar absorptance. Although absorptance decreases from 95.6% to 64.6% with the angle of incidence, Cu-Mn-Ni-O_x/SiO_2 exhibits a high absorption from 10° to 50° compared to other SSACs (Co-Cu-Mn-O_x/SiO_2) developed in the thesis work. Thus, Cu-Mn-Ni-O_x/SiO_2 SSAC can be considered for the upscaling and development of prototype receiver tubes.

5.5 Photothermal conversion efficiency

Photothermal conversion efficiency (PTCE) refers to the fraction of sunlight converted to heat by the solar selective absorber at a particular temperature T and solar optical concentration C. The PTCE of SSACs in a receiver is expressed (considering only radiative losses) by using the equation below

$$\eta_{rec} = \alpha - \varepsilon\sigma\left(\frac{T_{abs}^4 - T_{amb}^4}{CI}\right) \qquad \text{---------- 2}$$

To calculate the PTCE of developed SSACs, I have assumed the parabolic trough concentration ratio as 80 to attain the temperatures of 500 °C and DNI of 800 W/m^2. The conversion efficiencies of both SSACs (Co-Cu-Mn-O_x/SiO_2 & Cu-Mn-Ni-O_x/SiO_2) are calculated using the above parameters and their optical properties. The calculated PTCE values are tabulated in Table 5.5 and Figure 5.7 show that the Cu-Mn-Ni-O_x/SiO_2 SSACs exhibit a higher PTCE compared to the Co-Cu-Mn-O_x/SiO_2 SSACs. At the operating temperature of 300 °C, Cu-Mn-Ni-O_x/SiO_2 SSACs exhibit 95% of PTCE compared to the Co-Cu-Mn-O_x/SiO_2 SSACs efficiency (93.1%). It is due to the Cu-Mn-Ni-O_x/SiO_2 SSACs, which indicate high solar absorptance and low emittance from 300 °C to 500 °C compared to the Co-Cu-Mn-O_x/SiO_2 SSACs. In addition, decrements in the PTCE can be observed in Table 5.5 and Figure 5.7 with the increase of operating temperature from 300 °C to 500 °C in both SSACs. It is due to the increasing thermal emissivity of SSACs with the temperature.

Table 5.5. Photothermal conversion efficiencies of the developed SSACS with the experimental optical properties and radiation losses.

SSAC	Solar absorptance (α)	Thermal emissivity (ε_T)			Photothermal conversion efficiency (PTCE) %		
		300 °C	400 °C	500 °C	300 °C	400 °C	500 °C
Co-Cu-Mn-O_x/SiO_2	0.93	0.14	0.16	0.17	93.1	93.0	92.7
Cu-Mn-Ni-O_x/SiO_2	0.95	0.06	0.10	0.14	95.0	94.8	94.5

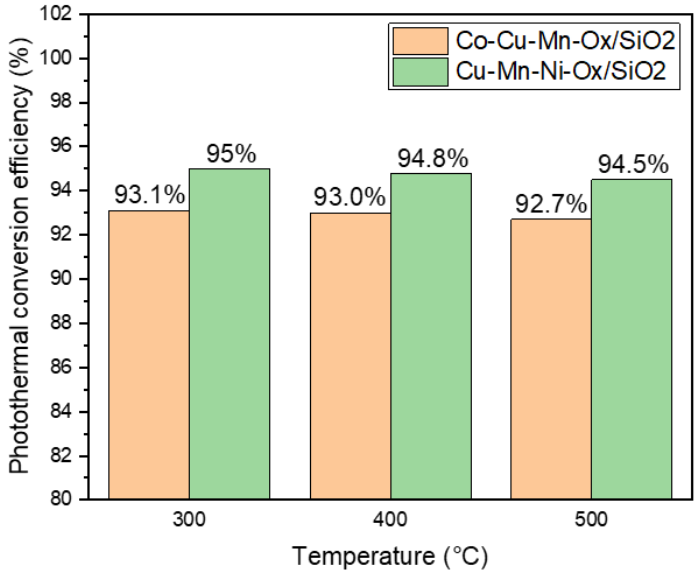

Figure 5.7. The photothermal conversion efficiencies of developed SSACs at different temperatures by considering the actual radiation losses for the corresponding temperatures.

In the present work, PTCE is calculated by considering the only radiative losses. It is important to be noted that, apart from the radiation losses, there are other losses from the absorber surface like conduction and convection losses at that particular temperature during the operation of the receiver system in field conditions. Thus, the obtained PTCE at different temperatures for Cu-Mn-Ni-O_x/SiO_2 SSACs may vary depending on the conduction and convection losses. The Cu-

Mn-Ni-O_x/SiO_2 SSACs displayed good PTCE compared to other developed SSACs. Thus, it can be used for upscaling and prototype development of receiver tubes.

5.6 Conclusion

Chapter 5 describes the performance comparison of developed SSACs ((Co-Cu-Mn-O_x/SiO_2 and Cu-Mn-Ni-O_x/SiO_2)) in terms of thermal stability, corrosion rate, adhesion, and wide-angular absorptance. Although both SSACs exhibit the same performance in terms of thermal stability, adhesion. However, the Cu-Mn-Ni-O_x/SiO_2 SSAC shows good optical properties, less corrosion rate, and high wide-angular absorptance. The increased solar absorptance and low thermal emissivity of Cu-Mn-Ni-O_x/SiO_2 SSAC lead to high photothermal conversion efficiency compared to the Co-Cu-Mn-O_x/SiO_2 SSACs. Hence, the Cu-Mn-Ni-O_x/SiO_2 SSAC can be used for upscaling and prototype development of receiver tubes.

Chapter 6: Upscaling of SS/Cu-Mn-Ni-O_x/SiO_2 Solar selective absorber coatings (SSACs)

Chapter 6 describes the development of prototype non-evacuated receiver tubes by using the best spectral selective absorber coatings (SSACs) developed in the present work (discussed in Chapter 5). Initially, the chapter describes the detailed synthesis of the absorber, anti-reflective coating (AR) solutions (6+6 litres), and preparation of multiple Nos. of 1-m absorber tubes by a dip-coating method. Further, the developed absorber tubes were characterized to determine the properties such as solar absorptance and spectral emittance. Finally, the prototype receivers (2-m length) were successfully assembled by joining absorber tubes with metal flanges and glass tubes (envelopes) having 2-m length with 42 mm outer-diameter (OD) for performance validation compared to the commercially procured non-evacuated receiver tubes using a parabolic test rig.

Cu-Mn-Ni-O_x/SiO_2 SSACs described in chapter 5 are found to be the best SSACs in terms of optical properties, thermal and corrosion-resistant compared to other SSACs (developed in Chapter 3). Thus, the coatings are considered for upscaling and the development of 10 Nos. of 1-m length absorber tubes.

6.1 Preparation of the substrates

Commercially available stainless steel (SS) 304-grade tubes (10 Nos.) were purchased from the market to upscale coatings. The dimensions of each SS tube are 1-m length, 42 mm in OD, and 2 mm in thickness. SS tubes were polished using different grit abrasive wheels and further buffed using cotton wheels to obtain a mirror finish. The digital image of unpolished and polished SS tubes is shown in below Figure 1.

Figure 6.1. Digital image of (a) unpolished and (b) polished SS 304 tubes.

Initially, the tubes were cleaned with a surfactant solution, followed by deionized water to eliminate the grease marks on the tubes. Further, NaOH solution was prepared and used for thorough cleaning as shown in Figure 6.2. [152].

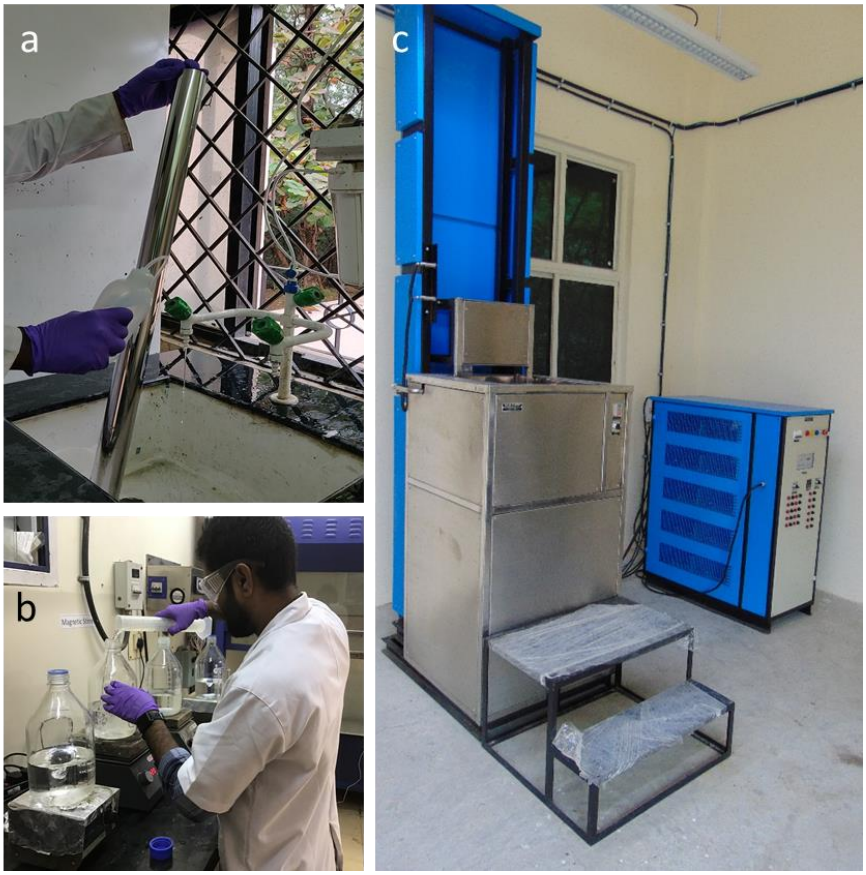

Figure 6.2. (a) Cleaning of SS tube with a surfactant solution, (b) preparation of NaOH solution, (c) large dimension ultrasonic cleaner.

For the cleaning process, 5 wt% of NaOH solution (6 litres) is prepared and transferred into an Acrylic cylindrical vessel having dimensions of 1050 mm (Length (L)), 80 mm (OD), and 3mm (Thickness (T)). A Trans-O-Sonic large dimension ultrasonic cleaner (Model: D-5000-H-DUN) is used to clean 10 Nos. of 1-m length SS tubes. The instrument has the capability to heat the solution up to 60 °C with a simultaneous ultrasonication process. The cylindrical vessel filled with NaOH solution is placed in an ultrasonicater and heated using a digital temperature controller. When the solution temperature of the solution reaches 60 °C, the SS tube is placed in the heated solution for 10 minutes with simultaneous ultrasonication. The heated NaOH solution helps in cleaning and degreasing the SS tubes. In addition, the metal or dust particles inside SS tubes were removed due to the vibrations, and the tube's surface is cleaned in and out thoroughly. After the ultrasonication process, the tubes were cleaned with normal

deionized (DI) water, wiped with a cotton cloth, and dried to remove the watermarks on the tubes. Finally, tubes were utilized for the preparation of the coatings.

Figure 6.3. Stainless steel tube after the complete cleaning process.

6.2 Large scale synthesis of absorber and AR coating solution

The synthesis procedure of absorber and AR coating solution is explained in chapter 2, section 2.2.2 and 2.5, respectively. The synthesis procedures of both absorber and AR coating solutions are facile, economical and scalable. To prepare multiple Nos. of absorber tubes (1-m length and 42mm OD), a large quantity of absorber and AR coating solutions (6 litres) were successfully synthesised precisely the same procedure mentioned in chapter 2. The concentration of precursors and solvents was calculated for the bulk synthesis of coating solutions. The digital images of the absorber and AR coating solutions stored in the glass containers (2 litres) are shown in Figure 6.4.

Figure 6.4. Large scale synthesised (a) absorber and (b) AR coating solution stored in the glass containers.

6.3 Dip coating and heating process

After successfully synthesising coating sols at a large scale, the solutions were transferred into a container. Both absorber and AR coatings were prepared by the dip-coating method. For the pilot deposition of 10 Nos. of 1-m length tubes, an Acrylic cylindrical vessel having dimensions 1050 mm (Length), 80 mm (OD), and 3mm (Thickness) is specially designed. A customized dip coater from Holmarc Opto-Mechatronics Pvt. Ltd., Kochi, India, has been used to develop coatings on 1-m SS tubes as shown in Figure 6.5. The dip-coating process is done as mentioned in chapter 2, section 2.3. The best optical properties were obtained for withdrawal speed of 2 mm/sec for SS plates on a lab scale. Thus, the same withdrawal speed is maintained in the case of 1-m tubes to obtain similar optical properties. The dip-coating process of a 1-m SS tube is shown in Figure 6.5 with the solution container.

The prepared coatings are further processed for annealing. A Nabertherm furnace (RS 120/1300/11) is used for the annealing of coated SS tubes. The furnace can be used to anneal >10 Nos. of 1-m length absorber tubes at a time. The optimized process conditions were utilized to anneal the coated SS tubes as mentioned in chapter 4, section 4.1. The coated SS tubes are

annealed at 500 °C for 1 hour with a 10 °C of the rate of heating. The tubes before and after annealing are shown in Figure 6.6.

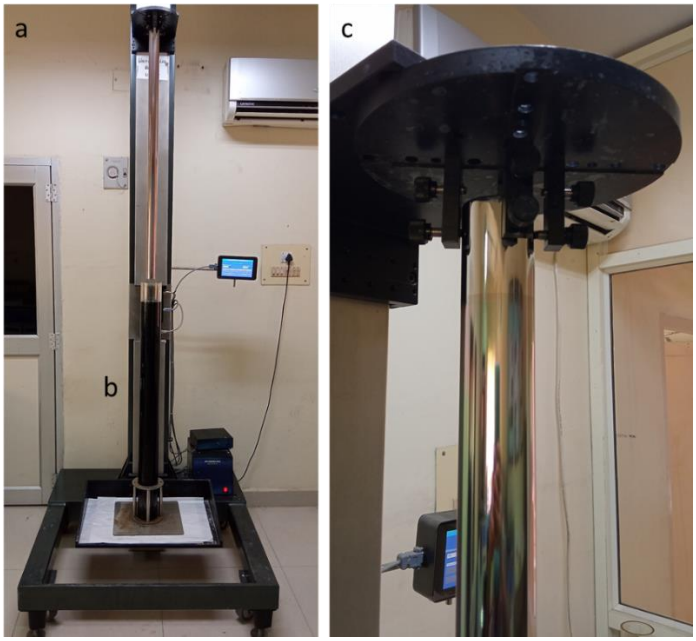

Figure 6.5. Dip-coating of 1-m length SS tube (b) acrylic container filled with absorber coating solution and (c) formation of wet absorber layer over on SS tube after the dip-coating process.

After the annealing process, absorber-coated tubes were characterized using handheld reflectometers to determine the optical properties. The characterization of tubes is discussed in further section 6.4.

Figure 6.6. Absorber coated tubes in a large-scale furnace before annealing, (b)1-m length absorber coated tube after annealing, and (c) display of 10 Nos. of absorber coated tubes.

The absorber-coated tubes were further coated with AR coating solution. The synthesised AR coating solution (Section 6.2) is transferred to the acrylic container to prepare AR coatings over absorber-coated tubes. The dip-coating process for the AR coatings on small samples is explained in chapter 2, section 2.5. A similar procedure was followed for the preparation of AR-coated tubes. After the dip-coating process, the tubes were annealed in an oven at 300 °C for 1 hour. The optimized process conditions such as 1 mm/sec of withdrawal speed, 300 °C of annealing temperature, and 1 hour of process duration were used as mentioned in chapter 4, section 4.4.3. The dip-coating process of AR coating over an absorber coated tube and the digital image of AR coated tubes after annealing is shown the Figure 6.7.

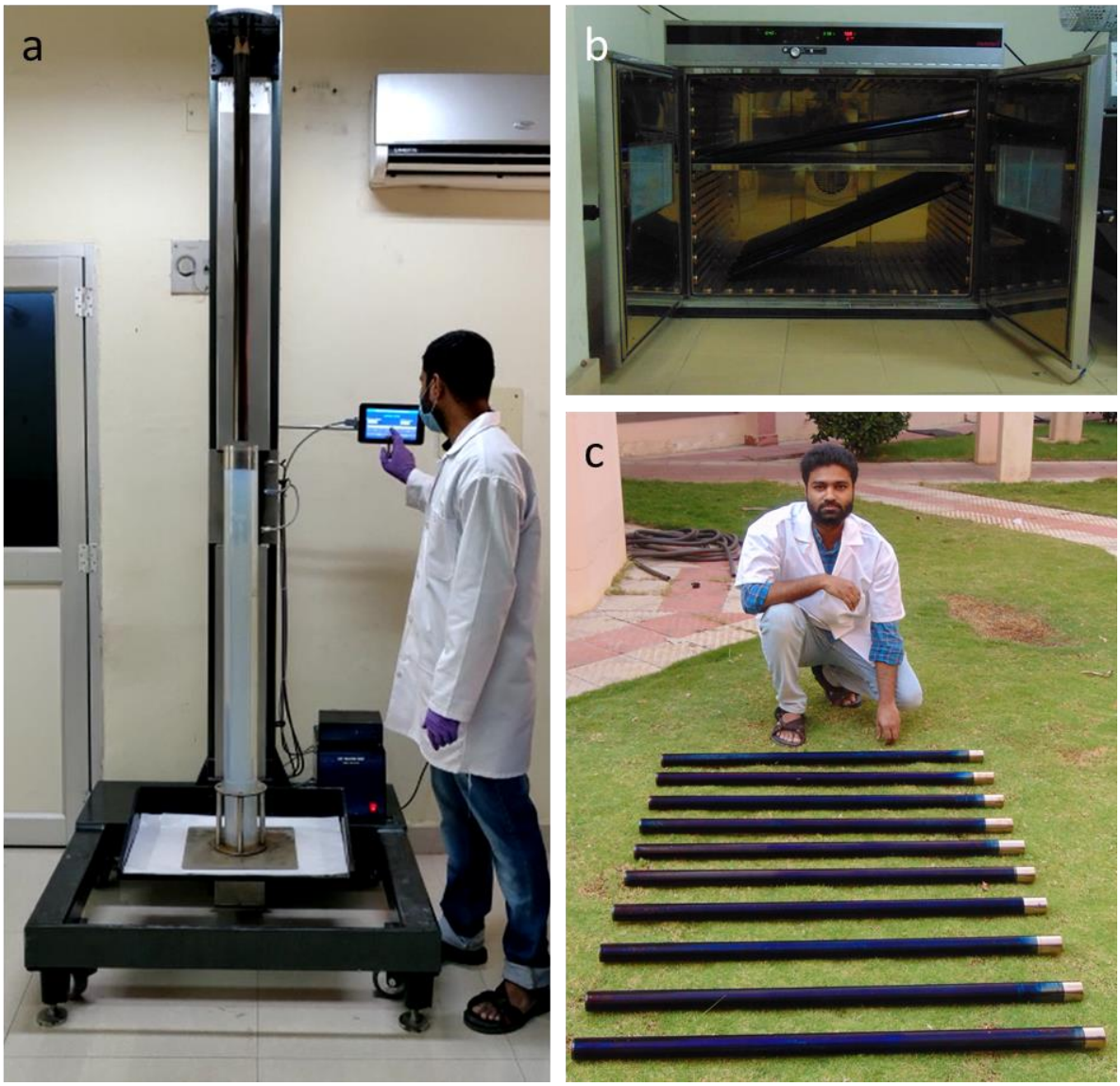

Figure 6.7. Dip-coating of 1-m length absorber coated tube (b) AR coated tubes in a large size oven (Before annealing) (b) display of 10 Nos. of AR coated tubes.

6.4 Characterization of absorber and AR coated tubes

The developed absorber and AR coated tubes were characterized by using Handheld reflectometers to determine the optical properties such as solar absorptance and spectral emittance. Initially, absorber-coated tubes were measured using a 410-Visible / NIR portable reflectometer and ET-100 Thermal Handheld Emissometer as mentioned in chapter 2, section 2.6.3 [153,154]. Measurements were taken at 10 places to investigate the uniformity of a 1-m length absorber-coated tubes are from top to bottom. The optical properties comparison of coatings developed at lab scale and 1-m tubes is presented in the table 6.2. The values of solar absorptance of absorber-coated tubes are 0.88-0.90, and spectral emittance of coating varied

from 0.14 to 0.15. Similarly, the optical properties were measured after development of AR coating (2nd layer on the absorber layer (Tandem)).

6.4.1 Optical properties comparison of coatings developed at lab scale and 1-m tubes

The values of solar absorptance of tandem coated tubes (2 layers) are 0.94-0.95, and spectral emittance of coating varied from 0.15 to 0.16. The solar absorptance and emittance of small samples (absorber) is 0.88 and 0.14 respectively, whereas for tandem absorber, it is found to be 0.95 (solar absorptance) and 0.15 (spectral emittance) as reported in the chapter 4.

Table 6.1. Optical properties comparison of coatings developed at lab scale and 1-m tubes

	Solar absorptance measured by		Spectral emittance measured by	
	UV-Vis-NIR spectrophotometer (300 to 2500nm)	410-Visible reflectometer (330 to 2500nm)	FT-IR spectrophotometer (2.5 to 25μm)	ET-100 emissometer (1.5 to 21μm)
Absorber (lab scale)	0.88	--	0.14	--
Tandem absorber (lab scale)	0.95	--	0.15	--
Absorber (1-m tube)	--	0.88-0.90	--	0.14-0.15
Tandem absorber (1-m tube)	--	0.94-0.95	--	0.15-0.16

The variation in the properties of 1-m tube in comparison with the small samples can be attributed to the measurement range of wavelengths as shown in the Table 6.1 with spectrophotometers and handheld reflectometers. In addition, the measurement of curved tubes with reflectometers also be another reason for the variation in the properties. Thus, 10 measurements were taken on 1-m tube. However, the optical properties as obtained on small samples is reproducible on 1-m tube also with minor fluctuations. The digital image of

measuring the optical properties of coated tubes by Handheld reflectometers is shown in Figure 6.8.

Figure 6.8. The digital image of measuring the (a, b) solar absorptance and (c, d) spectral emittance of tandem absorber tubes by 410-Visible / NIR portable reflectometer and ET-100 thermal handheld emissometer, respectively.

The developed 1-m absorber tubes were used to assemble 2-m receiver tubes for the installation in the parabolic trough test rig and performance comparison with the commercially non-evacuated receiver tubes. 5 Nos. of 2-m absorber tubes were assembled by joining 1-m coated tubes (10 Nos.) by Tungsten inert gas (TIG) welding process. TIG welding process produces high-quality, clean welds [155]. Thus, TIG welding is used for the joining of absorber tubes, as shown in Figure 6.9 (a). TIG process used a non-consumable tungsten electrode, filler rod of stainless steel for the weld. In addition, the Argon is used as inert shielding gases to protect the weld area and electrode from oxidation. After completion of TIG welding, the 5 Nos. of 2-m absorber tubes were displayed in Figure 6.9 (b).

Figure 6.9. Assembling of 2-m prototype receiver tubes for field validation: Digital images of (a) joining the absorber tubes (1-m) by welding, (b) 2-m absorber tubes after welding, (c) and (d) assembling of absorber tubes with metal flanges and glass envelops.

In addition, commercially available Borosilicate glass tubes were purchased and used to develop non-evacuated receiver tubes with addition to metal flanges by using TIG welding. The dimensions of glass tubes (envelops) are 1975-mm length, 60 OD, and thickness of 3mm. The glass tubes are melted and joined together to prepare 1975mm glass tubes. Further, metal flanges were prepared and welded to the 2-m absorber tubes along with the glass tube case. The images of the mentioned process are shown in Figure 6.9(c and d). Finally, the 2-m receivers with a glass tube (without vacuum) and metal flanges were developed for the performance comparison with the commercially procured receiver tubes. The digital image in Figure 6.10 shows the final developed 4 Nos. of 2-m prototype receiver tubes.

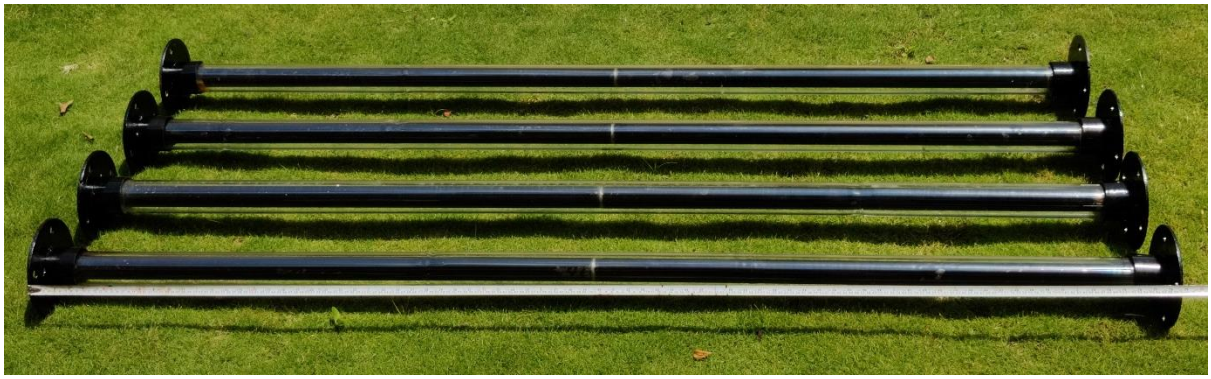

Figure 6.10. Digital image of a complete assembly of 2-m prototype receiver tubes (4 Nos.).

6.5 Parabolic trough (PT) test rig

The PT collector is the most developed and commercialized CSP technology. The first PT collector was introduced in the year 1880, and it has been improving ever since [156,157]. The PT collector has the components such as receivers, concentrators, Heat transfer fluid (HTF) etc. In the PT collector, the reflectors concentrate solar radiation, which is subsequently absorbed by the receiver in the focal line. The concentrated solar energy is transformed into thermal energy and transferred to an HTF. The sun-tracking system of the PT collector is driven in single-axis mode. After developing the prototype receiver tubes with the targeted properties, testing the performance with the commercial receiver tubes in the real-field condition is critical. In this connection, our department (Centre for Solar Energy Materials, International Advanced Research Centre for Powder Metallurgy and New Materials (ARCI), Hyderabad, India) has established the single-axis PT test rig facility under the programme of Technology Research Centre (Sponsored by Department of Science and Technology (DST), Govt. of India) and it is shown in Figure 6.11. The test rig facility can estimate the actual performance of the solar thermal components, especially receiver tubes (evacuated and non-evacuated) in real-field conditions. In addition, it is a closed-loop system that can have the facility compared to standard receivers (commercial receivers: Hi-min, China (PVD based receiver) in the same weather conditions. The key features of the test rig are

- Two parallel rows (8-m length and 2-m width) of parabolic trough systems for simultaneous testing of commercial and Indigenous solar receiver tubes
- Thermic fluid-based closed-loop system and can operate 50 to 350 °C temperature
- Heat gain studies in real-field conditions with the actual measurement of DNI
- Electrical heater support for measuring the actual heat loss of solar receivers at different operating temperatures
- Thermic fluid validation in the closed-loop system at different operating temperatures

- ❖ The efficiency of the system calculation with different sizes of receivers and in various flow conditions

The PT rig can withstand windspeeds of 51 m/s in stow position, 20 m/s in tracking positions. It can also accommodate the volume of 70 litres of HTF. In addition, it has satellite-based time synchronization and light-dependent resistors for finer tracking of DNI.

Figure 6.11. (a and b) Digital images of in-house parabolic test rig facility.

One of the main objectives of the thesis is to develop the receiver tubes with targeted optical properties and compare the performance with the commercially procured receivers. Thus, the developed receivers were successfully installed in the PT rig facility. In addition, other components such as receivers, mirrors, and HTF were commercially procured and used in the PT rig facility.

6.5.1 Solar receivers

The solar receiver is one of the critical components in the PT rig facility. Its thermal and optical properties determine the efficiency of the PT rig. To compare the performance of the developed receivers in the present work, commercially available Hi-Min solar absorber tubes (PVD based

multilayer absorber coatings on SS304 tubes (2-m length and 42mm OD) were purchased and assembled non-evacuated receivers with metal flanges and commercial borosilicate glass tubes similar to the indigenous non-evacuated receivers. The digital image of the complete assembly of 2-m receiver tubes (4 Nos.) using commercially purchased Hi-min solar receiver tubes is shown in Figure 6.12.

Figure 6.12. Digital image of a complete assembly of 2-m receiver tubes (4 Nos.) using commercially purchased Hi-min solar absorber tubes.

The technical specifications of Hi-min receivers are mentioned below

Table 6.2. The technical specifications of Hi-min receivers

Functional specifications of Hi-min receiver	Average solar absorptance	95 ± 1% (AM 1.5)
	Average spectral emittance	7 ± 2% (300 °C)
	Coating stability in the Air	350 °C, 2000 hours test, decrease of coating's efficiency ≤ 2%

6.5.2 Reflectors

Solar reflectors are used to concentrate the solar radiation towards the solar receivers to achieve high temperatures. Typically, glass or metal can be used as a solar reflector. The objective of a solar reflector is to reflect the maximum solar radiation. In addition, one of their most important characteristics is their durability, which entails the maintenance of their optical properties throughout their service lifetime, aimed at 10–30 years or more. In the present work, Rioglass

solar reflectors are purchased and used in the PT rig facility. The technical specifications of reflectors are mentioned below

Table 6.3. The technical specifications of reflectors.

Reflectors	Reflectance	Average reflectivity 94%
	Material used	Coated with Silver layer (Other layers included
	Shape	Parabolically curved

6.5.3 Heat-transfer fluid (HTF)

HTF plays a vital role in transferring heat from receiver tubes to heat exchangers in a solar thermal system. Currently, Therminol 66 is used as a liquid phase HTF in the PT rig facility in the present work. Therminol 66 is a highly stable synthetic HTF that can be operated from -3 °C to 345 °C. The specific properties of Therminol 66 HTF are presented in Table 6.3.

Table 6.4. Specific properties of Therminol 66.

Composition	Modified terphenyl
Maximum operating temperature	345 °C
Liquid density at 25°C (ASTM D-4052)	1005 kg/m^3
Coefficient of thermal expansion at 200 °C	0.000819/°C

6.5.4 Pyrheliometer and Pyranometers

The solar radiation incident on the Earth's surface can be categorized into three components. They are Global Horizontal Irradiance (GHI), Direct Normal Irradiance (DNI), and Diffuse Horizontal Irradiance (DHI)[2]. The GHI can be expressed as in equation 1

$$GHI = DHI + DNI * \cos(z) \quad \text{----------1}$$

The precise measurement of DNI is essential since the DNI value represents the heat input into the solar thermal system. There are two ways the measure the DNI. It can be measured directly by a Pyrheliometer. The device converts solar flux (W/m^2) into a proportional electrical signal using either a thermoelectric or photoelectric detector.

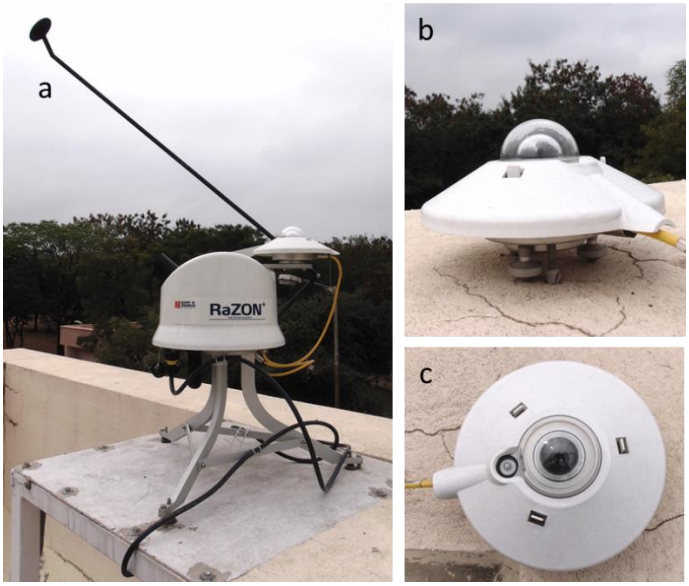

Figure 6.13. The digital images of installed (a) Pyrheliometer (b and c) Pyranometer.

In the present thesis work, RaZON^{+} PH1 Pyrheliometer is used to measure DNI of solar radiation. The spectral range of the device is from 310 to 2700nm, and the measurement range is from 0 to 1500 W/m^2. In addition, it can be operated in the operating temperature range -40 °C to +80 °C. The digital image of the pyrheliometer is shown in Figure 6.13(a). The spectral range of the device is from 310 to 2700 nm, and the measurement range is from 0 to 1500 W/m^2. In addition, it can be operated in the operating temperature range from -40 °C to +80 °C. The digital image of the pyrheliometer is shown in Figure 6.13(b and c).

6.6 Validation of Parabolic trough (PT) test rig

After successfully establishing a PT test rig facility, to confirm both rows are ideal for validating solar thermal components, the commercially purchased solar absorber tubes and assembled with glass and metal flanges as non-evacuated receiver tubes (mentioned in section 6.5.1) were installed in rows 1 and 2 of the PT test rig. Further, the PT test rig facility conducted heat loss and heat gain studies for the commercial non-evacuated receiver tubes. The temperature of HTF was measured by temperature sensors located at an inlet and outlet on east and west rows. The mass flow rate of HTF was measured by using a variable flowmeter H 250 M40, KROHNE and a cup anemometer were utilized to measure the wind speed. DNI was measured as mentioned in section 6.5.4.

6.6.1 Heat loss study

Heat losses of a receiver play a vital role in the efficiency of solar thermal systems. Therefore, it is necessary to understand the exact nature of heat losses from receivers. As the heat losses

increase, the solar thermal system efficiency decreases[158,159]. The heat losses in a receiver tube installed in a PT test rig are presented in Figure 6.14. The heat losses from a receiver can be classified into conduction (Q_{cond}), radiation (Q_{rad}), and convection (Q_{conv}) losses, as shown in Figure 6.14. The total heat loss from the receiver tube is calculated from the below equation 1:

$$Q_{total} = Q_{cond} + Q_{Conv} + Q_{rad} \quad \text{----------2}$$

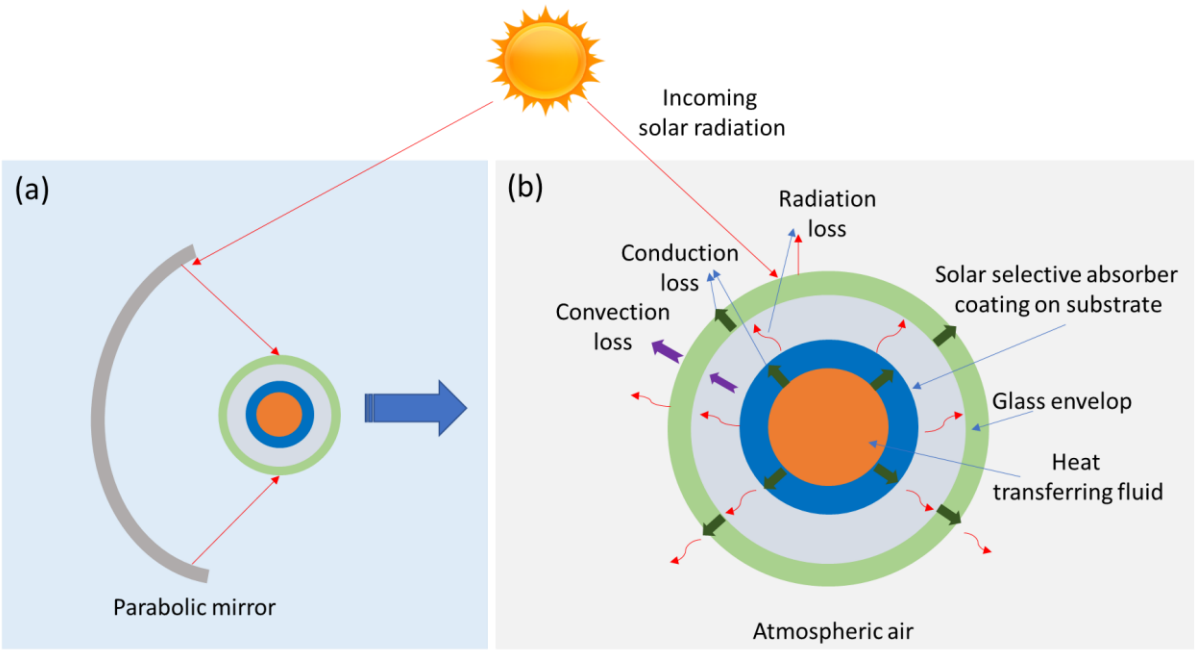

Figure 6.14. (a) Reflection of solar radiation towards the receiver tube by a parabolic mirror, (b) types of heat losses in a receiver tube.

Solar radiation is transmitted through the glass envelope in the receiver tube and reaches the spectral selective absorber coatings to get converted into heat. Further, heat is transferred to HTF by conduction, and HTF gets heated to a certain temperature depending upon the DNI and optical properties of the glass envelope and SSACs. The receiver tube with heated HTF emits the heat in radiation, which accounts for the radiation losses. Further, heat loss also happens through conduction of the receiver, which reaches through convection (via air) to glass envelop, as shown in Figure 6.14. It is essential to notice here that non-evacuated receivers are being used for validation in the present work. Furthermore, heat loss from glass cover to ambient air happens mostly by convection loss and radiation. Here, the heat exchange occurs between the ambient air of the atmosphere and the outer glass surface of the receiver. Hence, the convection heat loss from the glass cover majorly depends on the air temperature, wind flow condition, and glass cover temperature [158–161].

In the present work, to estimate the total heat losses from the receiver, the Therminol 66 is used as HTF, and it is heated up to 200 °C by using an electric heater. The heated HTF is pumped at a constant mass flow rate, i.e., 4 liters per minute (LPM), through the non-evacuated receivers installed in rows 1 and 2 of the PT test rig. The temperature of HTF is recorded by using the temperature sensors located at the inlet and outlet of loops in row 1 and row 2 and data sent to the installed computer to plot the heat loss graph as a function of time and temperature difference. The heat loss of receivers is calculated by using equation 2

$$Q = mC_p\Delta T \qquad \text{----------3}$$

In equation 2, the Q is the heat loss of receivers installed in row 1(East side) or row 2 (Westside), m is the mass flow rate, i.e., is a measurement of the amount of HTF flowing around the loop (4 LPM), C_p is the specific heat capacity of HTF (2.19 kJ/ (kg. K) at 200 °C), and ΔT = T_{outlet} -T_{inlet}. The PT test rig comprises two temperature sensors installed in the east side row and two of them in the west side row to measure the temperature of HTF flowing through the inlet and outlet. The temperature difference of T_{outlet} and T_{inlet} is used for the determination of Q. Figure 6.15 shows the heat loss study of receivers installed in row 1 and row 2.

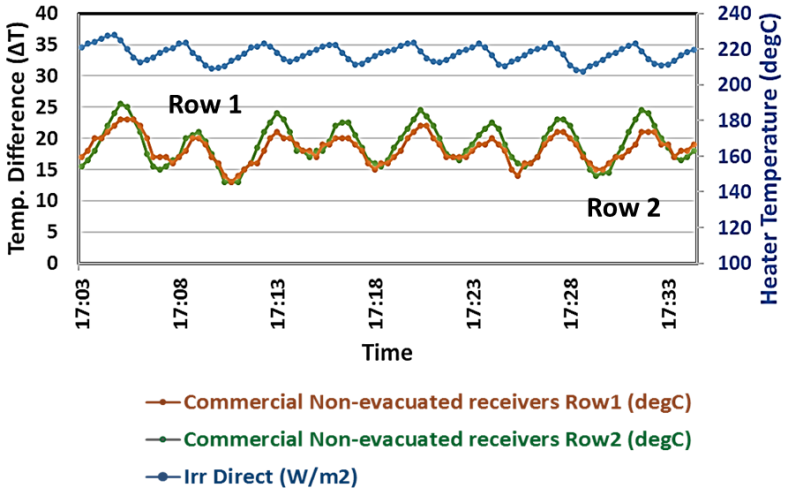

Figure 6.15. Heat loss studies of commercial receivers in row 1 and row 2 at 200 °C.

The heat loss of receivers installed in rows 1 and 2 is calculated as mentioned in equation 2. The heat loss obtained for row 1 is 202 W/m and for row 2 is 194 W/m. The difference in heat loss between receivers installed in row 1 and row 2 is significantly less. Thus, it can be concluded that both rows are ideal in a position to measure the heat losses for the solar receiver components in the PT test rig facility.

6.6.2 Heat gain study

To estimate the heat gain of receivers installed in row 1 and row 2, the HTF (Therminol 66) is pumped through receivers by using a constant mass flow rate of 4 liters per minute. The study is conducted on average from morning 11:00 AM to evening 3:00 PM to obtain the high DNI. The DNI obtained at a test site from morning to evening is varied from 600 to 800 DNI. The installed receiver in both rows absorbs the solar radiation and gets converted into heat. Further, the heat is transferred to the HTF flowing through the receiver at a constant flow rate of HTF. The HTF temperature is recorded using the temperature sensors located at the inlet and outlet of loops in row 1 and row 2, and data is sent to the installed computer to plot the heat gain graph as a function of DNI. The heat gain of receivers is calculated by using equation 3

$$Q = mC_p\Delta T \qquad \text{----------4}$$

where $\Delta T = T_{outlet} - T_{inlet}$. The heat gain graph of receivers as a function of time and DNI is shown in Figure 6.16.

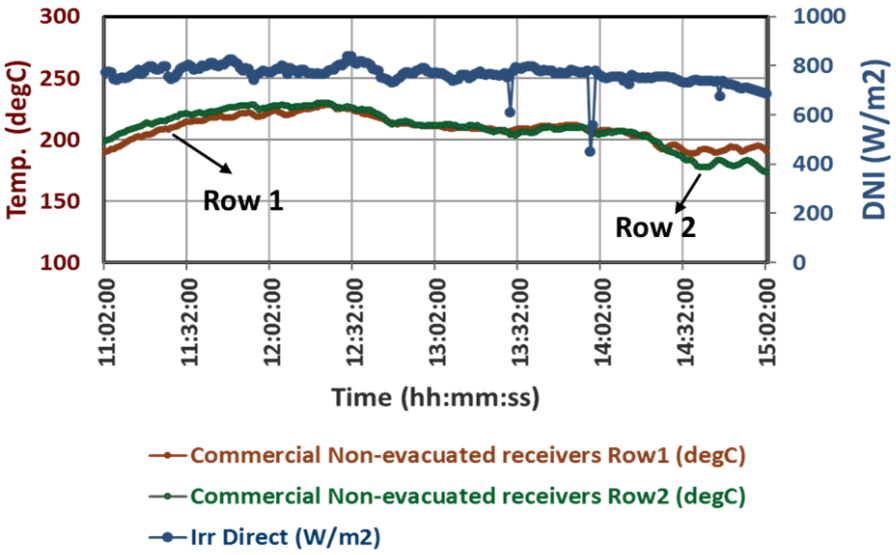

Figure 6.16. Heat gain studies of receivers in row 1 and row 2.

The heat loss is obtained for row 1 is 397 W/m and for row 2 is 407 W/m. The difference in heat gain between receivers installed in row 1 and row 2 is significantly less. Thus, it can be concluded that both rows are ideal in a position to measure the heat gain for the solar receiver components in the PT test rig facility.

6.7 Performance comparison of indigenous receivers and commercial receivers using PT test rig

To estimate the performance comparison of receivers in terms of heat loss and heat gain, the Indigenous 2-m non-evacuated receivers (Section 6.4, Figure 6.10) are installed in row 1 and commercially procured non-evacuated receivers are installed in row 2 of the PT test rig. The heat loss and heat gain studies are conducted as mentioned in section 6.6.1 and 6.6.2, respectively. In sections 6.6.1 and 6.6.2, heat loss and heat gain studies were conducted at a constant HTF temperature and flow condition. Here, the temperature of HTF via heater is varied from 100 °C to 200 °C and flow rate of HTF is kept constant (4 LPM) for both heat loss and heat gain measurements.

6.7.1 Heat loss study:

Heat loss studies at different temperatures such as 100, 150, and 200 °C were conducted to commercial receivers on one row of the test rig and indigenous receivers on another row. The mass flow rate of HTF was kept as a constant (4 LPM). HTF was heated to get the constant temperature with an electrical heater to estimate the heat loss of the receivers at different temperatures and sent to the receivers simultaneously. The tests were performed in the evening time to avoid sun irradiance interference. The test was carried out simultaneously under the same weather conditions. The heat loss is calculated according to equation 3 mentioned in section 6.6.1. The results of the heat loss studies at different temperatures from 100 ° to 200 °C is shown in Figure 6.17 and values are tabulated in Table 6.5.

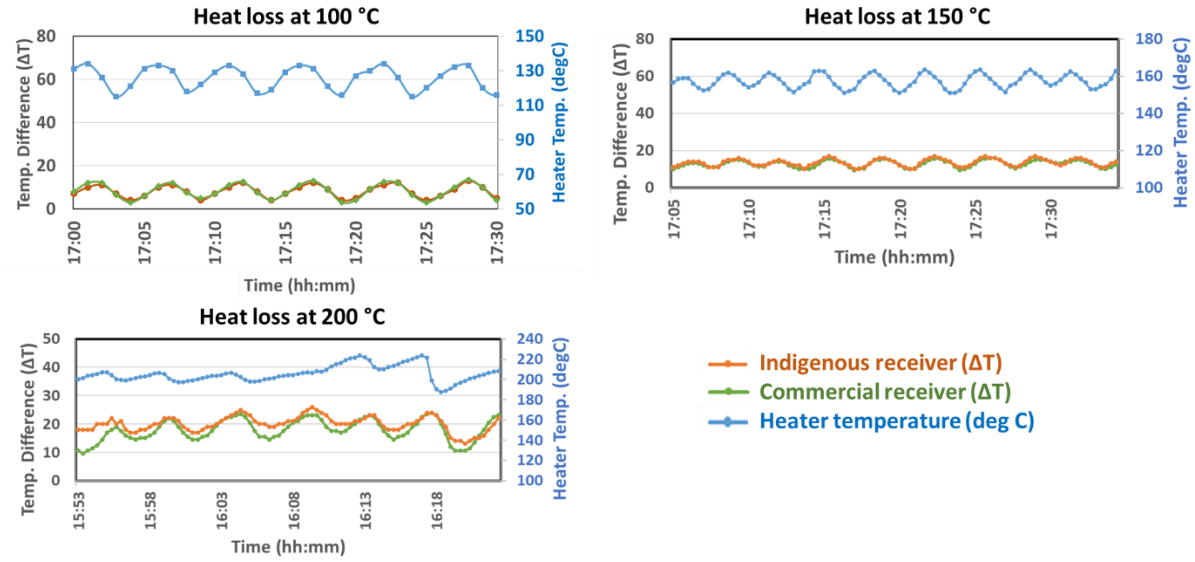

Figure 6.17. Indigenous vs. commercial receiver heat loss studies at temperatures from 100 °C, 150 °C and 200 °C.

From the above Figures 6.17 and Table 6.4, it is clearly observed that the indigenous receiver has high heat loss compared to a commercial non-evacuated receiver at temperatures from 100 °C to 200 °C. The difference in heat loss for both the receivers is in the range of 2 to 8 W/m. It is also observed that with increasing temperature, there is an increment in heat loss. It is due to the rise in the temperature of the receiver increases the thermal conductivity of air surrounding the receiver. When air conductivity increases, heat losses also increase. The main cause for heat loss is also due to the temperature gradient between receiver and surrounding wind velocity at an instant. Therefore, an increase in convective and radiative heat losses from the receiver [162].

Table 6.5. Heat loss values of indigenous and commercial receivers at temperatures from 100 °C, 150 °C and 200 °C.

Heat Loss at different heater temperatures	**Indigenous Receiver (W/m)**	**Commercial Receiver (W/m)**
100 °C	126	124
150 °C	204	198
200 °C	295	287

The receiver's emittance and vacuum pressure are the two parameters that mainly influence a receiver's heat losses [163]. In the present work, in both rows of the PT test rig, non-evacuated

receivers were used. Hence, the difference in the heat loss values for both receivers is due to the different thermal emissivity. The commercial receiver has a thermal emissivity of ≤7% at 200 °C, whereas the indigenous receiver developed with Cu-Mn-Ni-O_x/SiO_2 SSAC exhibits the thermal emissivity of 9% at 200 °C. Thus, the high thermal emissivity of the indigenous receiver leads to high thermal losses at different temperatures compared to the commercial receiver.

Comparison of indigenous receiver with the commercial Schott vaccum receiver

The Schott 4th generation commercial vacuum receiver with length of 4060mm exhibits the heat loss of 70 W/m at 250 °C. The receiver claims to be having thermal emittance of 9.5% [164]. The low heat loss of Schott receiver can be attributed to the its length and enclosure of receiver in a glass tube with vaccum. In case of indigenous receiver developed in the present work has length of 2-m and not enclosed in a vaccum. Enclosing a receiver in a vacuum will decrease the heat loss compared to working in an open-air atmospheric condition.

6.7.2 Heat gain study

Heat gain studies were carried out at a constant (4 LPM) mass flow condition of HTF with installed commercial receivers on one row of the test rig and indigenous receivers on another row. The test was carried out simultaneously with the same weather conditions. The heat gain is calculated according to equation 4 mentioned in section 6.6.2. The results of the heat gain studies presented in the form of a graph in Figure 6.18 and Table 6.6. The heat gain of receivers depends on the DNI, solar absorptance of receivers, and mass flow rate. The maximum heat gain of 553 W/m and 400 W/m is obtained for indigenous and commercial receivers.

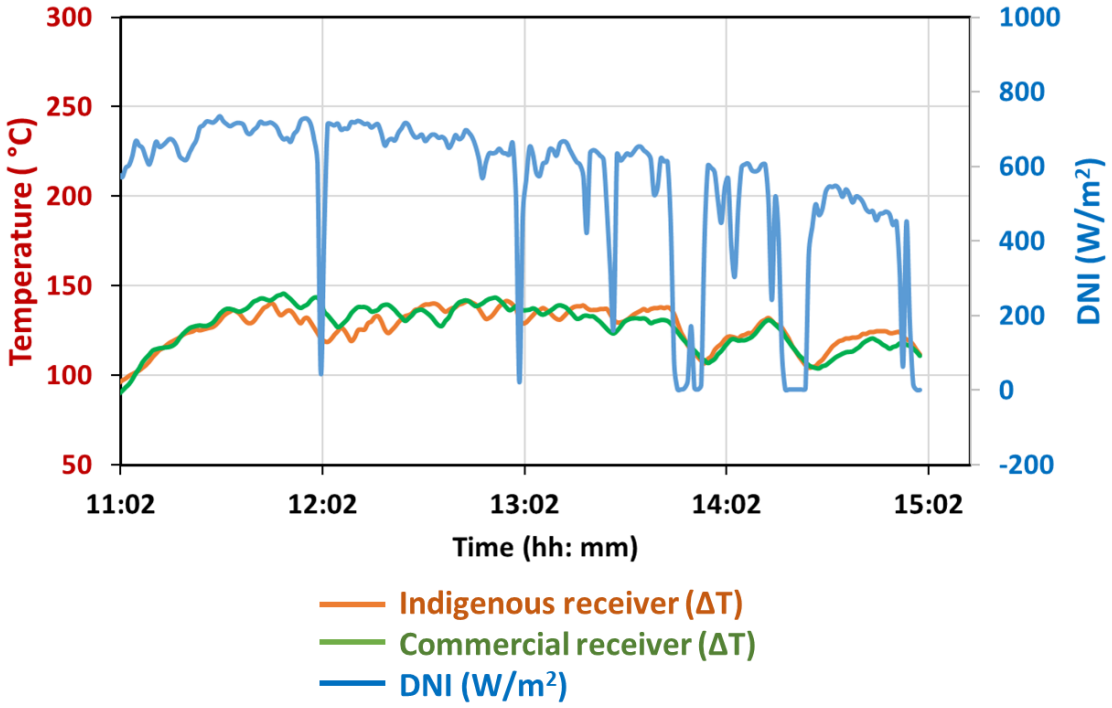

Figure 6.18. Indigenous vs commercial receiver heat gain study.

Table 6.6. Heat gain values of Indigenous and commercial receivers.

Heat gain at 4 LPM of HTF	**Indigenous Receiver (W/m)**	**Commercial Receiver (W/m)**
	553	400

From Figure 6.18 and Table 6.5, it is observed that the indigenous receivers exhibited high heat gain compared to the commercial receivers. Indigenous receivers were developed with Cu-Mn-Ni-O_x/SiO_2 SSAC, which exhibits solar absorptance of ~96%. In addition, the SSAC has a wide-angular absorptance of 96.8% to 95% from 10° to 40°. In the case of commercial receivers, they have a solar absorptance of 95%, and wide-angular absorption studies for coatings were not reported. Thus, the developed indigenous receivers are well-performing in-field condition with a comparison of commercial receivers.

6.8 Conclusion:

In chapter 6, the development of non-evacuated 2-m receiver tubes and a performance comparison study of developed non-evacuated receiver tubes are described in comparison with

a commercial receiver. Initially, 6 litres of Co-Cu-Mn-O_x absorber coating solutions and 6 litres of SiO_2 nanoparticle-based AR coating solutions were synthesised by the wet chemical method at lab scale with the same optimized concentrations. Further, absorber and tandem absorber coatings were successfully developed on 1-m stainless steel tubes (10 Nos.) using the dip-coating method. The optical properties such as solar absorptance of 0.96 and spectral emittance of 0.16 were achieved with good reproducibility. After that, 10 Nos. of 1-m receivers having 42 mm OD were joined by TIG welding with metal flanges and glass tubes to develop 2-m non-evacuated receivers. The indigenous and commercial non-evacuated receivers were installed in the in-house parabolic trough (PT) test rig. The heat loss and heat gain studies were conducted for both receiver's different temperatures and mass flow rates in a PT test rig.

The heat gain studies of both receivers confirmed that the indigenous receivers exhibit good heat gain compared to commercial receivers. Indigenous and commercial receivers exhibited the heat gain of 553 W/m and 400 W/m, respectively. It is due to the high solar absorptance (96%) and good wide-angular solar absorptance of indigenous receivers compared to the commercial receivers (94%). Heat loss study for both receivers confirmed that the indigenous receivers exhibit high heat losses compared to commercial receivers. Indigenous and commercial receivers showed heat losses of 295 W/m and 287 W/m, respectively, at 200 °C heater temperature. The difference in the heat loss, i.e., 8 W/m for indigenous and commercial receivers, can be attributed to the variation of thermal emissivity. The commercial receiver has the thermal emissivity of ≤ 7% at 200 °C, whereas the indigenous receiver developed with Cu-Mn-Ni-O_x/SiO_2 SSAC exhibits the thermal emissivity of 9% at 200 °C. However, the difference in the heat loss (8 W/m) is considered significantly less. Hence, the performance of both receivers in terms of heat loss is considered almost the same. In conclusion, the developed cost-efficient open-air atmospheric stable indigenous receivers have better performance with commercial receivers, making them suitable for medium and high temperature solar thermal applications.

Chapter 7: Conclusions and Future scope

7.1 Conclusions

In the present work, spectrally selective absorber coatings (SSACs) were developed using tri-transition metal precursors for concentrated solar thermal (CST) applications. In contrast to most commercially developed SSACs, facile wet chemical methods were utilized to develop the cost-efficient open-air atmospheric stable SSACs. Several attempts were made to develop SSACs with the best optical properties, good thermal, corrosion resistance, adhesion, and high photothermal efficiency.

Initially, Co-Cu-Mn-O_x/SiO_2 tandem SSAC was successfully developed by using transition metals such as Manganese, Copper, Cobalt, and SiO_2 nanoparticles. Several absorber coating solutions were synthesised by the wet chemical method, and coatings were developed by the dip-coating method on stainless steel (SS 304) substrate. In contrast to several reported articles, tri-transition metals were chosen to obtain good optical properties. After optimizing several process parameters, namely metal concentration and withdrawal speeds, high spectral selective coatings with 0.93 of solar absorptance and 0.19 of spectral emittance were obtained. Further, physicochemical properties of developed materials and coatings were detailly studied and described to understand the nature of developed coatings. Although developed SSACs have good solar absorptance, the spectral emittance and thermal emissivity (0.19 at 500 °C) are found to be high.

An attempt was made to understand the role of the substrate by developing coatings on Molybdenum (Mo) over on glass substrate by the sputtering method instead of SS 304 substrate. To reduce the emittance of SSACs, Mo layer is prepared on a soda-lime glass substrate and applied tri-transition metal absorber and SiO_2 AR layer by using sputtering and wet chemical methods, respectively. The developed tandem absorber (Glass/Mo/Nanocomposite base absorber/SiO_2) exhibited excellent optical properties such as 0.96 of solar absorptance, 0.12 of emittance, and selectivity of 8. However, the objective of the present work is to develop cost-effective SSACs by using wet chemical methods. So, the developed tandem absorber was not considered for further studies. Another attempt was made to incorporate the ZrO_2 nanoparticles in the absorber coating to understand the role in optical properties and thermal stability. Although developed Co-Cu-Mn-O_x + ZrO_2/SiO_2 exhibit, good solar absorptance of 0.97 & high-temperature stability (≤500 °C), thermal emissivity (0.17) is

found to be high. The high thermal emissivity is due to the increased thickness of the tandem absorber (~736 nm).

In the later section, the Cu-Mn-Ni-O_x/SiO_2 tandem SSAC is developed using Nickel, Manganese, and Copper precursors. The metal precursors used for the development of Co-Cu-Mn-O_x SSAC are kept the same. The Cobalt precursor is replaced with the Nickel and developed novel SSACs to obtain the targeted optical properties. The reason for replacing the Cobalt precursor is with Nickel that the cost is relatively high compared to other precursors used. Cu-Mn-Ni-O_x/SiO_2 tandem SSAC was successfully developed with transition metals such as Nickel, Manganese, and Copper using wet chemical and dip-coating methods. Similar to the development of Co-Cu-Mn-O_x/SiO_2 tandem SSAC, process parameters were varied and obtained excellent solar absorptance of 0.95 and a low spectral emittance of 0.15. Further, physicochemical properties of developed materials and coatings were detailly studied and explained to understand the nature of developed coatings.

In the later section, Co-Cu-Mn-O_x/SiO_2 and Cu-Mn-Ni-O_x/SiO_2 SSACs were compared in terms of thermal stability, corrosion rate, adhesion, and wide-angular absorptance. Both SSACs exhibit the same thermal stability up to 500 °C for 250h. However, the Cu-Mn-Ni-O_x/SiO_2 tandem SSAC dominates the Cu-Mn-Ni-O_x/SiO_2 tandem SSAC in terms of high solar absorptance and low thermal losses. Although both SSACs exhibit the same performance in terms of thermal stability, adhesion, the Cu-Mn-Ni-O_x/SiO_2 SSAC shows good optical properties, high corrosion resistance, and high wide-angular solar absorptance. The increased solar absorptance and low thermal emissivity of Cu-Mn-Ni-O_x/SiO_2 SSAC also lead to high photothermal conversion efficiency compared to the Co-Cu-Mn-O_x/SiO_2 SSACs.

Finally, the Cu-Mn-Ni-O_x/SiO_2 SSAC is chosen to upscale from lab scale to prototype level (1-m). After that, multiple Nos. of absorber tubes (10 x 1-m) with good optical properties, excellent adhesion was developed and joined each to the ends to make 2-m absorber tubes (5 x 2-m). Further, metals flanges and glass tubes were joined to the absorber tube ends to develop 2-m length non-evacuated receiver tubes for comparison study with commercially procured non-evacuated receivers using a Parabolic trough test rig. The heat gain studies of both receivers confirmed that the indigenous receivers exhibit good heat gain compared to commercial receivers. Indigenous and commercial receivers showed the heat gain of 553 W/m and 401 W/m, respectively. It is due to the high solar absorptance (96%) and wide-angular absorption nature of indigenous receivers compared to the commercial receivers (94%). The

heat loss studies of both receivers confirmed that the indigenous receivers exhibit slightly high heat losses compared to commercial receivers. Indigenous and commercial receivers showed heat losses of 295 W/m and 287 W/m, respectively, at a 200 °C heater temperature. The heat loss of 295 W/m for the indigenous receivers can be attributed to the Cu-Mn-Ni-O_x spinel layer developed by wet chemical and dip-coating methods. The developed cost-efficient, open-air atmospheric stable indigenous receivers have good performance in heat gain and are slightly higher in heat loss than commercial receivers. Hence, it is a promising candidate suitable for medium and high temperature solar thermal applications.

7.2 Future scope

In the current thesis, high spectral selective and open-air atmospheric stable coatings are developed on SS 304 substrate using low-cost wet chemical and dip-coating methods. The SSACs are upscaled successfully to develop non-evacuated receivers and found to be on par with the commercial non-evacuated receivers in heat loss and heat gain performance using a parabolic trough test rig. In this regard, the reported Co-Cu-Mn-O_x and Cu-Mn-Ni-O_x spinel structured materials in the current research have tremendous stability up to 800 °C. However, both SSACs developed with spinel structured materials on SS 304 substrate were tested only at 500 °C for 250-hours and found out to be very stable without degradation. The thermal cycle test can be conducted for long hours at 500 °C to estimate full potential of developed SSAC in terms of thermal stability. At temperatures greater than 500 °C, SSACs tend to be degrading interms of optical properties. It is due to degradation on SS 304 in open-air atmospheric conditions. The temperature stability of SSACs can be improved by replacing the stable metal or alloy substrates such as Inconel or others. This indicates that the SSACs developed with the reported spinels on high temperature stable substrates have a tremendous potential to fulfil the necessity of SSACs for CST systems. Further research towards replacing the stable substrate also leads to high photothermal conversion efficiency for robust solar thermal systems. The temperature stability of SSACs can also be improved by developing a diffusion barrier layer in between the substrate and absorber layer without affecting the optical properties and adhesion. In addition, the corrosion resistant of developed SSACs found to be low in comparison with the reported literature based on vapor deposition methods. The preparation and optimization of oxidation resistant layer over on tandem absorber can limit the reaction with environment and may lead to high corrosion resistance.

Recently, high-temperature falling particle receivers have attracted tremendous research attention due to their high operating temperatures, efficiency and lowering the energy storage

costs for concentrating solar power applications. The solid particles in the falling particle receiver absorb the concentrated sunlight to store the heat and transfer it to the working fluid for the power cycle. Thus, extensive research has been developing cost-effective solid particles with excellent solar absorption, high thermal stability, high heat capacity, high thermal conductivity, and high density. Thus, the extension of the present work on developing spinel structured solid particles can be a good candidate as they exhibit excellent absorption and thermal stability for the high-temperature falling particle receiver applications.

References

[1] Key World Energy Statistics 2020, (2020).

[2] J.A. Duffie, W.A. Beckman, Wiley: Solar Engineering of Thermal Processes, 4th Edition - John A. Duffie, William A. Beckman, 2013. http://eu.wiley.com/WileyCDA/WileyTitle/productCd-0470873663.html.

[3] A. Mass, Z. Solar, I. Tables, Standard Tables for References Solar Spectral Irradiance at Air Mass 1 . 5 : Direct Normal and Hemispherical for a 37 ° Tilted Surface 1, (2020) 1–10.

[4] India' s CST Sector - Vision 2022, (n.d.).

[5] G. Climate, E. Project, Global Climate & Energy Project An Assessment of Solar Energy Conversion Technologies and Research Opportunities, Assessment. (2006) 1–20.

[6] J. Ramanujam, D.M. Bishop, T.K. Todorov, J. Rath, R. Nekovei, E. Artegiani, A. Romeo, Flexible CIGS , CdTe and a-Si : H based thin film solar cells : A review, Progress in Materials Science. (2019) 100619. https://doi.org/10.1016/j.pmatsci.2019.100619.

[7] best-research-cell-efficiencies.20200104.pdf, (n.d.).

[8] R. Summary, Research opportunities to advance solar energy utilization, 351 (2016). https://doi.org/10.1126/science.aad1920.22.

[9] S. Bannur, Concentrated solar power in India: Current status, challenges and future outlook, Current Science. 115 (2018) 222–227. https://doi.org/10.18520/cs/v115/i2/222-227.

[10] Energy Sector Management Assistance Program: The World Bank, Development of Local Supply Chain: The Missing Link for Concentrated Solar Power Projects in India, (2013).

[11] H. Tabor, Selective Radiation I. Wavelength Discrimination, Bull. Res. Counc. of Isr. Sect. A: Chem. 5 (1956) 119–128.

[12] H. Tabor, Selective Radiation II. Wavelength Discrimination, Bull. Res. Counc. of Isr.

Sect. A: Chem. 5 (1954) 129–134.

[13] L.A. Weinstein, J. Loomis, B. Bhatia, D.M. Bierman, E.N. Wang, G. Chen, Concentrating Solar Power, Chemical Reviews. 115 (2015) 12797–12838. https://doi.org/10.1021/acs.chemrev.5b00397.

[14] C. Suresh, Review on solar thermal energy storage technologies and their geometrical configurations, (2020) 1–33. https://doi.org/10.1002/er.5143.

[15] A. Dan, H.C. Barshilia, K. Chattopadhyay, B. Basu, Solar energy absorption mediated by surface plasma polaritons in spectrally selective dielectric-metal-dielectric coatings: A critical review, Renewable and Sustainable Energy Reviews. 79 (2017) 1050–1077. https://doi.org/10.1016/j.rser.2017.05.062.

[16] C.E. Kennedy, Review of Mid- to High-Temperature Solar Selective Absorber Materials, 2002. https://doi.org/10.2172/15000706.

[17] M. Bello, S. Shanmugan, Achievements in mid and high-temperature selective absorber coatings by physical vapor deposition (PVD) for solar thermal Application-A review, Journal of Alloys and Compounds. 839 (2020) 155510. https://doi.org/10.1016/j.jallcom.2020.155510.

[18] N. Selvakumar, H.C. Barshilia, Review of physical vapor deposited (PVD) spectrally selective coatings for mid- and high-temperature solar thermal applications, Solar Energy Materials and Solar Cells. 98 (2012) 1–23. https://doi.org/10.1016/j.solmat.2011.10.028.

[19] R.K. P, U. Basavaraju, H.C. Barshilia, B. Basu, Solar Energy Materials and Solar Cells On the origin of spectrally selective high solar absorptance of TiB 2 -based tandem absorber with double layer antireflection coatings, Solar Energy Materials and Solar Cells. 220 (2021) 110839. https://doi.org/10.1016/j.solmat.2020.110839.

[20] Y. Zhu, C. Shen, J. Li, L. Zhong, X. Xu, X. Xiao, Superhydrophobic polytetrafluoroethylene film deposited on solar selective absorber by electron beam evaporation, Materials Chemistry and Physics. 257 (2021) 123828. https://doi.org/10.1016/j.matchemphys.2020.123828.

[21] C. Zou, W. Xie, L. Shao, Solar Energy Materials & Solar Cells Functional multi-layer solar spectral selective absorbing coatings of AlCrSiN / AlCrSiON / AlCrO for high temperature applications, Solar Energy Materials and Solar Cells. 153 (2016) 9–17. https://doi.org/10.1016/j.solmat.2016.04.007.

[22] B. Chen, D. Yang, P.A. Charpentier, S. Nikumb, Solar Energy Materials & Solar Cells Optical and structural properties of pulsed laser deposited Ti : Al_2O_3 thin films, 92 (2008) 1025–1029. https://doi.org/10.1016/j.solmat.2008.03.004.

[23] Y. Li, C. Lin, D. Zhou, Y. An, D. Li, C. Chi, H. Huang, S. Yang, C.Y. Tso, C.Y.H. Chao, B. Huang, Scalable all-ceramic nanofilms as highly efficient and thermally stable selective solar absorbers, Nano Energy. (2019) 103947.

https://doi.org/10.1016/j.nanoen.2019.103947.

[24] A. Soum-glaude, I. Bousquet, L. Thomas, G. Flamant, Solar Energy Materials & Solar Cells Optical modeling of multilayered coatings based on SiC(N)H materials for their potential use as high-temperature solar selective absorbers, Solar Energy Materials and Solar Cells. 117 (2013) 315–323. https://doi.org/10.1016/j.solmat.2013.06.030.

[25] A. Schüler, J. Geng, P. Oelhafen, S. Brunold, P. Gantenbein, U. Frei, Application of titanium containing amorphous hydrogenated carbon films (a-C:H/Ti) as optical selective solar absorber coatings, Solar Energy Materials and Solar Cells. 60 (2000) 295–307. https://doi.org/https://doi.org/10.1016/S0927-0248(99)00074-4.

[26] A. Schüler, I. Videnovic, P. Oelhafen, S. Brunold, Titanium-containing amorphous hydrogenated silicon carbon films (a-Si:C:H/Ti) for durable solar absorber coatings, Solar Energy Materials and Solar Cells. 69 (2001) 271–284. https://doi.org/10.1016/S0927-0248(00)00396-2.

[27] D.M. Herrera-Zamora, F.I. Lizama-Tzec, I. Santos-González, R.A. Rodríguez-Carvajal, O. García-Valladares, O. Arés-Muzio, G. Oskam, Electrodeposited black cobalt selective coatings for application in solar thermal collectors: Fabrication, characterization, and stability, Solar Energy. 207 (2020) 1132–1145. https://doi.org/10.1016/j.solener.2020.07.042.

[28] F. Cao, K. McEnaney, G. Chen, Z. Ren, A review of cermet-based spectrally selective solar absorbers, Energy and Environmental Science. 7 (2014) 1615–1627. https://doi.org/10.1039/c3ee43825b.

[29] D. Ding, W. Cai, M. Long, H. Wu, Y. Wu, Optical, structural and thermal characteristics of Cu–CuAl2O4 hybrids deposited in anodic aluminum oxide as selective solar absorber, Solar Energy Materials and Solar Cells. 94 (2010) 1578–1581. https://doi.org/10.1016/j.solmat.2010.04.075.

[30] A. Karoro, Z.Y. Nuru, L. Kotsedi, K. Bouziane, B.M. Mothudi, M. Maaza, Laser nanostructured Co nanocylinders-Al 2 O 3 cermets for enhanced & flexible solar selective absorbers applications, Applied Surface Science. 347 (2015) 679–684. https://doi.org/10.1016/j.apsusc.2015.04.098.

[31] R. Kumar, A.K. Saha, B. Usmani, A. Dixit, ScienceDirect Optimization and structure-property correlation of black chrome solar selective coating on Copper and Nickel plated copper substrates, Materials Today: Proceedings. 5 (2018) 23423–23427. https://doi.org/10.1016/j.matpr.2018.11.082.

[32] F.I. Lizama-tzec, D.M. Herrera-zamora, O. Arés-muzio, V.H. Gómez-espinoza, Electrodeposition of selective coatings based on black nickel for flat-plate solar water heaters, Solar Energy. 194 (2019) 302–310. https://doi.org/10.1016/j.solener.2019.10.066.

[33] K. Xu, M. Du, L. Hao, J. Mi, Q. Yu, S. Li, A review of high-temperature selective absorbing coatings for solar thermal applications, Journal of Materiomics. 6 (2020) 167–

182. https://doi.org/10.1016/j.jmat.2019.12.012.

[34] R.R. Chamberlin, J.S. Skarman, Chemical Spray Deposition Process for Inorganic Films, Journal of The Electrochemical Society. 113 (1966) 86. https://doi.org/10.1149/1.2423871.

[35] M. Madhusudan, H.K. Sehgal, Nickel sulphide-lead sulphide and nickel sulphide-cadmium sulphide selective coatings for solar thermal conversion, Energy Conversion and Management. 21 (1981) 199–204. https://doi.org/https://doi.org/10.1016/0196-8904(81)90015-7.

[36] K. Chidambaram, L.K. Malhotra, K.L. Chopra, Spray-pyrolysed cobalt black as a high temperature selective absorber, Thin Solid Films. 87 (1982) 365–371. https://doi.org/https://doi.org/10.1016/0040-6090(82)90289-9.

[37] E. Ienei, L. Isac, C. Cazan, A. Duta, Characterization of $Al/Al_2O_3/NiO_x$ solar absorber obtained by spray pyrolysis, Solid State Sciences. 12 (2010) 1894–1897. https://doi.org/10.1016/j.solidstatesciences.2010.05.028.

[38] L. Cindrella, S. Prabhu, CuO-PANI nanostructure with tunable spectral selectivity for solar selective coating application, Applied Surface Science. 378 (2016) 245–252. https://doi.org/10.1016/j.apsusc.2016.03.134.

[39] J.A. Phys, Effect of surface roughness on the solar photothermal conversion efficiency of spray- coated CuCo 2 O 4 films Effect of surface roughness on the solar photothermal conversion efficiency of spray-coated $CuCo_2O_4$ films, 145303 (2020). https://doi.org/10.1063/1.5143348.

[40] K. Zhang, L. Hao, M. Du, J. Mi, J.N. Wang, J. ping Meng, A review on thermal stability and high temperature induced ageing mechanisms of solar absorber coatings, Renewable and Sustainable Energy Reviews. 67 (2017) 1282–1299. https://doi.org/10.1016/j.rser.2016.09.083.

[41] C.E. Kennedy, Review of Mid- to High-Temperature Solar Selective Absorber Materials, 2002. https://doi.org/10.2172/15000706.

[42] Sol-Gel_Science_The_physics_and_chemistry_of_sol-gel_processing_-_Brinker_1990.pdf, (n.d.).

[43] C.J. Brinker, A. Hurd, C.J. Brinker, A. Hurd, J. De Physique, Fundamentals of sol-gel dip-coating To cite this version : HAL Id : jpa-00249179, 4 (1994) 1231–1242.

[44] Z. Jiang, Developments in the synthesis of flat plate solar selective absorber materials via sol – gel methods : A review, (2014). https://doi.org/10.1016/j.rser.2014.04.062.

[45] R. Bayón, G. San Vicente, Á. Morales, Durability tests and up-scaling of selective absorbers based on copper–manganese oxide deposited by dip-coating, Solar Energy Materials and Solar Cells. 94 (2010) 998–1004. https://doi.org/https://doi.org/10.1016/j.solmat.2010.02.006.

[46] T. Boström, E. Wäckelgård, G. Westin, Solution-chemical derived nickel-alumina coatings for thermal solar absorbers, Solar Energy. 74 (2003) 497–503. https://doi.org/10.1016/S0038-092X(03)00199-3.

[47] L. Landau, B. Levich, Dragging of a Liquid by a Moving Plate, Dynamics of Curved Fronts. XVII (1988) 141–153. https://doi.org/10.1016/b978-0-08-092523-3.50016-2.

[48] H.C. Hottel, T.A. Unger, 2 The properties of a copper oxidealuminum selective black surface absorber of solar energy, Solar Energy. 3 (1959) 10–15. https://doi.org/10.1016/0038-092X(59)90134-3.

[49] E. Barrera-Calva, J. Mendez-Vivar, M. Ortega-Lopez, L. Huerta-Arcos, J. Morales-Corona, R. Olayo-Gonzalez, Silica-copper oxide composite thin films as solar selective coatings prepared by dipping sol gel, Advances in Materials Science and Engineering. 2008 (2008). https://doi.org/10.1155/2008/190920.

[50] C. Choudhury, H.K. Sehgal, Black cobalt selective coatings by spray pyrolysis for photothermal conversion of solar energy, Solar Energy. 28 (1982) 25–31. https://doi.org/10.1016/0038-092X(82)90220-1.

[51] K. Chidambaram, L.K. Malhotra, K.L. Chopra, Spray-pyrolysed cobalt black as a high temperature selective absorber, Thin Solid Films. 87 (1982) 365–371. https://doi.org/10.1016/0040-6090(82)90289-9.

[52] C.S. Uma, L.K. Malhotra, K.L. Chopra, Cobalt oxide-iron oxide selective coatings for high temperature applications, Bulletin of Materials Science. 8 (1986) 385–389. https://doi.org/10.1007/BF02744150.

[53] A. Avila G., E. Barrera C., L. Huerta A., S. Muhl, Cobalt oxide films for solar selective surfaces, obtained by spray pyrolisis, Solar Energy Materials and Solar Cells. 82 (2004) 269–278. https://doi.org/10.1016/j.solmat.2004.01.024.

[54] K.J. Cathro, Preparation of cobalt-oxide-based selective surfaces by a dip-coating process, Solar Energy Materials. 9 (1984) 433–447. https://doi.org/10.1016/0165-1633(84)90017-0.

[55] E.C. Barrera, T.G. Viveros, U. Morales, Preparation of selective surfaces of black cobalt by the sol-gel process, Renewable Energy. 9 (1996) 733–736. https://doi.org/https://doi.org/10.1016/0960-1481(96)88388-1.

[56] E. Barrera, L. Huerta, S. Muhl, A. Avila, Synthesis of black cobalt and tin oxide films by the sol – gel process : surface and optical properties, 88 (2005) 179–186. https://doi.org/10.1016/j.solmat.2004.03.010.

[57] A.I.N. Press, Optimization of a solution-chemically derived solar absorbing spectrally selective surface, 91 (2007) 38–43. https://doi.org/10.1016/j.solmat.2006.07.002.

[58] J. Jensen, S. Valizadeh, G. Westin, E. Wa, Solar Energy Materials & Solar Cells ERDA of Ni – Al 2 O 3 / SiO 2 solar thermal selective absorbers, 92 (2008) 1177–1182. https://doi.org/10.1016/j.solmat.2008.02.014.

[59] G. Katumba, L. Olumekor, A. Forbes, G. Makiwa, B. Mwakikunga, J. Lu, E. Wa, Solar Energy Materials & Solar Cells Optical , thermal and structural characteristics of carbon nanoparticles embedded in ZnO and NiO as selective solar absorbers, 92 (2008) 1285–1292. https://doi.org/10.1016/j.solmat.2008.04.023.

[60] X. Wang, H. Li, X. Yu, X. Shi, J. Liu, X. Wang, H. Li, X. Yu, X. Shi, J. Liu, selective solar thermal absorbers, 203109 (2012) 1–6. https://doi.org/10.1063/1.4766730.

[61] K.T. Roro, N. Tile, B. Mwakikunga, B. Yalisi, A. Forbes, Solar absorption and thermal emission properties of multiwall carbon nanotube / nickel oxide nanocomposite thin films synthesized by sol – gel process, Materials Science & Engineering B. 177 (2012) 581–587. https://doi.org/10.1016/j.mseb.2012.03.017.

[62] Q. Zhao, Z. Yan, C. Chen, J. Chen, Spinels: Controlled Preparation, Oxygen Reduction/Evolution Reaction Application, and beyond, Chemical Reviews. 117 (2017) 10121–10211. https://doi.org/10.1021/acs.chemrev.7b00051.

[63] W.H. BRAGG, The Structure of Magnetite and the Spinels, Nature. 95 (1915) 561. https://doi.org/10.1038/095561a0.

[64] K.E. Sickafus, J.M. Wills, N.W. Grimes, Structure of spinel, Journal of the American Ceramic Society. 82 (1999) 3279–3292. https://doi.org/10.1111/j.1151-2916.1999.tb02241.x.

[65] R.J. Hill, J.R. Craig, G. V Gibbs, Systematics of the spinel structure type, Physics and Chemistry of Minerals. 4 (1979) 317–339. https://doi.org/10.1007/BF00307535.

[66] L. Kaluža, A. Šurca-Vuk, B. Orel, G. Dražič, P. Pelicon, Structural and IR spectroscopic analysis of sol-gel processed CuFeMnO4 spinel and $CuFeMnO_4$/silica films for solar absorbers, Journal of Sol-Gel Science and Technology. 20 (2001) 61–83. https://doi.org/10.1023/A:1008728717617.

[67] L.Kaluza, B.OrelL, G.Drazic, M.Kohl, Sol – gel derived $CuCoMnO_x$ spinel coatings for solar absorbers : Structural and optical properties, Solar Energy Materials & Solar Cell. 70 (2001) 187–201. https://doi.org/10.1016/S0927-0248(01)00024-1.

[68] J. Vince, A. Šurca Vuk, U. Opara Krašovec, B. Orel, M. Köhl, M. Heck, Solar absorber coatings based on CoCuMnOx spinels prepared via the sol-gel process: Structural and optical properties, Solar Energy Materials and Solar Cells. 79 (2003) 313–330. https://doi.org/10.1016/S0927-0248(02)00457-9.

[69] M. Joly, Y. Antonetti, M. Python, M. Gonzalez, T. Gascou, J.L. Scartezzini, A. Schüler, Novel black selective coating for tubular solar absorbers based on a sol-gel method, Solar Energy. 94 (2013) 233–239. https://doi.org/10.1016/j.solener.2013.05.009.

[70] D. Tulchinsky, V. Uvarov, I. Popov, D. Mandler, S. Magdassi, A novel non-selective coating material for solar thermal potential application formed by reaction between sol-gel titania and copper manganese spinel, Solar Energy Materials and Solar Cells. 120 (2014) 23–29. https://doi.org/10.1016/j.solmat.2013.08.004.

[71] R. Bayón, G. San Vicente, C. Maffiotte, Á. Morales, Preparation of selective absorbers based on CuMn spinels by dip-coating method, Renewable Energy. 33 (2008) 348–353. https://doi.org/10.1016/j.renene.2007.05.017.

[72] R. Bayón, G. San Vicente, C. Maffiotte, Á. Morales, Characterization of copper-manganese-oxide thin films deposited by dip-coating, Solar Energy Materials and Solar Cells. 92 (2008) 1211–1216. https://doi.org/10.1016/j.solmat.2008.04.011.

[73] A. Amri, Z.T. Jiang, T. Pryor, C.Y. Yin, Z. Xie, N. Mondinos, Optical and mechanical characterization of novel cobalt-based metal oxide thin films synthesized using sol-gel dip-coating method, Surface and Coatings Technology. 207 (2012) 367–374. https://doi.org/10.1016/j.surfcoat.2012.07.028.

[74] A. Amri, X. Duan, C.Y. Yin, Z.T. Jiang, M.M. Rahman, T. Pryor, Solar absorptance of copper-cobalt oxide thin film coatings with nano-size, grain-like morphology: Optimization and synchrotron radiation XPS studies, Applied Surface Science. 275 (2013) 127–135. https://doi.org/10.1016/j.apsusc.2013.01.081.

[75] A. Amri, Z. Jiang, X. Zhao, Z. Xie, C. Yin, N. Ali, N. Mondinos, M.M. Rahman, D. Habibi, Surface & Coatings Technology Tailoring the physicochemical and mechanical properties of optical copper – cobalt oxide thin fi lms through annealing treatment, Surface & Coatings Technology. 239 (2014) 212–221. https://doi.org/10.1016/j.surfcoat.2013.11.044.

[76] S.R. Atchuta, S. Sakthivel, H.C. Barshilia, Transition metal based $Cu_xNi_yCo_{z-x-y}O_4$ spinel composite solar selective absorber coatings for concentrated solar thermal applications, Solar Energy Materials and Solar Cells. 189 (2019) 226–232. https://doi.org/10.1016/j.solmat.2018.09.033.

[77] S.R. Atchuta, S. Sakthivel, H.C. Barshilia, Nickel doped cobaltite spinel as a solar selective absorber coating for efficient photothermal conversion with a low thermal radiative loss at high operating temperatures, Solar Energy Materials and Solar Cells. 200 (2019) 109917. https://doi.org/10.1016/j.solmat.2019.109917.

[78] S.R. Atchuta, S. Sakthivel, H.C. Barshilia, Selective properties of high-temperature stable spinel absorber coatings for concentrated solar thermal application, Solar Energy. 199 (2020) 453–459. https://doi.org/10.1016/j.solener.2020.02.048.

[79] F. Cao, K. McEnaney, G. Chen, Z. Ren, A review of cermet-based spectrally selective solar absorbers, Energy & Environmental Science. 7 (2014) 1615. https://doi.org/10.1039/c3ee43825b.

[80] H.K. Raut, V.A. Ganesh, A.S. Nair, S. Ramakrishna, Anti-reflective coatings: A critical, in-depth review, Energy and Environmental Science. 4 (2011) 3779–3804. https://doi.org/10.1039/c1ee01297e.

[81] S. Methods, MATERIALS Introduction to Microscopic, n.d.

[82] E.G. Gauglitz, Handbook of Spectroscopy Near-Infrared Spectroscopy Handbook of

Analytical Techniques In-situ Spectroscopy in Heterogeneous Catalysis, 2003.

[83] A. Srinivasa Rao, S. Sakthivel, A highly thermally stable Mn–Cu–Fe composite oxide based solar selective absorber layer with low thermal loss at high temperature, Journal of Alloys and Compounds. 644 (2015) 906–915. https://doi.org/10.1016/j.jallcom.2015.05.038.

[84] C.E. Kennedy, Progress To Develop an Advanced Solar-Selective Coating, Renewable Energy. (2008) 4–7.

[85] A. Ambrosini, T.N. Lambert, A. Boubault, A. Hunt, J. Davis, D. Adams, A.C. Hall, Thermal Stability of Oxide-Based Solar Selective Coatings for CSP Central Receivers, (2016) 1–10.

[86] C.K. Ho, A.R. Mahoney, T.N. Lambert, Characterization of Pyromark 2500 Paint for High-Temperature Solar Receivers, 136 (2016) 2014–2017. https://doi.org/10.1115/1.4024031.

[87] C. Suryanarayana, M.G. Norton, X-Ray Diffraction: A Practical Approach, Springer US, 2013. https://books.google.co.in/books?id=RRfrBwAAQBAJ.

[88] D. Briggs, X-ray photoelectron spectroscopy (XPS), Handbook of Adhesion: Second Edition. (2005) 621–622. https://doi.org/10.1002/0470014229.ch22.

[89] M. Feist, Thermal analysis: basics, applications, and benefit, ChemTexts. 1 (2015) 1–12. https://doi.org/10.1007/s40828-015-0008-y.

[90] N. Brodusch, APPLIED SCIENCES AND TECHNOLOGY Field Emission Scanning Electron Microscopy New Perspectives for Materials Characterization, n.d.

[91] I.S. Lyal'ko, V.N. Kaplichnyi, E.A. Shulyak, V.S. Gurin, E.A. Shapovalov, V.T. Savukov, P.A. Stoyanov, Em-125 Transmission Electron Microscope., Bulletin of the Academy of Sciences of the U.S.S.R. Physical Series. 47 (1981) 13–15.

[92] M. Tosa, Surface Profilometer, in: T.S.S.S. of Japan (Ed.), Compendium of Surface and Interface Analysis, Springer Singapore, Singapore, 2018: pp. 679–682. https://doi.org/10.1007/978-981-10-6156-1_110.

[93] H.G. Tompkins, E.A. Irene, Handbook of Ellipsometry, 2005. https://doi.org/10.1515/arh-2005-0022.

[94] D. Karthik, S. Pendse, S. Sakthivel, E. Ramasamy, S.V. Joshi, High performance broad band antireflective coatings using a facile synthesis of ink-bottle mesoporous MgF_2 nanoparticles for solar applications, Solar Energy Materials and Solar Cells. 159 (2017) 204–211. https://doi.org/10.1016/j.solmat.2016.08.007.

[95] M. Joly, Y. Antonetti, M. Python, M. Gonzalez, T. Gascou, J.L. Scartezzini, A. Schüler, Novel black selective coating for tubular solar absorbers based on a sol-gel method, Solar Energy. 94 (2013) 233–239. https://doi.org/10.1016/j.solener.2013.05.009.

[96] B. Usmani, A. Dixit, Impact of corrosion on microstructure and mechanical properties

of ZrOx/ZrC-ZrN/Zr absorber–reflector tandem solar selective structures, Solar Energy Materials and Solar Cells. 157 (2016) 733–741. https://doi.org/10.1016/j.solmat.2016.07.019.

[97] Q.F. Geng, X. Zhao, X.H. Gao, G. Liu, Sol-gel combustion-derived $CoCuMnO_x$ spinels as pigment for spectrally selective paints, Journal of the American Ceramic Society. 94 (2011) 827–832. https://doi.org/10.1111/j.1551-2916.2010.04182.x.

[98] M. Farchado, J.M. Rodríguez, G. San Vicente, N. Germán, A. Morales, Optical parameters of a novel competitive selective absorber for low temperature solar thermal applications, Solar Energy Materials and Solar Cells. 178 (2018) 234–239. https://doi.org/10.1016/j.solmat.2018.01.031.

[99] F.S. Alencastro, B.S. Archanjo, J.R. Araujo, M.E. Mendoza, R.A. Simao, E ff ect of HMVF and LMVF layers thickness and annealing on the optical properties of Ti-Si-O-N films for mid-temperature solar thermal absorbers, Solar Energy. 189 (2019) 318–324. https://doi.org/10.1016/j.solener.2019.07.084.

[100] S. Wu, C.-H. Cheng, Y.-J. Hsiao, R.-C. Juang, W.-F. Wen, Fe_2O_3 films on stainless steel for solar absorbers, Renewable and Sustainable Energy Reviews. 58 (2016) 574–580. https://doi.org/https://doi.org/10.1016/j.rser.2015.12.263.

[101] F. Cao, D. Kraemer, T. Sun, Y. Lan, G. Chen, Z. Ren, Enhanced thermal stability of W-Ni-Al_2O_3 Cermet-based spectrally selective solar absorbers with tungsten infrared reflectors, Advanced Energy Materials. 5 (2015) 1–7. https://doi.org/10.1002/aenm.201401042.

[102] S. Thota, A. Kumar, J. Kumar, Optical, electrical and magnetic properties of Co_3O_4 nanocrystallites obtained by thermal decomposition of sol-gel derived oxalates, Materials Science and Engineering B: Solid-State Materials for Advanced Technology. 164 (2009) 30–37. https://doi.org/10.1016/j.mseb.2009.06.002.

[103] J. Cheng, C. Wang, W. Wang, X. Du, Y. Liu, Y. Xue, T. Wang, B. Chen, Improvement of thermal stability in the solar selective absorbing Mo-Al_2O_3 coating, Solar Energy Materials and Solar Cells. 109 (2013) 204–208. https://doi.org/10.1016/j.solmat.2012.11.010.

[104] R. Amadelli, L. Samiolo, M. Andrea, A. Molinari, V. Mario, D. Gazzoli, Preparation, Characterisation, and Photocatalytic Behaviour of Co-TiO_2 with Visible Light Response, International Journal of Photoenergy. 2008 (2008). https://doi.org/10.1155/2008/853753.

[105] J.L. Gautier, E. Trollund, E. Ríos, P. Nkeng, G. Poillerat, Characterization of thin $CuCo_2O_4$ films prepared by chemical spray pyrolysis. Study of their electrochemical stability by ex situ spectroscopic analysis, Journal of Electroanalytical Chemistry. 428 (1997) 47–56. https://doi.org/https://doi.org/10.1016/S0022-0728(96)05072-3.

[106] X. Feng, D.F. Cox, AC PT US CR, Surface Science. (2018). https://doi.org/10.1016/j.susc.2018.04.022.

[107] Y. Xue, C. Wang, Y. Sun, Y. Wu, Y. Ning, W. Wang, Effects of the LMVF and HMVF absorption layer thickness and metal volume fraction on optical properties of the $MoSi_2$-Al_2O_3 solar selective absorbing coating, Vacuum. 104 (2014) 116–121. https://doi.org/10.1016/j.vacuum.2014.01.022.

[108] X. He, Y. Li, L. Wang, Y. Sun, S. Zhang, High emissivity coatings for high temperature application: Progress and prospect, Thin Solid Films. 517 (2009) 5120–5129. https://doi.org/10.1016/j.tsf.2009.03.175.

[109] D.B. Mahadik, S. Gujjar, G.M. Gouda, H.C. Barshilia, Double layer SiO_2 /Al_2O_3 high emissivity coatings on stainless steel substrates using simple spray deposition system, Applied Surface Science. 299 (2014) 6–11. https://doi.org/10.1016/j.apsusc.2014.01.159.

[110] K.W. Chien, H.P.D. Shieh, H. Cornelissen, Polarized backlight based on selective total internal reflection at microgrooves, Applied Optics. 43 (2004) 4672–4676. https://doi.org/10.1364/AO.43.004672.

[111] A. Thelen, Design of optical interference coatings, McGraw-Hill Companies., 1989.

[112] T. Tesfamichael, E. Wäckelgård, Angular solar absorptance of absorbers used in solar thermal collectors, Applied Optics. 38 (1999) 4189. https://doi.org/10.1364/ao.38.004189.

[113] T. Tesfamichael, E. Wäckelgård, Angular solar absorptance and incident angle modifier of selective absorbers for solar thermal collectors, Solar Energy. 68 (2000) 335–341. https://doi.org/10.1016/S0038-092X(00)00029-3.

[114] A. Sakurai, H. Tanikawa, M. Yamada, Computational design for a wide-angle cermet-based solar selective absorber for high temperature applications, Journal of Quantitative Spectroscopy and Radiative Transfer. 132 (2014) 80–89. https://doi.org/10.1016/j.jqsrt.2013.03.004.

[115] N.P. Sergeant, O. Pincon, M. Agrawal, P. Peumans, Design of wide-angle solar-selective absorbers using aperiodic metal-dielectric stacks, Optics Express. 17 (2009) 22800. https://doi.org/10.1364/oe.17.022800.

[116] L. Zheng, F. Zhou, Z. Zhou, X. Song, G. Dong, M. Wang, X. Diao, Angular solar absorptance and thermal stability of Mo-SiO_2 double cermet solar selective absorber coating, Solar Energy. 115 (2015) 341–346. https://doi.org/10.1016/j.solener.2015.02.013.

[117] A. Dan, K. Chattopadhyay, H.C. Barshilia, B. Basu, Angular solar absorptance and thermal stability of W/WAlN/WAlON/Al_2O_3-based solar selective absorber coating, Applied Thermal Engineering. 109 (2016) 997–1002. https://doi.org/10.1016/j.applthermaleng.2016.04.069.

[118] Q. Zhang, High efficiency Al-N cermet solar coatings with double cermet layer film structures, 1938 (1999).

[119] F. Cao, K. McEnaney, G. Chen, Z. Ren, A review of cermet-based spectrally selective solar absorbers, Energy & Environmental Science. 7 (2014) 1615. https://doi.org/10.1039/c3ee43825b.

[120] Y. Ning, W. Wang, Y. Sun, Y. Wu, Y. Liu, Effects of substrates, film thickness and temperature on thermal emittance of Mo/substrate deposited by magnetron sputtering, Vacuum. (2016). https://doi.org/10.1016/j.vacuum.2016.03.008.

[121] J. Wang, B. Wei, Q. Wei, D. Li, pss, 667 (2011) 664–667. https://doi.org/10.1002/pssa.201026301.

[122] L. Zheng, F. Gao, S. Zhao, F. Zhou, J. Pierre, Applied Surface Science Optical design and co-sputtering preparation of high performance Mo – SiO_2 cermet solar selective absorbing coating, Applied Surface Science. 280 (2013) 240–246. https://doi.org/10.1016/j.apsusc.2013.04.142.

[123] Y. Xue, C. Wang, Y. Sun, W. Wang, Y. Wu, Y. Ning, I. Solar, Preparation and spectral properties of solar selective absorbing $MoSi_2$ – Al_2O_3 coating, 1524 (2014) 1519–1524. https://doi.org/10.1002/pssa.201330658.

[124] Y. Zhang, B. Dai, J. Zhang, C. Wang, Y. Zhang, S. Zhao, selective absorbing coating, 167 (2017) 178–183. https://doi.org/10.1016/j.solmat.2017.04.017.

[125] Q. Zhang, Y. Yin, D.R. Mills, High efficiency Mo-AI203 cermet selective surfaces for high-temperature application, 40 (2006) 43–53.

[126] D. Xinkang, W. Cong, W. Tianmin, Z. Long, C. Buliang, R. Ning, Microstructure and spectral selectivity of Mo – Al 2 O 3 solar selective absorbing coatings after annealing, 516 (2008) 3971–3977. https://doi.org/10.1016/j.tsf.2007.07.193.

[127] H. Chen, C. Lee, W. Liao, Y. Chang, Y. Chen, M. Li, C. Lee, C. Kuo, coatings Analysis of High-E ffi ciency Mo-Based Solar Selective Absorber by Admittance Locus Method, (2019).

[128] Y. Zhang, B. Dai, J. Zhang, C. Wang, Y. Zhang, S. Zhao, selective absorbing coating, 167 (2017) 178–183. https://doi.org/10.1016/j.solmat.2017.04.017.

[129] X. Qiu, X. Gao, C. He, G. Liu, Infrared Physics & Technology A novel solar absorber coating based on Mo-MoO_3 nanocrystalline embedded into amorphous TiC : Microstructure , thermal stability and failure analysis, Infrared Physics and Technology. 109 (2020) 103407. https://doi.org/10.1016/j.infrared.2020.103407.

[130] A.C. Badgujar, S.R. Dhage, S. V Joshi, Process parameter impact on properties of sputtered large-area Mo bilayers for CIGS thin film solar cell applications Process parameter impact on properties of sputtered large-area Mo bilayers for CIGS thin fi lm solar cell applications, (2015). https://doi.org/10.1016/j.tsf.2015.04.046.

[131] N. Selvakumar, H.C. Barshilia, K.S. Rajam, A. Biswas, Structure, optical properties and thermal stability of pulsed sputter deposited high temperature HfO_x/Mo/HfO_2 solar selective absorbers, Solar Energy Materials and Solar Cells. 94 (2010) 1412–1420.

https://doi.org/10.1016/j.solmat.2010.04.073.

[132] V.A. Online, W. Ji, R. Shen, R. Yang, G. Yu, X. Guo, L. Peng, W. Ding, Partially nitrided molybdenum trioxide with promoted performance as an anode material for, (2014) 699–704. https://doi.org/10.1039/c3ta13708b.

[133] J.A. Phys, Structural , electrical , and magnetic properties of thin films grown by pulsed laser ablation, 043712 (2017). https://doi.org/10.1063/1.2885143.

[134] M.C. Biesinger, Advanced analysis of copper X-ray photoelectron spectra, (2017) 1325–1334. https://doi.org/10.1002/sia.6239.

[135] M.C. Biesinger, B.P. Payne, A.P. Grosvenor, L.W.M. Lau, A.R. Gerson, R. St, C. Smart, Applied Surface Science Resolving surface chemical states in XPS analysis of first row transition metals , oxides and hydroxides : Cr , Mn , Fe , Co and Ni, Applied Surface Science. 257 (2011) 2717–2730. https://doi.org/10.1016/j.apsusc.2010.10.051.

[136] M.S. Prasad, B. Sobha, K. Suresh, S. Sakthivel, Spectral Selectivity and High Thermal Stability, (2020). https://doi.org/10.1021/acsanm.0c01363.

[137] X. Paquez, G. Amiard, G. de Combarieu, C. Boissière, D. Grosso, Resistant RuO_2/SiO_2 absorbing sol-gel coatings for solar energy conversion at high temperature., Chemistry of Materials. 27 (2015) 2711–2717. https://doi.org/10.1021/acs.chemmater.5b00731.

[138] E. Sani, L. Mercatelli, J. Sans, D. Sciti, Solar Energy Materials & Solar Cells Optical properties of black and white ZrO_2 for solar receiver applications, Solar Energy Materials and Solar Cells. (2015) 1–6. https://doi.org/10.1016/j.solmat.2015.02.007.

[139] R.L. Jones, Thermal barrier coatings, 1970.

[140] M. Shiva Prasad, K. Chandra Sekhar Reddy, S. Sakthivel, Development of cost efficient solar receiver tube with a novel tandem absorber system, Applied Thermal Engineering. 109 (2016) 988–996. https://doi.org/10.1016/j.applthermaleng.2016.05.163.

[141] M. Farooq, Z.H. Lee, Computations of the optical properties of metal/insulator-composites for solar selective absorbers, Renewable Energy. 28 (2003) 1421–1431. https://doi.org/10.1016/S0960-1481(02)00033-2.

[142] N. Pauly, S. Tougaard, F. Yubero, Surface Science Determination of the Cu 2p primary excitation spectra for Cu, Cu_2O and CuO, 620 (2014) 17–22. https://doi.org/10.1016/j.susc.2013.10.009.

[143] A. Davidson, J.F. Tempere, M. Che, M. Curie, M. Curie, Spectroscopic Studies of Nickel (II) and Nickel (III) Species Generated upon Thermal Treatments of Nickel / Ceria-Supported Materials, (1996) 4919–4929.

[144] C.J. Reed, Electrochemical polarization, Journal of the Franklin Institute. 153 (1902) 259–268. https://doi.org/10.1016/s0016-0032(02)90236-x.

[145] H.C. Barshilia, M.S. Prakash, A. Poojari, K.S. Rajam, Corrosion behavior of nanolayered TiN/NbN multilayer coatings prepared by reactive direct current magnetron

sputtering process, Thin Solid Films. 460 (2004) 133–142. https://doi.org/10.1016/j.tsf.2004.01.096.

[146] V.K. William Grips, H.C. Barshilia, V.E. Selvi, Kalavati, K.S. Rajam, Electrochemical behavior of single layer CrN, TiN, TiAlN coatings and nanolayered TiAlN/CrN multilayer coatings prepared by reactive direct current magnetron sputtering, Thin Solid Films. 514 (2006) 204–211. https://doi.org/10.1016/j.tsf.2006.03.008.

[147] K. Kurokawa, T. Sudiro, T. Sano, S. Kyo, O. Ishibashi, M. Nakamori, Mini review High-temperature corrosion resistance of SiO_2 -forming materials, (2018) 1–10.

[148] I. Stambolova, S. Yordanov, L. Lakov, S. Vassilev, V. Blaskov, B. Jivov, Preparation of sol-gel SiO_2 coatings on steel and their corrosion resistance, MATEC Web of Conferences. 145 (2018) 11–16. https://doi.org/10.1051/matecconf/201814505011.

[149] R. Kumar, Ni-Co Co-Modified Anodized Spectrally Selective Coatings with Enhanced Corrosion and Thermal Stability, in: 2017: pp. 1–7. https://doi.org/10.18086/swc.2017.04.07.

[150] K. Zhang, M. Du, L. Hao, J. Meng, J. Wang, J. Mi, X. Liu, Highly Corrosion Resistant and Sandwich-like Si_3N_4/Cr-CrN_x/Si_3N_4 Coatings Used for Solar Selective Absorbing Applications, ACS Applied Materials and Interfaces. 8 (2016) 34008–34018. https://doi.org/10.1021/acsami.6b11607.

[151] J. Mandal, D. Wang, A.C. Overvig, N.N. Shi, D. Paley, A. Zangiabadi, Q. Cheng, K. Barmak, N. Yu, Y. Yang, M. Mwamburi, E. Wäckelgård, A. Roos, R. Kivaisi, N.P. Sergeant, O. Pincon, M. Agrawal, P. Peumans, A. Sakurai, H. Tanikawa, M. Yamada, A. Dan, K. Chattopadhyay, H.C. Barshilia, B. Basu, T. Tesfamichael, E. Wäckelgård, L. Zheng, F. Zhou, Z. Zhou, X. Song, G. Dong, M. Wang, X. Diao, N.P. Harder, P. Würfel, Scalable, "Dip-and-Dry" Fabrication of a Wide-Angle Plasmonic Selective Absorber for High-Efficiency Solar–Thermal Energy Conversion, Applied Optics. 29 (2017) 4189. https://doi.org/10.1002/adma.201702156.

[152] K. Antoniou, J.F. Frank, Removal of Pseudomonas putida biofilm and associated extracellular polymeric substances from stainless steel by alkali cleaning, Journal of Food Protection. 68 (2005) 277–281. https://doi.org/10.4315/0362-028X-68.2.277.

[153] S. Com, Quickly and accurately measure total, diffuse, and specular reflectance in seven bands from 330 nm to 2500 nm, 1 (2019).

[154] M.S. Prasad, K.K.P. Kumar, S.R. Atchuta, B. Sobha, S. Sakthivel, High performance and thermally stable tandem solar selective absorber coating for concentrated solar thermal power (CSP) application, AIP Conference Proceedings. 1961 (2018). https://doi.org/10.1063/1.5035197.

[155] R. Kumar, S. Bharathi, A Review Study on A-TIG Welding of 316(L) Austenitic Stainless Steel, (2015).

[156] J. Sun, Chapter 11 - Hybrid solar power system, in: A.K. Azad (Ed.), Advances in Clean

Energy Technologies, Academic Press, 2021: pp. 405–448. https://doi.org/https://doi.org/10.1016/B978-0-12-821221-9.00011-6.

[157] V.K. Jebasingh, G.M.J. Herbert, A review of solar parabolic trough collector, Renewable and Sustainable Energy Reviews. 54 (2016) 1085–1091. https://doi.org/10.1016/j.rser.2015.10.043.

[158] A.S. Tijani, A.M.S. Bin Roslan, Simulation Analysis of Thermal Losses of Parabolic trough Solar Collector in Malaysia Using Computational Fluid Dynamics, Procedia Technology. 15 (2014) 841–848. https://doi.org/10.1016/j.protcy.2014.09.058.

[159] Dhanaji M. Kale, Ramchandra G. Patil, Sudhir V. Panse, Jyeshtharaj B. Joshi, Experimental Study of Heat Loss from Receivers of Solar Collectors under Different Conditions, International Journal of Engineering Research And. V5 (2016) 567–578. https://doi.org/10.17577/ijertv5is010462.

[160] A.C. Ratzel, C.E. Hickox, D.K. Gartling, Energy Loss by Thermal Conduction and Natural Convection in Annular Solar Receivers, Thermal Conductivity 15. (1978) 423–432. https://doi.org/10.1007/978-1-4615-9083-5_46.

[161] M. Roesle, V. Coskun, A. Steinfeld, Numerical analysis of heat loss from a parabolic trough absorber tube with active vacuum system, ASME 2011 5th International Conference on Energy Sustainability, ES 2011. 133 (2011) 795–801. https://doi.org/10.1115/ES2011-54683.

[162] A.A. Sagade, N.N. Shinde, P.S. Patil, Effect of receiver temperature on performance evaluation of silver coated selective surface compound parabolic reflector with top glass cover, Energy Procedia. 48 (2014) 212–222. https://doi.org/10.1016/j.egypro.2014.02.026.

[163] Q. Yu, J. Mi, Y. Lang, M. Du, S. Li, H. Yang, L. Hao, X. Liu, L. Jiang, Thermal properties of high temperature vacuum receivers used for parabolic trough solar thermal power system, Progress in Natural Science: Materials International. 27 (2017) 410–415. https://doi.org/10.1016/j.pnsc.2017.04.001.

[164] SCHOTT, SCHOTT PTR 70 Receiver, (1992).

List of publications

1. Zirconia nanoparticles embedded spinel selective absorber coating for high performance in open atmospheric condition, M. Shiva Prasad, B. Mallikarjun, M. Ramakrishna, J. Joarder, B. Sobha, S. Sakthivel, Solar Energy Materials, and Solar Cells, 174, 423-432, 2018.
2. High performance and thermally stable tandem solar selective absorber coating for concentrated solar thermal power (CSP) application, M. Shiva Prasad, K. K. Phani Kumar, S.R. Atchuta, B. Sobha, S. Sakthivel, AIP Conference Proceedings, 02004-1 to 02004-7, 2018.
3. $Cu(Mn_{0.748}Ni_{0.252})_2O_4/SiO_2$ Nanoparticle Layers for Wide-Angle Spectral Selectivity and High Thermal Stability, M. Shiva Prasad, B. Sobha, Koppoju Suresh, and Shanmugasundaram Sakthivel, ACS Applied Nano Materials, 3, 7869-7878, 2020.
4. Development of High-Performance Tandem Layered Absorber with Wide-Angular Absorptance for Solar Thermal Systems, M. Shiva Prasad, P. Uday Bhaskar, S. R. Atchuta, P. Misra, B. Sobha, and Shanmugasundaram Sakthivel, 176, 579-589, 2021.